OPTICS OF DIRAC MATERIALS AND LIGHT-MATTER INTERACTION IN THE NANOPHOTONIC SYSTEMS

A Dissertation

by

QIANFAN CHEN

Submitted to the Graduate and Professional School of
Texas A&M University
in partial fulfillment of the requirements for the degree of

DOCTOR OF PHILOSOPHY

Chair of Committee,	Alexey Belyanin
Committee Members,	Artem Abanov
	Alexey Akimov
	Matthew Sheldon
Head of Department,	Grigory Rogachev

August 2021

Major Subject: Physics

ABSTRACT

In recent years condensed matter physics is witnessing a rapid expansion of materials with (massless)Dirac fermions as low-energy excitations, with examples ranging from graphene, topological insulators to Weyl semimetals (WSMs). These materials are named Dirac materials because the low-energy quasiparticles obey the Dirac equation, regardless of their origin. They have electronic and optical properties different from the conventional metals and (doped) semiconductors, which obey the nonrelativistic Schrödinger equation leading to quadratic spectra.

This dissertation is focused on the optics of Dirac materials, especially graphene and WSMs. We present systematic theoretical studies of both bulk and surface electromagnetic eigenmodes, or polaritons, in WSMs in the minimal model of two bands with two separated Weyl nodes. We derive the tensors of bulk and surface conductivity, taking into account all possible combinations of the optical transitions involving bulk and surface electron states. We show how information about Weyl semimetals' electronic structure, such as the position and separation of Weyl nodes, Fermi energy, and Fermi arc surface states, can be unambiguously extracted from measurements of the dispersion, transmission, reflection, and polarization of electromagnetic waves. We also explore the potential of popular tip-enhanced optical spectroscopy techniques for studies of bulk and surface topological electron states in WSMs. Strong anisotropy, anomalous dispersion, and the optical Hall effect for surface polaritons launched by a nanotip provide information about Weyl node position and separation in the Brillouin zone, the value of the Fermi momentum, and the matrix elements of the optical transitions involving both bulk and surface electron states. Furthermore, from the theoretical point of view, we systematically study the inverse Faraday effect in graphene and WSMs. Both semiclassical and quantum theories are presented, with dissipation and finite-size effects included. We find that the magnitude of the effect can be much stronger in Dirac materials as compared to conventional semiconductors. Analytic expressions for the optically induced magnetization in the low-temperature limit are obtained.

Additionally, we study the dynamics of strongly coupled nanophotonic systems with time-

variable parameters. The approximate analytic solutions are obtained for a broad class of open quantum systems, including a two-level fermion emitter strongly coupled to a multimode quantized electromagnetic field in a cavity with time-varying cavity resonances or the electron transition energy. The coupling of the fermion and photon subsystems to their dissipative reservoirs is included within the stochastic equation of evolution approach, equivalent to the Lindblad approximation in the master equation formalism. The analytic solutions for the quantum states and the observables are obtained under the approximation that the rate of parameter modulation and the amplitude of the frequency modulation are much smaller than the optical transition frequencies. At the same time, they can be arbitrary with respect to the generalized Rabi oscillation frequency, which determines the coherent dynamics. Therefore, our analytic theory can be applied to an arbitrary modulation of the parameters, both slower and faster than the Rabi frequency, for complete control of the quantum state. In particular, we demonstrate protocols for switching on and off the entanglement between the fermionic and photonic degrees of freedom, swapping between the quantum states, and decoupling the fermionic qubit from the cavity field due to modulation-induced transparency.

DEDICATION

To my mother, Yueyin Lin, and my father, Danzhu Chen.

ACKNOWLEDGMENTS

I would like to thank my advisor, Dr. Alexey Belyanin, for his continuous support for my Ph.D. study and research. His admirable patience, enthusiasm for physics, and immense knowledge deeply infect me. He gave me the best guidance I ever had in my physics research. I count myself fortunate to become his student.

I am grateful to my committee chair, Dr. Alexey Belyanin, and my committee members, Dr. Artem Abanov, Dr. Alexey Akimov, and Dr. Matthew Sheldon, for allowing me to have a portion of their valuable time. I am appreciative of your insights and suggestions. Thank you.

I would like to thank our collaboration Dr. Mikhail Tokman in Russian Academy of Sciences for his great ideas and the insightful discussions in my research projects.

I would like to thank former and present members of the Belyanin group, Sultan Almutairi, Arjunen Ryan Kutayiah, Zhongqu Long, and Yongrui Wang, for the numerous discussions we have had throughout the years. I especially owe a debt of gratitude to Yongrui Wang, who had given me so much help when I first began my research journey.

I am grateful to the faculty and staff of TAMU's physics department for facilitating a smooth and enjoyable transit through my doctorate program. I was particularly fond of the Physics Festival; thank you, Dr. Tatiana Erukhimova.

CONTRIBUTORS AND FUNDING SOURCES

Contributors

This work was supported by a dissertation committee consisting of Professors Alexey Belyanin [advisor/chair], Artem Abanov, and Alexey Akimov of the Department of Physics and Astronomy and Professor Matthew Sheldon of the Department of Chemistry.

The initial ideas for all projects presented in this dissertation were proposed by Dr. Alexey Belyanin and collaborator Dr. Mikhail Tokman of the Institute of Applied Physics, Russian Academy of Sciences.

Dr. I. D. Tokman of the Institute for Physics of Microstructures, Russian Academy of Sciences, lead the project presented in Chapter 4. Many of the calculations and theoretical developments are attributed to him. Dr. I. A. Shereshevsky and Dr. V. I. Pozdnyakova of the Institute for Physics of Microstructures, Russian Academy of Sciences and Dr. Ivan Oladyshkin of the Institute of Applied Physics, Russian Academy of Sciences also contributed to the theoretical development.

All other work conducted for the dissertation was completed by the student independently.

Funding Sources

Graduate study was supported by Air Force Office for Scientific Research Grant No. FA9550-17-1-0341, National Science Foundation Award No. 1936276, and Texas A&M University through STRP, X-grant, and T3-grant programs.

NOMENCLATURE

WSMs	Weyl Semimetals
TAMU	Texas A&M University
2D	Two-dimensional
3D	Three-dimensional
QED	Quantum Electrodynamics
IQHE	Integer Quantum Hall Effect
SP(s)	Surface Polariton(s)
IFE	Inverse Faraday Effect
EM	Electromagnetic
QDs	Quantum Dots
RWA	Rotating Wave Approximation

TABLE OF CONTENTS

Page

LIST OF FIGURES

FIGURE Page

1. INTRODUCTION

1.1 Dirac and Weyl Fermions

In 1928 P. A. M. Dirac successfully reconciled the special theory of relativity and quantum mechanics to propose his now eponymous Dirac equation [1]. Its form resulted from the principles of relativity that space and time must be treated on an equal footing, as well as constraints from positive probability in the probabilistic interpretation of the wave function that the equations of motion depend only on the first derivative of time. Dirac equation in 3D space composes of 4×4 complex gamma matrices and a four-component spinor wave function. The four components allowed for both positive and negative charge solutions and up and down spin. The discovery of the Dirac equation is an epochal event in the history of physics. It refreshed the understanding of the concept of spin, predicted the existence of antimatter, and led to the rise of quantum field theory.

The Dirac equation in 3D space and the natural units $\hbar = c = 1$ is

$$\left(i\gamma^{\mu}\partial_{\mu} - m\right)\psi = 0, \tag{1.1}$$

where m is the mass of particles, $\mu = 0, 1, 2, 3$ label the time and space dimensions, $\partial_{\mu} = (\partial_t, \nabla)$, and the 4×4 gamma matrices γ^{μ} satisfy the Clifford algebra,

$$\{\gamma^{\mu}, \gamma^{\nu}\} \equiv \gamma^{\mu}\gamma^{\nu} + \gamma^{\nu}\gamma^{\mu} = 2\eta^{\mu\nu}1_{4\times4}, \tag{1.2}$$

where $\eta^{\mu\nu} = diag\,(1, -1, -1, -1)$ is the metric tensor of spacetime and $1_{4\times4}$ is a 4×4 identity matrix. In 3D space, one can form another Hermitian matrix

$$\gamma_5 \equiv i\gamma^0\gamma^1\gamma^2\gamma^3, \tag{1.3}$$

which anticommutes with gamma matrices γ^μ, i.e. $\{\gamma_5, \gamma^\mu\} = 0$. There are many representations of gamma matrices satisfying Eq. (1.2). It is possible to show that an unitary transformation preserves the Clifford algebra. For example, the gamma matrices in the Weyl or chiral representation is given by

$$\gamma^0 = \begin{pmatrix} 0 & 1_{2\times2} \\ 1_{2\times2} & 0 \end{pmatrix}, \quad \gamma^j = \begin{pmatrix} 0 & \sigma^j \\ -\sigma^j & 0 \end{pmatrix}, \quad \gamma_5 = \begin{pmatrix} -1_{2\times2} & 0 \\ 0 & 1_{2\times2} \end{pmatrix} \tag{1.4}$$

where $1_{2\times2}$ is a 2×2 identity matrix and σ^j are the usual Pauli matrices. In general, the solutions of Dirac equation are four component spinors describing the massive spin-1/2 particles living in 3D space called massive Dirac fermions. For the massless Dirac fermions, i.e. $m = 0$, Dirac equation can be simplified into a new form in the Weyl or chiral representation, called Weyl equation

$$i\partial_t \psi_\pm = H_\pm \psi_\pm, \tag{1.5}$$

where

$$H_\pm = \pm \mathbf{p} \cdot \boldsymbol{\sigma}. \tag{1.6}$$

The solutions of Weyl equation $\psi_\pm$ are effectively two component spinors satisfying

$$\gamma_5 \psi_\pm = \pm \psi_\pm, \tag{1.7}$$

which describe massless fermions of opposite chirality living in 3D space called Weyl fermions.

1.2 Dirac materials

Although after 90 years of exploring, Weyl fermions have never been observed as fundamental particles in nature, in recent years condensed matter physics is witnessing a rapid expansion of materials with (massless) Dirac fermions as low-energy excitations. These seemingly diverse materials possess some universal properties because of the linear spectrum of the low-energy excitations. For example, Dirac nodes in the quasi-particles spectrum control low-energy properties,

such as the fermionic specific heat of these materials. These materials are named Dirac materials because the low-energy quasiparticles obey the Dirac equation, regardless of their origin. They have electronic and optical properties different from the conventional metals and (doped) semiconductors, which obey the nonrelativistic Schrödinger equation leading to quadratic spectra. The typical examples of Dirac materials include 2D graphene [2, 3], surface states in 2D/3D topological insulators [4, 5] and 3D Weyl semimetals(WSMs) [6, 7].

So far, most of the research on the Dirac materials has been focused on measuring and modeling their electronic structure and topological signatures in electron transport. There are relatively fewer works concerning the optical aspects of the Dirac materials. Chapters 2-4 of this dissertation focus on the optics of Dirac materials, especially graphene and WSMs. They have many potential applications in designing the new generation of optical and electronic devices and the development of quantum technologies.

1.2.1 Graphene

Graphene might arguably be the most famous Dirac material [8, 9]. One of graphene's most distinctive traits is that the quasi-electrons near the Dirac cone are massless 2D Dirac fermions [2, 3]. This linear energy spectrum for low-energy excitations mimics the relativistic quantum electrodynamics (QED) for massless fermions except that in graphene, the speed of Dirac fermions is 300 times slower than the speed of light in the vacuum [10]. The relativistic dispersion leads to a series of novel physical phenomena, such as the anomalous integer quantum Hall effect (IQHE) [11, 12], a trademark of Dirac fermion behavior. The IQHE in graphene can be observed at room temperature [13] due to graphene's large cyclotron energy. Other interesting features of graphene indicating the characteristics of Dirac fermions include the Klein paradox [45], insensitivity to external electrostatic potential; a 'minimum' conductivity even when the carrier concentration is almost zero [14], and a phase shift of Shubnikov-de Haas oscillations [15]. Besides the electronic structure and electron transport in graphene, graphene's optical properties also attract enormous interest. For example, graphene exhibits constant white light absorbance [16], where the transmittance can be expressed in terms of the fine-structure constant. Hot luminescence is observed as due

to non-equilibrium carriers [17], and Pauli blocking results in saturable absorption [18]. Additionally, graphene's linear dispersion exhibits promising applications in photonics and optoelectronics [19]. Graphene possesses low sheet resistance and high transparency [20], making the graphene sheet a promising material to build optoelectronic devices such as displays, touch screens, and light-emitting diodes [19]. Graphene-based photodetectors are demonstrated to be ultrafast and work over an extensive wavelength range [21]. Graphene devices can also be used for terahertz detection and frequency conversion, including modulators, filters, switches, and polarizers [19].

1.2.1.1 Band structure of monolayer graphene

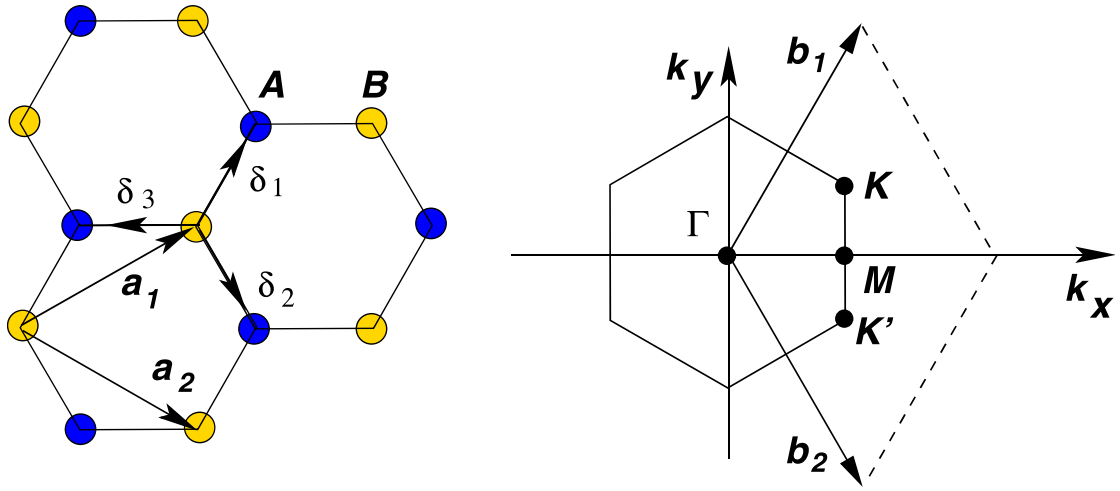

Figure 1.1: Left: lattice structure of graphene. a_1 and a_2 are the lattice unit vectors, and $\mathbf{ffi}_1$, $\mathbf{ffi}_2$ and $\mathbf{ffi}_3$ are the nearest-neighbor vectors. Right: the corresponding first Brillouin zone. (Reprinted figure with permission from Castro Neto et al., *Rev. Mod. Phys.*, Vol.81, No.1, Jan.-Mar. 2009. Copyright (2009) by the American Physical Society.)

Monolayer graphene consists of a single layer of carbon atoms tightly packed into a honeycomb lattice, as shown in the left part of Figure 1.1. The hexagonal Bravais lattice's each unit cell contains two carbon atoms giving rise to two sublattices, A and B. Obviously, atoms in sublattice A are surrounded by three nearest neighbors in sublattice B and vice versa. Therefore, if one only considers nearest-neighbor coupling, the lattice is bipartite.

Nearby the Fermi surface, all electronic states consist of the out-of-plane carbon p_z orbitals. These form π-bonds with neighboring atoms, and the resulting π-bands can be easily understood from a tight-binding Hamiltonian:

$$H = -t \sum_{\langle i,j \rangle} a_i^\dagger b_j + a_j^\dagger b_i \tag{1.8}$$

which consists of a hopping term $t \approx 2.7$ eV between nearest-neighbor atoms. Here, a_i and b_i annihilate electrons in the p_z carbon atomic orbitals in unit cell i in sublattices A and B, respectively. As there are two atoms per unit cell, the Hamiltonian Eq. (1.8) leads to a 2×2 matrix in momentum space representation:

$$H(\mathbf{k}) = \begin{pmatrix} 0 & \xi(\mathbf{k}) \\ \xi^*(\mathbf{k}) & 0 \end{pmatrix}, \tag{1.9}$$

with $\xi(\mathbf{k}) = -t\left(e^{i\boldsymbol{\delta}_1 \cdot \mathbf{k}} + e^{i\boldsymbol{\delta}_2 \cdot \mathbf{k}} + e^{i\boldsymbol{\delta}_3 \cdot \mathbf{k}}\right)$. The three partial hopping amplitudes entering in $\xi(\mathbf{k})$ come from the hopping processes connecting each atom in the sublattice A with its three nearest neighbors in the sublattice B through the vectors $\boldsymbol{\delta}_i$ and vice versa. The energy bands result $\epsilon(\mathbf{k}) = \pm|\xi(\mathbf{k})|$. It is only at the Brillouin zone's two inequivalent corners $\mathbf{K}$ and $\mathbf{K}' = -\mathbf{K}$, which are called Dirac points, that the dispersive term vanishes, i.e. $\xi(\mathbf{k}) = 0$, so that there the two bands are degenerate.

Because one unit cell contains two atoms, and each one contributes one p_z electron, the lower π band is completely filled while the upper π^* band is empty in the undoped graphene. The Fermi level thus lies at the band degeneracy points at $\mathbf{K}$ and $\mathbf{K}'$ where energy $\epsilon(\pm\mathbf{K}) = 0$. In the vicinity

of Dirac points, one can expand full band structure close to $\pm\mathbf{K}$ as $\mathbf{k} = \pm\mathbf{K} + \mathbf{q}$, yielding up to a constant phase factor

$$H\left(\pm\mathbf{K}+\mathbf{q}\right) = \hbar v_F \begin{pmatrix} 0 & q_x \mp i q_y \\ q_x \pm i q_y & 0 \end{pmatrix}, \tag{1.10}$$

where the vector $\mathbf{q} = (q_x, q_y)$ is given in the coordinate frame indicated in the right part of Figure 1.1. This is the 2D Dirac Hamiltonian, with the effective speed of light (Fermi velocity) $v_F \approx 10^8\ cm/s$. Graphene thus hosts fourfold degenerate of Dirac fermions: two (real electron) spin degenerate cones in each of the two valleys near $\mathbf{K}$ and $\mathbf{K}'$. The pseudo-spin in the graphene corresponds to the sublattice degree of freedom and is thus fundamentally different from the real electron spin. It can be shown that under rotations of the entire graphene sheet by an angle of 2π, the pseudo-spin acquires a phase of π. Thus, the transformation behavior under rotation is the same as for a real spin-1/2 [22].

1.2.1.2 Landau levels of graphene

The characteristics of graphene in an external magnetic field show stark contrast to the conventional 2D degenerate electron gases. In an external constant magnetic field $B\mathbf{z}$ perpendicular to the plane of monolayer graphene, the continuous energy bands near the Dirac points split into discrete Landau levels. The 2D Dirac Hamiltonian near the $\mathbf{K}$ point becomes

$$H\left(\mathbf{K}+\boldsymbol{\pi}\right) = v_F \begin{pmatrix} 0 & \pi_x - i\pi_y \\ \pi_x + i\pi_y & 0 \end{pmatrix}, \tag{1.11}$$

under the standard Peierls substitution [23] $\mathbf{p} \to \boldsymbol{\pi} = \mathbf{p} + \frac{e}{c}\mathbf{A}$, where e is the elementary electric charge, $\mathbf{p} = \hbar\mathbf{q}$ is the quasimomentum and $\mathbf{A} = (0, Bx)$ is the vertor potential for a constant magnetic field in the Landau gauge. The resulting eigenfunction is characterized by two good quantum number n and q_y, where $n = 0, \pm1, \pm2\cdots$ are principal numbers of the Landau levels,

and q_y is the y-component of electron wave vector $\mathbf{q}$ [24]:

$$\Psi_{n,\mathbf{K}}\left(q_y,\mathbf{r}\right)=\frac{C_n}{\sqrt{L_y}}e^{-iq_y y}\begin{pmatrix}\operatorname{sgn}\left(n\right)i^{|n|-1}\phi_{|n|-1}\\ i^{|n|}\phi_{|n|}\end{pmatrix} \tag{1.12}$$

$$\phi_{|n|}=\frac{H_{|n|}\left(\frac{x-q_y l_c^2}{l_c}\right)}{\sqrt{2^{|n|}\,|n|!\sqrt{\pi}l_c}}\exp\left[-\frac{1}{2}\left(\frac{x-q_y l_c^2}{l_c}\right)^2\right], \tag{1.13}$$

where $H_n\left(\xi\right)$ is the Hermite polynomial, $l_c=\sqrt{\frac{\hbar c}{eB_z}}$ is the magnetic length, $C_0=1$, $C_{n\neq 0}=\frac{1}{\sqrt{2}}$. The eigenenergy ε depends only on the Landau level number:

$$\varepsilon=\varepsilon_n=\operatorname{sgn}\left(n\right)\hbar\omega_c\sqrt{|n|}, \tag{1.14}$$

where $\omega_c=\frac{\sqrt{2}v_F}{l_c}$ is the cyclotron frequency. A positive or negative value of n corresponds to the electrons or holes. Comparing with Landau levels for the 2D degenerate electron gases with a parabolic dispersion, $E_n=\left(n+\frac{1}{2}\right)\frac{\hbar eB}{m^*}$; Landau levels in graphene are unequally spaced: $\propto\sqrt{B}$. The magnetic field 'condenses' the original electron states in the Dirac cone into discrete Landau levels and each Landau level contains the same areal density of states $N_\Phi=\frac{2}{\pi l_c^2}$, including (real electron) spin and valley degeneracy factors. Infrared spectroscopy of Landau levels of graphene has already been realized in experiments [25], and becomes a strong tool to study IQHE as well as graphene's magneto-optical properties [26].

1.2.2 Weyl semimetals

Dirac materials without degeneracy in the crossing bands, creating a Weyl node, has been referred to as WSMs [27]. The simplest form of a low-energy effective Hamiltonian describing Weyl fermions in WSMs, consisting of two Weyl nodes is

$$H=\pm\hbar v_F\mathbf{k}\cdot\boldsymbol{\sigma}. \tag{1.15}$$

Here $\boldsymbol{\sigma} = (\sigma_x, \sigma_{y,}\sigma_z)$ are the three Pauli matrices acting in the space of the two bands, causing the band crossings, and $\hbar\mathbf{k} = \hbar\,(k_x, k_{y,}k_z)$ measures the momentum counted from the Weyl nodes $\mathbf{k}_\pm$. The velocity $\mathbf{v} = \pm v_F\boldsymbol{\sigma}$ is either parallel or antiparallel to the (pseudo)-spin and set by the chirality. The above Hamiltonian has a linear energy spectrum $E = \hbar v_F|\mathbf{k}|$ in the vicinity of both Weyl nodes, as expected of a Dirac material. This Hamiltonian is a simplified version of a general anisotropic Weyl Hamiltonian where Weyl fermions have different velocities in three independent but not necessarily orthogonal directions.

Even with the simplification of an isotropic velocity, Eq. (1.15) reveals several unique features of WSMs. First of all, the Weyl points are topological objects in momentum space. The Weyl point looks like a magnetic monopole in momentum space, with the spin vectors are parallel or antiparallel to the momentum of electrons depending on the chirality. Mathematically, this can be seen by constructing the effective vector potential $\mathbf{A}\,(\mathbf{k})$ and the corresponding magnetic field strength $\mathbf{B}(\mathbf{k})$ for the Bloch states $|u_{n,\mathbf{k}}\rangle$:

$$\mathbf{A}\,(\mathbf{k}) = -i\sum_{n,occ}\langle u_{n,\mathbf{k}}|\,\nabla_{\mathbf{k}}\,|u_{n,\mathbf{k}}\rangle\,, \tag{1.16}$$

$$\mathbf{B}(\mathbf{k}) = \nabla\times\mathbf{A}\,(\mathbf{k})\,, \tag{1.17}$$

where the summation is over-occupied bands n. $\mathbf{B}(\mathbf{k})$ is also known as the Berry curvature or flux. Integrating this flux through a small Fermi surface containing the Weyl point yields $\pm 2\pi$, as e.g. shown in Reference [28]. According to Gauss's law, this is then also the flux through any surface containing the Weyl point, and the Weyl point can thus be regarded as a magnetic monopole. If we instead apply Gauss's law around the whole Brillouin zone, we need to obtain a net-zero flux; there cannot be an overall magnetic source or sink. This means that Weyl points always come in pairs with opposite chirality. This is known as the fermion doubling theorem [29, 30] and explains why Eq. (1.15) has two crossing points $\mathbf{k}_\pm$ with opposite chirality.

Magnetic charge conservation also directly gives the stability of a single Weyl point because it cannot just suddenly disappear. The stability of the Weyl points can also be seen directly from

the Hamiltonian in Eq. (1.15) since it uses all three Pauli matrices. Thus, there is no 2×2 matrix left that anticommutes with the Hamiltonian and can open a gap in the spectrum. Therefore, the only way to destroy a Weyl point is to annihilate it with another Weyl point of opposite chirality. This can be done either by moving the Weyl points in momentum space and finally merging them, leading to a fully gapped insulator, or breaking translational symmetry by scattering between the two Weyl points. Furthermore, the topological protection of the Weyl points crucially requires the non-degenerate bands. Otherwise, there can be terms that cause band hybridization within the degenerate subspaces and, in that way, produce an energy gap. Non-degenerate bands require either time reversal symmetry or inversion symmetry breaking. Time-reversal symmetry breaking due to a type of magnetic order can realize the minimal case of a single pair of Weyl points [27]. Inversion symmetry breaking has been shown to generate at least four Weyl points in the Brillouin zone [31].

One of the most striking features of WSMs is that their surface states can form Fermi arcs [27]. We usually expect the Fermi surface to form closed loops, but in WSMs, this is not true. The Fermi arc on the top surface is instead complemented by the Fermi arc on the bottom surface, such that they together form a closed surface, as expected for a 2D system. In a thin film, two halves of the Fermi surface will spatially separate to opposite sides of the film as the film thickness is increased. These separated Fermi arcs can be understood by the following reasoning. Let us assume a 3D thick film of WSMs with surfaces in the xy plane. We can use translational invariance for a clean surface and label the single-electron states by the crystal momentum in this plane. Further, let us assume that we have a single pair of Weyl points described in Eq. (1.15). We thus find both the surface states and the states associated with the bulk Weyl points at the Fermi energy. For momenta away from the Weyl points, the surface states are well defined because there are no other bulk excitations available. On the other hand, at the Weyl points, the surface states will terminate, and they will thus describe an arc between the two Weyl points, as illustrated by the pink plane in Figure 1.2 (b) cutting the green horizontal Fermi level. The Fermi arc surface states also follow by noting that the Weyl points are monopoles of the Berry flux. If we place two 2D momentum

space surfaces in, say, the yz-plane, one between the two Weyl points and one on the outside as shown in Figure 1.2 (a) there will be a non-zero net flux through the two of them. Thus, the Chern numbers associated with each plane differ by one, and thus at least one plane has a non-zero Chern number. Each non-zero Chern number plane describes a 2D quantum Hall state or Chern insulator, which have, per definition, a chiral surface state which crosses the Fermi level. Putting the edge states of all possible 2D momentum space planes together, we arrive at a Fermi arc connecting the two Weyl points. This unique Fermi arc feature of the WSMs should provide strong evidence for a WSMs state for surface-sensitive probes.

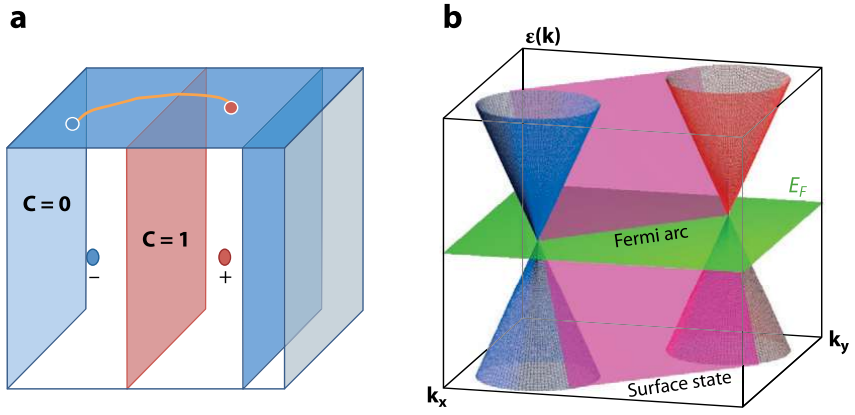

Figure 1.2: Weyl semimetal. (a) The Fermi arc surface states of a Weyl semimetal. (b) The surface states of a Weyl SM form a Fermi arc connecting the two Weyl points. The bulk dispersion of the two Weyl cones (blue and red) along with the surface states (pink plane) crossing the horizontal Fermi level and thus forming a Fermi arc. (Reprinted figure with permission from Oskar Vafek and Ashvin Vishwanath, *Annu. Rev. Condens.Matter Phys.*, 2014. 5:83-112. Copyright (2014) by Annual Reviews.)

1.3 Jaynes-Cummings model

The Jaynes–Cummings model is a theoretical model in quantum optics. It describes a two-level system interacting with a quantized mode of a bosonic field, with or without the presence of light (in the form of an electromagnetic radiation bath that can cause spontaneous emission and absorption). It was originally developed to study the interaction of atoms with the quantized electromagnetic field in order to investigate the phenomena of spontaneous emission and absorption of photons in a cavity [32].

The Jaynes–Cummings model is of great interest to atomic physics, quantum optics, and solid-state physics, both experimentally and theoretically [33]. It also has many applications in coherent control and quantum information processing. Chapter 5 of this dissertation exploit a time-dependent Jaynes–Cummings model to study the dynamics of strongly coupled nanophotonic systems with time-variable parameters.

1.3.1 Jaynes-Cummings Hamiltonian and dressed states

The Jaynes–Cummings Hamiltonian can be written as

$$\hat{H} = \hbar\omega\hat{a}^{\dagger}\hat{a} + \frac{1}{2}\hbar\omega_A\hat{\sigma}_z - \hbar g\left(\hat{a}\hat{\sigma}^{\dagger} + \hat{a}^{\dagger}\hat{\sigma}\right), \tag{1.18}$$

where the coupling constant g is effectively the product of the dipole moment and the mode function of the cavity mode at the position of the atom. The Hamiltonian (1.18) describes one of the few exactly solvable models in quantum optics. Since the interaction Hamiltonian only couples pairs of atom-field states $\{|n+1,g\rangle, |n,e\rangle\}$, the Jaynes–Cummings Hamiltonian (1.18) decouples into an infinite direct product of 2×2-matrix Hamiltonians

$$\hat{H}_n \begin{pmatrix} |n+1,g\rangle \\ |n,e\rangle \end{pmatrix} = \hbar \begin{pmatrix} (n+1)\,\omega - \frac{1}{2}\omega_A & -g\sqrt{n+1} \\ -g\sqrt{n+1} & n\omega + \frac{1}{2}\omega_A \end{pmatrix} \begin{pmatrix} |n+1,g\rangle \\ |n,e\rangle \end{pmatrix}.$$

The eigenvalue problem for this Hamiltonian yields the eigenfrequencies

$$\omega_{n,\pm} = \left(n + \frac{1}{2}\right)\omega \pm \frac{1}{2}\sqrt{\delta^2 + \Omega_n^2} \tag{1.19}$$

where $\delta = \omega - \omega_A$ is the detuning of the radiation frequency from the atomic resonance. The parameter $\Omega_n = 2g\sqrt{n+1}$ is called the n-photon Rabi frequency. The corresponding eigenstates are

$$\begin{aligned} |n,+\rangle &= \cos\theta_n \,|n+1,g\rangle - \sin\theta_n \,|n,e\rangle\,, \\ |n,-\rangle &= \sin\theta_n \,|n+1,g\rangle + \cos\theta_n \,|n,e\rangle\,, \end{aligned} \tag{1.20}$$

where

$$\cos\theta_n = \frac{\triangle_n - \delta}{\sqrt{\left(\triangle_n - \delta\right)^2 + \Omega_n^2}}, \quad \sin\theta_n = \frac{\Omega_n}{\sqrt{\left(\triangle_n - \delta\right)^2 + \Omega_n^2}} \tag{1.21}$$

with $\triangle_n = \sqrt{\delta^2 + \Omega_n^2}$.

The eigenstates $|n,\pm\rangle$ are called *dressed-atom* states. The unperturbed (bared) atomic eigenstates $|g\rangle$ and $|e\rangle$ are modified (dressed) by the interaction with the cavity field, and their eigenfrequencies are shifted by an amount determined by the coupling strength. This is the dynamical Stark effect. For zero detuning, i.e. $\delta = 0$, the unperturbed (degenerate) eigenfrequencies of the states $|n+1,g\rangle$ and $|n,e\rangle$ are $\left(n+\frac{1}{2}\right)\omega$ which are split due to the interaction by an amount $\Omega_n = 2g\sqrt{n+1}$. Even if no photon is present in the cavity, there will be a level splitting, the *vacuum Rabi splitting* $\Omega_0 = 2g$, between the exact eigenstates of the atom-cavity system.

Since we know the eigenvalues and eigenstates of the Jaynes–Cummings Hamiltonian (1.18), we know how to compute the unitary time evolution operator $\hat{U}(t) = e^{-i\frac{\hat{H}}{\hbar}t}$. The dressed states (1.20), together with the ground state $|0,g\rangle$, form a complete set of eigenstates of the Hamiltonian. Hence, the unitary operator $\hat{U}(t)$ can be written as

$$\hat{U}(t) \;=\; e^{-i\frac{\hat{H}}{\hbar}t}$$

$$
\begin{aligned}
&= e^{i\frac{\omega_A}{2}t}\left|0,g\right\rangle\left\langle 0,g\right| + \sum_{\sigma=\pm}\sum_{n=0}^{\infty} e^{-i\omega_{n,\sigma}t}\left|n,\sigma\right\rangle\left\langle n,\sigma\right| \\
&= e^{i\frac{\omega_A}{2}t}\left|0,g\right\rangle\left\langle 0,g\right| + \sum_{n=0}^{\infty} e^{-i\left(n+\frac{1}{2}\right)\omega t}\left[e^{-i\frac{\triangle_n}{2}\omega t}\left|n,+\right\rangle\left\langle n,+\right| + e^{i\frac{\triangle_n}{2}\omega t}\left|n,-\right\rangle\left\langle n,-\right|\right] \qquad (1.22) \\
&= e^{i\frac{\omega_A}{2}t}\left|0,g\right\rangle\left\langle 0,g\right| + \sum_{n=0}^{\infty} e^{-i\left(n+\frac{1}{2}\right)\omega t} \\
&\quad \times \left[\begin{array}{c} \left(\cos\frac{\triangle_n t}{2} + i\frac{\delta}{\triangle_n}\sin\frac{\triangle_n t}{2}\right)\left|n+1,g\right\rangle\left\langle n+1,g\right| + \left(\cos\frac{\triangle_n t}{2} - i\frac{\delta}{\triangle_n}\sin\frac{\triangle_n t}{2}\right)\left|n,e\right\rangle\left\langle n,e\right| \\ +i\frac{\Omega_n}{\triangle_n}\sin\frac{\triangle_n t}{2}\left(\left|n+1,g\right\rangle\left\langle n,e\right| + \left|n,e\right\rangle\left\langle n+1,g\right|\right) \end{array}\right]
\end{aligned}
$$

where we used the expressions (1.20) to write the dressed states in terms of the unperturbed eigenstates.

The unitary operator (1.22) describes the full dynamics of the Jaynes–Cummings model. In particular, we can compute the time evolution of the density operator

$$\hat{\rho}\left(t\right) = \hat{U}\left(t\right)\hat{\rho}\left(0\right)\hat{U}^{\dagger}\left(t\right). \qquad (1.23)$$

Let the density operator at the initial time be in a product state, $\hat{\rho}\left(0\right) = \hat{\rho}_F\left(0\right)\otimes\hat{\sigma}\left(0\right)$. The quantum state of the atom alone is then obtained by taking the trace over the photonic degrees of freedom,

$$
\begin{aligned}
\hat{\sigma}\left(t\right) &= Tr_F\hat{\rho}\left(t\right) \\
&= Tr_F\left[\hat{U}\left(t\right)\left(\hat{\rho}_F\left(0\right)\otimes\hat{\sigma}\left(0\right)\right)\hat{U}^{\dagger}\left(t\right)\right] \\
&= \sum_{n=0}^{\infty}\left\langle n\right|\hat{U}\left(t\right)\left(\hat{\rho}_F\left(0\right)\otimes\hat{\sigma}\left(0\right)\right)\hat{U}^{\dagger}\left(t\right)\left|n\right\rangle. \qquad (1.24)
\end{aligned}
$$

Let us concentrate on the atomic excited-state population $\sigma_{ee}\left(t\right)$. Note that it is an experimentally accessible quantity that can be measured by ionizing the atom state selectively. If a sample of equally prepared atoms is sent through the cavity and, after having left the cavity is irradiated with a laser of a frequency that just exceeds the ionization energy of the excited state, the recorded fraction of ions out of the total atom number is just $\sigma_{ee}\left(t\right)$.

The excited-state population can be computed from Eq. (1.24) as

$$\sigma_{ee}(t) = \sum_{n=0}^{\infty} \langle n, e| \hat{U}(t) \left(\hat{\rho}_F(0) \otimes \hat{\sigma}(0)\right) \hat{U}^{\dagger}(t) |n, e\rangle . \tag{1.25}$$

The general expression (1.25) with $\hat{U}(t)$ given by Eq. (1.22) is of rather complicated form. It has a simplified version in the case of zero detuning, i.e. $\delta = 0$,

$$\sigma_{ee}(t) = \sum_{n=0}^{\infty} \left\{ \cos^2 \frac{\Omega_n t}{2} \rho_{n,n}(0) \sigma_{ee}(0) + \sin^2 \frac{\Omega_n t}{2} \rho_{n+1,n+1}(0) \sigma_{gg}(0) + \mathrm{Im}\left[\frac{1}{2} \sin \Omega_n t \rho_{n+1,n}(0) \sigma_{ge}(0)\right] \right\}. \tag{1.26}$$

If the atom has been initially prepared in its excited state, i.e. $\sigma_{ee}(0) = 1$, then the time evolution simplifies to

$$\sigma_{ee}(t) = \frac{1}{2}\left[1 + \sum_{n=0}^{\infty} \cos \Omega_n t \rho_{n,n}(0)\right]. \tag{1.27}$$

1.3.2 Collapse and revival of atomic populations

The atomic excited-state population, Eq. (1.27), is an incoherent sum of oscillations with the n-photon Rabi frequencies $\Omega_n = 2g\sqrt{n+1}$. Only if the cavity field had initially been prepared in a number state $|k\rangle$, the atomic population oscillates as a single sinusoidal function, $\sigma_{ee}(t) = \frac{1}{2}(1 + \cos \Omega_k t)$. Thus the incoherent summation of oscillatory terms with incommensurable frequencies in Eq. (1.27) seems to wash out all the oscillations if the cavity field contains more than one number state contribution. However, a coherent state with amplitude α shows a Poissonian distribution of photon numbers, i.e. $\rho_{n,n}(0) = \frac{|\alpha|^{2n}}{n!} e^{-|\alpha|^2}$, in which case

$$\sigma_{ee}(t) = \frac{1}{2}\left[1 + \sum_{n=0}^{\infty} \frac{|\alpha|^{2n}}{n!} e^{-|\alpha|^2} \cos\left(2g\sqrt{n+1}t\right)\right]. \tag{1.28}$$

The oscillations collapse after a certain time but reappear periodically. This *collapse and revival* is a quantum interference effect and has nothing to do with dissipation as in resonance fluorescence.

For large mean photon number, $|\alpha|^2 \gg 1$, the Rabi frequencies can be approximated by

$$\Omega_n \approx 2g\sqrt{|\alpha|^2+1}\left(1+\frac{n-|\alpha|^2}{2\left(|\alpha|^2+1\right)}+\cdots\right) \approx 2g\,|\alpha|\left(1+\frac{n-|\alpha|^2}{2\,|\alpha|^2}\right). \tag{1.29}$$

With that, we can perform the summation analytically to obtain

$$\sigma_{ee}(t) \simeq \frac{1}{2}\left[1+e^{-|\alpha|^2}\mathrm{Re}e^{i|\alpha|gt}e^{|\alpha|^2\exp\left(\frac{igt}{|\alpha|}\right)}\right]. \tag{1.30}$$

For sufficiently short times such that $gt \ll |\alpha|$, we can expand the double exponential to second order and are left with

$$\sigma_{ee}(t) \simeq \frac{1}{2}\left[1+e^{-\frac{g^2t^2}{2}}\cos 2g\,|\alpha|\,t\right], \tag{1.31}$$

which shows that the oscillations with an effective Rabi frequency $\Omega_{eff} = 2g\,|\alpha|$ collapse after a characteristic time $t_c = \frac{\sqrt{2}}{g}$.

2. ELECTROMAGNETIC PROPERTIES AND POLARITONS OF TYPE-I MAGNETIC WEYL SEMIMETALS*

In this chapter, we present systematic theoretical studies of both bulk and surface electromagnetic eigenmodes, or polaritons, in Weyl semimetals in the minimal model of two bands with two separated Weyl nodes. We derive the tensors of bulk and surface conductivity taking into account all possible combinations of the optical transitions involving bulk and surface electron states. We show how information about electronic structure of Weyl semimetals, such as position and separation of Weyl nodes, Fermi energy, and Fermi arc surface states, can be unambiguously extracted from measurements of the dispersion, transmission, reflection, and polarization of electromagnetic waves.

2.1 Introduction

Weyl semimetals (WSMs) have attracted a lot of interest as a new class of gapless three-dimensional topological materials. Their Brillouin zone contains an even number of band-touching points, or Weyl nodes, that can be described by topological invariants defined as integrals over the two-dimensional Fermi surface. For each pair of Weyl nodes, these invariants can be viewed as topological chiral charges of opposite sign of chirality [34]. The electron dispersion near each Weyl node corresponds to three-dimensional massless Weyl fermions. For crystals with broken time-reversal or inversion symmetry (or both), the Weyl nodes of opposite chirality are separated in momentum space. The separation makes them stable against small perturbations and also gives rise to surface states with Fermi arcs. For reviews of WSMs discovered so far and their properties, see [35, 36, 6, 7, 37, 38].

So far, the bulk of the research has been focused on measuring and modeling the electronic structure of WSMs and topological signatures in electron transport. However, it is becoming

increasingly clear that optical methods (e.g. [39]) can provide a sensitive and sometimes more selective probe into the unique properties of these materials as compared to other approaches. Furthermore, analogies between light propagation in materials and topological effects in propagation of massless Weyl fermions in WSMs have been pointed out [40, 41]. For a WSM in a magnetic field several proposals explored the signatures of the chiral anomaly in the interband optical absorption and plasmon mode properties; see e.g. the calculations of the magnetooptical conductivity in the quasiclassical limit [42, 43, 44, 45, 46, 47, 48] and the quantum-mechanical theory in a strong magnetic field [49, 50]. Note that these studies did not include finite separation of Weyl nodes in a microscopic Hamiltonian.

Here we study electromagnetic eigenmodes of WSMs in the presence of finite separation between Weyl nodes in momentum space and without an external magnetic field. To calculate the optical response, one needs to determine a realistic low-energy Hamiltonian that captures the essential topological structure of WSMs. While many WSMs discovered in experiment have a complicated arrangement of several pairs of Weyl nodes, essential physics and electronic properties of WSMs are already revealed in a model containing only two Weyl nodes separated in momentum space. Such models serve as a usual starting point for theoretical studies of transport and optical phenomena. Probably the simplest approach is to add a Zeeman-like constant shift term to the Hamiltonian for a Dirac semimetal, which preserves the linear form of the Hamiltonian with respect to momentum operators [51]. The bulk optical conductivity for this model was calculated in [52]. In another approach, developed in [53] and used in many optical response studies to date, a phenomenological axion θ-term is introduced in the action for the electromagnetic field. This gives rise to the gyrotropic terms in the dielectric permittivity tensor and associated effects of Faraday and Kerr rotation, linear dichroism, modification of surface plasmon dispersion etc.; see e.g. [54, 55, 56, 38].

In yet another approach, Burkov and Balents [57] derived a minimal 2x2 Hamiltonian (one conduction and one valence band) containing one parameter which describes the transition from the normal insulator to the WSM with two Weyl nodes separated in momentum space. In the

WSM phase, this Hamiltonian allows for surface state solutions with Fermi arcs. Therefore, a single microscopic Hamiltonian can be used to describe optical transitions between the bulk states, surface states, and surface-to-bulk states. As a result, both bulk and surface tensors of the optical conductivity can be derived. Subsequent studies [58] explored the dispersion of bulk and surface states within the minimal Hamiltonian model and their evolution from the WSM phase to bulk insulating phases including topological insulators. The Hamiltonian of [58] has been recently used to develop a quantum-mechanical theory of surface plasmons (Fermi arc plasmons) and their dissipation [59].

Here we use a slightly more general Hamiltonian, which is free of certain surface state pathologies, to perform quantum-mechanical derivation of the tensors of both bulk and surface conductivity. We take into account all possible combinations of transitions between bulk and surface electron states. We then proceed to determine the properties of bulk and surface electromagnetic eigenmodes, or polaritons. We show how information about the electronic structure of WSMs, such as position and separation of Weyl nodes, Fermi energy, surface states, Fermi arcs, etc. can be extracted from the transmission, dispersion, reflection, and polarization of electromagnetic modes. We identify the most sensitive optical signatures of the electronic properties of WSMs and discuss the potential use of WSM thin films for optoelectronic applications.

Since our model includes only two Weyl nodes of opposite chirality, it describes WSMs with time reversal symmetry breaking, i.e. the materials with some kind of magnetic ordering. Examples discovered so far include pyrochlore iridates [27], ferromagnetic spinels [60], and Heusler compounds [61]. WSMs with the crystal structure which breaks the inversion symmetry but preserves the time-reversal symmetry should have a minimum of four Weyl nodes, and in some cases show much more than four [62], see e.g. recent reviews cited above. Therefore, our quantitative results below can be applied only to magnetic WSMs. However, some qualitative conclusions for inversion-symmetry breaking WSMs can be still made, as discussed in Sec. 2.8. Another limitation stems from an effective two-band model, which neglects higher bands. This limits the frequency range by the onset of the optical transitions to higher bands, typically at several hundred meV.

Finally, we limit ourselves to the linear optical response, assuming that the electromagnetic field is weak enough and neglecting any strong-field modification of electron states.

Section 2.2 describes the effective Hamiltonian, or rather a family of Hamiltonians used in this study and derives the properties of corresponding bulk and surface electron states. Section 2.3 gives the classification of possible optical transitions and outlines all steps in the derivation of tensors of bulk and surface optical conductivity. The explicit expressions for the tensor elements are given in the Appendixes A, B, and C. Section 2.4 provides a detailed description of the electromagnetic normal modes (polaritons) in bulk WSMs. Section 2.5 provides boundary conditions which are then used in Section 2.6 to calculate the reflection of incident radiation from the surface of a WSM. Section 2.7 describes surface electromagnetic eigenmodes, i.e. surface plasmon-polaritons. Conclusions are in Section 2.8. The Appendixes A-E contains matrix elements of the current density operator, general expressions for elements of the bulk and surface conductivity tensor, their low-frequency limit and the limit of small Weyl node separation.

2.2 Effective Hamiltonian

In this section we describe the family of Hamiltonians that serve as a microscopic basis in this study. We derive the properties of bulk and surface electron states and use them to calculate the optical conductivity. Consider a family of Hamiltonians of the type

$$\hat{H} = v_F \left(\frac{\hat{Q}^2 - \hbar^2 m(z)}{2\hbar b} \hat{\sigma}_x + \hat{p}_y \hat{\sigma}_y + \hat{p}_z \hat{\sigma}_z \right), \tag{2.1}$$

where the function $m(z)$ takes into account that the system may be nonuniform along z and, in particular, has boundaries. Here $\hat{\sigma}_{x,y,z}$ are Pauli matrices and the operator $\hat{Q}^2$ is defined by one of the following three expressions:

$$\begin{aligned} (1)\ \hat{Q}^2 &= \hat{p}_x^2 \\ (2)\ \hat{Q}^2 &= \hat{p}_x^2 + \hat{p}_y^2 \end{aligned}$$

$$(3)\ \hat{Q}^2 \;=\; \hat{p}_x^2 + \hat{p}_y^2 + \hat{p}_z^2$$

The first option is the Hamiltonian in [57, 58].

To make the derivation of surface states more convenient [58], we apply the unitary transformation $\hat{H} \Longrightarrow \hat{S}^{-1}\hat{H}\hat{S}$ to Eq. (2.1), where $\hat{S} = \frac{1}{\sqrt{2}}\left(1 - i\hat{\sigma}_x\right)$. This gives

$$\hat{H} = v_F \left(\frac{\hat{Q}^2 - \hbar^2 m(z)}{2\hbar b}\hat{\sigma}_x + \hat{p}_z\hat{\sigma}_y - \hat{p}_y\hat{\sigma}_z \right), \tag{2.2}$$

One can check that this Hamiltonian violates time-reversal symmetry due to the term proportional to $\hat{\sigma}_x$. The gyrotropy axis is the x-axis. In $\boldsymbol{k}$-representation the Hamiltonian of Eq. (2.2) becomes

$$\hat{H_{\boldsymbol{k}}} = \hbar v_F \left(K_x\left(\boldsymbol{k}\right)\hat{\sigma}_x + k_z\hat{\sigma}_y - k_y\hat{\sigma}_z \right), \tag{2.3}$$

where $K_x\left(\boldsymbol{k}\right)$ for the same three Hamiltonians is given by

$$\begin{aligned}
(1)\ K_x &= \frac{k_x^2 - m}{2b} \\
(2)\ K_x &= \frac{k_x^2 + k_y^2 - m}{2b} \\
(3)\ K_x &= \frac{k_x^2 + k_y^2 + k_z^2 - m}{2b}
\end{aligned}$$

In all three cases the Weyl nodes are located at $k_x = \pm\sqrt{m}$ assuming that $m > 0$. We have found bulk and surface eigenstates for all three Hamiltonians. Below is a summary of main results related to electron states.

2.2.1 Hamiltonians 1 and 2

2.2.1.1 Bulk states

The stationary spinor eigenstate of the Hamiltonian in Eq. (2.3) is

$$|\Psi_{\boldsymbol{k}}\rangle = \begin{pmatrix} \Psi_1 \\ \Psi_2 \end{pmatrix} e^{i\boldsymbol{k}\boldsymbol{r} - i\frac{E}{\hbar}t}, \tag{2.4}$$

where the components are determined from

$$\begin{pmatrix} -k_y - \frac{E}{\hbar v_F} & K_x(\boldsymbol{k}) - ik_z \\ K_x(\boldsymbol{k}) + ik_z & k_y - \frac{E}{\hbar v_F} \end{pmatrix} \begin{pmatrix} \Psi_1 \\ \Psi_2 \end{pmatrix} = 0., \tag{2.5}$$

From Eq. (2.5) one can get the eigenenergy of the bulk states $E(\boldsymbol{k})$

$$E = s\hbar v_F \sqrt{K_x^2 + k_y^2 + k_z^2}, \tag{2.6}$$

and corresponding components of the spinor eigenstate in Eq. (2.4):

$$\begin{pmatrix} \Psi_1 \\ \Psi_2 \end{pmatrix} = \frac{1}{\sqrt{2V}} \begin{pmatrix} \sqrt{1 - s\cos\theta_{\boldsymbol{k}}}\, e^{-i\phi_{\boldsymbol{k}}} \\ s\sqrt{1 + s\cos\theta_{\boldsymbol{k}}} \end{pmatrix}, \tag{2.7}$$

where $\cos\theta_{\boldsymbol{k}} = \frac{k_y}{\sqrt{K_x^2+k_y^2+k_z^2}}$, $e^{i\phi_{\boldsymbol{k}}} = \frac{K_x+ik_z}{\sqrt{K_x^2+k_z^2}}$; $s = \pm 1$ denotes the conduction and valence bands, and V is the quantization volume.

To visualize the dispersion of electron states, we take for simplicity $m = b^2$. The 3D plot for one projection of 3D dispersion of the Hamiltonian 2 is shown in Fig. 2.1. For small energies $|\frac{E}{\hbar v_F}| \ll b$ the constant energy surface consists of two disconnected spheres, each of them enclosing a corresponding Weyl point; see Fig. 2.2. At $|\frac{E}{\hbar v_F}| = \frac{b}{2}$ a separatrix isoenergy surface is a 3D "figure of eight". For $|\frac{E}{\hbar v_F}| > \frac{b}{2}$ the constant energy surface is simply connected and encloses both Weyl points. Figures 2.2(a) and 2.2(b) shows contours of constant energy surfaces on the plane

$k_z = 0$ for the Hamiltonians 2 and 1, respectively. The electron dispersion is strongly anisotropic. This will result in different values for the diagonal elements of the bulk dielectric permittivity tensor, as in two-axial crystals. The dotted circle in Fig. 2.2(a) is the boundary of a region that contains surface states. For Hamiltonian 1 in Fig. 2.2(b) the surface states exist between the dotted lines.

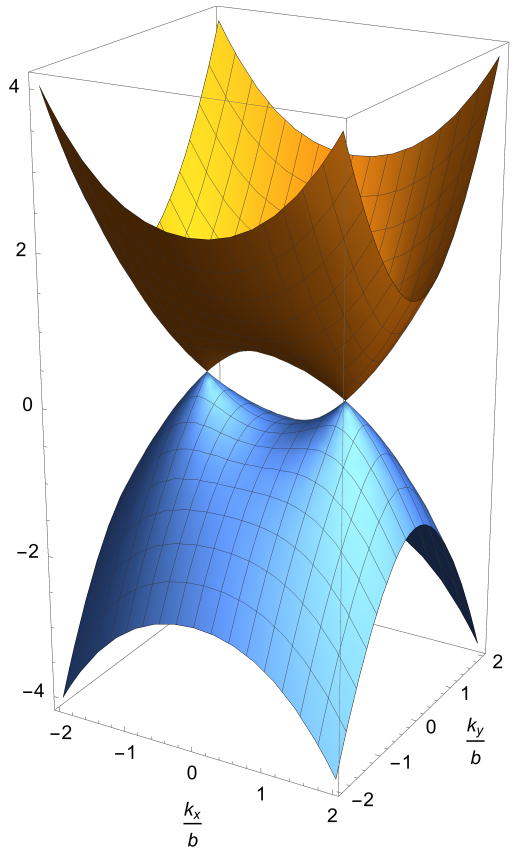

Figure 2.1: Bulk energy dispersion for Hamiltonian 2 on the surface $k_z = 0$. Here the energy is normalized by $\hbar v_F b$ and $k_{x,y}$ are normalized by b.

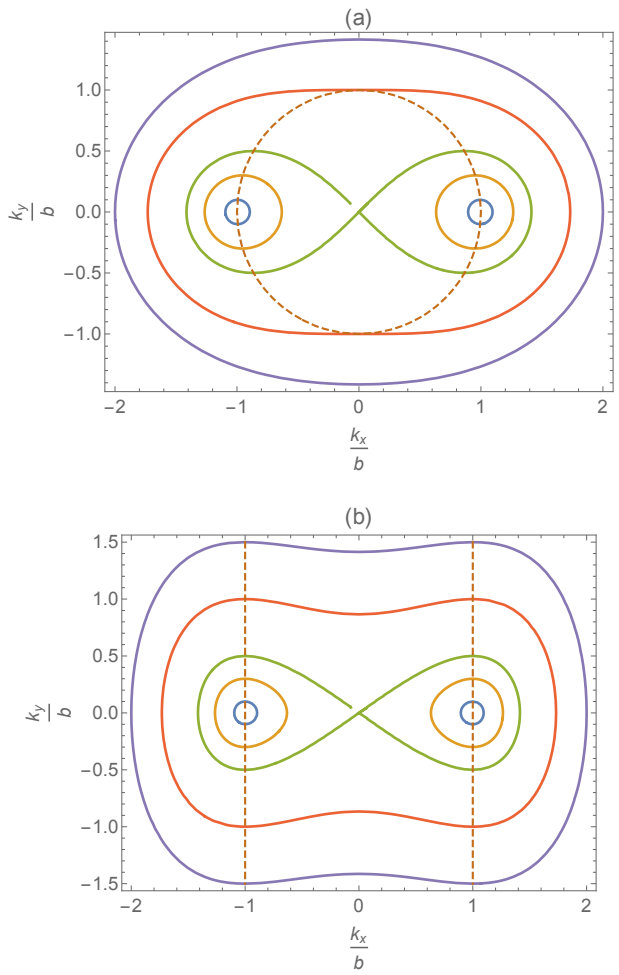

Figure 2.2: (a) Contours of constant energy surfaces for Hamiltonian 2 on the surface $k_z = 0$. The dotted circle is the boundary of a region $k_x^2 + k_y^2 \leq b^2$ where surface states exist. (b) Contours of constant energy surfaces for Hamiltonian 1 on the surface $k_z = 0$. Here $x, y = k_{x,y}/b$. The dotted lines indicate the boundary of a region $k_x^2 \leq b^2$ where surface states exist.

2.2.1.2 Reflection from the boundary. Surface states and Fermi arcs

Following [58], we define the boundary as a jump in the parameter m, so that $m = b^2$ inside the WSM and $m = -m_\infty$ outside. Then Eqs. (2.3) and (2.5) will contain the parameter m as a function of the coordinate r_j orthogonal to the boundary, and the corresponding component of the quasimomentum k_j is replaced by $k_j \Longrightarrow -i\frac{\partial}{\partial r_j}$.

For the boundary parallel to the gyrotropy axis x, we assume that it coincides with the surface

$z = 0$ and the WSM fills the halfspace $z < 0$. In this case $m = b^2$ for $z < 0$ and $m = -m_\infty$, $m_\infty \to \infty$ for $z > 0$.

For Hamiltonian 3, the Schrödinger equation given by Eq. (2.5) is a 4th order differential equation, since its matrix elements contain $\frac{\partial^2}{\partial z^2}$. For Hamiltonians 1 and 2 we get a 2nd order set of equations. The velocity operator $\hat{v}_z = \frac{i}{\hbar}[H, z]$ for Hamiltonian 3 is $\hat{v}_z = -i\frac{v_F}{b}\hat{\sigma}_x\frac{\partial}{\partial z} + v_F\hat{\sigma}_y$, i.e. it depends on the coordinate derivative. In contrast, the velocity operator $\hat{v}_z = v_F\hat{\sigma}_y$ for Hamiltonians 1 and 2 does not depend on the coordinate derivative. Therefore, for Hamiltonian 3 at $z = 0$, the continuity of both the eigenstate and its derivative is required, whereas one only needs the continuity of the eigenstates for Hamiltonians 1 and 2.

Using Eq. (2.5) one can find that the eigenstate of Hamiltonians 1 and 2 in the region $z > 0$ at $m_\infty \to \infty$ is $|\Psi_\infty\rangle \propto \begin{pmatrix} 1 \\ 0 \end{pmatrix} e^{ik_x x + ik_y y - \frac{m_\infty}{2b} z}$. In the region $z < 0$ we take the eigenstate $|\Psi_B\rangle$ which is given by Eq. (2.7). Stitching together these two eigenstates $|\Psi_\infty\rangle$ and $|\Psi_B\rangle$ at the boundary yields the following expression for the bulk state:

$$|\Psi_B\rangle = \frac{e^{ik_x x + ik_y y}}{2\sqrt{V}} \left[\begin{pmatrix} \sqrt{1 - s\cos\theta_{\boldsymbol{k}}}\, e^{-i\phi_{\boldsymbol{k}}} \\ s\sqrt{1 + s\cos\theta_{\boldsymbol{k}}} \end{pmatrix} e^{ik_z z} - \begin{pmatrix} \sqrt{1 - s\cos\theta_{\boldsymbol{k}}}\, e^{i\phi_{\boldsymbol{k}}} \\ s\sqrt{1 + s\cos\theta_{\boldsymbol{k}}} \end{pmatrix} e^{-ik_z z} \right], \quad (2.8)$$

where the quantization volume is limited from one side by the $z = 0$ plane. The eigenenergy is still given by Eq. (2.6), and the angles $\theta_{\boldsymbol{k}}$ and $\phi_{\boldsymbol{k}}$ are defined below Eq. (2.7).

If $\frac{E^2}{\hbar^2 v_F^2} < k_y^2 + K_x^2$ the value of k_z in Eq. (2.6) is imaginary: $k_z = \pm i\kappa$. In order to connect the eigenstate $|\Psi_\infty\rangle \propto \begin{pmatrix} 1 \\ 0 \end{pmatrix}$ in $z > 0$ with the eigenstate localized at $z < 0$ which is $e^{\kappa z}$, the localized eigenstate should be also a spinor $\begin{pmatrix} 1 \\ 0 \end{pmatrix}$. After replacing $k_z \Rightarrow -i\kappa$ in Eq. (2.5), we

obtain the following eigenenergies and eigenvectors for surface states in the limit $m_\infty \to \infty$:

$$\frac{E}{\hbar v_F} = -k_y,\ |\Psi_S\rangle = \sqrt{\frac{2\kappa}{S}} \begin{pmatrix} 1 \\ 0 \end{pmatrix} \Theta(-z)\, e^{\kappa z + ik_x x + ik_y y}, \tag{2.9}$$

where Θ is a step function, S is the quantization area, $\kappa = -K_x > 0$. For Hamiltonian 2 the surface states exist inside a dashed circle $b^2 > k_x^2 + k_y^2$ in Fig. 2.2(a). For Hamiltonian 1 the surface states exist in the region $b^2 > k_x^2$ in Fig. 2.2(b).

If a WSM occupies the region $z > 0$, instead of Eqs. (2.9) we obtain

$$\frac{E}{\hbar v_F} = +k_y,\ |\Psi_S\rangle = \sqrt{\frac{2\kappa}{S}} \begin{pmatrix} 0 \\ 1 \end{pmatrix} \Theta(z)\, e^{-|\kappa| z + ik_x x + ik_y y}, \tag{2.10}$$

where $\kappa = +K_x < 0$. Equations (2.9),(2.10) can be easily generalized to the case of a parameter $m(z)$ which varies continuously between the values b^2 and $-m_\infty$ [58]. For example, instead of Eqs. (2.9) we get

$$\frac{E}{\hbar v_F} = -k_y,\ |\Psi_S\rangle = N \begin{pmatrix} 1 \\ 0 \end{pmatrix} e^{ik_x x + ik_y y} \begin{cases} e^{\int_0^z \frac{m(z) - k_x^2}{2b} dz} & \text{for Hamiltonian 1} \\ e^{\int_0^z \frac{m(z) - k_x^2 - k_y^2}{2b}\, dz} & \text{for Hamiltonian 2,} \end{cases} \tag{2.11}$$

where N is a normalization factor.

Note that the constant surface energy lines $k_y = \text{const}$ are tangent to the points where the bulk-state constant energy surface intersects the boundary of the surface states, shown as dotted lines in Fig. 2.2(a) and 2(b). The union of these $k_y = \text{const}$ lines and the bulk-state constant energy surface is a set of bulk and surface energy states with the same energy. In particular, at the energy equal to the Fermi energy E_F the $k_y = E_F/(\hbar v_F)$ line forms a Fermi arc.

2.2.2 Hamiltonian 3

For a 4th order set of differential equations the construction of electron states including their interaction with a boundary is more complicated.

First, we use Eq. (2.6) to find the value of k_z for given $k_{x,y}$ and E. Consider the parameter range $m \leq b^2$, including both positive and negative values of m. If $\frac{E^2}{\hbar^2 v_F^2} > k_y^2 + \frac{\left(k_x^2+k_y^2-m\right)^2}{4b^2}$, one always has two real solutions $k_{z1} = -k_{z2} > 0$ together with two imaginary solutions corresponding to evanescent states: $k_{z3,4} = i\kappa_{3,4}$, where $0 < \kappa_3 = -\kappa_4$. If $\frac{E^2}{\hbar^2 v_F^2} < k_y^2 + \frac{\left(k_x^2+k_y^2-m\right)^2}{4b^2}$, all four solutions are imaginary and correspond to evanescent states: $k_{z1,2,3,4} = i\kappa_{1,2,3,4}$, where $0 < \kappa_1 = -\kappa_3$, $0 < \kappa_2 = -\kappa_4$. In the region $z > 0$ (i.e. outside the sample, where $m = -m_\infty$) it is reasonable to take the solution as a superposition of two localized modes $e^{-|\kappa_{3,4}|z}$. In this case for $z < 0$, i.e. inside the sample where $m = b^2$, there could be two options:

(i) A superposition of two counterpropagating waves with quasimomenta $k_{z1} = -k_{z2}$ together with a localized wave $e^{\kappa_3 z}$. The localized solution cannot be discarded, since without it the number of constants becomes smaller than the number of the boundary conditions.

(ii) A superposition of two localized waves i.e. the surface state. In this option the number of constants is always smaller than the number of the boundary conditions, so such a state can exist only at certain values of energy.

The procedure of stitching the spinor components and their derivatives is simplified if $m_\infty \to \infty$ since in this limit the continuity of the derivative is equivalent to setting both components of a spinor $\Psi_{1,2}$ equal to zero in the cross section $z = 0$.

2.2.2.1 Bulk states near the boundary

In case (i) we obtain

$$|\Psi_B\rangle \approx \frac{e^{ik_x x + ik_y y}}{2\sqrt{V}}$$
$$\times \left[\begin{pmatrix} \sqrt{1 - s\cos\theta_{\boldsymbol{k}}} e^{-i\phi_{\boldsymbol{k}}} \\ s\sqrt{1 + s\cos\theta_{\boldsymbol{k}}} \end{pmatrix} e^{ik_z z} + r \begin{pmatrix} \sqrt{1 - s\cos\theta_{\boldsymbol{k}}} e^{i\phi_{\boldsymbol{k}}} \\ s\sqrt{1 + s\cos\theta_{\boldsymbol{k}}} \end{pmatrix} e^{-ik_z z} + l \begin{pmatrix} \sqrt{1 - s\cos\theta_{\boldsymbol{k}}} e^{\alpha_\kappa} \\ -s\sqrt{1 + s\cos\theta_{\boldsymbol{k}}} \end{pmatrix} e^{\kappa z} \right] \tag{2.12}$$

where

$$k_z = \sqrt{2b\sqrt{\frac{E^2}{\hbar^2 v_F^2} + k_x^2} - \left(k_x^2 + k_y^2 + b^2\right)},\ \kappa = \sqrt{2b\sqrt{\frac{E^2}{\hbar^2 v_F^2} + k_x^2} + \left(k_x^2 + k_y^2 + b^2\right)},$$

$$r = -\frac{e^{\alpha_\kappa} + e^{-i\phi_{\boldsymbol{k}}}}{e^{\alpha_\kappa} + e^{i\phi_{\boldsymbol{k}}}},\ \sinh\alpha_\kappa = \frac{\kappa}{\sqrt{\frac{E^2}{\hbar^2 v_F^2} - k_y^2}},\ l = 2i\frac{\sin\phi_{\boldsymbol{k}}}{e^{\alpha_\kappa} + e^{i\phi_{\boldsymbol{k}}}}.$$

Clearly, $|r|^2 = 1$, which corresponds, as expected, to the total reflection from the boundary. The quantization volume in Eq. (2.12) is chosen in such a way that its length along the z axis is much larger than $k_z^{-1} > \kappa^{-1}$. Therefore, the last term in the brackets in Eq. (2.12) is unimportant in a sense that it does not affect the eigenstate normalization or the matrix elements.

2.2.2.2 Surface states

To construct the surface states (option (ii)) it is convenient to to go back to Eq. (2.5), use $m = b^2$, and make the substitution $k_z = -i\kappa$:

$$\begin{pmatrix} -k_y - \frac{E}{\hbar v_F} & \frac{k_x^2+k_y^2-\kappa^2-b^2}{2b} - \kappa \\ \frac{k_x^2+k_y^2-\kappa^2-b^2}{2b} + \kappa & k_y - \frac{E}{\hbar v_F} \end{pmatrix} \begin{pmatrix} \Psi_1 \\ \Psi_2 \end{pmatrix} = 0 \tag{2.13}$$

Consider the solution of Eq. (2.13), corresponding to different positive values of $\kappa_{1,2}$ but the same spinor constant $\begin{pmatrix} a \\ b \end{pmatrix}$. One can build a nontrivial localized solution $|\Psi_S\rangle \propto \begin{pmatrix} a \\ b \end{pmatrix} \Theta(-z)\left(e^{\kappa_1 z} - e^{\kappa_2 z}\right)$, which corresponds to the null boundary conditions at the surface $z = 0$. Such a solution of Eq. (2.13) is possible under the following conditions:

$-k_y - \frac{E}{\hbar v_F} = \frac{k_x^2+k_y^2-\kappa^2-b^2}{2b} + \kappa = 0$, or $k_y - \frac{E}{\hbar v_F} = \frac{k_x^2+k_y^2-\kappa^2-b^2}{2b} - \kappa = 0$, where $\begin{pmatrix} a \\ b \end{pmatrix} = \begin{pmatrix} 1 \\ 0 \end{pmatrix}$ or $\begin{pmatrix} a \\ b \end{pmatrix} = \begin{pmatrix} 0 \\ 1 \end{pmatrix}$ respectively. It is easy to see that the first option corresponds to the surface state when the WSM occupies the halfspace $z < 0$, whereas the second option corresponds to the WSM in the region $z > 0$, since in this case the values of $\kappa_{1,2}$ are negative. The resulting states are

as follows.

(i) WSM in $z < 0$:

$$\frac{E}{\hbar v_F} = -k_y,\ |\Psi_S\rangle = \sqrt{\frac{2}{S\left(\frac{1}{\kappa_1}+\frac{1}{\kappa_2}-\frac{4}{\kappa_1+\kappa_2}\right)}} \begin{pmatrix} 1 \\ 0 \end{pmatrix} \Theta\left(-z\right)\left(e^{\kappa_1 z} - e^{\kappa_2 z}\right) \cdot e^{ik_x x + ik_y y}; \quad (2.14)$$

(ii) WSM in $z > 0$:

$$\frac{E}{\hbar v_F} = k_y,\ |\Psi_S\rangle = \sqrt{\frac{2}{S\left(\frac{1}{\kappa_1}+\frac{1}{\kappa_2}-\frac{4}{\kappa_1+\kappa_2}\right)}} \begin{pmatrix} 0 \\ 1 \end{pmatrix} \Theta\left(z\right)\left(e^{-\kappa_1 z} - e^{-\kappa_2 z}\right) \cdot e^{ik_x x + ik_y y}. \quad (2.15)$$

Here $\kappa_{1,2} = b \mp \sqrt{k_x^2 + k_y^2}$.

In the region $b^2 < k_x^2 + k_y^2$ there is only one localized evanescent solution for any fixed value of energy, which is not enough to satisfy the boundary conditions. Therefore, the region $b^2 > k_x^2 + k_y^2$, where the surface states exist, is the same in the models described by the Hamiltonian 2 and Hamiltonian 3 (see the dotted circle in Fig 2.2(a)).

Taking into account a finite value of m_∞ modifies the above expression, but their general structure remains the same. For example, when a WSM fills the halfspace $z < 0$, then the eigenstate in Eq. (2.14) is replaced by

$$|\Psi_{S;z<0}\rangle \propto \begin{pmatrix} 1 \\ 0 \end{pmatrix} \left(e^{\kappa_1 z} - \zeta e^{\kappa_2 z}\right) e^{ik_x x + ik_y y},$$

$$|\Psi_{S;z>0}\rangle \propto \begin{pmatrix} 0 \\ 1 \end{pmatrix} \frac{\kappa_2 - \kappa_1}{\kappa_2 + \sqrt{m_\infty}} e^{-\sqrt{m_\infty} z} e^{ik_x x + ik_y y}, \quad (2.16)$$

where $\zeta = \dfrac{\kappa_1 + \sqrt{m_\infty}}{\kappa_2 + \sqrt{m_\infty}}$.

2.2.3 The boundary orthogonal to the gyrotropy axis

Any Hamiltonian, 1, 2, or 3, contains the second derivative $\frac{\partial^2}{\partial x^2}$. Therefore, the analysis of the bulk and surface states near the boundary orthogonal to the gyrotropy axis is similar to the one for the boundary parallel to the gyrotropy axis when the Hamiltonian contains the second derivative $\frac{\partial^2}{\partial z^2}$. Repeating the same arguments as in the previous section, we obtain that the orthogonal boundary is trivial and does not contain surface states.

2.2.4 Comparison of Hamiltonians 1, 2, and 3

The only principal difference between the eigenstates of the effective Hamiltonians considered above is the region where the surface states exist. Such a region is determined by the inequality $b > \sqrt{k_x^2 + k_y^2}$ for Hamiltonians 2 and 3, and the inequality $b > |k_x|$ for Hamiltonian 1. The latter condition leads to an infinite density of surface states, which is unphysical and would have to be restricted artificially. Therefore, it is better to work with Hamiltonian 2 or 3. Hamiltonian 2 leads to a simpler z-component of the velocity operator: $\hat{v}_z = v_F\hat{\sigma}_y$ instead of $\hat{v}_z = -i\frac{v_F}{b}\hat{\sigma}_x\frac{\partial}{\partial z} + v_F\hat{\sigma}_y$, which corresponds to Hamiltonian 3. The velocity operator of Hamiltonian 2 makes calculations of the surface current easier without losing any essential physics. Therefore, we will use Hamiltonian 2 for subsequent calculations of the optical properties.

2.3 Optical transitions and the tensors of bulk and surface conductivity

In the presence of external fields one should replace $\hat{\boldsymbol{p}} \Longrightarrow \hat{\boldsymbol{p}} - \frac{e}{c}\boldsymbol{A}$, and also add the electrostatic potential $\hat{H} \Longrightarrow \hat{H} + e\varphi\hat{1}$ in Eq. (2.2). Particles are assumed to have charge e where $-e$ is the magnitude of the electron charge. If the potential has a coordinate dependence $\boldsymbol{A}(\boldsymbol{r})$ we assume symmetrized operators

$$\left(\hat{p}_{x,y,z} - \frac{e}{c}A_{x,y,z}\right)^2 \Longrightarrow \hat{p}_{x,y,z}^2 + \frac{e^2}{c^2}A_{x,y,z}^2 - \frac{e}{c}\left(\hat{p}_{x,y,z}A_{x,y,z} + A_{x,y,z}\hat{p}_{x,y,z}\right),$$

and in the expressions for the velocity operator we need to replace

$$-i\frac{\partial}{\partial x,\partial y,\partial z}\Longrightarrow -i\frac{\partial}{\partial x,\partial y,\partial z}-\frac{e}{c\hbar}A_{x,y,z}.$$

Throughout this chapter, we will consider the potentials corresponding to a monochromatic electromagnetic field propagating in the arbitrary direction $\boldsymbol{r}$ with angular frequency ω and wavevector $\boldsymbol{q}$, i.e.

$$\phi=\frac{1}{2}\phi(\omega)e^{-i\omega t+i\boldsymbol{q}\cdot\boldsymbol{r}}+c.c., \tag{2.17}$$

$$\boldsymbol{A}=\frac{1}{2}[\boldsymbol{x_0}A_x(\omega)+\boldsymbol{y_0}A_y(\omega)+\boldsymbol{z_0}A_z(\omega)]e^{-i\omega t+i\boldsymbol{q}\cdot\boldsymbol{r}}+c.c. \tag{2.18}$$

Bulk-to-bulk and surface-to-surface transitions contribute to the bulk and surface conductivity tensors, respectively. The contributions are detailed in the Appendix. Surface-to-bulk transitions contribute to the surface conductivity tensor only. They have to be handled with more care, as we briefly describe below.

Generally, the electron and current densities expressed in terms of the density matrix are given by

$$n\left(\boldsymbol{r}\right)=\sum_{\alpha\beta}n_{\beta\alpha}\left(\boldsymbol{r}\right)\rho_{\alpha\beta},\ \boldsymbol{j}\left(\boldsymbol{r}\right)=\sum_{\alpha\beta}\boldsymbol{j}_{\beta\alpha}\left(\boldsymbol{r}\right)\rho_{\alpha\beta}, \tag{2.19}$$

$$n_{\beta\alpha}=\Psi_\beta^*\Psi_\alpha,\ \boldsymbol{j}_{\beta\alpha}=\frac{1}{2}\left[\Psi_\beta^*\left(\hat{\boldsymbol{j}}\Psi_\alpha\right)+\left(\hat{\boldsymbol{j}}^*\Psi_\beta^*\right)\Psi_\alpha\right], \tag{2.20}$$

where $\hat{\boldsymbol{j}}=e\hat{\boldsymbol{v}}$.

The Fourier harmonics of the the electron and current densities are

$$\boldsymbol{j}\left(\boldsymbol{r}\right)=\frac{1}{2}\sum_{\boldsymbol{q}}\boldsymbol{j}^{(\boldsymbol{q})}e^{i\boldsymbol{q}\boldsymbol{r}}+c.c.,\ \ n\left(\boldsymbol{r}\right)=\frac{1}{2}\sum_{\boldsymbol{q}}n^{(\boldsymbol{q})}e^{i\boldsymbol{q}\boldsymbol{r}}+c.c.,$$

where

$$\frac{1}{2}\boldsymbol{j}^{(\boldsymbol{q})}=\frac{1}{V}\int_V\boldsymbol{j}\left(\boldsymbol{r}\right)e^{-i\boldsymbol{q}\boldsymbol{r}}d^3r,\ \ \frac{1}{2}n^{(\boldsymbol{q})}=\frac{1}{V}\int_V n^{(\boldsymbol{q})}e^{-i\boldsymbol{q}\boldsymbol{r}}d^3r.$$

For their matrix elements we have

$$\boldsymbol{j}^{(\boldsymbol{q})} = \sum_{\alpha\beta} \boldsymbol{j}^{(\boldsymbol{q})}_{\beta\alpha} \rho_{\alpha\beta}, \quad n^{(\boldsymbol{q})} = \sum_{\alpha\beta} n^{(\boldsymbol{q})}_{\beta\alpha} \rho_{\alpha\beta}, \tag{2.21}$$

where

$$\boldsymbol{j}^{(\boldsymbol{q})}_{\beta\alpha} = 2 \left\langle \beta \right| e^{-i\boldsymbol{q}\boldsymbol{r}} \hat{\boldsymbol{j}} \left| \alpha \right\rangle, \quad n^{(\boldsymbol{q})}_{\beta\alpha} = 2 \left\langle \beta \right| e^{-i\boldsymbol{q}\boldsymbol{r}} \left| \alpha \right\rangle \tag{2.22}$$

To find the current without the effect of a boundary we can use the states given by Eq. (2.7).

Now consider the states near the surface. We will denote the bulk states with latin indices and surface states with greek ones. For convenience we rewrite them, having in mind an upper boundary $z = 0$ with the WSM located at $z < 0$:

$$|\Psi_m\rangle = \frac{e^{ik_x x + ik_y y}}{2\sqrt{V}} \left[\begin{pmatrix} \sqrt{1 + s\cos\theta_{\boldsymbol{k}}} e^{-i\phi_{\boldsymbol{k}}} \\ s\sqrt{1 - s\cos\theta_{\boldsymbol{k}}} \end{pmatrix} e^{ik_z z} - \begin{pmatrix} \sqrt{1 - s\cos\theta_{\boldsymbol{k}}} e^{i\phi_{\boldsymbol{k}}} \\ s\sqrt{1 + s\cos\theta_{\boldsymbol{k}}} \end{pmatrix} e^{-ik_z z} \right], \tag{2.23}$$

where $E_m = s\hbar v_F \sqrt{\left(\frac{k_x^2 + k_y^2 - b^2}{2b}\right)^2 + k_y^2 + k_z^2}$ is the eigenenergy, $s = \pm 1$ is the band index, the values $k_{x,y}$ can be of either sign whereas $k_z > 0$; $\cos\theta_{\boldsymbol{k}_\parallel} = \frac{k_z}{\frac{|E|}{\hbar v_F}}$.

$$|\Psi_\alpha\rangle = \sqrt{\frac{2\kappa}{S}} \begin{pmatrix} 1 \\ 0 \end{pmatrix} \Theta(-z)\, e^{ik_x x + ik_y y + \kappa z}, \tag{2.24}$$

where S is the area; the energy of the state is $E_\alpha = -\hbar v_F k_y$, $\kappa = \frac{b^2 - k_x^2 - k_y^2}{2b}$, $\sqrt{k_x^2 + k_y^2} < b$.

Let us limit the surface states by the condition $\kappa > \kappa_{min}$, where the latter could be a typical scattering length $\sim \kappa_{min}^{-1}$. We will assume that κ_{min}^{-1} is much smaller than L, which enters the quantization volume $V = SL$ in Eq. (2.23). When we calculate the matrix elements of the interaction Hamiltonian in the von Neumann equation, the matrix elements $V^{(int)}_{mn}$,$V^{(int)}_{\alpha\beta}$ and $V^{(int)}_{m\alpha}$ have no peculiarities: the integration is carried out over the whole volume. However when we calculate the matrix elements of the density and current, and if at least one of the indices belongs to the surface

state, we will perform the integration over dz:

$$n_{\beta\alpha} = \int_{-\infty}^{0} \Psi_{\beta}^{*} \Psi_{\alpha} dz, \quad n_{m\alpha} = \int_{-\infty}^{0} \Psi_{m}^{*} \Psi_{\alpha} dz, \tag{2.25}$$

$$\boldsymbol{j}_{\beta\alpha} = \frac{1}{2} \int_{-\infty}^{0} \left[\Psi_{\beta}^{*} \left(\hat{\boldsymbol{j}} \Psi_{\alpha} \right) + \left(\hat{\boldsymbol{j}}^{*} \Psi_{\beta}^{*} \right) \Psi_{\alpha} \right] dz, \; \boldsymbol{j}_{m\alpha} = \frac{1}{2} \int_{-\infty}^{0} \left[\Psi_{m}^{*} \left(\hat{\boldsymbol{j}} \Psi_{\alpha} \right) + \left(\hat{\boldsymbol{j}}^{*} \Psi_{m}^{*} \right) \Psi_{\alpha} \right] dz. \tag{2.26}$$

These quantities will depend only on x and y, and therefore determine the surface current and density.

The following current component is nontrivial: $\sum_{\alpha\beta} (j_z)_{\beta\alpha} \rho_{\alpha\beta} + \sum_{m\alpha} (j_z)_{m\alpha} \rho_{\alpha m}$. It determines the polarization of a thin double layer:

$$\frac{\partial}{\partial t} p_z (x, y) = \sum_{\alpha\beta} (j_z)_{\beta\alpha} \rho_{\alpha\beta} + \sum_{m\alpha} (j_z)_{m\alpha} \rho_{\alpha m}, \tag{2.27}$$

This layer radiates, but not normally to the layer, and it cannot affect the surface density of carriers.

With properly defined matrix elements of the current and density the continuity equation is satisfied automatically, so we can consider the volume current flowing toward the boundary $\left(\sum_{mn} (j_z)_{nm} \rho_{mn}\right)_{z=0}$ as a source in the surface continuity equation.

2.3.1 Tensors of bulk and surface conductivity

The matrix elements of the Fourier components of the current density operator are evaluated in Appendix A. After evaluating them, in Appendix B and C we used the Kubo-Greenwood formula to calculate the bulk and surface conductivity tensors, respectively; e.g.

$$\sigma_{\alpha\beta}(\omega) = g \frac{i\hbar}{V} \sum_{mn} \left(\frac{f_n - f_m}{E_m - E_n} \right) \frac{\langle n | \hat{j}_{\alpha} | m \rangle \langle m | \hat{j}_{\beta} | n \rangle}{\hbar(\omega + i\gamma) + (E_n - E_m)}, \tag{2.28}$$

for the bulk conductivity, where $g = 2$ is the spin degeneracy factor and α, β denote Cartesian coordinate components. The surface conductivity tensor has a similar structure, but the contribution is summed over surface-to-surface and surface-to-bulk transitions, and the normalization is over

the surface area S instead of a volume V. Both interband and intraband transitions are included. Three-dimensional integrals over electron momenta in Appendix B and C cannot be evaluated analytically, except limiting cases of small frequencies or small b (see Appendix D and E). Therefore, integrals were calculated numerically at zero temperature for all plots below.

The bulk (3D) conductivity tensor due to low-energy electrons near Weyl points is

$$\sigma_{ij}^{B}(\omega) = \begin{pmatrix} \sigma_{xx}^{B} & 0 & 0 \\ 0 & \sigma_{yy}^{B} & \sigma_{yz}^{B} \\ 0 & \sigma_{zy}^{B} & \sigma_{zz}^{B} \\ \end{pmatrix} \tag{2.29}$$

where $\sigma_{zy}^{B} = -\sigma_{yz}^{B}$. The surface conductivity tensor at $z = 0$ has a similar structure, with superscript B replaced by S and $\sigma_{zy}^{S} = -\sigma_{yz}^{S}$.

The background bulk dielectric tensor in the most general form which corresponds to the one for a two-axial nongyrotropic crystal is

$$\varepsilon_{ij}^{(0)}(\omega) = \begin{pmatrix} \varepsilon_{xx}^{(0)} & 0 & 0 \\ 0 & \varepsilon_{yy}^{(0)} & 0 \\ 0 & 0 & \varepsilon_{zz}^{(0)} \\ \end{pmatrix} \tag{2.30}$$

so that the total dielectric permittivity tensor is

$$\varepsilon_{ij}(\omega) = \varepsilon_{ij}^{(0)}(\omega) + i\frac{4\pi\sigma_{ij}^{B}(\omega)}{\omega} = \begin{pmatrix} \varepsilon_{xx} & 0 & 0 \\ 0 & \varepsilon_{yy} & ig \\ 0 & -ig & \varepsilon_{zz} \\ \end{pmatrix} \tag{2.31}$$

where

$$g = \frac{4\pi\sigma_{yz}^{B}}{\omega}. \tag{2.32}$$

Note that for Hamiltonian 3 we would have $\sigma_{yy}^{B} = \sigma_{zz}^{B}$, whereas for Hamiltonian 2 (used in all calculations of the conductivity tensors in this chapter) we have $\sigma_{yy}^{B} \neq \sigma_{zz}^{B}$. Therefore, even if the background dielectric tensor is isotropic, the contribution of massless Weyl electrons will create a two-axial anisotropy. In the numerical plots below we will take an isotropic background dielectric tensor and neglect its frequency dependence at low frequencies, $\varepsilon_{xx}^{(0)} = \varepsilon_{yy}^{(0)} = \varepsilon_{zz}^{(0)} = 10$, so that all nontrivial effects of anisotropy and gyrotropy are due to Weyl fermions.

The salient feature of both bulk and surface conductivity tensor is the presence of nonzero off-diagonal (gyrotropic) components due to time-reversal symmetry breaking in the Hamiltonian. These terms originate from the finite separation of the Weyl nodes in momentum space and the existence of surface states (Fermi arcs). The gyrotropic effects in the propagation, reflection, and transmission of bulk and surface modes can serve as a definitive diagnostic of Weyl nodes, surface states, and Fermi surface. They could also find applications in optoelectronic devices such as Faraday isolators, modulators etc.

Figures 2.3-2.6 show spectra of $\varepsilon_{xx}(\omega)$, $\varepsilon_{yy}(\omega)$, $\varepsilon_{zz}(\omega)$, and $g(\omega)$ for several values of the Fermi momentum k_F (at zero temperature), when the Weyl node separation $2\hbar v_F b = 200$ meV. The characteristic feature in all plots is strong absorption and dispersion at the onset of interband transitions, when $\omega = 2v_F k_F$. Another common feature is a Drude-like increase in the absolute value of all tensor components at low frequencies. Indeed, as shown in Appendix D, in the limit $\omega \ll v_F k_F \ll v_F b$ when only the intraband transitions in the vicinity of each Weyl point are important, the off-diagonal components are equal to zero and the diagonal conductivity components are reduced to the same Drude form:

$$\sigma_{xx}^{intra}(\omega) = \sigma_{yy}^{intra}(\omega) = \sigma_{zz}^{intra}(\omega) = \frac{ge^2 v_F k_F^2}{3\pi^2\hbar(-i\omega+\gamma)}. \tag{2.33}$$

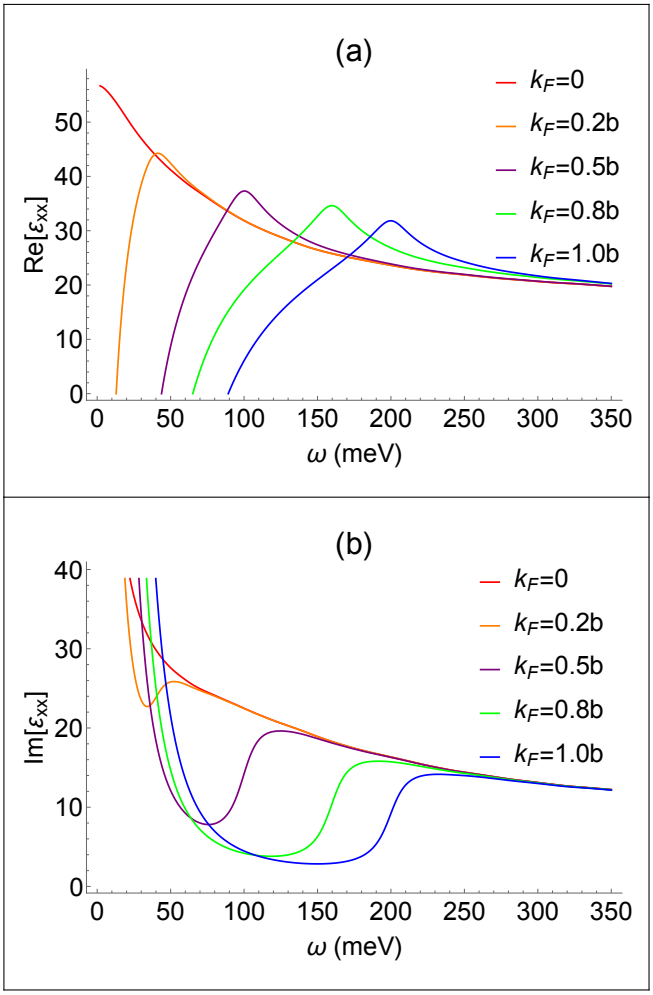

Figure 2.3: Real and imaginary parts of the ε_{xx} component of the dielectric tensor as a function of frequency for $\hbar v_F b = 100$ meV, dephasing rate $\gamma = 10$ meV, and $\varepsilon_{xx}^{(0)} = 10$.

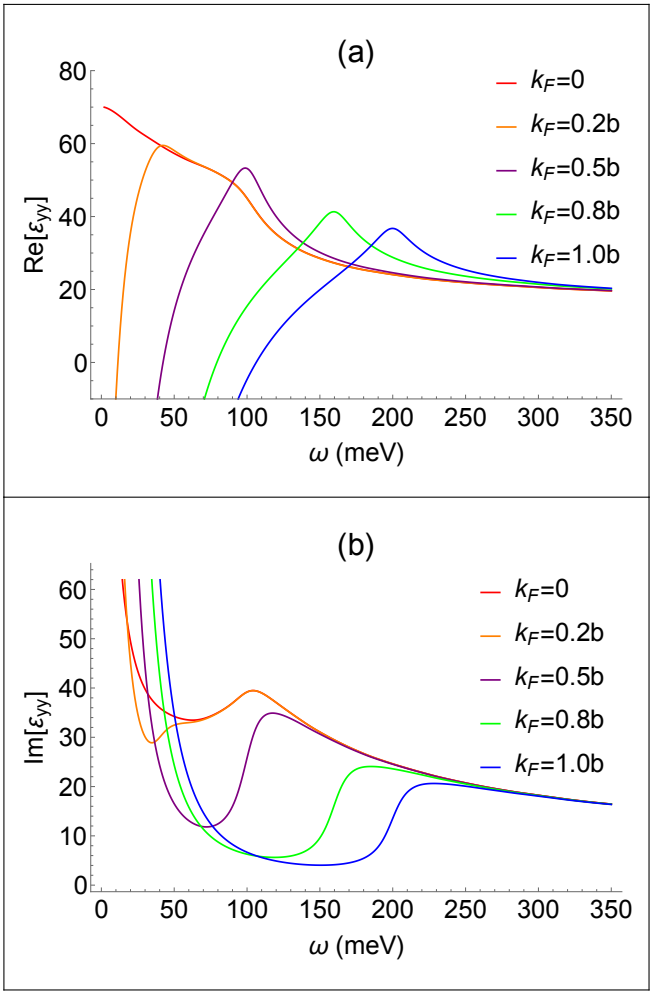

Figure 2.4: Real and imaginary parts of the ε_{yy} component of the dielectric tensor as a function of frequency for $\hbar v_F b = 100$ meV, dephasing rate $\gamma = 10$ meV, and $\varepsilon_{yy}^{(0)} = 10$.

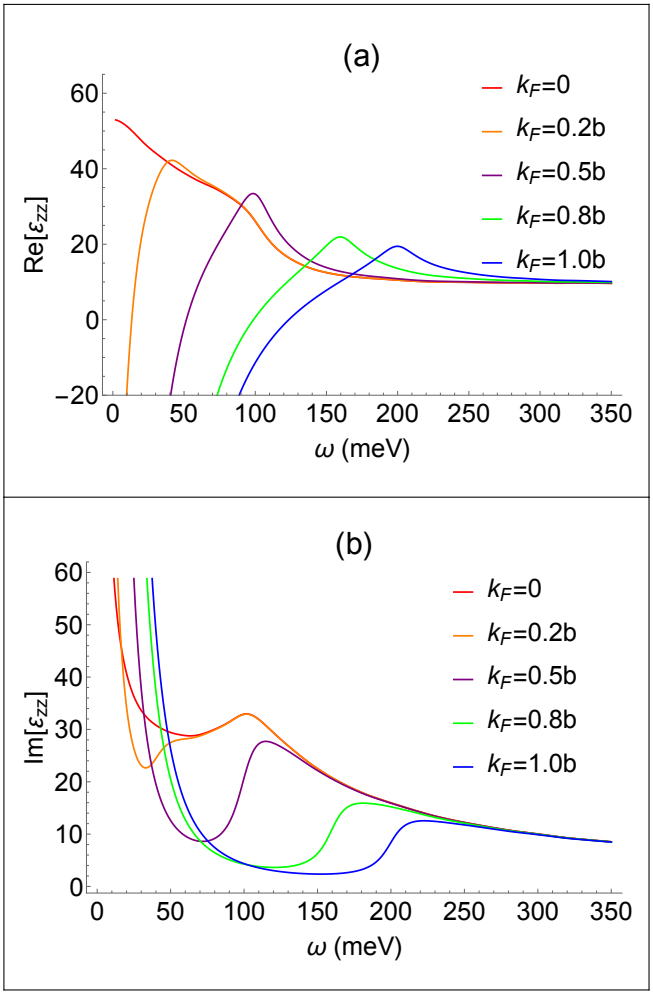

Figure 2.5: Real and imaginary parts of the ε_{zz} component of the dielectric tensor as a function of frequency for $\hbar v_F b = 100$ meV, dephasing rate $\gamma = 10$ meV, and $\varepsilon_{zz}^{(0)} = 10$.

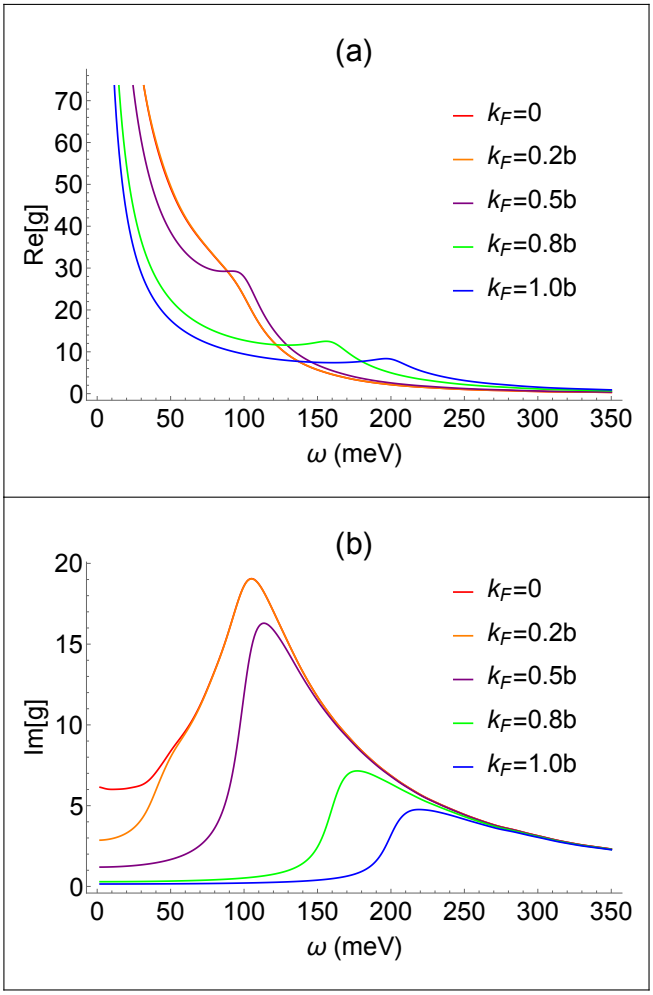

Figure 2.6: Real and imaginary parts of $g = \frac{4\pi\sigma^B_{yz}}{\omega}$ as a function of frequency for $\hbar v_F b = 100$ meV and dephasing rate $\gamma = 10$ meV.

Note an absorption peak at $\omega = 100$ meV at low Fermi momenta, which corresponds to a Van Hove singularity at the interband transitions between saddle points of conduction and valence bands at $k = 0$, i.e. in the middle between the Weyl points.

Note also that diagonal and off-diagonal parts of the conductivity tensor are of the same order at low frequencies comparable to the Weyl node separation, which indicates that gyrotropic effects should be quite prominent.

All figures in this chapter are plotted for a relatively high dephasing rate $\gamma = 10$ meV, which

smoothes out all spectral features and introduces strong losses for electromagnetic eigenmodes even below the interband transition edge. The dephasing rate originates from electron scattering and obviously depends on the temperature and material quality in realistic materials. Its derivation is beyond the scope of the present chapter.

2.4 Bulk polaritons in Weyl semimetals

Consider first the propagation of plane monochromatic waves in a bulk Weyl semimetal. For complex amplitudes of the electric field and induction, $(\boldsymbol{D}, \boldsymbol{E})e^{i\boldsymbol{kr}-i\omega t}$, where $\boldsymbol{D} = \hat{\varepsilon}\boldsymbol{E}$ and $\hat{\varepsilon}$ is a bulk dielectric tensor, Maxwell's equations give $\boldsymbol{n} \cdot \boldsymbol{D} = 0$, where $\boldsymbol{n} = \frac{c\boldsymbol{k}}{\omega}$. The resulting dispersion equations are

$$\boldsymbol{n}\left(\boldsymbol{n} \cdot \boldsymbol{E}\right) - n^2\boldsymbol{E} + \hat{\varepsilon}\boldsymbol{E} = 0, \tag{2.34}$$

or

$$\begin{pmatrix} \varepsilon_{xx} - n^2 + n_x^2 & n_x n_y & n_x n_z \\ n_y n_x & \varepsilon_{yy} - n^2 + n_y^2 & ig + n_y n_z \\ n_z n_x & -ig + n_z n_y & \varepsilon_{zz} - n^2 + n_z^2 \end{pmatrix} \begin{pmatrix} E_x \\ E_y \\ E_z \end{pmatrix} = 0. \tag{2.35}$$

The structure of these equations indicate strongly anisotropic and gyrotropic properties of bulk polaritons. The dispersion is drastically different for normal modes propagating perpendicular to the x-axis and to the y-axis. For each direction, there are furthermore two normal modes with different refractive indices. We will consider each case separately.

2.4.1 Propagation perpendicular to the anisotropy x-axis

In this case we have $n_x = 0$, $n^2 = n_y^2 + n_z^2$, $n_z = n\cos\theta$, $n_y = n\sin\theta$, where θ is the angle between the wave vector and z-axis. From Eqs. (2.35) we obtain two normal modes that can be called an ordinary (O) and extraordinary (X) wave. An O-wave has an electric field along x and the refractive index

$$n_O^2 = \varepsilon_{xx}. \tag{2.36}$$

Therefore, its dispersion and absorption are completely described by the spectrum of $\varepsilon_{xx}(\omega)$. As shown in Fig. 2.7, at low frequencies the O-mode experiences strong metallic absorption and at $\omega = 2E_F = 160$ meV there is an onset of interband transitions.

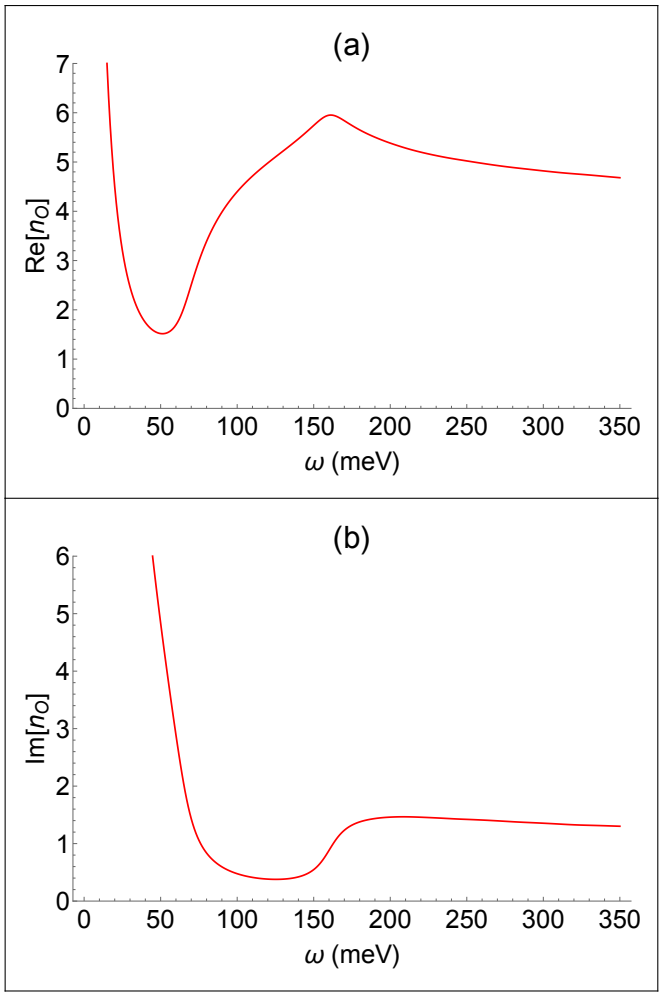

Figure 2.7: Real and imaginary parts of the refractive index n_O of an O-wave as a function of frequency for $E_F = 80$ meV, $\hbar v_F b = 100$ meV, and dephasing rate $\gamma = 10$ meV.

An X-wave have an electric field in the (y, z) plane and the refractive index showing strong

θ-dependence and resonances:

$$n_X^2 = \frac{\varepsilon_{yy}\varepsilon_{zz} - g^2}{\cos^2\theta\varepsilon_{zz} + \sin^2\theta\varepsilon_{yy}}. \tag{2.37}$$

For normal incidence $\theta = 0$,

$$n_X^2 = \varepsilon_{yy} - \frac{g^2}{\varepsilon_{zz}}. \tag{2.38}$$

It is obvious from Eq. (2.37) that the refractive index for an X-wave is strongly enhanced (singular in the absence of losses) when

$$\cos^2\theta\varepsilon_{zz} + \sin^2\theta\varepsilon_{yy} = 0 \tag{2.39}$$

which corresponds to the bulk plasmon excitation. Indeed, from Maxwell's equations in the Coulomb gauge one can show that $|\frac{1}{c}\frac{\partial A}{\partial t}|/|\nabla\varphi| \sim |\frac{\omega^2}{\omega^2 - c^2k^2}||\frac{j_\perp}{j_\parallel}|$, where $\boldsymbol{j} = \boldsymbol{j}_\perp + \boldsymbol{j}_\parallel$, $\nabla \times \boldsymbol{j}_\parallel = 0$, $\nabla \cdot \boldsymbol{j}_\perp = 0$. Therefore, if $|\boldsymbol{j}_\perp| \sim |\boldsymbol{j}_\parallel|$, which corresponds to a general oblique propagation in an anisotropic medium, the wave is quasi-electrostatic at $n^2 \gg 1$. Eq. (2.39) corresponds to the condition $\boldsymbol{n} \cdot \boldsymbol{D} = 0$ for $\boldsymbol{E} = -\nabla\varphi \parallel \boldsymbol{n}$. If $\varepsilon_{yy} = \varepsilon_{zz} = \varepsilon_\perp$ the dispersion equation for a plasmon propagating in the plane orthogonal to the x-axis has a simple form $\varepsilon_\perp = 0$.

Figure 2.8 shows real and imaginary parts of the refractive index n_X of an X-wave as a function of frequency for different values of the propagation angle θ. Near the bulk plasmon resonance, i.e. around 100 meV for normal incidence, the value of n_X^2 becomes negative in the absence of losses according to Eq. (2.38)This corresponds to a non-propagating photonic gap. Since we include significant loss rate $\gamma = 10$ meV in all simulations, the real part of n_X does not go all the way to zero, but there is a strong absorption peak in the imaginary part of n_X. We will later see that this spectral region leads to a telltale change of phase in reflection. The second feature in all plots is an onset of interband transitions at $2E_F = 160$ meV.

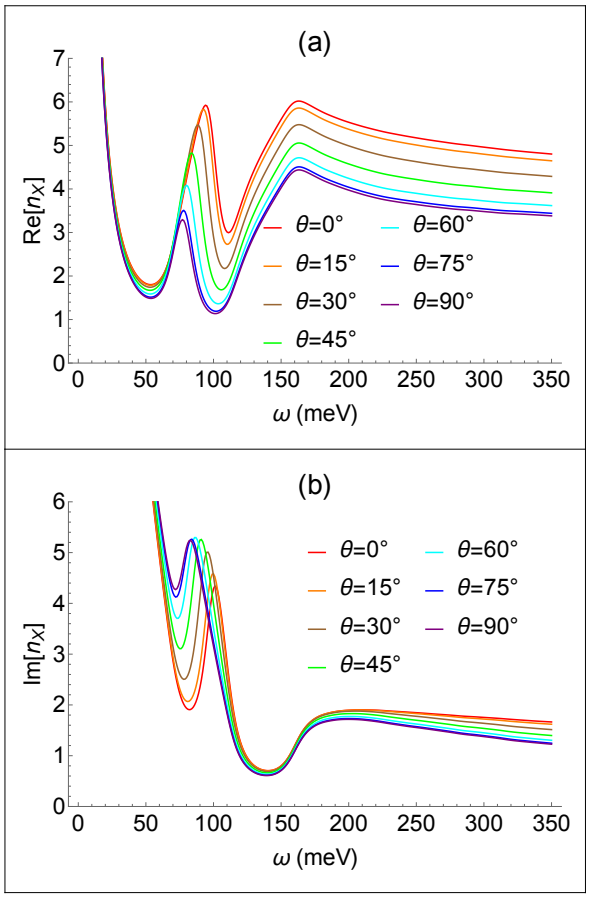

Figure 2.8: Real and imaginary parts of the refractive index n_X of an X-wave as a function of frequency for different values of the propagation angle θ. Other parameters are $E_F = 80$ meV, $\hbar v_F b = 100$ meV, and dephasing rate $\gamma = 10$ meV.

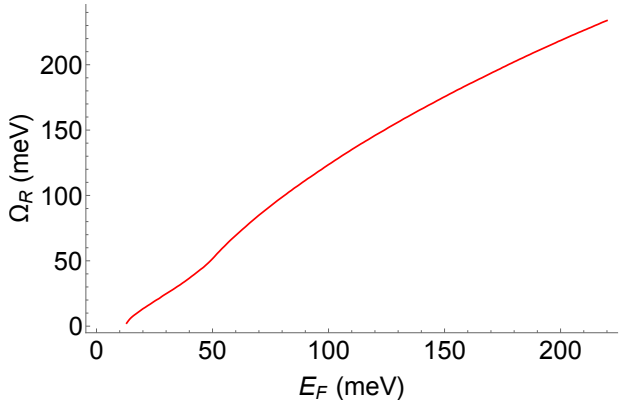

Figure 2.9: Real part of the bulk plasmon resonance frequency at normal incidence $\theta = 0$ as a function of the Fermi energy.

The real part of the bulk plasmon resonance frequency at normal incidence as a function of the Fermi energy is shown in Fig. 2.9. Note that according to Eq. (2.38) the magnitude of the refractive index at frequencies around plasmon resonance is determined by the value of the off-diagonal component of the dielectric tensor g. Therefore, measurements of the transmission and reflection provide a sensitive measure of the Weyl node separation.

The same is true about the polarization effects. From the third row of Eqs. (2.35) one can get the expression for the polarization coefficient:

$$K_X = \frac{E_z}{E_y} = \frac{ig - n_X^2 \sin\theta\cos\theta}{\varepsilon_{zz} - n_X^2 \sin^2\theta}. \tag{2.40}$$

Substituting Eq. (2.37) into Eq. (2.40) we get

$$K_X = \frac{ig\left(\cos^2\theta\varepsilon_{zz} + \sin^2\theta\varepsilon_{yy}\right) - (\varepsilon_{yy}\varepsilon_{zz} - g^2)\sin\theta\cos\theta}{\varepsilon_{zz}\left(\cos^2\theta\varepsilon_{zz} + \sin^2\theta\varepsilon_{yy}\right) - (\varepsilon_{yy}\varepsilon_{zz} - g^2)\sin^2\theta}. \tag{2.41}$$

At the resonant plasmon frequency defined by $\cos^2\theta\varepsilon_{zz} + \sin^2\theta\varepsilon_{yy} = 0$ we obtain $K_X = \frac{1}{\tan\theta}$, which is expected. If we set $\theta = 0$, which corresponds to normal incidence, $K_X = \frac{ig}{\varepsilon_{zz}}$, i.e. again proportional to g. In this case, the plasmon frequency is given by $\varepsilon_{zz} = 0$, and $K_X \to \infty$ in the absence of losses. If $\varepsilon_{yy} = \varepsilon_{zz} = \varepsilon_\perp$, Eq. (2.41) gives

$$K_X = \frac{ig\varepsilon_\perp - (\varepsilon_\perp^2 - g^2)\sin\theta\cos\theta}{\varepsilon_\perp^2\cos^2\theta + g^2\sin^2\theta}. \tag{2.42}$$

For an isotropic medium, when $g^2 = 0$, the last expression gives $K_X = -\tan\theta$, as it should be for a transverse wave in an isotropic medium.

2.4.2 Propagation transverse to the y-axis

In this case $n_y = 0$, $n^2 = n_x^2 + n_z^2$, $n_x = n\cos\phi$, $n_z = n\sin\phi$;

$$\begin{pmatrix} \varepsilon_{xx} - n_z^2 & 0 & n_x n_z \\ 0 & \varepsilon_{yy} - n^2 & ig \\ n_z n_x & -ig & \varepsilon_{zz} - n_x^2 \\ \end{pmatrix} \begin{pmatrix} E_x \\ E_y \\ E_z \end{pmatrix} = 0 \tag{2.43}$$

$$\left(\sin^2\phi\varepsilon_{zz} + \cos^2\phi\varepsilon_{xx}\right) n^4 - n^2\left[\varepsilon_{xx}\varepsilon_{zz} + \varepsilon_{yy}\left(\sin^2\phi\varepsilon_{zz} + \cos^2\phi\varepsilon_{xx}\right) - \sin^2\phi g^2\right] + \varepsilon_{xx}\left(\varepsilon_{yy}\varepsilon_{zz} - g^2\right) = 0. \tag{2.44}$$

Note that the solution of Eq. (2.44) at $\phi = \frac{\pi}{2}$ corresponds to the normal incidence propagation along z and therefore should coincide with Eqs. (2.36), (2.37) at $\theta = 0$. Indeed, from Eq. (2.44) for $\phi = \frac{\pi}{2}$ we obtain

$$\left(n^2 - \varepsilon_{xx}\right)\left[n^2 - \left(\varepsilon_{yy} - \frac{g^2}{\varepsilon_{zz}}\right)\right] = 0; \tag{2.45}$$

from which $n_O^2 = \varepsilon_{xx}$, $n_X^2 = \varepsilon_{yy} - \frac{g^2}{\varepsilon_{zz}}$, as expected.

The case $n^2 \to \infty$ in the absence of losses, when

$$\sin^2\phi\varepsilon_{zz} + \cos^2\phi\varepsilon_{xx} = 0 \tag{2.46}$$

corresponds to the condition $\boldsymbol{n}\cdot\boldsymbol{D} = 0$ where $\boldsymbol{E} = -\nabla\varphi \parallel \boldsymbol{n}$. From Eq. (2.44) we obtain

$$n_{O,X}^2 = \frac{\varepsilon_{xx}\varepsilon_{zz} + \varepsilon_{yy}\left(\sin^2\phi\varepsilon_{zz} + \cos^2\phi\varepsilon_{xx}\right) - \sin^2\phi g^2}{2\left(\sin^2\phi\varepsilon_{zz} + \cos^2\phi\varepsilon_{xx}\right)} \pm$$

$$\frac{\sqrt{\left[\varepsilon_{xx}\varepsilon_{zz}+\varepsilon_{yy}\left(\sin^2\phi\varepsilon_{zz}+\cos^2\phi\varepsilon_{xx}\right)-\sin^2\phi g^2\right]^2-4\left(\sin^2\phi\varepsilon_{zz}+\cos^2\phi\varepsilon_{xx}\right)\varepsilon_{xx}\left(\varepsilon_{yy}\varepsilon_{zz}-g^2\right)}}{2\left(\sin^2\phi\varepsilon_{zz}+\cos^2\phi\varepsilon_{xx}\right)} \tag{2.47}$$

In Eq. (2.47) the signs $\pm$ are chosen for $n^2_{O,X}$ according to the limiting case $\phi = \frac{\pi}{2}$.

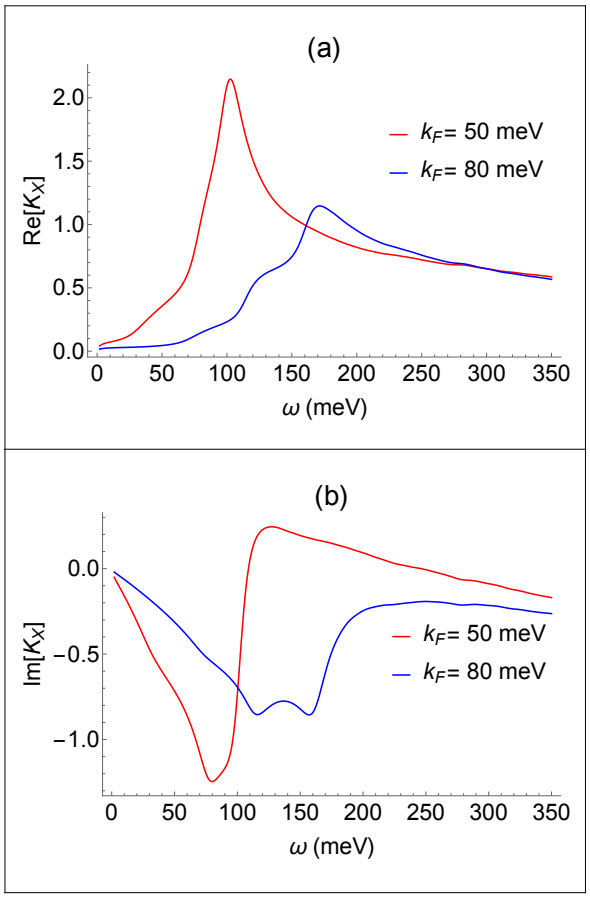

Figure 2.10: Spectra of real and imaginary parts of the polarization coefficient $K = E_z/E_y$ for an incident wave linearly polarized in y-direction after traversing a 1-μm film in x-direction.

For the propagation along the x-axis of anisotropy, when $\phi = 0$, Eq. (2.44) gives

$$n^2_{O,X} = \frac{\varepsilon_{zz}+\varepsilon_{yy}}{2} \pm \sqrt{\left(\frac{\varepsilon_{zz}-\varepsilon_{yy}}{2}\right)^2 + g^2} \tag{2.48}$$

Note that the x-axis is also a gyrotropy axis related to the Weyl node separation along x. Therefore, the propagation along x is similar to the Faraday geometry in a magnetic field. In our case the normal modes are elliptically polarized, and an incident linearly polarized wave experiences Faraday rotation and gains ellipticity after traversing a sample in x-direction. To quantify the effect, Fig. 2.10 shows the polarization coefficient $K = E_z/E_y$ after traversing a 1-μm thick film for a wave initially linearly polarized in y-direction. (Note that K includes the contribution of both normal modes as opposed to K_X in Eqs. (40), (41) for the extraordinary mode.) The real part of K is a measure of the polarization rotation whereas its imaginary part is a measure of ellipticity. Clearly, a rotation by $\sim \pi/2$ by very thin (0.5-1 μm) Weyl semimetal films is possible at frequencies near the interband absorption edge. This is a giant Faraday rotation, comparable to the one observed at THz frequencies in narrow-gap semiconductors in the vicinity of a cyclotron resonance in Tesla-strength magnetic fields; see e.g. [63] for the review. Note that in our case no magnetic field is needed and the effect is controlled by the Weyl node separation and by the Fermi level. Previously Faraday rotation and nonreciprocity in light propagation associated with it was studied in [54, 38] using the model with an axion θ-term in the electromagnetic field action.

2.4.3 Oblique propagation of bulk polaritons

In the general case the direction of the wave vector is determined by two angles θ and ϕ:

$$n_x = n\cos\phi\,, n_z = n\sin\phi\cos\theta\,, n_y = n\sin\phi\sin\theta.$$

The general expression for $n^2_{O,X}$ is quite cumbersome. At the same time, in the particular case of $\varepsilon_{yy} = \varepsilon_{zz} = \varepsilon_\perp$, the result should not depend on the angle θ and should coincide with the one for a magnetized plasma:

$$n^2_{O,X} = \frac{\varepsilon_\perp\left[\varepsilon_{xx}\left(1+\cos^2\phi\right)+\sin^2\phi\varepsilon_\perp\right]-\sin^2\phi g^2}{2\left(\sin^2\phi\varepsilon_\perp+\cos^2\phi\varepsilon_{xx}\right)}\pm$$

$$\frac{\sqrt{\left(\varepsilon_\perp\left[\varepsilon_{xx}\left(1+\cos^2\phi\right)+\sin^2\phi\varepsilon_\perp\right]-\sin^2\phi g^2\right)^2-4\varepsilon_{xx}\left(\sin^2\phi\varepsilon_\perp+\cos^2\phi\varepsilon_{xx}\right)\left(\varepsilon_\perp^2-g^2\right)}}{2\left(\sin^2\phi\varepsilon_\perp+\cos^2\phi\varepsilon_{xx}\right)} \tag{2.49}$$

The condition $\boldsymbol{n}\cdot\boldsymbol{D}=0$ at $\boldsymbol{E}=-\nabla\varphi\parallel\boldsymbol{n}$ in the case of an oblique propagation gives

$$\varepsilon_{xx}\cos^2\phi+\sin^2\phi\left(\sin^2\theta\varepsilon_{yy}+\cos^2\theta\varepsilon_{zz}\right)=0. \tag{2.50}$$

Therefore, Eq. (2.50) determines the frequencies of bulk plasmons in the general case. Under the condition $\varepsilon_{yy}=\varepsilon_{zz}=\varepsilon_\perp$ the plasmon dispersion equation takes a form similar to plasmons in a magnetized plasma:

$$\varepsilon_{xx}\cos^2\phi+\sin^2\phi\varepsilon_\perp=0. \tag{2.51}$$

2.5 Boundary conditions

So far we considered propagation and transmission of electromagnetic waves in bulk samples. Now we turn to effects of reflection and surface wave propagation that are equally sensitive to the electronic structure of WSMs. Moreover, in many situations they are easier to observe than bulk propagation effects.

We start with the derivation of the boundary conditions at $z=0$ surface. Assume that there is an isotropic dielectric medium with dielectric constant $n_{up}^2=\varepsilon_{up}$ above a WSM. The boundary conditions include:

(i) Gauss' law for the normal components of the electric induction vector:

$$\varepsilon_{up}E_z\left(z=+0\right)-D_z\left(z=-0\right)=4\pi\rho^S=-i\frac{4\pi}{\omega}\left(\frac{\partial}{\partial x}j_x^S+\frac{\partial}{\partial y}j_y^S\right) \tag{2.52}$$

where ρ^S, j_x^S and j_y^S are the surface charge and components of the surface current that are connected by the continuity equation. For the wave field we have $\frac{\partial}{\partial x,\partial y}\to ik_{x,y}$.

(ii) Equations for the magnetic field components:

$$B_z\left(z=-0\right)=B_z\left(z=+0\right), \tag{2.53}$$

$$B_y\left(z=+0\right)-B_y\left(z=-0\right)=-\frac{4\pi}{c}j_x^S, \tag{2.54}$$

$$B_x\left(z=+0\right)-B_x\left(z=-0\right)=\frac{4\pi}{c}j_y^S. \tag{2.55}$$

Due to the presence of the components of the surface conductivity σ_{zz}^S and $\sigma_{zy}^S=-\sigma_{yz}^S$ a surface dipole layer is formed at the boundary between the two media. Its dipole moment is

$$\begin{aligned}\boldsymbol{d}&=\Re\left[\boldsymbol{z_0}d_z e^{-i\omega t+ik_x x+ik_y y}\right],\\ d_z&=\frac{i}{\omega}\left[\sigma_{zy}^S E_y\left(z=-0\right)+\sigma_{zz}^S E_z\left(z=-0\right)\right].\end{aligned} \tag{2.56}$$

Note that when dealing with a surface response, we will always choose the fields at $z=-0$ in Eq. (2.56) and similar relationships. The presence of the dipole layer changes the boundary conditions for the tangential field components of $\boldsymbol{E}$. Consider Maxwell's equations

$$\frac{\partial E_z}{\partial y}-\frac{\partial E_y}{\partial z}=i\frac{\omega}{c}B_x,\ \frac{\partial E_x}{\partial z}-\frac{\partial E_z}{\partial x}=i\frac{\omega}{c}B_y.$$

For convenience, let's assume that the dipole layer has a small but finite thickness L:

$$|k_{x,y}|L\ll 1\quad\text{and}\quad\frac{\omega}{c}L\ll 1.$$

Using $\frac{\partial}{\partial x,\partial y}\to ik_{x,y}$ and integrating $\int_{-\frac{L}{2}}^{\frac{L}{2}}\ldots dz$, we obtain

$$ik_{x,y}\int_{-\frac{L}{2}}^{\frac{L}{2}}E_z\,dz=E_{x,y}\left(z=\frac{L}{2}\right)-E_{x,y}\left(z=-\frac{L}{2}\right) \tag{2.57}$$

We neglect the integral over the magnetic field components assuming that $\frac{\omega}{c}L\to 0$. Next we use

Gauss' law under the condition $|k_{x,y}|L \to 0$, which will yield in the region of the dipole layer:

$$\frac{\partial E_z}{\partial z} = 4\pi\rho\left(z\right), \quad \rho\left(z\right) = -\left(\frac{\partial P_z}{\partial z} + \frac{\partial p_z}{\partial z}\right).$$

Here P_z is a component of the volume polarization whereas p_z describes the distribution of the polarization in the dipole layer, so that

$$\int_{-\frac{L}{2}}^{\frac{L}{2}} \frac{\partial p_z}{\partial z}\, dz = 0 \quad \text{and} \quad \int_{-\frac{L}{2}}^{\frac{L}{2}} p_z\, dz = d_z.$$

Substituting $E_z = -4\pi\left(P_z + p_z\right)$ into Eq. (2.57) and integrating over dz at $|k_{x,y}|L \to 0$ and finite P_z , we obtain

$$E_{x,y}\left(z = \frac{L}{2}\right) - E_{x,y}\left(z = -\frac{L}{2}\right) = -i4\pi k_{x,y} d_z \tag{2.58}$$

The boundary condition Eq. (2.58) looks unusual but it can be easily deduced from the radiation field of an individual dipole.

Figures 2.11-2.14 show spectra of the surface conductivity components for different values of the Fermi momentum. Note that the surface conductivity in Gaussian units has a dimension of velocity and its value is normalized by $e^2/(2\pi\hbar) \simeq 3.5 \times 10^7$ cm/s in all plots. In contrast with the bulk conductivity, the surface conductivity had a Drude-like behavior at low frequencies only for the yy-component because of the surface state dispersion $E = -\hbar v_F k_y$. The surface optical response decreases with increasing Fermi energy and vanishes when all surface states within $k_x^2 + k_y^2 < b^2$ are occupied.

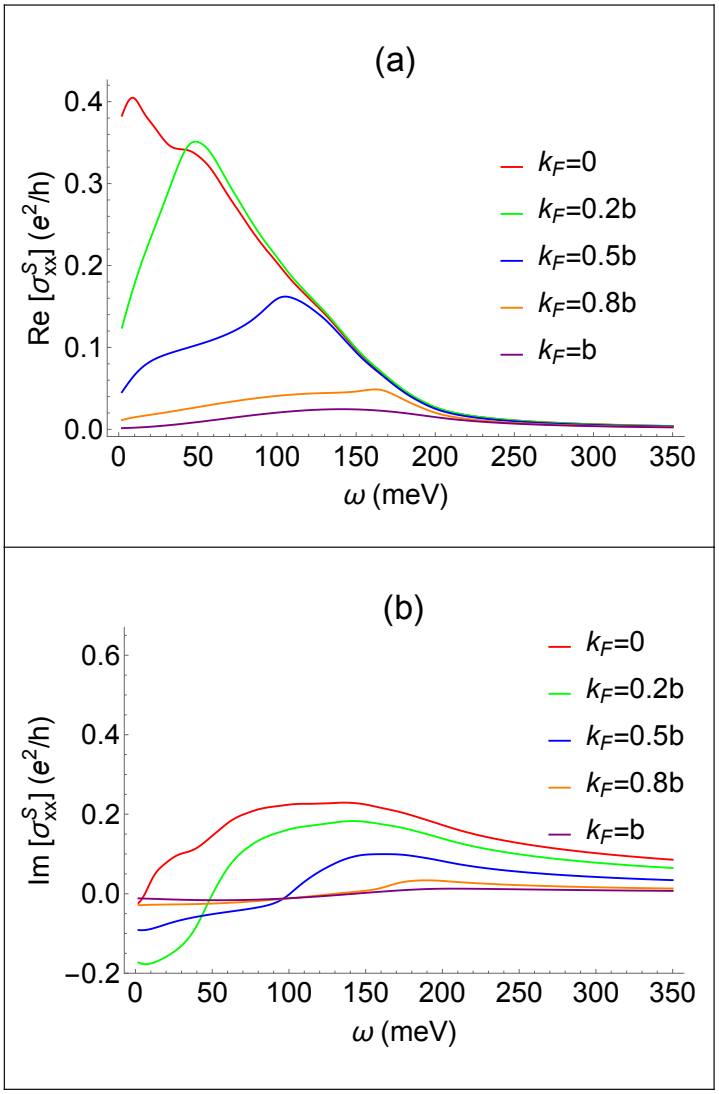

Figure 2.11: Spectra of the real and imaginary parts of the xx component of the surface conductivity at several values of the Fermi momentum for $\hbar v_F b = 100$ meV and dephasing rate $\gamma = 10$ meV.

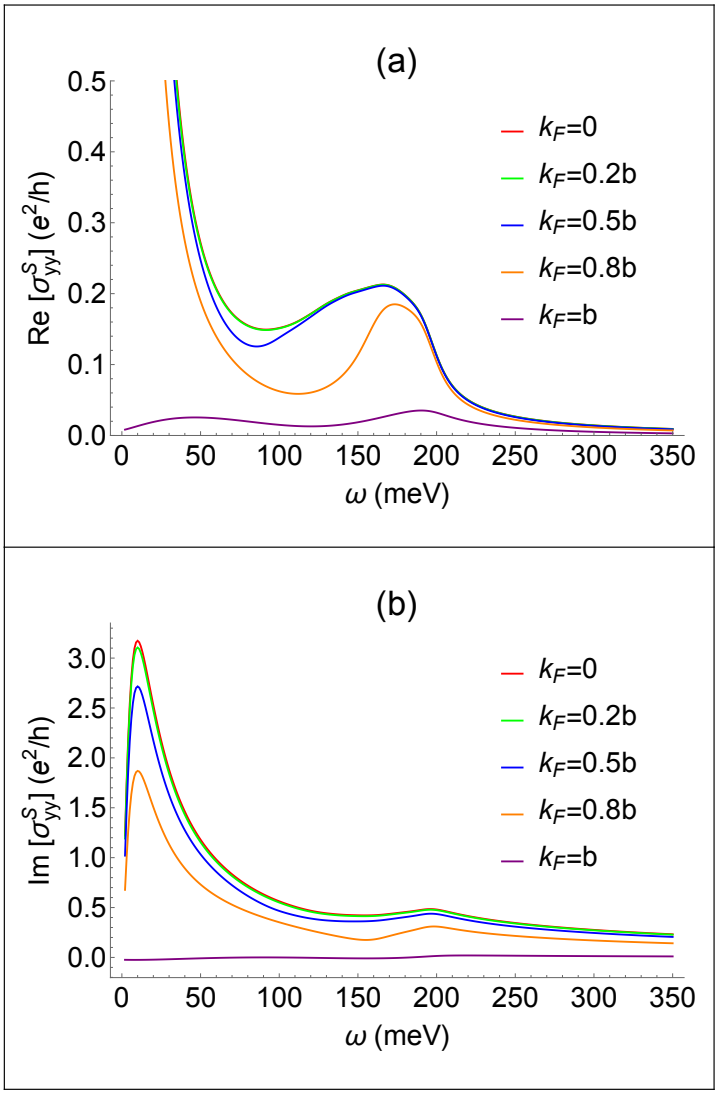

Figure 2.12: Spectra of the real and imaginary parts of the yy component of the surface conductivity at several values of the Fermi momentum for $\hbar v_F b = 100$ meV and dephasing rate $\gamma = 10$ meV.

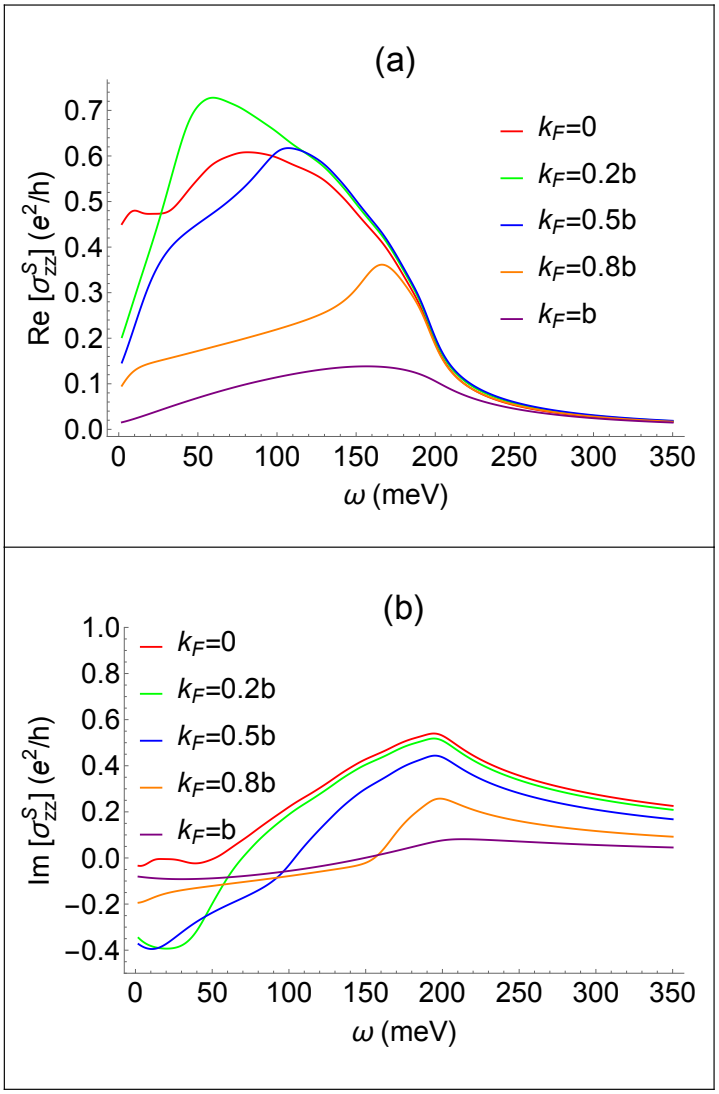

Figure 2.13: Spectra of the real and imaginary parts of the zz component of the surface conductivity at several values of the Fermi momentum for $\hbar v_F b = 100$ meV and dephasing rate $\gamma = 10$ meV.

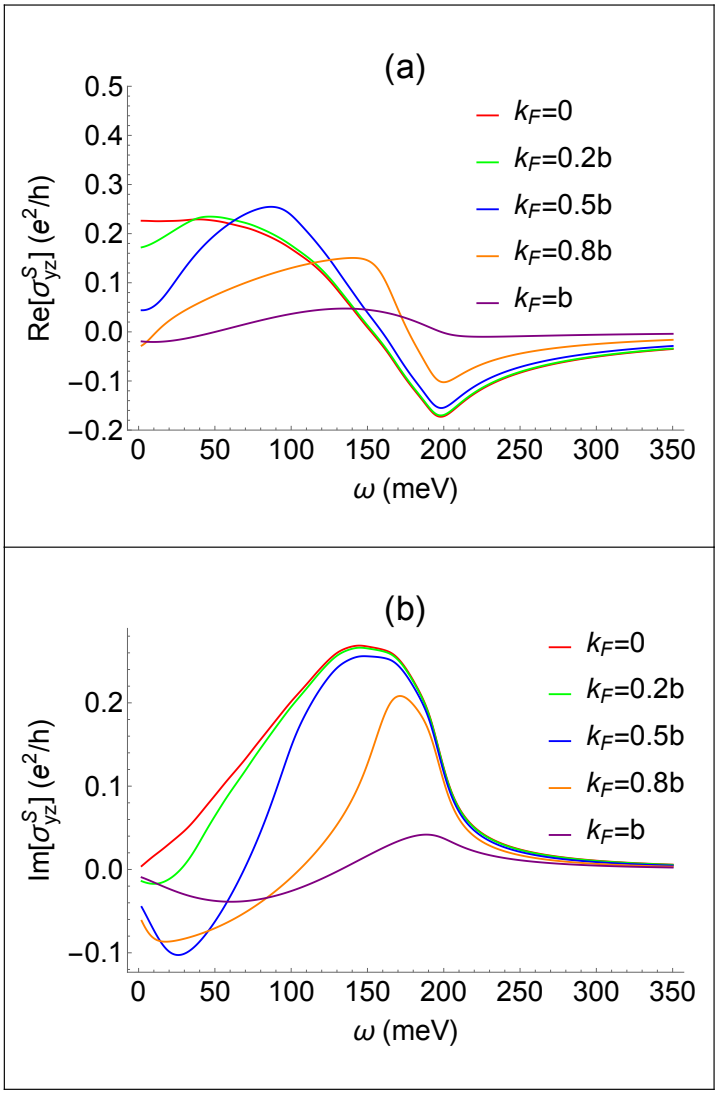

Figure 2.14: Spectra of the real and imaginary parts of the yz component of the surface conductivity at several values of the Fermi momentum for $\hbar v_F b = 100$ meV and dephasing rate $\gamma = 10$ meV.

2.6 Reflection from the surface of a Weyl semimetal

Consider radiation incident from a medium with refractive index n_{up} on a WSM at an angle θ between the wavevector of the wave and the normal to a WSM. For simplicity consider the propagation transverse to the x-axis. The reflection spectra provide information about both bulk and surface conductivity components. Here we will pay particular attention to the case when the

contribution of the surface states becomes significant or dominant, thus allowing one to probe surface states by optical means.

2.6.1 Reflection with excitation of an O-mode

In this geometry, the complex amplitudes of the electric field of the incident E_1, reflected E_2, and transmitted E_O wave are parallel to the x-axis. The refractive index of the transmitted wave is $n_O^2 = \varepsilon_{xx} = \varepsilon_{xx}^{(0)} + i\frac{4\pi}{\omega}\sigma_{xx}^B$ (see Eq. (2.36)).

Applying Maxwell's equations with standard boundary conditions including the surface current, we arrive at

$$R = \frac{E_2}{E_1} = -\frac{\cos\theta_O\sqrt{\varepsilon_{xx}^{(0)} + i\frac{4\pi}{\omega}\sigma_{xx}^B} + \frac{4\pi}{c}\sigma_{xx}^S - \cos\theta n_{up}}{\cos\theta_O\sqrt{\varepsilon_{xx}^{(0)} + i\frac{4\pi}{\omega}\sigma_{xx}^B} + \frac{4\pi}{c}\sigma_{xx}^S + \cos\theta n_{up}} \tag{2.59}$$

where $n_{up}\sin\theta = n_O\sin\theta_O$. Assuming $\sigma_{xx}^S = 0$ we obtain $R = \frac{E_2}{E_1} = \frac{\cos\theta n_{up} - \cos\theta_O n_O}{\cos\theta_O n_O + \cos\theta n_{up}}$, which is a standard Fresnel formula.

For the same magnitude of σ_{xx}^S, the relative contribution of surface states to the reflected field depends on the parameter $\frac{|\varepsilon_{xx}^{(0)}|}{4\pi|\sigma_{xx}^B|/\omega}$. If $\frac{\omega|\varepsilon_{xx}^{(0)}|}{4\pi|\sigma_{xx}^B|} \gg 1$, the relative contribution of surface states is determined by the expression: $\frac{2\omega|\sigma_{xx}^S|/c}{|\sigma_{xx}^B|/|\varepsilon_{xx}^{(0)}|}$. If $\frac{\omega|\varepsilon_{xx}^{(0)}|}{4\pi|\sigma_{xx}^B|} \ll 1$, one needs to evaluate the ratio $\frac{2\sqrt{\pi}\sigma_{xx}^S/c}{\sqrt{\sigma_{xx}^B/\omega}}$.

2.6.2 Reflection with excitation of an X-mode

In this geometry, the complex Fourier harmonics for the incident and reflected waves are

$$(\boldsymbol{y_o} \mp \boldsymbol{z_o}\tan\theta)\, E_{1,2} e^{\mp i\frac{\omega}{c}n_{up}\cos\theta z - i\frac{\omega}{c}n_{up}\sin\theta y - i\omega t}.$$

The transmitted wave is

$$(\boldsymbol{y_o} + \boldsymbol{z_o}K_X)\, E_X e^{-i\frac{\omega}{c}n_X\cos\theta_X z - i\frac{\omega}{c}n_X\sin\theta_X y - i\omega t},$$

where n_X^2 and K_X are given by Eqs. (2.37) and (2.40), in which one should substitute $\theta \to \theta_X$. The corresponding complex amplitudes of the magnetic field are $B_{1x} = \frac{n_{up}}{\cos\theta}E_1$, $B_{2x} = -\frac{n_{up}}{\cos\theta}E_2$,

$B_{(X)x} = n_X \left(\cos\theta_X - \sin\theta_X K_X\right) E_X$.

At the plasmon frequency, when $K_X = \frac{1}{\tan\theta_X}$, the last equation gives $B_{(X)x} = 0$, as should be expected. For an isotropic medium, when $K_X = -\tan\theta_X$, we obtain $B_{(X)x} = \frac{n_X}{\cos\theta_X} E_X$ which is also expected for a transverse wave (note that E_X is an amplitude of the y-component of the extraordinary (X-)mode).

We will use the boundary conditions

$$E_1 + E_2 - E_X = i\omega \frac{4\pi}{c} n_{up} \sin\theta d_z, \quad d_z = \frac{i}{\omega}\left(\sigma^S_{zy} + \sigma^S_{zz} K_X\right) E_X \tag{2.60}$$

$$\frac{n_{up}}{\cos\theta}\left(E_1 - E_2\right) - n_X \left(\cos\theta_X - \sin\theta_X K_X\right) E_X = \frac{4\pi}{c} j^S_y, \quad j^S_y = \left(\sigma^S_{yy} + \sigma^S_{yz} K_X\right) E_X \tag{2.61}$$

to obtain

$$R = \frac{E_2}{E_1} = \frac{n_{up}\left[1 - \frac{4\pi}{c} n_{up} \sin\theta \left(\sigma^S_{zy} + \sigma^S_{zz} K_X\right)\right] - n_X \cos\theta \left(\cos\theta_X - \sin\theta_X K_X\right) + \frac{4\pi}{c}\cos^2\theta \left(\sigma^S_{yy} + \sigma^S_{yz} K_X\right)}{n_X \cos\theta \left(\cos\theta_X - \sin\theta_X K_X\right) + \frac{4\pi}{c}\cos^2\left(\sigma^S_{yy} + \sigma^S_{yz} K_X\right) + n_{up}\left[1 - \frac{4\pi}{c} n_{up} \sin\theta \left(\sigma^S_{zy} + \sigma^S_{zz} K_X\right)\right]} \tag{2.62}$$

where $n_{up} \sin\theta = n_X \sin\theta_X$. In the limit of an isotropic medium, where $K_X = -\tan\theta_X$, $\sigma^S_{ij} = 0$, we obtain $R = \frac{E_2}{E_1} = \frac{n_{up}\cos\theta_X - n_X \cos\theta}{n_X \cos\theta + n_{up}\cos\theta_X}$ which is a standard Fresnel equation.

For the normal incidence the expressions are simplified:

$$n^2_X = \varepsilon_{yy} - \frac{g^2}{\varepsilon_{zz}} = \varepsilon^{(0)}_{yy} + i\frac{4\pi}{\omega}\sigma^B_{yy} - \frac{\left(\frac{4\pi\sigma^B_{yz}}{\omega}\right)^2}{\varepsilon^{(0)}_{zz} + i\frac{4\pi}{\omega}\sigma^B_{zz}}, \quad K_X = \frac{ig}{\varepsilon_{zz}} = i\frac{\frac{4\pi\sigma^B_{yz}}{\omega}}{\varepsilon^{(0)}_{zz} + i\frac{4\pi}{\omega}\sigma^B_{zz}},$$

which gives

$$R = \frac{n_{up} - n_X + \frac{4\pi}{c}\left(\sigma^S_{yy} + i\sigma^S_{yz}\frac{g}{\varepsilon_{zz}}\right)}{n_{up} + n_X + \frac{4\pi}{c}\left(\sigma^S_{yy} + i\sigma^S_{yz}\frac{g}{\varepsilon_{zz}}\right)} \tag{2.63}$$

The contribution of surface states is less trivial for X-mode excitation as compared to the excitation of an O-mode. For normal incidence (see Eq. (2.63)) one can see that at the plasmon

resonance frequency, when $\varepsilon_{zz} \to 0$ in the absence of losses, the contribution of the surface conductivity can become dominant. Indeed, in Eq. (2.63) the term $\sigma_{yz}^S \frac{g}{\varepsilon_{zz}}$ diverges as $\frac{1}{\varepsilon_{zz}}$, whereas the refractive index n_X diverges weaker, as $\frac{1}{\sqrt{\varepsilon_{zz}}}$. When $\sigma_{ij}^S = 0$ while $n_X \gg n_{up}$ we have $R = -1$ (we take into account that the magnitude of n_X is large at the plasmon frequency). In the opposite case, when the contribution of the surface conductivity dominates, i.e. $\frac{4\pi}{c}|\sigma_{yz}^S \frac{g}{\varepsilon_{zz}}| \gg |n_X| \approx \frac{g}{\sqrt{|\varepsilon_{zz}|}}$, we obtain $R = +1$, i.e. the phase of the reflected field is rotated by 180 degrees.

The enhanced contribution of the surface conductivity at normal incidence in the vicinity of the bulk plasmon resonance is expected. Indeed, at plasmon resonance the z-component E_z of the field in the medium becomes very large, which leads to a dominant contribution of the surface current $j_y^S = \sigma_{yz}^S E_z$.

For oblique incidence $\theta \neq 0$ and small losses the calculations of the reflection in the vicinity of plasmon resonance have a technical subtlety, related to the presence of the term $n_X \cos\theta \left(\cos\theta_X - \sin\theta_X K_X\right)$ in Eq. (2.62). Indeed, at the plasmon frequency $n_X \to \infty$ as losses $\gamma \to 0$; however, for a plasmon we also have $K_X \to \frac{1}{\tan\theta_X}$, i.e. $\left(\cos\theta_X - \sin\theta_X K_X\right) \to 0$. One needs to treat the resulting uncertainty of the product with caution. The details are presented in Appendix F.

The main result is that the contribution of surface states to the reflected wave is determined by the ratio

$$\frac{|\sigma_{yz}^S|}{c\sqrt{|\varepsilon_{zz}|}/4\pi}$$

and therefore becomes significant or dominant at the plasmon resonance frequency, when $\varepsilon_{zz} = \varepsilon_{zz}^{(0)} + i\frac{4\pi}{\omega}\sigma_{zz}^B \to 0$. When the bulk contribution dominates the reflection coefficient R is close to -1. When the surface contribution dominates, R is close to $+1$ i.e. the phase of the reflected field flips.

2.7 Surface plasmon-polaritons

Surface plasmon-polaritons can be supported by both bulk and surface electron states. Here we derive dispersion relations for surface waves including both bulk and surface conductivity for several specific cases. Emphasis is placed on the situations where the dispersion is significantly

affected or dominated by surface states and can therefore be used for diagnostics of surface states and Fermi arcs. Previously, surface plasmons in WSMs have been considered in the low-frequency limit within a semiclassical description of particle motion with added ad hoc anomalous Hall term [64] and with a quantum-mechanical description [59] based on the Hamiltonian in [58]. Both studies indicated strong anisotropy and dispersion of surface plasmons.

2.7.1 Quasielectrostatic approximation

Within the quasielectrostatic approximation the electric field can be defined through the scalar potential:

$$\vec{\mathcal{E}} = \Re\left[\vec{E}\,(z)\,e^{ik_x x+ik_y y-i\omega t}\right] = -\nabla\mathcal{F}, \quad \mathcal{F} = \Re\left[\Phi\,(z)\,e^{ik_x x+ik_y y-i\omega t}\right].$$

We introduce the vector of electric induction, $\vec{\mathcal{D}} = \Re\left[\vec{D}\,(z)\,e^{ik_x x+ik_y y-i\omega t}\right] = \hat{\varepsilon}\vec{\mathcal{E}}$ and use Gauss' law for each halfspace:

$$\nabla\cdot\vec{\mathcal{D}} = 0. \tag{2.64}$$

In general, there can be an electric dipole layer at the boundary between the two media. The dipole layer has a jump in the scalar potential $\Phi\,(z)$,

$$\Phi\,(z=+0) - \Phi\,(z=-0) = 4\pi d_z, \tag{2.65}$$

where d_z is determined by Eqs. (2.56).

Next, we define the potential $\Phi\,(z)$ for the surface mode as

$$\Phi\,(z>0) = \Phi_{up}e^{-\kappa_{up}z}, \quad \Phi\,(z<0) = \Phi_W e^{+\kappa_W z}.$$

Using Eq. (2.64) in each halfspace, we obtain

$$k_x^2 + k_y^2 - \kappa_{up}^2 = 0, \tag{2.66}$$

$$k_x^2\varepsilon_{xx} + k_y^2\varepsilon_{yy} - \kappa_W^2\varepsilon_{zz} = 0. \tag{2.67}$$

Using the boundary condition Eq. (2.52) we get

$$n_{up}^2\kappa_{up}\Phi_{up} - \left[\varepsilon_{zz}\left(-\kappa_W\Phi_W\right) + \varepsilon_{zy}\left(-ik_y\Phi_W\right)\right] = -i\frac{4\pi}{\omega}\left(\frac{\partial}{\partial x}j_x^S + \frac{\partial}{\partial y}j_y^S\right)$$

which gives

$$n_{up}^2\kappa_{up}\Phi_{up} + \left[\kappa_W\left(\varepsilon_{zz} + \frac{4\pi}{\omega}k_y\sigma_{yz}^S\right) + gk_y + i\frac{4\pi}{\omega}\left(k_x^2\sigma_{xx}^S + k_y^2\sigma_{yy}^S\right)\right]\Phi_W = 0 \tag{2.68}$$

where $\varepsilon_{yz} = -\varepsilon_{zy} = ig = i\frac{4\pi\sigma_{yz}^B}{\omega}$. Using also the boundary condition Eq. (2.65) together with Eqs. (2.56), we obtain

$$\Phi_{up} + \left(i\frac{4\pi}{\omega}\kappa_W\sigma_{zz}^S - \frac{4\pi}{\omega}k_y\sigma_{zy}^S - 1\right)\Phi_W = 0 \tag{2.69}$$

From these relationships one can get the dispersion equation for surface waves. Note that the confinement constants κ_W and κ_{up} are generally complex-valued. Their imaginary parts give rise to a Poynting flux away from the surface which contributes to surface wave attenuation.

2.7.1.1 Neglecting surface states

First, we neglect the surface conductivity to consider surface plasmons supported by bulk carriers only. In this case from Eqs. (2.66), (2.69) we get $\kappa_{up} = \sqrt{k_x^2 + k_y^2}$, $\Phi_{up} = \Phi_W$. Denoting $k_x^2 + k_y^2 = k^2$, $k_x = k\cos\phi$, $k_y = k\sin\phi$, we obtain from Eq. (2.67)

$$\kappa_W = k\sqrt{\frac{\cos^2\phi\varepsilon_{xx} + \sin^2\phi\varepsilon_{yy}}{\varepsilon_{zz}}}. \tag{2.70}$$

Furthermore, from Eq. (2.68) for $\kappa_{up} = k$ and $\Phi_{up} = \Phi_W$ we have

$$n_{up}^2 k + \kappa_W\varepsilon_{zz} + gk\sin\phi = 0, \tag{2.71}$$

where $\varepsilon_{yz} = ig = i\frac{4\pi\sigma^B_{yz}}{\omega}$. Substituting Eq. (2.70) into Eq. (2.71), we obtain the dispersion relation

$$D(\omega,\phi) = n_{up}^2 + \varepsilon_{zz}\sqrt{\frac{\cos^2\phi\varepsilon_{xx} + \sin^2\phi\varepsilon_{yy}}{\varepsilon_{zz}}} + g\sin\phi = 0. \tag{2.72}$$

The dispersion equation Eq. (2.72) gives the dependence $\omega(\phi)$, but does not have any dependence on the magnitude of k. This situation is similar to the dispersion relation for bulk plasmons in the quasielectrostatic approximation, Eq. (2.50). It is also similar to waves in classical magnetized plasmas. Of course the range of values of k is constrained by the validity of the quasielectrostatic approximation.

2.7.1.2 Including surface states

If we now include the surface conductivity, Eqs. (2.66)-(2.69) give

$$D(\omega,\phi) - \frac{4\pi}{\omega}k\Bigg[\sqrt{\frac{\cos^2\phi\varepsilon_{xx} + \sin^2\phi\varepsilon_{yy}}{\varepsilon_{zz}}}\left(in_{up}^2\sigma^S_{zz} - \sin\phi\sigma^S_{yz}\right) - n_{up}^2\sin\phi\sigma^S_{yz} - i\left(\cos^2\phi\sigma^S_{xx} + \sin^2\phi\sigma^S_{yy}\right)\Bigg] = 0 \tag{2.73}$$

where the function $D(\omega,\phi)$ is determined by Eq. (2.72). As we see, taking the surface conductivity into account brings the dependence on the magnitude of the wave vector k into the dispersion relation. Therefore, measuring the frequency dispersion of the surface plasmon resonance provides a direct characterization of surface states.

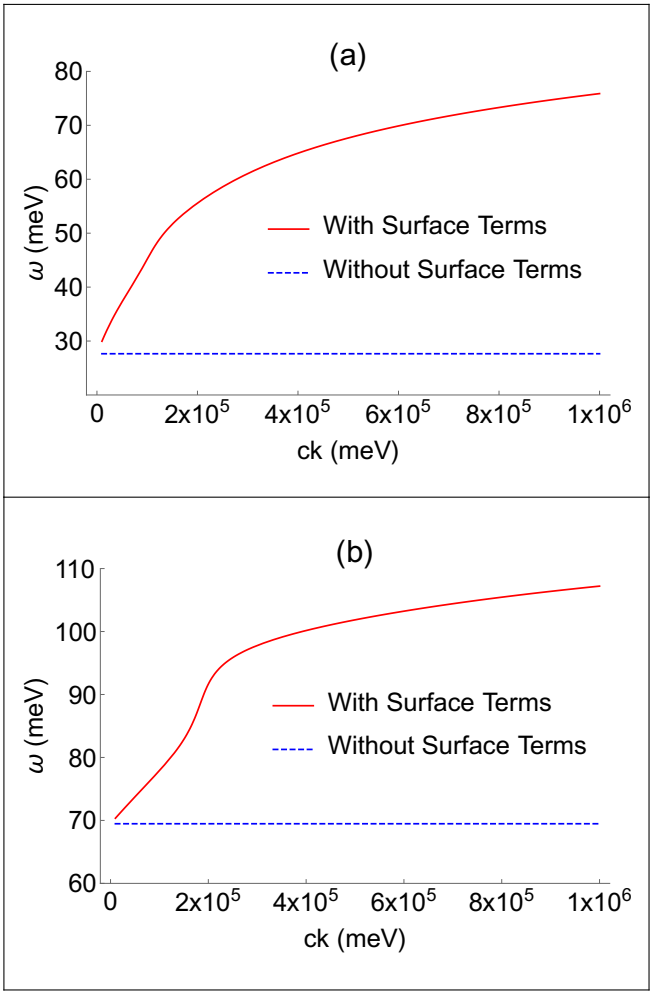

Figure 2.15: Real part of the surface plasmon frequency as a function of real plasmon wavenumber obtained as a solution to the dispersion equation Eq. (2.73) for $\phi = \pi/2$, $\hbar v_F b = 100$ meV and two values of the electron Fermi momentum $k_F = 0.5b$ and $0.8b$. The surface plasmon frequency neglecting surface conductivity contribution is shown as a dashed line.

Figure 2.15 shows the surface plasmon dispersion for propagation along y, i.e. transverse to the gyrotropy x-axis, for two values of the Fermi momentum. The real part of the surface plasmon frequency ignoring the contribution of the surface conductivity is shown as a dashed horizontal line for each value of k_F. Clearly, the contribution of surface electron states is important everywhere, except maybe in a narrow region of small wavenumbers k where the quasistatic approximation breaks down. The plot has a horizontal axis ck in units of meV in order to directly compare with

frequencies. The inequality $ck \gg \omega$ is satisfied almost everywhere.

The fact that the contribution of the surface current is so important can be understood from the structure of Eq. (2.73). Clearly, the relative contribution of the bulk and surface terms can be estimated by comparing the magnitudes of $|\sigma^B|$ and $|k\sigma^S|$ where σ^B and σ^S are appropriate components of bulk and surface conductivity tensors and k is a wavenumber of a given electromagnetic mode. This is true not only for surface modes but also for other electromagnetic wave processes at the boundary such as reflection. In the mid/far-infrared spectral region of interest to us, $|k\sigma^S| \ll |\sigma^B|$ for vacuum wavelengths $ck \sim \omega$. However, for large surface plasmon wavenumbers shown in Fig. 2.15 the opposite condition $|k\sigma^S| \geq |\sigma^B|$ is satisfied.

Note the dispersion in Fig. 2.15 is stronger (the slope is steeper) at frequencies corresponding to $\mathrm{Re}[\epsilon_{zz}] \approx 0$, i.e. near the resonance for bulk plasmons propagating along z. This follows from Eq. (2.73) where the surface terms contain a factor $1/\sqrt{\epsilon_{zz}}$. Physically, this is expected: indeed, as we already commented, at the plasmon resonance the z-component E_z of the field in the medium becomes very large, which leads to an enhanced contribution of the surface current $j_y^S = \sigma_{yz}^S E_z$.

2.7.2 Surface waves beyond the quasielectrostatic approximation

For small wavenumbers the quasielectrostatic approximation is no longer valid. On the other hand, in this case one can neglect the surface conductivity as we pointed out in the previous paragraph. This is not an interesting limit as far as the spectroscopy of surface states is concerned, but we still derive the resulting dispersion relation for completeness. For the electric field of a surface mode in the upper halfspace with the refractive index n_{up},

$$\vec{\mathcal{E}}_{up} = \Re\left[\vec{E}_{up} e^{ik_x x + ik_y y - \kappa_{up} z - i\omega t}\right],$$

the Maxwell's equation for $\nabla \times \vec{\mathcal{E}}$ gives

$$k_y E_z - i\kappa_{up} E_y = \frac{\omega}{c} B_x, \quad k_x E_z - i\kappa_{up} E_x = -\frac{\omega}{c} B_y, \quad k_x E_y - k_y E_x = \frac{\omega}{c} B_z. \tag{2.74}$$

For the field in the Weyl semimetal,

$$\vec{\mathcal{E}}_W = \Re\left[\vec{E}_W e^{ik_x x + ik_y y + \kappa_W z - i\omega t}\right]$$

the same equation gives, after replacing $\kappa_{up} \to -\kappa_W$ in Eq. (2.74),

$$k_y E_z + i\kappa_W E_y = \frac{\omega}{c} B_x, \quad k_x E_z + i\kappa_W E_x = -\frac{\omega}{c} B_y, \quad k_x E_y - k_y E_x = \frac{\omega}{c} B_z. \tag{2.75}$$

The inverse decay length for the field in the upper halfspace is given by $\kappa_{up}^2 = k^2 - n_{up}^2 \frac{\omega^2}{c^2}$.

In a WSM we can use a version of Eq. (2.35) after replacing $k_z \to -i\kappa_W$:

$$\begin{pmatrix} \frac{\omega^2}{c^2}\varepsilon_{xx} - k_y^2 + \kappa_W^2 & k_x k_y & -ik_x\kappa_W \\ k_y k_x & \frac{\omega^2}{c^2}\varepsilon_{yy} - k_x^2 + \kappa_W^2 & i\frac{\omega^2}{c^2} g - ik_y\kappa_W \\ -ik_x\kappa_W & -i\frac{\omega^2}{c^2} g - ik_y\kappa_W & \frac{\omega^2}{c^2}\varepsilon_{zz} - k^2 \end{pmatrix} \begin{pmatrix} E_x \\ E_y \\ E_z \end{pmatrix} = 0, \tag{2.76}$$

where $k^2 = k_x^2 + k_y^2$.

Consider again a surface wave propagating transverse to the anisotropy axis ($k_x = 0$). In this case, there are two solutions to the dispersion equation Eq. (2.76), an O-wave and an X-wave. However, one can show that an O-wave with $E_x \neq 0$ does not exist as a surface wave. Moreover, this statement remains true even with the surface current taken into account. Only the X-wave with $E_{y,z} \neq 0$ can exist as a surface wave. Its inverse confinement length in the Weyl semimetal is given by

$$\kappa_W^2 = \frac{\varepsilon_{yy}}{\varepsilon_{zz}} \left(k^2 - n_X^2 \frac{\omega^2}{c^2}\right) \tag{2.77}$$

where

$$n_X^2 = \varepsilon_{zz} - \frac{g^2}{\varepsilon_{yy}}$$

is the refractive index of an extraordinary wave propagating in the volume in the y-direction (see

Eq. (2.37) for $\theta = \frac{\pi}{2}$). The polarization of an extraordinary wave is determined by

$$i\left(\frac{\omega^2}{c^2}g + k\kappa_W\right)E_y = \left(\frac{\omega^2}{c^2}\varepsilon_{zz} - k^2\right)E_{zW} \tag{2.78}$$

which follows from Eq. (2.76). After some straightforward algebra, we obtain the dispersion relation for a surface wave:

$$\left(k^2 - \frac{\omega^2}{c^2}n_{up}^2\right)\left(gk + \varepsilon_{zz}\sqrt{\frac{\varepsilon_{yy}}{\varepsilon_{zz}}}\sqrt{k^2 - \frac{\omega^2}{c^2}n_X^2}\right) + \sqrt{k^2 - \frac{\omega^2}{c^2}n_{up}^2}\left(k^2 - \frac{\omega^2}{c^2}\varepsilon_{zz}\right)n_{up}^2 = 0. \tag{2.79}$$

In the limit of large wavenumbers k this equation becomes the quasielectrostatic dispersion relation Eq. (2.72) at $\phi = \frac{\pi}{2}$.

For the propagation in x-direction, one can repeat the above analysis for the case $k_y = 0$ and obtain that there are no surface wave solutions when the surface conductivity is neglected.

One interesting solution of the dispersion equation Eq. (2.79) is a strongly nonelectrostatic case when the surface mode is weakly localized in a medium above the WSM surface, e.g. in the air. The energy of this wave is mostly contained in an ambient medium above the WSM surface where there is no absorption. Therefore, such surface waves can have a long propagation length; see e.g. [65, 66, 67].

To find this solution we assume $n_{up}^2 = 1$ and introduce the notation $\frac{\omega}{c} = k_0$. A weak localization outside a WSM means that $|\kappa_{up}| \ll k_0$. Then, assuming $k \simeq k_0 + \delta k$, where $k_0 \gg |\delta k|$, we obtain $\kappa_{up} \simeq \sqrt{2k_0\delta k}$. From Eqs. (2.79) and (2.77) in the first order with respect to $\sqrt{\frac{\delta k}{k_0}}$ we get

$$\delta k \simeq \frac{k_0}{2}\frac{\left(\varepsilon_{zz} - 1\right)^2}{\left[g + \sqrt{\varepsilon_{zz}\varepsilon_{yy}\left(1 - \varepsilon_{zz} + \frac{g^2}{\varepsilon_{yy}}\right)}\right]^2}, \tag{2.80}$$

$$\mathrm{Re}\kappa_W^2 \simeq \mathrm{Re}\left[k_0^2\frac{\varepsilon_{yy}}{\varepsilon_{zz}}\left(1 - \varepsilon_{zz} + \frac{g^2}{\varepsilon_{yy}}\right)\right]. \tag{2.81}$$

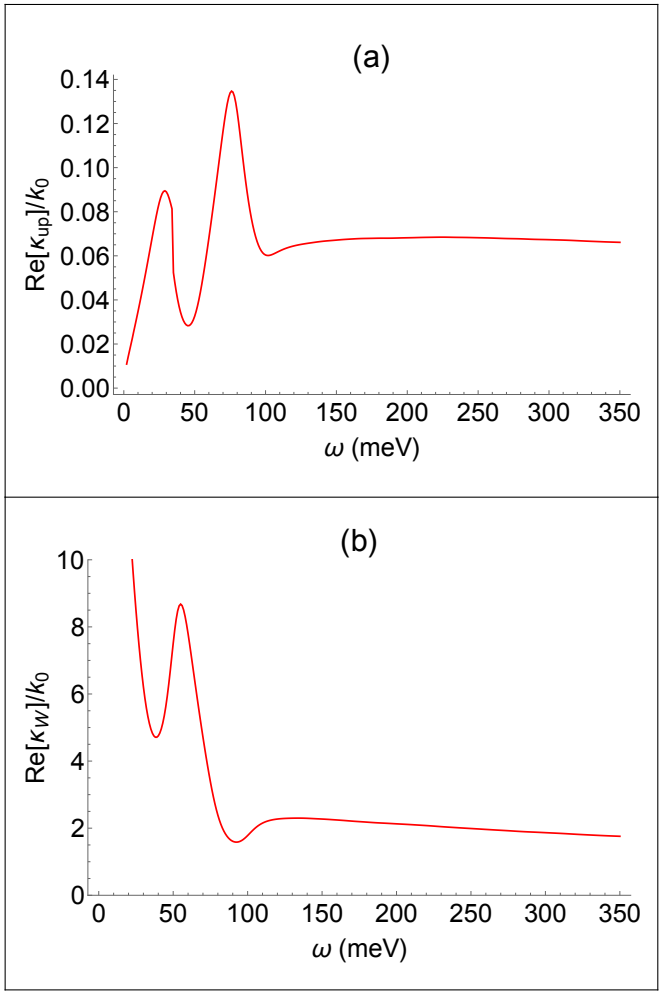

Figure 2.16: Normalized confinement constants (a) $\mathrm{Re}[\kappa_{up}]/k_0 \simeq \mathrm{Re}[\sqrt{2\delta k/k_0}]$ and (b) $\mathrm{Re}[\kappa_W]/k_0$ as functions of frequency, for the Fermi momentum $k_F = 0.5b$. Other parameters are $\hbar v_F b = 100$ meV and $\gamma = 10$ meV.

This solution describes surface waves if $\mathrm{Re}[\kappa_W] > 0$ and $\mathrm{Re}[\kappa_{up}] > 0$. In addition, $|\delta k| \ll k_0$ has to be satisfied. We checked that all three inequalities are satisfied for the numerical parameters chosen to calculate the conductivity tensor. As an example, Fig. 2.16 shows normalized confinement constants $\mathrm{Re}[\kappa_W]/k_0$ and $\mathrm{Re}[\kappa_{up}]/k_0 \simeq \mathrm{Re}[\sqrt{2\delta k/k_0}]$ as functions of frequency, for the Fermi momentum $k_F = 0.5b$. Clearly, the solution describes a surface wave which is weakly confined in the air and strongly confined in the WSM. The spectra remain qualitatively the same with increasing Fermi momentum, but the oscillating feature moves to higher energies, roughly

following the spectral region where the real parts of ε_{zz} and ε_{yy} cross zero. We note again that the confinement constants κ_W and κ_{up} are complex-valued. Their imaginary parts give rise to a Poynting flux away from the surface which contributes to surface wave attenuation.

2.8 Summary and conclusions

We presented systematic studies of the optical properties and electromagnetic modes of Weyl semimetals in the minimal two-band model with two separated Weyl nodes. Both bulk and surface conductivity tensors are derived from a single microscopic Hamiltonian. The presence of separated Weyl nodes and associated surface states gives rise to distinct signatures in the transmission, reflection, and polarization of bulk and surface electromagnetic waves. These signatures can be used for quantitative characterization of electronic structure of Weyl semimetals. Particularly sensitive spectroscopic probes of bulk electronic properties include strong anisotropy in propagation of both bulk and surface modes, birefringent dispersion and absorption spectra of ordinary and extraordinary normal modes, the frequency of bulk plasmon resonance as a function of incidence angle and doping level, and the polarization rotation and ellipticity for incident linearly polarized light. The sensitive characterization of surface electronic states can be achieved by measuring the phase change of the reflection coefficient of incident plane waves, the frequency dispersion of surface plasmon-polariton modes, and strong anisotropy of surface plasmon-polaritons with respect to their propagation direction and polarization.

The quantitative results in this chapter are valid only for magnetic WSMs with time-reversal symmetry breaking. One can still make some qualitative conclusions regarding the optical response of WSMs with inversion symmetry breaking. In particular, one should expect the off-diagonal conductivity components to be zero in this case, and therefore gyrotropic effects will be absent. However, there should still be strong anisotropy of both bulk and surface mode propagation, related to the position of Weyl node pairs. One should still expect strong dispersion of surface plasmon-polaritons associated with the presence of Fermi arc surface states. The features in absorption and dispersion associated with the bulk plasmon resonance, Fermi edge, and saddle points between Weyl nodes will be present. The low-frequency response related to bulk Dirac cones will be similar.

Potential optoelectronic applications of magnetic WSM films in the mid-infrared and THz spectral regions will benefit from the strong anisotropy, gyrotropy, and birefringence of these materials, giant polarization rotation for light transmitted along the gyrotropy axis of submicron films, and strongly localized surface plasmon-polariton modes. All effects are tunable by doping.

3. OPTICAL HALL EFFECT AND ANOMALOUS DISPERSION OF SURFACE POLARITONS IN TYPE-I MAGNETIC WEYL SEMIMETALS*

Weyl semimetals possess unique electrodynamic properties due to a combination of strongly anisotropic and gyrotropic bulk conductivity, surface conductivity, and surface dipole layer. In particular, the gyrotropy caused by Weyl node separation in momentum space gives rise to the optical Hall effect for surface polaritons at the boundaries parallel to the gyrotropic axis. In this chapter, we explore the potential of popular tip-enhanced optical spectroscopy techniques for studies of bulk and surface topological electron states in these materials. Strong anisotropy, anomalous dispersion, and the optical Hall effect for surface polaritons launched by a nanotip provide information about Weyl node position and separation in the Brillouin zone, the value of the Fermi momentum, and the matrix elements of the optical transitions involving both bulk and surface electron states.

3.1 Introduction

A number of recent studies have suggested that Weyl semimetals (WSMs) should have highly unusual optical response originated from unique topological properties of their bulk and surface electron states; see e.g. [54, 55, 52, 56, 68, 38, 59, 69, 70, 71, 72, 73, 74] and references therein. Their optical response can be used to provide detailed spectroscopic information about their electronic structure which could be difficult to obtain by any other means. Furthermore, inversion or time reversal symmetry breaking inherent to WSMs makes their optical response strongly anisotropic or gyrotropic, enables strong optical nonlinearity, creates anomalous dispersion of normal electromagnetic modes, breaks Lorentz reciprocity, and leads to many other optical phenomena of potential use in new generations of the optoelectronic devices.

In a recent paper [71], we investigated general optical properties of Type I WSMs. Starting from a class of microscopic Hamiltonians for WSMs with two separated Weyl nodes ([57, 58]),

*Reprinted with permission from: "Optical Hall effect and gyrotropy of surface polaritons in Weyl semimetals" by Q. Chen, M. Erukhimova, M. Tokman, and A. Belyanin, 2019. Phys. Rev. B 100, 235454, Copyright 2019 by the American Physical Society.

we obtained both bulk and surface electron states, derived bulk and surface conductivity tensors, and described the properties of electromagnetic eigenmodes.

Here we focus on one of the most popular and convenient ways to study the properties of novel materials by optical means: a tip-based optical spectroscopy, in which a tip brought in close proximity to the material surface is illuminated with laser light and the linear or nonlinear scattered signal is collected. Strong near-field enhancement at the tip apex may overcompensate the decrease in the volume of the material where light-matter interaction occurs [75, 76]. Even more importantly in the context of this chapter, nanoscale concentration of the incident light at the tip apex relaxes the optical selection and momentum matching rules. In particular, it allows one to launch various kinds of surface polariton modes which provide valuable information about the properties of both bulk and surface electron states.

We use the microscopic model of the optical response of Type I WSMs developed in [71] to predict and describe theoretically the properties of surface polaritons (SPs) launched by a nanotip. Their unique feature is the optical Hall effect. It originates from the presence of the gyrotropy axis (an axial vector) and the boundary between the topological and trivial material which provides a polar vector of surface normal. The gyrotropy is generated by the separation of Weyl nodes in momentum space, which is the quintessential feature of Weyl semimetals. It is described by off-diagonal elements of the conductivity tensors. In contrast, the anisotropy is described by difference in diagonal tensor elements. We demonstrate strong sensitivity of SPs to the relative values of the frequency of light, the Fermi momentum and the Weyl node separation, which makes them a sensitive diagnostic tool and may form the basis of efficient light modulators and switches.

Note a novel electrodynamics of WSM surface modes: they are supported by a highly anisotropic and gyrotropic surface current and the surface dipole layer sitting on top of a highly anisotropic and gyrotropic bulk WSM material. One can find other materials with some particular features from this list, but the combination of these features in one bulk material is novel. One can even make a stronger statement: while materials with surface conductivity certainly exist (e.g. topological insulators), we are not aware of any natural bulk material which also has a surface double

layer with a dipole moment oriented perpendicular to the surface. This changes dramatically the boundary conditions, in particular creates a jump in the tangential component of the electric field. It is this peculiar surface response that makes the studies of SPs so exciting. One can safely say that WSMs represent a new class of gyrotropic materials.

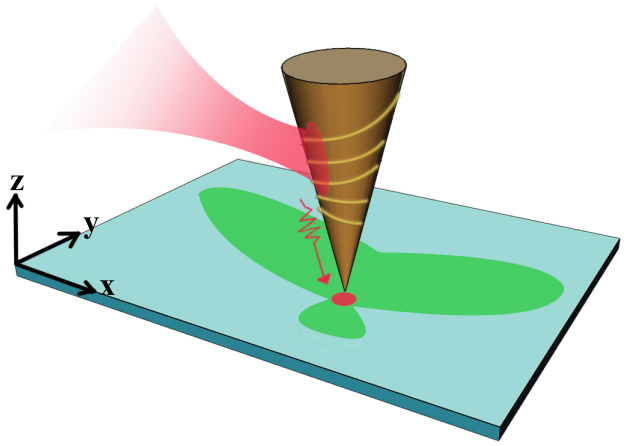

Figure 3.1: A sketch of tip-enabled SP excitation on the WSM surface. Radiation pattern of SPs is indicated in green for a particular combination of the excitation frequency and Fermi momentum, and for Weyl nodes located along the k_x axis in the Brillouin zone.

Figure 3.1 shows one possible schematic of SP excitation with a gold nanotip. Here the tip apex of ~ 10 nm radius is brought to a distance of ~ 10 nm from the WSM surface $z = 0$ in order to get access to large SP wavevectors $\sim 10^6$ cm^{-1}; see the SP dispersion curves in Fig. 3.2. A laser beam either illuminates the apex directly (e.g. [77]) or excites SPs on the surface of a gold tip via grating, as indicated in the figure [75, 76]. In the latter case, gold surface plasmon-polaritons propagate to the apex, experiencing strong adiabatic amplification of the field intensity as they reach the apex [78, 75]. Either way, excitation of SPs on a WSM surface is concentrated under the tip within a spot of ~ 10 nm. In the linear excitation regime, the frequency spectrum of SPs coincides with the spectrum of an incident laser pulse, whereas the spatial spectrum is extremely broadband, with a cutoff around 10^7 cm^{-1}. The SPs propagate away from the tip, forming a

strongly anisotropic radiation pattern which depends on the Weyl node position and separation and the Fermi momentum. They can be detected (converted into an outgoing EM wave) with another tip, a grating or a notch, or they can be reflected from edges of a sample and outcoupled by the same tip.

For the most sensitive diagnostics of the electronic structure of WSMs, the frequency of the probing light should be of the order of $\omega \sim v_F b$, where $2b$ is the distance between Weyl nodes in momentum space along k_x; see the electron bandstructure plot in Fig. 3.1 of [71]. In all numerical examples in this chapter we assume for definiteness that $\hbar v_F b = 100$ meV, so the incident laser light should be in the mid-infrared range. However, the formalism presented in this chapter is general and does not depend on the choice of incident frequencies as long as the latter are low enough, so that the interband transitions to electron states in remote bands can be neglected. The remote states have a trivial topology and they are not of interest to this study.

The Hamiltonian of a WSM with two separated Weyl nodes breaks time-reversal symmetry, which is expected for WSMs with magnetic ordering, e.g. pyrochlore iridates [27], ferromagnetic spinels [60], and Heusler compounds [61]. As we showed in [71], the tensors of both bulk and surface conductivity for Type I WSMs with time-reversal symmetry breaking have a structure corresponding to a biaxial-anisotropic and gyrotropic medium:

$$\sigma_{mn}^{B,S}(\omega) = \begin{pmatrix} \sigma_{xx}^{B,S} & 0 & 0 \\ 0 & \sigma_{yy}^{B,S} & \sigma_{yz}^{B,S} \\ 0 & \sigma_{zy}^{B,S} & \sigma_{zz}^{B,S} \end{pmatrix} \tag{3.1}$$

where the Weyl points are on the k_x axis, $\sigma_{zy}^{B,S} = -\sigma_{yz}^{B,S}$, and superscripts B and S denote bulk and surface conductivity elements, respectively. We add background dielectric constant ε_b due to transitions to remote bulk bands, assuming it to be isotropic and dispersionless at low frequencies, so that the total bulk dielectric tensor is $\varepsilon_{mn}(\omega) = \varepsilon_b \delta_{mn} + 4\pi i \sigma_{mn}^{B}/\omega$. We will take $\varepsilon_b = 10$ for the numerical examples below. The surface conductivity is due to optical transitions between different

electron surface states (often called "Fermi arc states", although they exist for all momentum states within $k_x^2 + k_y^2 \leq b^2$, not only on the Fermi arc) and between surface and bulk states.

3.2 Surface polaritons excited by a point-like source

The surface polaritons excited on WSM surfaces parallel to the x-axis (assuming that the Weyl points are located along k_x) can be supported by both bulk and surface electron states. However, in the quasielectrostatic approximation $ck \gg \omega$ the SPs are highly localized and the surface states make a dominant contribution to the SP dispersion and radiation pattern [71]. Here k is the magnitude of the SP wavevector in the $z = 0$ plane.

We model the nanotip-induced excitation source of SPs as an external point dipole,

$$\mathbf{p}^e(\mathbf{r}, z, t) = \mathrm{Re}\left[\mathbf{p}\delta(\mathbf{r})\,\delta(z)\,e^{-i\omega t}\right] \tag{3.2}$$

where $\mathbf{r} = (x, y)$. The point source approximation is valid if the tip apex radius and its distance to the surface are smaller than the exponential extent of the excitation field. Our case is borderline as these scales are actually of the same order, but we will still assume a point source for simplicity. One can always generalize the analysis for any spatial distribution of the excitation specific to a given experiment. The corresponding external current is $\mathbf{j}_\omega^e(\mathbf{r}) = -i\omega\mathbf{p}\delta(\mathbf{r})$. Within the quasielectrostatic approximation the electric field of SPs can be defined through the scalar potential: $\mathbf{E} = -\nabla\Phi$, where

$$\Phi(\mathbf{r}, z, t) = \mathrm{Re}\left[\Phi_\omega(\mathbf{r}, z)\,e^{-i\omega t}\right]. \tag{3.3}$$

Outside the surface, Φ_ω is described by the Poisson equation at $z > 0$ (in the air or an ambient medium), $\nabla^2\Phi_\omega = 0$, and Gauss's law in the bulk WSM at $z < 0$: $\nabla \cdot \mathbf{D}_\omega = 0$, which can be expanded in components as

$$\frac{\partial}{\partial x}(\varepsilon_{xx}E_x) + \frac{\partial}{\partial y}(\varepsilon_{yy}E_y + \varepsilon_{yz}E_z) + \frac{\partial}{\partial z}(\varepsilon_{zz}E_z + \varepsilon_{zy}E_y) = 0. \tag{3.4}$$

We assume that the medium above the surface is described by an isotropic dielectric constant ε_{up}

and take $\varepsilon_{up} = 1$ in all numerical examples. The boundary conditions yield

$$\varepsilon_{up} E_z\left(z=+0\right) - D_z\left(z=-0\right) = 4\pi\rho^S = -i\frac{4\pi}{\omega}\left(\frac{\partial}{\partial x} j_x^S + \frac{\partial}{\partial y} j_y^S\right) \tag{3.5}$$

where D_z is a z-component of electric induction, ρ^S is the surface charge due to surface electron states and an external source; j_x^S, j_y^S are the components of the total surface current that are connected with the surface charge by the in-plane continuity equation.

The total surface current, $\mathbf{j}_\omega^S\left(\mathbf{r}\right) = \mathbf{j}_\omega^l\left(\mathbf{r}\right) + \mathbf{j}_\omega^e\left(\mathbf{r}\right)$, is the sum of the current $\mathbf{j}_\omega^l\left(\mathbf{r}\right)$ representing the linear response to Φ_ω and the current $\mathbf{j}_\omega^e\left(\mathbf{r}\right)$ induced by the external dipole source. All currents and charges are on the surface so we can drop the index S.

The equations for the scalar potential can be solved by expansion over spatial harmonics in the (x, y) plane:

$$\mathbf{j}_\omega^{e,l}\left(\mathbf{r}\right) = \int\int \mathbf{j}_{\omega\mathbf{k}}^{e,l} e^{i\mathbf{k}\cdot\mathbf{r}} d^2k, \tag{3.6}$$

$$\Phi_\omega\left(\mathbf{r}, z\right) = \int\int \Phi_{\omega\mathbf{k}}\left(z\right) e^{i\mathbf{k}\cdot\mathbf{r}} d^2k. \tag{3.7}$$

Here $\mathbf{j}_{\omega\mathbf{k}}^l = \hat{\sigma}^S \cdot \mathbf{E}_\omega\left(z=-0\right)$, $\mathbf{E}_\omega\left(z=-0\right) = -i\mathbf{k}\Phi_{\omega\mathbf{k}}(z=-0)$. The inverse transformation is

$$\mathbf{j}_{\omega\mathbf{k}}^{e,l} = \frac{1}{\left(2\pi\right)^2}\int\int \mathbf{j}_\omega^{e,l}\left(\mathbf{r}\right) e^{-i\mathbf{k}\cdot\mathbf{r}} d^2r. \tag{3.8}$$

A surface double layer is formed at the boundary between the two media. Its dipole moment is oriented along the normal to the surface,

$$\mathbf{d} = \mathrm{Re}\left[\mathbf{d}_\omega\left(\mathbf{r}\right) e^{-i\omega t}\right],$$

$$\mathbf{d}_\omega\left(\mathbf{r}\right) = \mathbf{z_0}\int\int d_{z\mathbf{k}} e^{i\mathbf{k}\cdot\mathbf{r}} d^2k,$$

where the space-time Fourier components can be related to the z-component of the current density

supported by surface electron states:

$$d_{z\mathbf{k}} = \frac{i}{\omega}\left[\sigma_{zy}^{S} E_y\left(z=-0\right) + \sigma_{zz}^{S} E_z\left(z=-0\right)\right]. \tag{3.9}$$

The sum of an external and induced dipole creates a jump in the scalar potential $\Phi\left(z\right)$,

$$\Phi_{\omega\mathbf{k}}\left(z=+0\right) - \Phi_{\omega\mathbf{k}}\left(z=-0\right) = 4\pi d_{z\mathbf{k}} + \frac{1}{\pi}\mathbf{p}\cdot\mathbf{z_0}, \tag{3.10}$$

which corresponds to a jump in the tangential component of the electric field.

The solution for the SP field evanescent in $\pm z$ direction is

$$\Phi_{\omega\mathbf{k}}(z>0) = \phi_{\omega\mathbf{k}}^{up} e^{-\kappa_{up} z}, \qquad \Phi_{\omega\mathbf{k}}(z<0) = \phi_{\omega\mathbf{k}}^{W} e^{\kappa_W z}. \tag{3.11}$$

Here the spatial harmonics of the potential satisfy algebraic equations

$$\varepsilon_{up}\kappa_{up}\phi_{\omega\mathbf{k}}^{up} + \left[\kappa_W\left(\varepsilon_{zz} + \frac{4\pi}{\omega}k_y\sigma_{yz}^{S}\right) + gk_y + i\frac{4\pi}{\omega}\left(k_x^2\sigma_{xx}^{S} + k_y^2\sigma_{yy}^{S}\right)\right]\phi_{\omega\mathbf{k}}^{W} = \frac{4\pi}{\omega}\mathbf{k}\cdot\mathbf{j}_{\omega\mathbf{k}}^{e}, \tag{3.12}$$

$$\phi_{\omega\mathbf{k}}^{up} + \left(i\frac{4\pi}{\omega}\kappa_W\sigma_{zz}^{S} - \frac{4\pi}{\omega}k_y\sigma_{zy}^{S} - 1\right)\phi_{\omega\mathbf{k}}^{W} = \frac{1}{\pi}\mathbf{p}\cdot\mathbf{z_0} \tag{3.13}$$

where $g = \frac{4\pi\sigma_{yz}^{B}}{\omega}$ and the decay constants $\kappa_{up,W}$ can be found from Poisson's equation and Eq. (3.4):

$$k^2 - \kappa_{up}^2 = 0, \quad \varepsilon_{xx}k^2\cos^2\phi + \varepsilon_{yy}k^2\sin^2\phi - \varepsilon_{zz}\kappa_W^2 = 0, \tag{3.14}$$

where $k_x = k\cos\phi$, $k_y = k\sin\phi$. This formalism allows one to add spatial dispersion of the conductivity $\hat{\sigma}^{S}\left(\omega,\mathbf{k}\right)$ and $\hat{\varepsilon}\left(\omega,\mathbf{k}\right)$ if needed, but we will ignore it below.

3.2.1 Dispersion of surface polaritons

In the absence of an external dipole, Eqs. (3.12,3.13) give the dispersion equation for SPs derived in [71],

$$\mathscr{D}\left(\omega,\phi,k\right) = D\left(\omega,\phi\right) - k\Sigma\left(\omega,\phi\right) = 0, \tag{3.15}$$

where

$$\Sigma(\omega,\phi)=\frac{4\pi}{\omega}\left[\sqrt{\frac{\varepsilon_{xx}\cos^2\phi+\varepsilon_{yy}\sin^2\phi}{\varepsilon_{zz}}}\left(in_{up}^2\sigma_{zz}^S-\sigma_{yz}^S\sin\phi\right)-\right.$$
$$\left.n_{up}^2\sigma_{yz}^S\sin\phi-i\left(\sigma_{xx}^S\cos^2\phi+\sigma_{yy}^S\sin^2\phi\right)\right], \tag{3.16}$$

and

$$D(\omega,\phi)=n_{up}^2+\varepsilon_{zz}\sqrt{\frac{\varepsilon_{xx}\cos^2\phi+\varepsilon_{yy}\sin^2\phi}{\varepsilon_{zz}}}+g\sin\phi. \tag{3.17}$$

Note that $\Sigma=0$ if the surface terms are neglected. Therefore, $D(\omega,\phi)=0$ is the dispersion equation of SPs supported by bulk electron states only. Such modes would have no dispersion since $D(\omega,\phi)$ does not depend on the SP wavenumber. Moreover, bulk states would support surface modes only below the plasma resonance, when the real part of the diagonal components of the bulk dielectric tensor is negative enough. For $\hbar v_F k_F=50$ meV, the plasma resonance is around 50 meV [71]. SP modes plotted in Fig. 3.2 below show a very strong dispersion in every direction and exist way beyond 50 meV. Therefore they are supported by surface electron states, with bulk WSM serving mainly as a dielectric substrate.

Including an external source, Eqs. (3.12), (3.13) give the Fourier amplitudes of the scalar potential in both half-spaces:

$$\phi_{\omega\mathbf{k}}^{up}=\frac{4\pi\mathbf{k}\cdot\mathbf{j}_{\omega\mathbf{k}}^e}{\omega\mathscr{D}(\omega,\phi,k)}\left(\frac{4\pi}{\omega}\sin\phi\sigma_{zy}^S+\frac{1}{k}-i\frac{4\pi}{\omega}\sqrt{\frac{\varepsilon_{xx}\cos^2\phi+\varepsilon_{yy}\sin^2\phi}{\varepsilon_{zz}}}\sigma_{zz}^S\right)$$
$$+\frac{\mathbf{p}\cdot\mathbf{z_0}}{\pi\mathscr{D}(\omega,\phi,k)}\left[\varepsilon_{zz}\sqrt{\frac{\varepsilon_{xx}\cos^2\phi+\varepsilon_{yy}\sin^2\phi}{\varepsilon_{zz}}}+g\sin\phi\right.$$
$$\left.+\frac{4\pi}{\omega}k\left(\sqrt{\frac{\varepsilon_{xx}\cos^2\phi+\varepsilon_{yy}\sin^2\phi}{\varepsilon_{zz}}}\sigma_{yz}^S\sin\phi+i\left(\sigma_{xx}^S\cos^2\phi+\sigma_{yy}^S\sin^2\phi\right)\right)\right], \tag{3.18}$$

$$\phi_{\omega\mathbf{k}}^{W}=\frac{\frac{4\pi}{\omega k}\mathbf{k}\cdot\mathbf{j}_{\omega\mathbf{k}}^e-\frac{1}{\pi}(\mathbf{p}\cdot\mathbf{z_0})n_{up}^2}{\mathscr{D}(\omega,\phi,k)}. \tag{3.19}$$

Then the spatial field distributions on both sides of the interface can be obtained from Eqs. (3.18) and (3.19) by Fourier transform Eq. (3.7). We will perform integration only in the case of a vertical external Hertz dipole, i.e. $\mathbf{p} = p\mathbf{z_0}$, when $\mathbf{k} \cdot \mathbf{p} = 0$ and the source is isotropic in plane of the interface. Therefore, all anisotropy in the SP propagation comes from the properties of topological electron states.

The Fourier integral in polar coordinates (k, ϕ) in momentum space can be written as

$$\begin{aligned} \Phi_{\omega}^{(+)} \equiv \Phi_{\omega}(\mathbf{r}, z = +0) &= \frac{p}{\pi} \int \int d^2 k e^{i\mathbf{k}\cdot\mathbf{r}} \frac{H(\omega, \phi, k)}{\mathscr{D}(\omega, \phi, k)} \\ &\approx -\frac{p}{\pi} \int_0^{2\pi} d\phi \frac{1}{\Sigma(\omega, \phi)} \int_0^{\infty} \frac{e^{ikr\cos(\phi-\theta)} H(\omega, \phi, k)}{k - k_{\omega}(\phi) - i\eta_{\omega}(\phi)} k dk, \end{aligned} \tag{3.20}$$

where (r, θ) are polar coordinates in real 2D space and we introduced the shortcut notation

$$H(\omega, \phi, k) = D(\omega, \phi) - n_{up}^2 + \frac{4\pi}{\omega} k \left[\sqrt{\frac{\varepsilon_{xx}\cos^2\phi + \varepsilon_{yy}\sin^2\phi}{\varepsilon_{zz}}} \sigma_{yz}^S \sin\phi + i\left(\sigma_{xx}^S \cos^2\phi + \sigma_{yy}^S \sin^2\phi\right) \right]. \tag{3.21}$$

The scalar potential just under the interface, $\Phi_{\omega}^{(-)} \equiv \Phi_{\omega}(\mathbf{r}, z = -0)$, can be introduced in a similar way as a 2D Fourier transform of the Fourier amplitude in Eq. (3.19).

In the second line of Eq. (3.20) we also introduced the solution to the dispersion equation for SPs, Eq. (3.15) in terms of the real and imaginary parts of the SP wave number, $k_{\omega}(\phi)$ and $\eta_{\omega}(\phi)$. We will also assume for simplicity that the SP dissipation is sufficiently weak so that the real part of the solution can be found from

$$\mathrm{Re}\mathscr{D}(\omega, \phi, k_{\omega}(\phi)) \approx 0, \tag{3.22}$$

i.e.

$$k_{\omega}(\phi) = \mathrm{Re}\left[\frac{D(\omega, \phi)}{\Sigma(\omega, \phi)}\right], \tag{3.23}$$

whereas the imaginary part of the SP wavenumber can be calculated as

$$\eta = -\frac{\mathrm{Im}\mathscr{D}\left(\omega,\phi,k_\omega\right)}{\left[\frac{\partial \mathrm{Re}\mathscr{D}(\omega,\phi,k_\omega)}{\partial k}\right]_{k=k_\omega(\phi)}}. \tag{3.24}$$

To calculate the integrals in Eq. (3.20), we use the known expansion of the exponent in terms of Bessel functions,

$$e^{iz\cos\alpha} = J_0(z) + 2\sum_{n=1}^{\infty} i^n J_n(z)\cos(n\alpha), \tag{3.25}$$

which gives

$$\Phi_\omega^{(+)} = -\frac{p}{\pi}\int_0^{2\pi} d\phi \frac{1}{\Sigma\left(\phi\right)}\int_0^{\infty} \frac{\left\{J_0\left(kr\right) + 2\sum_{n=1}^{\infty} i^n J_n\left(kr\right)\cos\left[n\left(\phi-\theta\right)\right]\right\} H\left(\omega,\phi,k\right)}{k - k_\omega\left(\phi\right) - i\eta\left(\phi\right)} kdk. \tag{3.26}$$

This integral can be calculated analytically in the far zone of the source dipole, i.e. at large $kr \gg 1$. In this case the Bessel Functions in Eq. (3.26) oscillate much faster than other k-dependent terms in the numerator, so we can take $H\left(\omega,\phi,k\right)$ out of the integral over dk and replace k with $k_\omega(\phi)$ in its argument. After that, the integral over dk can be evaluated using the following integral identity for Bessel functions:

$$\int_0^{\infty} \frac{k^n J_n(kr)}{k^2 - k_\omega^2 - i0} kdk = \left(k_\omega\right)^n \frac{i\pi}{2}\left(J_n(k_\omega r) + iY_n(k_\omega r)\right) \tag{3.27}$$

Equation (3.27) can be derived by applying the operator $\left(\frac{1}{r}\frac{d}{dr}\right)^m$ to both sides of the known Hankel transformation [79]

$$\int_0^{\infty} \frac{J_0(kr)}{k^2 - k_\omega^2 - i0} kdk = \frac{i\pi}{2}\left(J_0(k_\omega r) + iY_0(k_\omega r)\right) \tag{3.28}$$

and using the recurrent formula

$$\left(\frac{1}{z}\frac{d}{dz}\right)^m \left[z^{-\nu}\mathfrak{G}_\nu(z)\right] = (-1)^m z^{-\nu-m}\mathfrak{G}_{\nu+m}(z), \tag{3.29}$$

where $\mathfrak{G}_\nu(z) = J_\nu(z), Y_\nu(z)$ [80].

Applying Eq. (3.27) to the integral over dk in Eq. (3.26) yields

$$\begin{aligned}
\Phi_\omega^{(+)} &= -ip\int_0^{2\pi} d\phi \frac{k_\omega(\phi)}{\Sigma(\phi)} H[\omega,\phi,k_\omega(\phi)] \times \\
&\left\{ \left(J_0[k_\omega(\phi)r] + iY_0[k_\omega(\phi)r]\right) + 2\sum_{n=1}^{\infty} i^n \cos[n(\phi-\theta)] \left(J_n[k_\omega(\phi)r] + iY_n[k_\omega(\phi)r]\right) \right\} \\
&\approx -ip\sqrt{\frac{2}{\pi r}} \int_0^{2\pi} e^{ik_\omega(\phi)r} \left\{ e^{-i\frac{\pi}{4}} + 2\sum_{n=1}^{\infty} i^n e^{-i\left(\frac{n\pi}{2}+\frac{\pi}{4}\right)} \cos[n(\phi-\theta)] \right\} \\
&\times \frac{\sqrt{k_\omega(\phi)}}{\Sigma(\phi)} H[\omega,\phi,k_\omega(\phi)]\, d\phi.
\end{aligned}$$

In the last approximate equality we also took an advantage of the fact that in the far zone, namely when the Bessel functions argument $z \gg \left|n^2 - \frac{\pi}{4}\right|$, one can use their asymptotic values [80]

$$J_n(z) \approx \sqrt{\frac{2}{\pi z}} \cos\left(z - \frac{n\pi}{2} - \frac{\pi}{4}\right),\ Y_n(z) \approx \sqrt{\frac{2}{\pi z}} \sin\left(z - \frac{n\pi}{2} - \frac{\pi}{4}\right).$$

Then the integral over ϕ can be evaluated by using the delta-function identity:

$$\begin{aligned}
\Phi_\omega^{(+)} &= -\frac{p}{\sqrt{\pi}}\sqrt{\frac{2}{r}} \int_0^{2\pi} e^{i\left[k_\omega(\phi)r+\frac{\pi}{4}\right]} \frac{\sqrt{k_\omega(\phi)}}{\Sigma(\phi)} H[\omega,\phi,k_\omega(\phi)] \sum_{n=-\infty}^{\infty} \cos[n(\phi-\theta)]\, d\phi \\
&= -2\sqrt{\pi}p\sqrt{\frac{2}{r}} \int_0^{2\pi} e^{i\left[k_\omega(\phi)r+\frac{\pi}{4}\right]} \frac{\sqrt{k_\omega(\phi)}}{\Sigma(\phi)} H[\omega,\phi,k_\omega(\phi)]\, \delta(\phi-\theta)\, d\phi \\
&= -\frac{2\sqrt{\pi}p}{\Sigma(\theta)}\sqrt{\frac{2k_\omega(\theta)}{r}} H[\omega,\theta,k_\omega(\theta)] \exp\left[ik_\omega(\theta)r + i\frac{\pi}{4}\right].
\end{aligned} \tag{3.30}$$

Applying the same procedure, we derive the spatial distribution for the scalar potential just below the surface, i.e. inside the WSM:

$$\Phi_\omega^{(-)} \equiv \Phi_\omega(\mathbf{r}, z=-0) = \frac{2\sqrt{\pi}pn_{up}^2}{\Sigma(\theta)}\sqrt{\frac{2k_\omega(\theta)}{r}} \exp\left[ik_\omega(\theta)r + i\frac{\pi}{4}\right]. \tag{3.31}$$

As we see, in the far-field zone of the tip the scalar potential scales with distance as $\frac{\exp[ik_\omega(\theta)r]}{\sqrt{r}}$. Figures 3.2 (a),(b) show the polar plots of the real part of the in-plane SP wavenumber $k_\omega(\theta)$ for

several values of frequency and Fermi momentum.

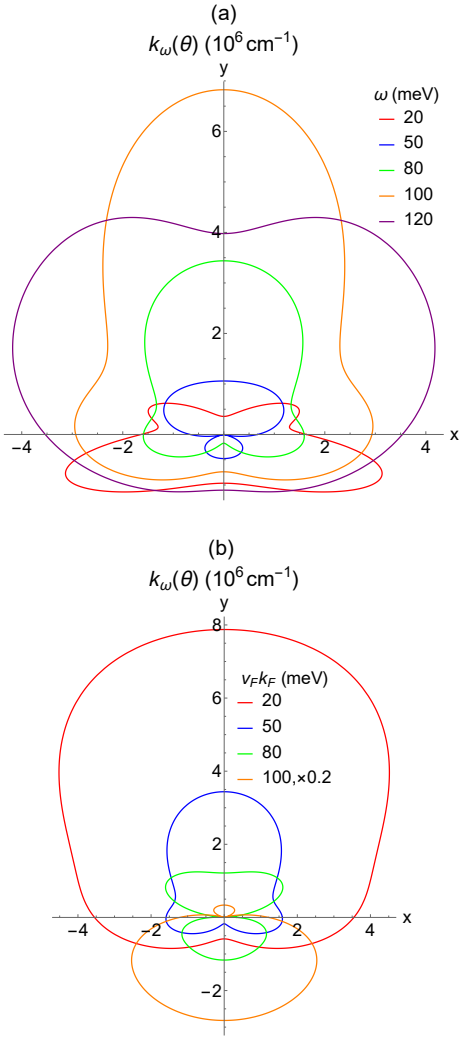

Figure 3.2: Polar plot of the real part of the in-plane SP wavenumber $k_\omega(\theta)$ for (a) several values of frequency at a given Fermi momentum $\hbar v_F k_F = 50$ meV and (b) several values of the Fermi momentum at a given frequency $\hbar\omega = 80$ meV.

These plots and all plots below were calculated for a vertical dipole orientation. In this case the excitation itself is isotropic in the plane (no θ dependence) and therefore all anisotropy comes from the properties of topological bulk and surface electron states. The conductivity tensors used in all plots were calculated assuming strongly disordered samples with high SP decay rate $\gamma = 10$

meV. In this case SPs have a low Q-factor: the imaginary part of the wave vector is only a few times lower than the real part. Obviously, in higher quality samples one should expect longer-lived SP excitations with longer propagating lengths, at least at frequencies lower than the Fermi energy-dependent interband transition cutoff determined by the Pauli blocking.

If the contribution of surface conductivity were ignored and only the bulk carriers were taken into account, the SPs would have no dispersion at all: their frequency would depend only on the propagation angle but not on the magnitude of the wave vector, as follows from Eq. (3.15) in the limit $\Sigma = 0$; see also [71]. Therefore, the dispersion (wavenumber dependence) shown in Fig. 3.2 is anomalous: it is entirely due to surface states. Moreover, bulk electron states would support surface EM modes only below the plasma resonance, when the real part of the diagonal components of the bulk dielectric tensor is negative enough. For $\hbar v_F k_F = 50$ meV in Fig. 3.2(a), the plasma resonance is around 50 meV [71]. SP modes plotted in Fig. 3.2(a) show a very strong dispersion in every direction and exist way beyond 50 meV. Therefore they are supported by "Fermi arc" surface electron states via surface current sheet and surface dipole that they create in response to the field, with bulk WSM serving mainly as a dielectric substrate. That is why the surface polaritons is a more appropriate term for these surface modes than surface plasmon-polaritons that would exist at low frequencies below plasma resonance.

Note strong anisotropy of the wavevector and its extreme sensitivity to the relative values of frequency, Fermi momentum, and Weyl node separation in momentum space. Note also that all plots are symmetric with respect to the y-axis, which is perpendicular to the gyrotropy axis x. Similar behavior is found in the Poynting flux radiation patterns in Fig. 3.3. It can be interpreted as the realization of the optical Hall effect. Indeed the symmetry properties of the optical response of the system are determined by the polar symmetry axis vector $\mathbf{a} = \mathbf{n} \times \mathbf{b}$, where the axial gyrotropy vector $\mathbf{b} \parallel \hat{x}_0$ and the polar vector $\mathbf{n} \parallel \hat{z}_0$ is the normal to the surface, so that $\mathbf{a} \parallel \hat{y}_0$. This is in analogy with the Hall effect in which the current direction is determined by the cross product of the axial gyrotropy vector of the magnetic field and the polar vector of the electric field.

3.2.2 Radiation pattern of surface polaritons

To calculate the Poynting flux in a SP wave, we need to go beyond electrostatic approximation. Following the perturbation method detailed in [81], we use the Maxwell's equation $\nabla \times \mathbf{B}(\omega, \mathbf{r}, z) = -\frac{i\omega}{c}\mathbf{D}(\omega, \mathbf{r}, z)$ in each half-space to calculate the magnetic field from the electric field obtained in the electrostatic approximation:

$$\frac{1}{r}\frac{\partial B_z}{\partial \theta} - \frac{\partial B_\theta}{\partial z} = i\frac{n_{up}^2\omega}{c}\frac{\partial}{\partial r}\Phi_\omega^{(+)}e^{-\kappa_+ z} \quad (z>0), \tag{3.32}$$

$$\frac{1}{r}\frac{\partial B_z}{\partial \theta} - \frac{\partial B_\theta}{\partial z} = i\frac{\omega}{c}\left[\left(\varepsilon_{xx}\cos^2\theta + \varepsilon_{yy}\sin^2\theta\right)\frac{\partial}{\partial r} + i\kappa_- g\sin\theta\right]\Phi_\omega^{(-)}e^{\kappa_- z} \quad (z<0), \tag{3.33}$$

where $\kappa_+^2 = k_\omega^2(\theta) - n_{up}^2\frac{\omega^2}{c^2}$, $\kappa_-^2 = \frac{\varepsilon_{yy}}{\varepsilon_{zz}}\left[k_\omega^2(\theta) - \left(\varepsilon_{zz} - \frac{g^2}{\varepsilon_{yy}}\right)\frac{\omega^2}{c^2}\right]$. In the quasielectrostatic approximation and far field zone, i.e. $c\to\infty$ and $r\to\infty$, we have $\kappa_+ \approx k_\omega(\theta)$, $\kappa_- \approx \left|\mathrm{Re}\left[\sqrt{\frac{\varepsilon_{yy}}{\varepsilon_{zz}}}\right]\right| k_\omega(\theta)$, $\frac{\partial}{\partial r} \approx ik_\omega(\theta)$. Furthermore, one can neglect the term $\frac{1}{r}\frac{\partial B_z}{\partial \theta}$ in the far field zone. Then we get

$$B_\theta(z>0) = -\frac{n_{up}^2\omega}{c}\Phi_\omega^{(+)}e^{-k_\omega(\theta)z}, \tag{3.34}$$

$$B_\theta(z<0) = \frac{\omega}{c}\left(\frac{\varepsilon_{xx}\cos^2\theta + \varepsilon_{yy}\sin^2\theta}{\left|\mathrm{Re}\left[\sqrt{\frac{\varepsilon_{yy}}{\varepsilon_{zz}}}\right]\right|} + g\sin\theta\right)\Phi_\omega^{(-)}e^{\left|\mathrm{Re}\left[\sqrt{\frac{\varepsilon_{yy}}{\varepsilon_{zz}}}\right]\right|k_\omega(\theta)z}, \tag{3.35}$$

$$E_z(z>0) = k_\omega(\theta)\Phi_\omega^{(+)}e^{-k_\omega(\theta)z}, \tag{3.36}$$

$$E_z(z<0) = -\left|\mathrm{Re}\left[\sqrt{\frac{\varepsilon_{yy}}{\varepsilon_{zz}}}\right]\right| k_\omega(\theta)\Phi_\omega^{(-)}e^{\left|\mathrm{Re}\left[\sqrt{\frac{\varepsilon_{yy}}{\varepsilon_{zz}}}\right]\right|k_\omega(\theta)z}. \tag{3.37}$$

Therefore the time-averaged Poynting flux $\mathbf{S}(\mathbf{r}, z) = \mathrm{Re}[\frac{c}{8\pi}(\mathbf{E}\times\mathbf{B}^*)]$ is

$$S_r(\mathbf{r}, z>0) = \frac{n_{up}^2\omega}{8\pi}k_\omega(\theta)\left|\Phi_\omega^{(+)}\right|^2 e^{-2k_\omega(\theta)z}, \tag{3.38}$$

$$S_r(\mathbf{r}, z<0) = \frac{\omega}{8\pi}k_\omega(\theta)\,\mathrm{Re}\left[\varepsilon_{xx}^*\cos^2\theta + \varepsilon_{yy}^*\sin^2\theta + g^*\left|\mathrm{Re}\left[\sqrt{\frac{\varepsilon_{yy}}{\varepsilon_{zz}}}\right]\right|\sin\theta\right]\left|\Phi_\omega^{(-)}\right|^2 e^{2\left|\mathrm{Re}\left[\sqrt{\frac{\varepsilon_{yy}}{\varepsilon_{zz}}}\right]\right|k_\omega(\theta)z}. \tag{3.39}$$

After integrating over dz, i.e. $S_r(r,\theta) = \int_{-\infty}^{\infty} S_r(\mathbf{r},z)\,dz$ we finally obtain the total in-plane energy flux in the far field zone:

$$S_r(r,\theta) = \frac{\omega}{16\pi}\left[n_{up}^2\left|\Phi_\omega^{(+)}\right|^2 + \mathrm{Re}\left(\frac{\varepsilon_{xx}^*\cos^2\theta + \varepsilon_{yy}^*\sin^2\theta}{\left|\mathrm{Re}\left[\sqrt{\frac{\varepsilon_{yy}}{\varepsilon_{zz}}}\right]\right|} + g^*\sin\theta\right)\left|\Phi_\omega^{(-)}\right|^2\right]$$
$$= \frac{2\pi^2\omega p^2 n_{up}^2 k_\omega(\theta)}{|\Sigma(\theta)|^2 r}\left[|H[\omega,\theta,k_\omega(\theta)]|^2 + n_{up}^2\mathrm{Re}\left(\frac{\varepsilon_{xx}\cos^2\theta + \varepsilon_{yy}\sin^2\theta}{\left|\mathrm{Re}\left[\sqrt{\frac{\varepsilon_{yy}}{\varepsilon_{zz}}}\right]\right|} + g\sin\theta\right)\right] \tag{3.40}$$

Figures 3.3(a),(b) show the radiation pattern of the SPs, namely polar plots of the SP Poynting vector integrated over the vertical z-direction, Eq. (3.40), for several values of frequency and Fermi momentum. The numerical values for the SP Poynting flux density in the plots were calculated at a distance of 250 μm from the tip and assuming that the excitation is created by the pump field of magnitude 10^6 V/cm localized within (10 nm)^3. Such fields are far below damage threshold; for example, in experiments reported in [76] the pump field under the tip was estimated at 5×10^7 V/cm. Only $1/r$ divergence of the in-plane Poynting vector was included. The actual SP attenuation length is determined by the material quality and is likely to be much shorter than 250 μm.

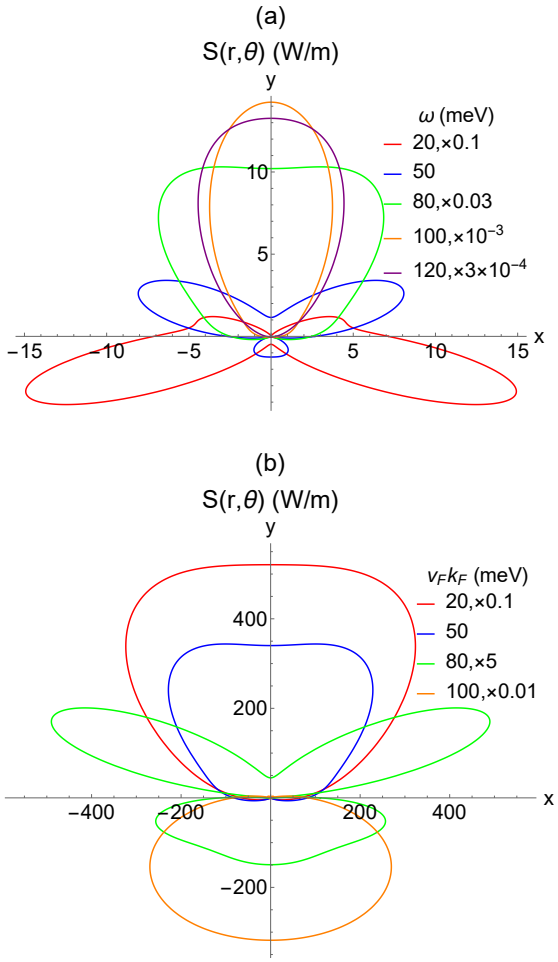

Figure 3.3: Polar plot of the in-plane Poynting vector integrated over the vertical z-direction, for (a) several values of frequency at a given Fermi momentum $\hbar v_F k_F = 50$ meV and (b) several values of the Fermi momentum at a given frequency $\hbar\omega = 80$ meV. The magnitudes of the Poynting flux are multiplied by different numerical factors indicated in the figure, in order to fit to one plot.

The energy flow of SPs is highly anisotropic and strongly frequency and Fermi momentum-dependent. There is again extreme sensitivity of the radiation pattern to the relative values of frequency, Fermi momentum, and Weyl node separation in momentum space. Furthermore, all plots are symmetric with respect to the y axis and with increasing frequency the SP flux is mainly directed along $\hat{y}_0$. This is the manifestation of the optical Hall effect induced by Weyl node separation, as discussed above. Note an enhancement in the SP flux at low frequencies in Fig. 3.3(a),

related to intraband transitions and Drude-like enhancement of the conductivity, especially its σ_{yy}^{S} element related to free-carrier motion of surface electron states with dispersion $E = \hbar v_F k_y$ [71]. Note also strong enhancement of the Poynting flux at high frequencies around 100 meV due to an increase in the wavenumber $k_\omega(\theta)$ and magnitude of the conductivity tensor associated with interband transitions; see the conductivity spectra in [71]. Since the surface states exist only at electron momenta $k_x^2 + k_y^2 < b^2$, at frequencies higher than 200 meV (or for high enough Fermi momenta $k_F > b$) the surface conductivity approaches zero whereas the bulk dielectric tensor approaches its background value. Therefore, there will be no SP modes supported by topological states in this limit $\omega \gg v_F b$, although other kinds of surface polariton modes could still exist due to e.g. phonon resonances.

3.3 Conclusions

In conclusion, we showed that spectroscopy of surface polaritons can be a powerful diagnostics of topological electron states in WSMs. Strong anisotropy, gyrotropy, and the optical Hall effect for SPs launched by a nanotip provides information about Weyl node position and separation, the value of the Fermi momentum, and the matrix elements of the optical transitions involving both bulk and surface electron states. Although the quantitative results in this paper chapter are valid only for magnetic WSMs with time-reversal symmetry breaking, one can still make some qualitative conclusions regarding the optical response of WSMs with inversion symmetry breaking. In particular, one can still expect anisotropy of SP propagation, related to the position and orientation of Weyl node pairs in the Brillouin zone, although the anisotropy could be weaker, for example if Weyl node pairs are oriented orthogonal to each other. There will be strong dispersion of SPs associated with the presence of Fermi arc surface states. The relative enhancement or suppression of SPs associated with the Fermi edge and interband transitions will be present. The low-frequency response related to massless free carriers will be similar.

4. INVERSE FARADAY EFFECT IN GRAPHENE AND WEYL SEMIMETALS*

In this chapter, we report systematic theoretical studies of the inverse Faraday effect in materials with massless Dirac fermions, both in two dimensions such as graphene and surface states in topological insulators, and in three dimensions such as Dirac and Weyl semimetals. Both semiclassical and quantum theories are presented, with dissipation and finite-size effects included. We find that the magnitude of the effect can be much stronger in Dirac materials as compared to conventional semiconductors. Analytic expressions for the optically induced magnetization in the low-temperature limit are obtained. Strong inverse Faraday effect in Dirac materials can be used for the optical control of magnetization, all-optical modulation, and optical isolation.

4.1 Introduction

Inverse Faraday Effect (IFE) is a fascinating nonlinear optical phenomenon. Its key feature is generation of a permanent magnetization in a medium as a result of interaction with circularly polarized radiation [82]. The effect was predicted by Pitaevskii [83], and the name IFE was coined in [84, 85, 86]. IFE was studied extensively in plasmas, metals, and semiconductors [87, 88, 89, 90, 91, 92, 93, 94]. More recent studies explored the use of IFE for ultrafast modulation of magnetization with femtosecond laser pulses [95, 96, 97, 98, 99, 100, 101, 102, 103, 104].

There has been a lot of recent interest in the optical properties of 2D and 3D materials with Dirac and Weyl fermions, including the nonlinear optical [105, 19, 106, 107, 108, 109, 110, 111, 112, 113, 114, 115, 116, 117, 118] and magnetooptical [119, 120, 121, 122, 123, 50] response of graphene and Dirac/Weyl semimetals. Strong light-matter coupling in these systems makes them promising for IFE studies. In [105, 124] the generation of edge photocurrent in graphene was studied theoretically and in experiments. We show below that generation of edge photocurrent is related to IFE.

*Reprinted with permission from: "Inverse Faraday effect in graphene and Weyl semimetals" by I.D.Tokman, Q. Chen, I.A. Shereshevsky, V.I.Pozdnyakova, I. Oladyshkin, M. Tokman, and A. Belyanin, 2020. Phys. Rev. B 101, 174429, Copyright 2020 by the American Physical Society.

In the Introduction we discuss general features of IFE based on the Pitaevskii formula Eq. (4.1) obtained from thermodynamic considerations. Section 4.2 develops a quasiclassical theory of IFE in graphene based on the kinetic equation. The quantum-mechanical derivation of IFE in graphene including interband transitions is given in Sec. 4.3. Both Sec. 4.2 and 4.3 neglect dissipation. In Sec. 4.4 we calculate the magnetization of graphene by directly summing over the magnetic moments of individual electrons (in quasiclassical approximation), instead of using the Pitaevskii formula. That is why we can include dissipation in this treatment. Sec. 4.5 takes into account finite-size effects and calculates edge photocurrent. Sec. 4.6 develops the kinetic-equation theory for the IFE in Weyl semimetals. In Appendix A we evaluate the effect of the depolarization field on the IFE in a finite sample, whereas Appendix B studies saturation of IFE in strong fields. Throughout this chapter, we include only the electric-dipole interaction with the electric field of the electromagnetic waves, ignoring a much smaller contribution of electron spins.

In a transparent nonmagnetic medium, i.e. in the medium with magnetic permeability $\mu = 1$, the magnetization excited by a monochromatic field can be determined from thermodynamic considerations. The resulting expression is [82]:

$$\mathbf{m} = \sum_{ij} \frac{\partial \varepsilon_{ij}}{\partial \mathbf{H}} \frac{\widetilde{E}_j \widetilde{E}_i^*}{16\pi}, \tag{4.1}$$

where the optical field is given by $\mathbf{E} = \mathrm{Re}\left(\tilde{\mathbf{E}} e^{-i\omega t}\right)$, i, j are Cartesian indices, ε_{ij} is a Hermitian tensor of the dielectric permittivity, $\mathbf{H}$ is the vector of a constant magnetic field. Here the Gaussian units are assumed. In the absence of an external magnetic field, the derivative in Eq. (4.1) should be calculated in the limit $\lim_{\mathbf{H}\longrightarrow 0}\left(\frac{\partial \varepsilon_{ij}}{\partial \mathbf{H}}\right)$. If the medium is isotropic at $\mathbf{H} \to 0$ the induced magnetic moment will be orthogonal to the plane containing the electric field vector $\mathbf{E}$ (see Fig. 4.1). The magnitude of magnetization is determined by the difference between the intensities of right- and left-circularly polarized components of the optical field. It is obviously zero for a linearly polarized field.

It is remarkable that Eq. (4.1) remains valid for media with frequency dispersion: there is no

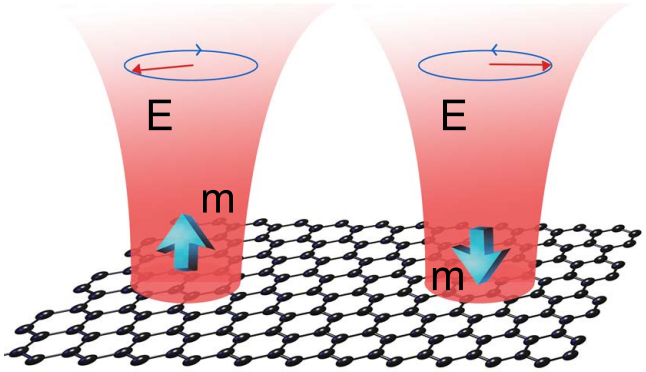

Figure 4.1: A sketch of inverse Faraday effect: an incident circularly polarized light induces magnetization in a sample.

need to add frequency derivatives $\frac{\partial \varepsilon_{ij}}{\partial \omega}$ to Eq. (4.1) whereas such derivatives are present in the expression for an averaged energy of the optical field in a dispersive medium [82, 83]. The limit of zero dissipation is more subtle. As we show in Sec. 4.5 in the quasiclassical approximation, Eq. (4.1) cannot be obtained by taking the real part of the complex dielectric function of the dissipative medium.

Equation (4.1) underscores another unique feature of the IFE. It is well known that any optical response that is quadratic in powers of the field can be calculated within a standard perturbative approach from the second-order (with respect to the field) perturbation of the density matrix. For a photoinduced magnetic moment in a system with discrete energy spectrum such an approach was developed e.g. in [125]. At the same time, Eq. (4.1) shows that it is possible to calculate photoinduced magnetization from the *linear* dielectric response of the medium.

It follows from Eq. (4.1) that IFE exists only in the media that become gyrotropic in an external constant magnetic field. Examples of the systems that *do not* become gyrotropic in an external

magnetic field include an electron-positron plasma and magnetized vacuum [126]. Condensed matter systems with complete electron-hole symmetry are also not gyrotropic in an external magnetic field. One obvious example is a material with electronic bandstructure in the form of isotropic Dirac cones, when the Fermi level crosses the Dirac points, such as graphene or certain types of Dirac/Weyl semimetals [50]. Of course this also implies low enough photon frequencies that probe only the range of electron energies close to the Dirac point. The selection rules for such systems allow one to group all electric-dipole allowed optical transitions into symmetric pairs $n \to -(n+1)$ and $n+1 \to -n$ with the same transition frequency but opposite direction of rotation of a circularly polarized optical field [50, 127, 24]. Gyrotropy, and therefore the IFE, will appear in these materials only when the Fermi level is shifted with respect to the Dirac/Weyl point; see Fig. 4.2. Moreover, as we argue below, the IFE is strongest in the limit of small frequencies and large Fermi energies, when resonant interband transitions are Pauli-blocked minimizing absorption and the main contribution to IFE comes from intraband transitions in the vicinity of the Fermi level.

Since the model leading to Eq. (4.1) does not include dissipation, for condensed matter systems it can give only a qualitative description. Nevertheless, it provides a useful limit based on general thermodynamic relations. In Sec. 4.5 we compare it with a specific model that does take dissipation into account.

4.2 Quasiclassical theory of IFE in graphene

For a 2D system such as graphene, it is convenient to use the electric susceptibility tensor instead of the dielectric permittivity in Eq. (4.1), namely $\chi_{ij} = \frac{\varepsilon_{ij}-\delta_{ij}}{4\pi}$, and integrate this equation over the layer thickness. In this case Eq. (4.1) becomes

$$\mathbf{m} = \sum_{ij} \frac{\partial \chi_{ij}}{\partial \mathbf{H}} \frac{\widetilde{E}_j \widetilde{E}_i^*}{4}. \tag{4.2}$$

Now the tensor χ_{ij} is a 2D surface susceptibility tensor which has the dimension of length; $i, j = x, y$ are coordinates in the graphene plane. The vector $\mathbf{m}$ in Eq. (4.2) has a meaning of a magnetic moment of a unit area (see Fig. 4.1). We will use a standard low-energy effective Hamiltonian for

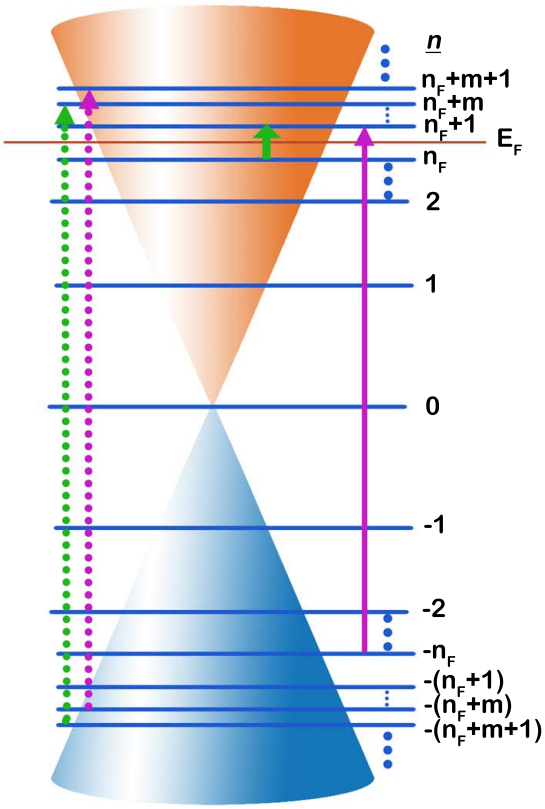

Figure 4.2: Landau levels and optical transitions in graphene. The highest Landau level below the Fermi energy is denoted as n_F. Dotted arrows indicate a pair of transitions with contributions to the induced magnetic moment that cancel each other. Only the transitions shown with solid arrows (one interband and one intraband) contribute to inverse Faraday effect at low temperature.

electrons near the Dirac point [3]:

$$\hat{H}_0 = v_F \hat{\mathbf{p}} \cdot \hat{\boldsymbol{\sigma}}, \tag{4.3}$$

where $\hat{\boldsymbol{\sigma}} = \mathbf{x}_0\hat{\sigma}_x + \mathbf{y}_0\hat{\sigma}_y$, $\hat{\mathbf{p}} = \mathbf{x}_0\hat{p}_x + \mathbf{y}_0\hat{p}_y$, $\hat{\sigma}_{x,y}$ are Pauli matrices, $\hat{p}_{x,y}$ are Cartesian components of the momentum operator, $\mathbf{x}_0$, $\mathbf{y}_0$ are unit vectors of coordinate axes, v_F is the Fermi velocity. In this model the degeneracy factor $g = 4$ (two spin states and two valleys). The corresponding electron energies are

$$W(p) = s v_F p, \tag{4.4}$$

where $p = \sqrt{p_x^2 + p_y^2}$; index $s = \pm 1$ corresponds to the conduction and valence band, respectively.

The analysis below is applicable also to 2D surface states in 3D topological insulators such as Bi_2Se_3. Their low-energy Hamiltonian is related to that of graphene by a unitary transformation, and the resulting linear and nonlinear optical responses are both very similar, after rescaling the values of the Fermi velocity and degeneracy, see e.g. [109, 122, 111].

Since in this model the IFE appears only when the Fermi energy is shifted from the Dirac point, we consider doped graphene and assume that the Fermi level is in the conduction band for definiteness. In the limit of small enough frequencies, low temperatures, and large Fermi energies (so that the contribution of interband transitions can be neglected) the quasiclassical theory is adequate. (This is the most interesting limit anyway: the results for a classical plasma, metals, and semiconductors [87, 88, 89, 90, 91, 92, 93, 94] indicate that the photogenerated magnetic moment grows with decreasing frequency as $\propto \omega^{-3}$.) Indeed, it was shown in [111] that under rather weak restrictions on the nonuniformity of the electromagnetic field in the plane of graphene both linear and quadratic intraband susceptibilities derived within the quantum-mechanical density matrix formalism coincide with the results obtained from the kinetic equation based on the quasiclassical equations of motion for carriers. The nonuniformity restriction is $L \gg \frac{\hbar}{p_F}$, where L is the spatial scale of the nonuniformity of the field and p_F is the Fermi momentum related to the Fermi energy by $W_F = v_F p_F$. The contribution of interband transitions will be small when electrons are degenerate and

$$W_F \gg \hbar\omega. \tag{4.5}$$

This is confirmed by fully quantum treatment in Sec. 4.3.

Under a more restrictive condition $L \gg \frac{v_F}{\omega}$ one can calculate the response neglecting spatial nonuniformity of the optical field [111]. We will use the kinetic equation which corresponds to the quasiclassical equations of motion [107, 108, 115, 120, 121]. To calculate the derivative in Eq. (4.2) it is enough to know the dependence of the tensor elements χ_{ij} on the external constant magnetic field in linear approximation with respect to $\mathbf{H}$. Here the magnetic field is orthogonal to

the monolayer: $\mathbf{H} = \mathbf{z}_0 H_z$. The kinetic equation has the form

$$\frac{\partial f}{\partial t} - e\left\{\mathbf{E}\left(t\right) + [\frac{1}{c}\left(\frac{\partial W}{p\partial p}\right)\mathbf{p}\times\mathbf{H}]\right\}\cdot\frac{\partial f}{\partial \mathbf{p}} = \hat{Q}\left(f\right). \tag{4.6}$$

Here $\hat{Q}\left(f\right)$ is the relaxation operator, the electric field vector $\mathbf{E}$ is in the graphene plane, $-e$ is electron charge. We don't specify any particular electron dispersion $W(p)$ in Eq. (4.6) in order to compare the results for linear and quadratic dispersion (see also [94]).

Consider Eq. (4.6) when $\hat{Q}\left(f\right) = 0$. We need to calculate the linear response to the uniform high-frequency field $E_{x,y} = \mathrm{Re}\left(\tilde{E}_{x,y}\, e^{-i\omega t}\right)$. We will seek the solution to Eq. (4.6) in the form $f = \mathrm{Re}\left[\delta f\left(\theta, p\right) e^{-i\omega t}\right] + f_F\left(p\right)$, where $p_x = p\cos\theta$, $p_y = p\sin\theta$, $|\delta f| \ll f_F$. Linearization of Eq. (4.6) gives

$$-i\omega\delta f + \frac{\partial W}{p\partial p}\frac{eH_z}{c}\frac{\partial \delta f}{\partial\theta} - e\left(\tilde{E}_x\cos\theta + \tilde{E}_y\sin\theta\right)\frac{\partial f_F}{\partial p} = 0.$$

This equation has an exact solution:

$$\delta f = \frac{e}{\omega^2 - \left(\frac{\partial W}{p\partial p}\frac{eH_z}{c}\right)^2}\frac{\partial f_F}{\partial p}\left[\tilde{E}_x\left(i\omega\cos\theta - \frac{\partial W}{p\partial p}\frac{eH_z}{c}\sin\theta\right) + \tilde{E}_y\left(i\omega\sin\theta + \frac{\partial W}{p\partial p}\frac{eH_z}{c}\cos\theta\right)\right]. \tag{4.7}$$

The surface current is determined by

$$\begin{aligned} j_x &= -eg\mathrm{Re}\left(e^{-i\omega t}\int\frac{\partial W}{\partial p}\cos\theta\delta f d^2p\right), \\ j_y &= -eg\mathrm{Re}\left(e^{-i\omega t}\int\frac{\partial W}{\partial p}\sin\theta\delta f d^2p\right). \end{aligned}$$

Substituting Eq. (4.7) in these equations and keeping only the terms linear with respect to the magnetic field we obtain the following expressions for the elements of the conductivity tensor σ_{ij} :

$$\begin{aligned} &\sigma_{xx} = \sigma_{yy} = \sigma = -i\tfrac{g\pi e^2}{\omega}\int_0^\infty \tfrac{\partial W}{\partial p}\tfrac{\partial f_F}{\partial p}pdp, \\ &\sigma_{xy} = -\sigma_{yx} = -\tfrac{e^3 g\pi H_z}{\omega^2 c}\int_0^\infty\left(\tfrac{\partial W}{\partial p}\right)^2\tfrac{\partial f_F}{\partial p}dp. \end{aligned} \tag{4.8}$$

Using Eqs. (4.2), (4.8), and the relationship between the complex conductivity and complex susceptibility $\chi_{ij} = \frac{i\sigma_{ij}}{\omega}$, we arrive at

$$m_z^{(0)} = -\frac{g\pi e^3}{2c\omega^2}\int_0^\infty \left(\frac{\partial W}{\partial p}\right)^2 \frac{\partial f_F}{\partial p} dp \times \mathrm{Re}\left(i\tilde{E}_y\tilde{E}_x^*\right), \tag{4.9}$$

where the superscript (0) indicates the transparent medium approximation used to derive the Pitaevskii equation Eq. (4.1).

Since the effect is strongest when the electrons are strongly degenerate, we consider a zero-temperature 2D Fermi distribution as an unperturbed electron distribution:

$$f_F(p) = \frac{1}{(2\pi\hbar)^2}\Theta(p_F - p), \tag{4.10}$$

where $\Theta(x)$ is the Heaviside step function. In this case the integrals are easily calculated to give

$$\begin{aligned} \sigma_{xx} &= \sigma_{yy} = \sigma = i\tfrac{ge^2 p_F}{4\pi\hbar^2\omega}\left(\tfrac{\partial W}{\partial p}\right)_{p=p_F}, \\ \sigma_{xy} &= -\sigma_{yx} = \tfrac{ge^3 H_z}{4\pi c\hbar^2\omega^2}\left(\tfrac{\partial W}{\partial p}\right)^2_{p=p_F}. \end{aligned} \tag{4.11}$$

In particular, for graphene with linear dispersion ($g = 4$, $\frac{\partial W}{\partial p} = v_F$) the last of Eqs. (4.11) yields

$$\sigma_{xy}^{(intra)} = \frac{e^3 v_F^2 H_z}{\pi c\hbar^2\omega^2} \tag{4.12}$$

Here we added the label (intra) to emphasize the fact that the quasiclassical calculation gives only the intraband conductivity. For the magnetic moment we obtain

$$m_z^{(0)} = \frac{ge^3}{8\pi c\hbar^2\omega^3}\left(\frac{\partial W}{\partial p}\right)^2_{p=p_F} \times \mathrm{Re}\left(i\tilde{E}_y\tilde{E}_x^*\right). \tag{4.13}$$

It follows from Eq. (4.13) that if the electron dispersion is quadratic, the magnetization is proportional to the surface electron density $n_F = \frac{gp_F^2}{4\pi\hbar^2}$ and inversely proportional to the square of their effective mass. For a linear dispersion near the Dirac point as in Eq. (4.4) and degenerate electron

distribution of Eq. (4.10) the magnetization does not depend on the Fermi momentum p_F, i.e. it does not depend on the carrier density. One can write the result in the same form for both cases by introducing an effective mass for electrons at the Fermi level in graphene: $m_{\text{eff}} = \frac{p_F}{v_F}$. One has to keep in mind that the limit of small $p_F \to 0$ is not allowed as it would violate not only the criterion of negligible contribution from interband transitions but also the applicability of the method of small perturbations that we used when solving the kinetic equation. The latter condition has the form $p_F \gg \frac{eE_0}{\omega}$, where $E_0 = \left|\tilde{\mathbf{E}}\right|$, as follows from the solution for the strong-field nonlinear problem solved in Appendix B.

4.3 Quantum theory of the IFE in graphene

The magnetic moment generated as a result of IFE is determined by the magnetic field dependence of the off-diagonal element of the conductivity tensor. To find this dependence within full quantum theory we use the Kubo-Greenwood formula [128]:

$$\sigma_{xy} = -\sigma_{yx} = i\hbar g \sum_{\alpha\beta} \left(\frac{f_\alpha - f_\beta}{E_\beta - E_\alpha} \right) \frac{\langle \alpha | \hat{j}_x | \beta \rangle \langle \beta | \hat{j}_y | \alpha \rangle}{\hbar(\omega + \frac{i}{\tau}) - (E_\beta - E_\alpha)}, \tag{4.14}$$

where $|\alpha\rangle$ are basis 2D surface states normalized by unit area $L_x \times L_y = 1$, E_α and f_α are the energy and population of state $|\alpha\rangle$, $\hat{j}_{x,y} = -ev_F\hat{\sigma}_{x,y}$ are Cartesian components of the current density operator [3], $g = 4$ is the degeneracy factor, τ is the relaxation time.

To determine the distribution function of carriers in a magnetic field oriented along z-axis, we extend the momentum operator in the Hamiltonian Eq. (4.3) in a standard way [23]: $\hat{\mathbf{p}} \Longrightarrow \hat{\mathbf{p}} - \mathbf{x}_0 \frac{eH_z}{c} y$. The resulting electron eigenstates are [24]

$$|\alpha\rangle = |n, k\rangle = \frac{C_n}{\sqrt{L_y}} e^{-ik_y y} \begin{pmatrix} \operatorname{sgn}(n)\, i^{|n|-1} \phi_{|n|-1} \\ i^{|n|} \phi_{|n|} \end{pmatrix} \tag{4.15}$$

$$\phi_{|n|} = \frac{H_{|n|}\left(\frac{x - kl_c^2}{l_c}\right)}{\sqrt{2^{|n|}\,|n|!\sqrt{\pi} l_c}} \exp\left[-\frac{1}{2} \left(\frac{x - kl_c^2}{l_c} \right)^2 \right], \tag{4.16}$$

where $H_n(\xi)$ is the Hermite polynomial, $l_c = \sqrt{\frac{\hbar c}{eH_z}}$ is the magnetic length, $n = 0, \pm 1, \pm 2, ...$are principal numbers of the Landau levels, $C_0 = 1$, $C_{n\neq 0} = \frac{1}{\sqrt{2}}$. The eigenenergy E_α depends only on the Landau level number: $E_\alpha = E_n = \mathrm{sgn}(n)\hbar\omega_c\sqrt{|n|}$, where $\omega_c = \frac{\sqrt{2}v_F}{l_c}$ is the cyclotron frequency.

Introducing the notations $|\alpha\rangle = |n,k\rangle$ and $|\beta\rangle = |m,k'\rangle$ and using Eqs. (4.15) and (4.16) we obtain the matrix elements of the components of the current density operator:

$$\langle\alpha|\,\hat{j}_{x,y}\,|\beta\rangle = -ev_F\,\langle\alpha|\,\hat{\sigma}_{x,y}\,|\beta\rangle = (j_{x,y})_{nm}\,\delta_{kk'}, \tag{4.17}$$

where

$$(j_x)_{nm} = -ev_F i^{|m|-|n|+1} C_n C_m \left[\mathrm{sgn}(n)\,\delta(|n|-|m|-1) - \mathrm{sgn}(m)\,\delta(|n|-|m|+1)\right], \tag{4.18}$$

$$(j_y)_{nm} = -ev_F i^{|m|-|n|} C_n C_m \left[\mathrm{sgn}(m)\,\delta(|n|-|m|+1) + \mathrm{sgn}(n)\,\delta(|n|-|m|-1)\right]. \tag{4.19}$$

The δ-functions in Eqs. (4.18), (4.19) determine the selection rules.

Performing the summation over k in Eq. (4.14) (see [23]) and using Eqs. (4.18),(4.19), we arrive at the expression which contains the summation over the Landau level numbers:

$$\sigma_{xy} = -\frac{2\hbar}{\pi l_c^2} e^2 v_F^2 \sum_{mn} (C_n C_m)^2\,\frac{f_n - f_m}{E_m - E_n}\,\frac{\delta(|n|-|m|-1) - \delta(|n|-|m|+1)}{\hbar(\omega + \frac{i}{\tau}) + (E_n - E_m)} \tag{4.20}$$

where $1 \geq f_n \geq 0$; the degeneracy of a given Landau level per unit area is $\frac{2\hbar}{\pi l_c^2}$ including both spin and valley degeneracy.

In the case of a complete electron-hole symmetry, i.e.$f_0 = \frac{1}{2}$, $f_{n>0} = 0$, $f_{n<0} = 1$, from Eq. (4.20) we obtain $\sigma_{xy} \equiv 0$ for any H_z (see also [50]). Now consider an n-doped system. Let the number n_F correspond to the highest occupied Landau level just below the Fermi energy, i.e. $W_F \geq \hbar\omega_c\sqrt{n_F}$. Since we need the limit of small magnetic fields, we assume that $W_F \gg \hbar\omega_c$, which

can be written as

$$p_F l_c \gg \hbar. \tag{4.21}$$

This means that $n_F \gg 1$.

4.3.1 The contribution of intraband transitions

In this case we put $n, m > 0$ in Eq. (4.20). Consider a narrow vicinity of the Fermi energy where $|n - n_F| \ll n_F$ and $|E_{n_F} - W_F| \ll W_F$. In the limit of large n the distance between neighboring Landau levels is

$$\Delta E = E_{n+1} - E_n = \hbar\omega_c \left(\sqrt{n+1} - \sqrt{n}\right) \approx \frac{1}{2}\frac{\hbar\omega_c}{\sqrt{n_F}}, \tag{4.22}$$

or

$$\Delta E = \frac{\hbar^2 v_F^2}{l_c^2 W_F} \tag{4.23}$$

Note that introducing the effective mass $m_{\text{eff}} = \frac{p_F}{v_F}$ we obtain a standard relation $\Delta E = \frac{\hbar e H_z}{c m_{\text{eff}}}$.

Taking into account that $f_{n+1} - f_n \neq 0$ only in the near vicinity of the Fermi energy, from Eq. (4.20) we can get

$$\sigma_{xy}^{(intra)} = -\frac{\hbar}{2\pi l_c^2} e^2 v_F^2 \frac{1}{\Delta E}\left[\frac{1}{\hbar(\omega + \frac{i}{\tau}) - \Delta E} - \frac{1}{\hbar(\omega + \frac{i}{\tau}) + \Delta E}\right] \sum_{n>0} (f_{n+1} - f_n), \tag{4.24}$$

where $\sum_{n>0} (f_{n+1} - f_n) \Longrightarrow \int_0^\infty df = -1$. The result is

$$\sigma_{xy}^{(intra)} = \frac{1}{\pi\hbar^2 c} \frac{e^3 v_F^2 H_z}{(\omega + \frac{i}{\tau})^2 - \left(\frac{e H_z v_F}{c p_F}\right)^2}. \tag{4.25}$$

The last expression coincides with the semiclassical result derived from the kinetic equation Eq. (4.6) for $\hat{Q}(f) = \frac{f_F - f}{\tau}$. In particular, when $\tau \to \infty$ and $H_z \to 0$ we obtain Eq. (4.12).

4.3.2 The contribution of interband transitions

In this case the numbers n and m in Eq. (4.20) have different signs. Taking this into account, we can write the sum in Eq. (4.20) as

$$\begin{aligned}\sigma_{xy}^{(inter)} &= \frac{-\hbar e^2 v_F^2}{2\pi l_c^2}\Big[\sum_{n<0,m>0}\frac{f_n-f_m}{E_m+|E_n|}\frac{\delta\left(n+m+1\right)-\delta\left(n+m-1\right)}{\hbar(\omega+\frac{i}{\tau})-(|E_n|+E_m)} \\ &\quad -\sum_{n>0,m<0}\frac{f_n-f_m}{|E_m|+E_n}\frac{\delta\left(n+m-1\right)-\delta\left(n+m+1\right)}{\hbar(\omega+\frac{i}{\tau})+(E_n+|E_m|)}\Big]. \end{aligned} \tag{4.26}$$

Since in an n-doped degenerate system $f_{n>n_F}=0$, $f_{n\leqslant n_F}=1$, Eq. (4.26) yields

$$\begin{aligned}&\sigma_{xy}^{(inter)} = -\frac{\hbar e^2 v_F^2}{2\pi\hbar^2 l_c^2}\times \\ &\Bigg(\sum_{-(n_F+2)}^{-\infty}\frac{1}{\frac{E_{-n-1}+|E_n|}{\hbar}\left[(\omega+\frac{i}{\tau})-\frac{E_{-n-1}+|E_n|}{\hbar}\right]}-\sum_{-n_F}^{-\infty}\frac{1}{\frac{E_{-n+1}+|E_n|}{\hbar}\left[(\omega+\frac{i}{\tau})-\frac{E_{-n+1}+|E_n|}{\hbar}\right]} \\ &-\sum_{n_F+1}^{\infty}\frac{1}{\frac{|E_{-n+1}|+E_n}{\hbar}\left[(\omega+\frac{i}{\tau})+\frac{|E_{-n+1}|+E_n}{\hbar}\right]}+\sum_{n_F+1}^{\infty}\frac{1}{\frac{|E_{-n-1}|+E_n}{\hbar}\left[(\omega+\frac{i}{\tau})+\frac{|E_{-n-1}|+E_n}{\hbar}\right]}\Bigg)\end{aligned} \tag{4.27}$$

Since the energy spectrum is symmetric, $\left|E_{-|n|}\right| = E_{|n|}$, we can regroup the terms on the rhs of Eq. (4.27) as

$$\begin{aligned}(...) &= -\frac{2}{(\omega+\frac{i}{\tau})^2-\left(\frac{E_{n_F+1}+\left|E_{-n_F}\right|}{\hbar}\right)^2}-\sum_{n_F+2}^{\infty}\frac{2}{(\omega+\frac{i}{\tau})^2-\left(\frac{|E_{-n+1}|+E_n}{\hbar}\right)^2} \\ &+\sum_{n_F+1}^{\infty}\frac{2}{(\omega+\frac{i}{\tau})^2-\left(\frac{|E_{-n-1}|+E_n}{\hbar}\right)^2}\end{aligned}$$

It is easy to see that the sums on the rhs of the last equation cancel each other, leaving only the first term which is the contribution of the transition $-n_F \Longrightarrow n_F+1$ (see Fig. 4.2). Taking into account that $\frac{E_{n_F+1}+\left|E_{-n_F}\right|}{\hbar}\approx\frac{2W_F}{\hbar}$ when the inequality Eq. (4.21) is satisfied, we obtain

$$\sigma_{xy}^{(inter)} = \frac{1}{\pi\hbar^2 c}\frac{e^3 v_F^2 H_z}{(\omega+\frac{i}{\tau})^2-\left(\frac{2W_F}{\hbar}\right)^2} \tag{4.28}$$

Note that the expressions for the optical conductivity of graphene in a magnetic field were obtained in [129] where the direct Faraday effect was investigated.

In the absence of dissipation the magnitude of the magnetic moment is determined by Eq. (4.2), which gives

$$m_z^{(0)} = \frac{1}{2\omega}\left[\frac{\partial\left(\sigma_{xy}^{(intra)}+\sigma_{xy}^{(inter)}\right)}{\partial H_z}\right]_{\tau\to\infty, H_z\to 0} \mathrm{Re}\left(i\tilde{E}_y\tilde{E}_x^*\right). \tag{4.29}$$

Using Eqs. (4.25) and (4.28) we finally arrive at

$$m_z^{(0)} = \frac{e^3 v_F^2}{2\pi c\hbar^2\omega^3}\frac{\left(\frac{2W_F}{\hbar}\right)^2 - 2\omega^2}{\left(\frac{2W_F}{\hbar}\right)^2 - \omega^2}\mathrm{Re}\left(i\tilde{E}_y\tilde{E}_x^*\right). \tag{4.30}$$

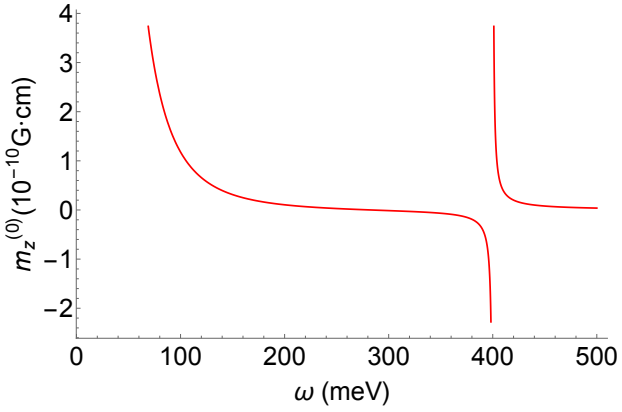

Figure 4.3: Frequency dependence of the magnetization in Eq. (4.30) induced by a circularly polarized optical field of intensity 10 kW/cm^2. The Fermi energy $W_F = 0.2$ eV.

The frequency dependence of the magnetization is shown in Fig. 4.3. The incident light intensity was assumed to be 10 kW/cm^2, which is much less than the saturation intensity, so that the contribution of photoexcited carriers can be neglected. The magnitude of magnetization increases with decreasing frequency as $1/\omega^3$ when $\hbar\omega \ll W_F$ and the effect is dominated by intraband transitions. The magnetization changes sign twice: at $\hbar\omega = \sqrt{2}W_F$ and $\hbar\omega = 2W_F$. There is also

a resonance at the interband transition edge $\hbar\omega = 2W_F$ where the magnitude of magnetization diverges. The divergence is an artifact of the dissipationless approximation which was used to relate magnetization to the off-diagonal susceptibility elements in Eq. (4.2). Obviously, relaxation processes cannot be neglected near resonance. Therefore the validity of Eq. (4.30) in the resonance region is limited by $|\omega - 2W_F/\hbar| > \tau_{inter}^{-1}$, where τ_{inter} is the interband relaxation time. It is interesting that taking relaxation processes into account in the calculation of magnetization is not equivalent to using the complex susceptibility in Eq. (4.2) and taking the real part of the resulting expression. We will illustrate it in the next section within quasiclassical derivation.

As is clear from Fig. 4.3 and Eqs. (4.25), (4.28), and (4.30), when Eq. (4.5) is satisfied the interband transitions give only a small contribution to the IFE. In the analysis of the IFE in dissipative systems below, we will therefore neglect interband transitions.

4.4 IFE in a dissipative system: a quasiclassical theory

Here we calculate the photogenerated magnetic moment per unit area without any assumptions of a dissipationless system. Therefore, we cannot use the Pitaevskii formula Eq. (4.1). Instead, we sum over magnetic moments of individual electrons undergoing induced motion in the optical field. First we introduce surface polarization $\mathbf{P}$ and relate it with the surface current $\mathbf{j}$ in a standard way $\dot{\mathbf{P}} = \mathbf{j}$. Next, we represent polarization as $\mathbf{P} = -en_F\mathbf{R}$, where the vector $\mathbf{R}$ has a meaning of an average displacement of carriers and n_F is the surface density of a degenerate 2D electron gas. The magnetic moment per unit area is $\mathbf{m} = -n_F \times \frac{e}{2c}\left\langle \mathbf{R} \times \dot{\mathbf{R}} \right\rangle$, where the angular brackets mean averaging over the optical period $\frac{2\pi}{\omega}$. This expression is convenient to write as

$$\mathbf{m} = \mathbf{z}_0 m_z = -\frac{1}{2cen_F} \left\langle \mathbf{P} \times \mathbf{j} \right\rangle . \tag{4.31}$$

Substituting

$$\mathbf{j} = \mathrm{Re}\left(\sigma(\omega)\,\tilde{\mathbf{E}}e^{-i\omega t}\right), \quad \mathbf{P} = \mathrm{Re}\left(\frac{i}{\omega}\sigma(\omega)\,\tilde{\mathbf{E}}e^{-i\omega t}\right) \tag{4.32}$$

into Eq. (4.31), we obtain

$$m_z = \frac{|\sigma(\omega)|^2}{2ce\omega n_F} \mathrm{Re}\left(i\tilde{E}_y \tilde{E}_x^*\right), \tag{4.33}$$

where $\sigma = \sigma_{xx} = \sigma_{yy}$; see Eq. (4.8). For a classical plasma Eq. (4.33) was derived in [**?**].

To connect with the dissipationless limit in Eq. (4.2) we note that the elements of the conductivity tensor given by Eqs. (4.11) in a dissipationless system for any electron dispersion are related as

$$\frac{1}{ecn_F}\frac{i}{\omega}|\sigma|^2 = \left(\frac{i}{\omega}\frac{\partial \sigma_{xy}}{\partial H_z}\right)_{H_z\to 0} = \left(\frac{\partial \chi_{xy}}{\partial H_z}\right)_{H_z\to 0} \tag{4.34}$$

Substituting this into Eq. (4.33), we obtain the expression for magnetization which coincides with the phenomenological formula of Eq. (4.2).

Therefore, an approach based on Eqs. (4.31) and (4.32) which uses the conductivity $\sigma(\omega)$ calculated within a suitable microscopic model, leads to a correct result. Note that this approach is not based on dissipationless approximation. An advantage of an approach based on Eq. (4.31) is that there is no need to calculate the dielectric susceptibility tensor in the limit of a linear dependence on the external magnetic field $\mathbf{H}$. It is enough to calculate linear conductivity without an external magnetic field. In order to include dissipation, we use Eq. (4.6), assuming $\mathbf{H} = \mathbf{0}$ from the very beginning and adopting the simplest approximation for the relaxation operator: $\hat{Q}(f) = \frac{f_F - f}{\tau}$, where τ is the relaxation time. This is equivalent to the substitution $\omega \to \omega + \frac{i}{\tau}$ in the dissipationless formula for the conductivity. Then Eq. (4.33) gives

$$m_z = m_z^{(0)} \frac{\omega^2}{\omega^2 + \tau^{-2}} \tag{4.35}$$

where $m_z^{(0)}$ is the magnetization of a dissipationless system, see Eq. (4.13). One can see that Eq. (4.35) is not equivalent to using the complex susceptibility in Eq. (4.2) and taking the real part of the resulting expression.

At low frequencies, the finite size of a sample starts affecting the result; see Appendix G. The expression for the magnetic moment which is valid beyond the linearized theory is derived in Appendix H.

4.5 The magnetization current and finite-size effects

The magnetization current density generated in a 2D system as a result of IFE is given by $\mathbf{j} = c\left(\mathbf{x}_0 \frac{\partial m_z}{\partial y} - \mathbf{y}_0 \frac{\partial m_z}{\partial x}\right)$. This equation yields a simple expression for the photocurrent around the boundary of a light beam or along the edge of an illuminated sample:

$$\mathbf{I} = c\left[\mathbf{n}_0 \times \mathbf{z}_0\right] m_z, \tag{4.36}$$

where $\mathbf{n}_0$ s a unit vector in the monolayer plane which is directed outside from the illuminated area perpendicularly to the boundary, see Fig. 4.4.

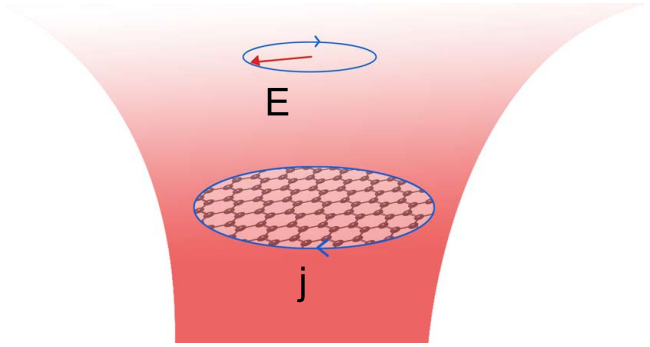

Figure 4.4: A sketch of an edge photocurrent in a finite-size sample generated by an incident circularly polarized beam.

In a dissipative system a simple expression Eq. (4.36) may be used with certain reservations. For example, the magnetization current far from the sample edges can be affected by the viscosity of an electron fluid [130] whereas edge photocurrent can be affected by interaction of carriers with a sample boundary. (These effects can be responsible for various ways of detecting a constant current along the edge that are not related to IFE.) In fact, Eq. (4.36) corresponds to a mirror reflection of carriers from the boundary. Indeed, consider the edge $x = 0$ of a graphene sample, assuming that graphene extends to $x > 0$. The field component $E_x = \mathrm{Re}\left(\tilde{E}_x e^{-i\omega t}\right)$ excites oscillations of

carrier density in a boundary layer near the edge: $\delta n\left(x\right)=\mathrm{Re}\left(\delta\tilde{n}\left(x\right)e^{-i\omega t}\right)$. Oscillations of an uncompensated charge $\delta\rho=-e\delta n$ should obey the continuity equation, which gives

$$i\omega e\int_{0}^{\infty}\delta\tilde{n}\left(x\right)dx=\sigma\left(\omega\right)\tilde{E}_{x}, \tag{4.37}$$

where the conductivity $\sigma\left(\omega\right)$ corresponds to the region where there is no uncompensated charge. Although the integration here should be formally extended to $x\rightarrow\infty$, in practice it is localized within a certain boundary layer much smaller than the sample dimensions.

The field component $E_{y}=\mathrm{Re}\left(\tilde{E}_{y}e^{-i\omega t}\right)$ gives rise to the oscillations of carrier velocity along the edge. We can prove that for the elastic reflection of electrons from the boundary the average (hydrodynamic) velocity of electrons along the boundary (along y) is conserved up to cubic terms with respect to the field amplitude. Indeed, let us write the particle momentum as $\mathbf{p}=\mathbf{P}+\tilde{\mathbf{p}}\left(t\right)$, where $\mathbf{P}$ is its value averaged over time and $\tilde{\mathbf{p}}=\frac{e}{\omega}\mathrm{Re}\left(i^{-1}\tilde{\mathbf{E}}e^{-i\omega t}\right)$ is an oscillating component. The velocity $\mathbf{v}=v_{F}\,\frac{\mathbf{p}}{|\mathbf{p}|}$ in the linear approximation with respect to the field $\mathbf{E}$ is given by $\tilde{\mathbf{v}}\approx v_{F}\left(\frac{\tilde{\mathbf{p}}}{|\mathbf{P}|}-\frac{\mathbf{P}(\mathbf{P}\cdot\tilde{\mathbf{p}})}{|\mathbf{P}|^{3}}\right)$, which gives

$$\tilde{v}_{y}=v_{F}\left(\tilde{p}_{y}\frac{P_{x}^{2}}{\left(P_{x}^{2}+P_{y}^{2}\right)^{\frac{3}{2}}}-\tilde{p}_{x}\frac{P_{y}P_{x}}{\left(P_{x}^{2}+P_{y}^{2}\right)^{\frac{3}{2}}}\right). \tag{4.38}$$

If the particle distribution is symmetric with respect to P_{y}, the ensemble-averaged velocity obtained from Eq. (4.38) is

$$\left\langle v_{y}\right\rangle=V_{y}=v_{F}\tilde{p}_{y}\frac{\left\langle P_{x}^{2}\right\rangle}{\left(P_{x}^{2}+P_{y}^{2}\right)^{\frac{3}{2}}}. \tag{4.39}$$

For elastic reflection the momentum components P_{y} and $\tilde{p}_{y}$ are conserved separately whereas the magnitude of P_{x}^{2} changes upon reflection. If P_{x1} and P_{x2} are the values before and after the reflection, then $P_{x2}=-\left[P_{x1}+2\tilde{p}_{x}\left(t^{*}\right)\right]$, where t^{*} is the moment when the particle hits the edge. If the phases ωt^{*} are uniformly distributed, this effect contributes with the terms of the order of $\left|\tilde{E}_{x}\right|^{2}$, which leads to corrections cubic with respect to the field amplitude in Eq. (4.39). Neglecting these terms and also any effects of viscosity in the transition layer we obtain $V_{y}=\mathrm{Re}\left(\tilde{V}_{y}e^{-i\omega t}\right)$,

where $\tilde{V}_y = \text{const}$. The result is

$$\tilde{V}_y = \tilde{V}_y(\infty) = \frac{\sigma(\omega) E_y}{-en_F}. \tag{4.40}$$

Now we can calculate the constant (time-averaged) nonlinear edge photocurrent as

$$I_y = -\frac{e}{2}\mathrm{Re}\int_0^\infty \tilde{V}_y \delta\tilde{n}^*(x)\, dx. \tag{4.41}$$

Substituting here Eqs. (4.37),(4.40) yields

$$I_y = \frac{1}{2en_F}\mathrm{Re}\frac{i}{\omega}|\sigma(\omega)|^2 \tilde{E}_y \tilde{E}_x^*. \tag{4.42}$$

This result is exactly the same as the substitution of Eq. (4.33) into Eq. (4.36).

In the case of a very strong dissipation, when carriers are thermalized near the edge, one calculates the edge current using the approach described in [105]. This method relates the perturbation of carrier density with the perturbation of the chemical potential in the Fermi distribution. Applying this approach to a 2D system with linear electron dispersion gives the result which differs from Eq. (4.42) by a factor of $\frac{1}{2}$, whereas in a 3D with linear dispersion system the difference is a factor of $\frac{2}{3}$. In materials with a constant effective mass the result is the same as Eq. (4.42). Note that in graphene and in typical semiconductors the thermalization time for carriers in a given band is longer than their scattering time by at least one order of magnitude; see e.g. [113] and references therein. For a model with diffuse scattering at the boundary [124], the expression in Eq. (4.42) gives only an order of magnitude estimate.

4.6 IFE in Weyl semimetals

We consider the simplest model of a Dirac or Weyl Type I semimetal (hereafter WSM) valid only at low enough frequencies in the near vicinity of a Weyl point, which is basically a 3D generalization of Eqs. (4.3),(4.4), in which $\hat{\mathbf{p}}$ is a 3D momentum operator, $\hat{\boldsymbol{\sigma}} = \mathbf{x}_0\hat{\sigma}_x + \mathbf{y}_0\hat{\sigma}_y + \mathbf{z}_0\hat{\sigma}_z$ is

a 3D vector of Pauli matrices, $(\mathbf{x}_0, \mathbf{y}_0, \mathbf{z}_0)$ are unit vectors along the coordinate axes, and

$$W(p) = sv_F\sqrt{p_x^2 + p_y^2 + p_z^2}. \tag{4.43}$$

Here the number of Weyl nodes only adds to the degeneracy of electron states and the optical anisotropy and gyrotropy effects related to the finite separation of Weyl nodes [71] are neglected. The volume conductivity can be derived from a single-band kinetic equation if the radiation frequency ω, Fermi energy $v_F p_F$ and the distance b between Weyl nodes in k-space are related by [71]:

$$\hbar\omega \ll v_F p_F \ll \hbar v_F b$$

For an unperturbed Fermi distribution in the conduction band,

$$f_F(p) = \frac{1}{(2\pi\hbar)^3}\Theta(p_F - p), \tag{4.44}$$

the conductivity has a Drude-like form [71]:

$$\sigma = i\frac{e^2 n_F}{\omega + \frac{i}{\tau}} \times \frac{v_F}{p_F}, \tag{4.45}$$

where $n_F = \frac{g p_F^3}{6\pi^2\hbar^3}$ is a volume density of electrons corresponding to the Fermi distribution Eq. (4.44); the degeneracy g takes into account the contribution of all Weyl nodes, including those with opposite chiralities.

First consider the collisionless limit. We can again use Eq. (4.6), taking $\hat{Q}(f) = 0$ and $\mathbf{E} \perp \mathbf{H} \parallel \mathbf{z}_0$. For a 3D system the solution to Eq. (4.6) can be sought as $f = \mathrm{Re}\left[\delta f(\theta, \phi, p)\, e^{-i\omega t}\right] + f_F(p)$, where $p_x = p\cos\theta\sin\phi, p_y = p\sin\theta\sin\phi, p_z = p\cos\phi; |\delta f| \ll f_F$. Linearizing Eq. (4.6) and taking into account electron dispersion Eq. (4.43) gives

$$-i\omega\delta f + \frac{v_F}{p}\frac{eH_z}{c}\frac{\partial\delta f}{\partial\theta} - e\left(\tilde{E}_x\cos\theta + \tilde{E}_y\sin\theta\right)\sin\phi\frac{\partial f_F}{\partial p} = 0. \tag{4.46}$$

Eq. (4.46) has the following solution:

$$\delta f = \frac{e}{\omega^2 - \left(\frac{v_F}{p}\frac{eH_z}{c}\right)^2}\frac{\partial f_F}{\partial p}\sin\phi\left[\tilde{E}_x\left(i\omega\cos\theta - \frac{v_F}{p}\frac{eH_z}{c}\sin\theta\right) + \tilde{E}_y\left(i\omega\sin\theta + \frac{v_F}{p}\frac{eH_z}{c}\cos\theta\right)\right]. \tag{4.47}$$

The corresponding current density is

$$\begin{aligned} j_x &= -egv_F\mathrm{Re}\left(e^{-i\omega t}\int \sin\phi\cos\theta\delta f d^3p\right), \\ j_y &= -egv_F\mathrm{Re}\left(e^{-i\omega t}\int \sin\phi\sin\theta\delta f d^3p\right). \end{aligned} \tag{4.48}$$

From Eqs. (4.47) and (4.48) one can obtain the components of the conductivity tensor, keeping only the terms linear with respect to the magnetic field:

$$\begin{aligned} \sigma_{xx} &= \sigma_{yy} = \sigma = \frac{4\pi i e^2 g v_F}{3\omega}\int_0^\infty 2f_F p dp, \\ \sigma_{xy} &= -\sigma_{yx} = \frac{4\pi e^3 g H_z v_F^2}{3\omega^2 c}\int_0^\infty f_F dp. \end{aligned} \tag{4.49}$$

This gives the desired components of the dielectric permittivity tensor, $\varepsilon_{ij} = \delta_{ij} + 4\pi\frac{i\sigma_{ij}}{\omega}$, and finally the magnetic moment calculated using Eq. (4.1):

$$\begin{aligned} m_z^{(0)} &= \frac{1}{8\pi}\mathrm{Re}\left[\left(\frac{\partial\varepsilon_{xy}^{(intra)}}{\partial H_z}\right)_{H_z\to 0}\tilde{E}_y\tilde{E}_x^*\right] \\ &= \frac{2\pi e^3 g H_z v_F^2}{3\omega^2 c}\int_0^\infty f_F dp \times \mathrm{Re}\left(i\widetilde{E}_y\widetilde{E}_x^*\right), \end{aligned} \tag{4.50}$$

where the superscript (0) is again to indicate an approximation of a transparent medium.

For a degenerate electron distribution in the zero-temperature limit Eq. (4.44) we have

$$\begin{aligned} \sigma_{xx} &= \sigma_{yy} = \sigma = i\frac{e^2 g p_F^2 v_F}{6\hbar^3\pi^2\omega}, \\ \sigma_{xy} &= -\sigma_{yx} = \frac{e^3 g H_z p_F v_F^2}{6\hbar^3\pi^2\omega^2 c}, \end{aligned} \tag{4.51}$$

and

$$m_z^{(0)} = \frac{e^3 g p_F v_F^2}{12\hbar^3\pi^2\omega^3 c}\mathrm{Re}\left(i\tilde{E}_y\tilde{E}_x^*\right). \tag{4.52}$$

As in the case of a 2D material, these components of the conductivity tensor coincide with those obtained for particles with a constant mass m_{eff}, if we express them through a particle density n_F and introduce the effective mass as $m_{\text{eff}} = \frac{p_F}{v_F}$.

It is also easy to find out that Eqs. (4.49) satisfy the equations similar to those for 2D systems in Eq. (4.34):

$$\frac{1}{ecn_F}\frac{i}{\omega}\left|\sigma\right|^2 = \left(\frac{i}{\omega}\frac{\partial\sigma_{xy}}{\partial H_z}\right)_{H_z\to 0} = \frac{1}{4\pi}\left(\frac{\partial\varepsilon_{xy}}{\partial H_z}\right)_{H_z\to 0}. \tag{4.53}$$

When scattering and dissipation are taken into account, one can repeat the same derivation steps as above for a 2D system and arrive at the expression for the photogenerated magnetic moment in the form of Eq. (4.33), in which one should substitute the volume conductivity Eq. (4.45) and volume carrier density n_F.

4.7 Discussion

In order to compare the magnitude of the IFE in Dirac materials with that in conventional semiconductors, we note that for materials with conventional quadratic dispersion of carriers the induced magnetic moment per free carrier scales inversely proportional to their effective mass squared. As we already pointed out, the same dependence exists in both 2D and 3D Dirac materials if we denote $m_{\text{eff}} = \frac{p_F}{v_F} = \frac{W_F}{v_F^2}$ as an effective mass. Assuming $v_F \approx c/300$, the ratio of the effective to free electron mass is $\frac{m_{\text{eff}}}{m_0} \simeq 2\times 10^{-4}\frac{W_F}{1\text{ meV}}$. For example, when $W_F = 50$ meV, the effective mass is 0.01 m_0, which is one order of magnitude lower that in a typical semiconductor with a bandgap of the order of 1 eV. Therefore, at low frequencies $\hbar\omega \ll W_F$ the IFE in Dirac materials can be stronger than in conventional semiconductors by a couple of orders of magnitude.

Let us estimate the magnetization obtained in the experiment [124], where the excitation of edge photocurrent in graphene was investigated. They used an NH_3 laser with 10 kW power and minimum frequency of 1.1 THz. For a 1 mm radius of a laser focus and Fermi energy of 0.2-0.3 eV the condition $p_F \gg \frac{eE_0}{\omega}$ is satisfied. Using the current dissipation time $\tau \sim 100$ fs (which

corresponds to $\omega\tau \sim 1$), the magnetic moment of an illuminated spot is about $\sim 10^{-7}$ G cm^3, and the photoinduced average magnetic moment per free carrier particle is of the order of 100 Bohr magnetons.

If the optical pumping creates the magnetic moment of 100 Bohr magnetons per carrier, the magnetic moment per unit area of graphene scales as $4\pi m_z \sim 10^{-5} \left(\frac{W_F}{100\text{ meV}}\right)^2$ G cm. Similarly, the magnetic moment per unit volume in an illuminated volume of a Weyl semimetal sample scales roughly as $4\pi m_z \sim 2.2g \left(\frac{W_F}{100\text{ meV}}\right)^3$ G, where g is degeneracy including the total number of Weyl nodes.

One possible application for the IFE is to provide all-optical modulation of the polarization of the probe light transmitted through (or reflected from) an area of the optical excitation. For example, a probe light passing along z-axis through the area of optically induced magnetization m_z experiences *direct* Faraday effect. The magnitude of the polarization rotation χ can be calculated using textbook Faraday effect formulas in which an external magnetic field B_z is replaced by $4\pi m_z$, where m_z is an optically induced magnetic moment per unit volume:

$$\chi(L) = \int_0^L \alpha dz, \tag{4.54}$$

where

$$\alpha = \frac{\omega}{2c}(n_O - n_X) \tag{4.55}$$

and $n_{O,X}$ are refractive indices of normal EM modes, i.e. ordinary and extraordinary modes. In the simplest case of a dielectric tensor with $\varepsilon_{xx} = \varepsilon_{yy}$ the normal modes are circularly polarized and

$$n_{O,X}^2 = \varepsilon_{xx} \pm |\varepsilon_{xy}|, \tag{4.56}$$

where $\varepsilon_{xx} = \varepsilon_{yy} = 1 + 4\pi i\sigma/\omega$. For small magnetic fields $\varepsilon_{xy} \propto B_z$, so Eqs. (4.55) and (4.56) give

$$\alpha \approx \frac{\omega}{2c\sqrt{\varepsilon_{xx}}}|\varepsilon_{xy}| \approx \frac{\omega}{2c\sqrt{\varepsilon_{xx}}} \left| \left(\frac{\partial \varepsilon_{xy}}{\partial B_z}\right)_{B_z \to 0} B_z \right|. \tag{4.57}$$

Note that for the material with no intrinsic magnetic order and for linear dependence of the off-diagonal component of the dielectric tensor on the magnetic field, we can replace the magnetic field H_z with the magnetic induction B_z in all expressions in this chapter. Then, taking into account that

$$m_z = \frac{1}{8\pi}\left(\frac{\partial \varepsilon_{xy}}{\partial B_z}\right)_{B_z\to 0}|E|^2,$$

we obtain

$$\alpha = \frac{\omega}{4c}\frac{1}{\sqrt{1+4\pi i\sigma/\omega}}\left(\frac{\partial \varepsilon_{xy}}{\partial B_z}\right)^2_{B_z\to 0}|E|^2, \tag{4.58}$$

where

$$\sigma = i\frac{e^2 g v_F p_F^2}{6\hbar^3\pi^2\omega},$$

$$\left|\frac{\partial \varepsilon_{xy}}{\partial B_z}\right|_{B_z\to 0} = \frac{4\pi}{\omega}\left|\frac{\partial \sigma_{xy}}{\partial B_z}\right|_{B_z\to 0} = \frac{2e^3 g v_F^2 p_F}{3\hbar^3\pi\omega^3 c}.$$

For a specific example, consider an incident optical pump with the electric field of magnitude 10 kV/cm at frequency $\omega/2\pi = 1$ THz. For the Fermi energy of 100 meV in a WSM sample the Faraday rotation parameter $\alpha \approx 6.6g^{3/2}$ rad/cm, which is already interesting for applications. The modulation magnitude could be further enhanced by integration of a Dirac material with a suitable plasmonic structure which supports highly localized plasmon modes. For example, in [131] a strong enhancement of Faraday rotation was predicted for a graphene sheet encapsulated in a 2D metallic grating.

4.8 Conclusions

In conclusion, we investigated the inverse Faraday effect in materials with massless Dirac fermions, both in two dimensions such as graphene and surface states in topological insulators, and in three dimensions such as Dirac and Weyl semimetals. Both semiclassical and quantum theories were presented. The dissipation, finite size, and strong field effects were analyzed in the quasiclassical approximation. We found that the magnitude of the IFE can be significantly enhanced in Dirac materials as compared to conventional semiconductors. This makes Dirac materials promising for the optical control of magnetization, all-optical modulation, and optical

isolation in compact optoelectronic devices.

5. DYNAMICS AND CONTROL OF ENTANGLED ELECTRON-PHOTON STATES IN NANOPHOTONIC SYSTEMS WITH TIME-VARIABLE PARAMETERS*

In this chapter, we study the dynamics of strongly coupled nanophotonic systems with time-variable parameters. The approximate analytic solutions are obtained for a broad class of open quantum systems including a two-level fermion emitter strongly coupled to a multimode quantized electromagnetic field in a cavity with time-varying cavity resonances or the electron transition energy. The coupling of the fermion and photon subsystems to their dissipative reservoirs is included within the stochastic equation of evolution approach, which is equivalent to the Lindblad approximation in the master equation formalism. The analytic solutions for the quantum states and the observables are obtained under the approximation that the rate of parameter modulation and the amplitude of the frequency modulation are much smaller than the optical transition frequencies. At the same time, they can be arbitrary with respect to the generalized Rabi oscillation frequency, which determines the coherent dynamics. Therefore, our analytic theory can be applied to an arbitrary modulation of the parameters, both slower and faster than the Rabi frequency, for complete control of the quantum state. In particular, we demonstrate protocols for switching on and off the entanglement between the fermionic and photonic degrees of freedom, swapping between the quantum states, and the decoupling of the fermionic qubit from the cavity field due to modulation-induced transparency.

5.1 Introduction

Solid-state photonic qubits based on the fermion systems coupled to a quantized electromagnetic (EM) field in a plasmonic or dielectric nanocavity are promising for a variety of quantum information and quantum sensing applications [132, 133, 134]. Their benefits include compatibility with semiconductor technology, scalability, and potential for operation at temperatures much high-

*Reprinted with permission from: "Dynamics and control of entangled electron-photon states in nanophotonic systems with time-variable parameters" by Q. Chen, Y. Wang, S. Almutairi, M. Erukhimova, M. Tokman, and A. Belyanin, 2021. Phys. Rev. A 103, 013708, Copyright 2021 by the American Physical Society.

er than the alternative platforms based on superconducting qubits or trapped ions. Indeed, strong coupling to single quantum emitters in dielectric nanocavities was demonstrated in various systems, for example color centers [135] or quantum dots (QDs) Refs. [136, 137]. In plasmonic cavities, strong coupling to single molecules Refs. [138, 139, 140] and colloidal QDs [141, 142, 143] has been achieved at room temperature; see, e.g., Refs. [133, 144, 145, 146, 147] for recent reviews.

While the quantum dynamics of entangled nanophotonic systems is interesting by itself, many applications would benefit from to control and modify the qubit states by time-dependent variation of certain parameters, while taking into account various processes of decoherence and dissipation. There is of course a large body of work related to cavity quantum electrodynamics (QED) with time-variable parameters. For example, the dynamics of nanophotonics systems with periodic modulation of some parameter, such as the cavity size or the position of a quantum emitter in a cavity, has been studied extensively in the burgeoning fields of cavity optomechanics [148, 149, 150] and quantum acoustics [151, 152, 153]. In this case the most interesting new element added to the nanophotonic system is the parametric resonance or the dressing of the electron-photon coupling by mechanical oscillations. Near the parametric resonance, the system can be mapped to an exactly solvable time-independent Hamiltonian within the rotating-wave approximation [154].

There is a class of time-dependent Hamiltonians for which the nonstationary Schrödinger equation can be solved exactly in the analytic form, notably multistate Landau-Zener Hamiltonians and driven Tavis-Cummings Hamiltonians [155, 156]; see also [157] where this technique was applied to the quantum annealing problem. Here we are interested in the nanophotonic applications, so we have to consider open multimode photonic systems with an arbitrary time dependence of the parameters. Therefore, we restrict ourselves to the adiabatic dynamics, for which the analytic solution can be found for a broad variety of systems with time-dependent cavity or fermion emitter parameters, and with dissipation included at the level of the Lindblad formalism. We find that the condition of adiabaticity is not that restrictive; in particular it still allows one to consider the parameter variation at a rate comparable to or faster than the generalized Rabi frequency in strongly coupled systems, which may be required for qubit manipulation.

We will also stick to the rotating wave approximation (RWA) [158]. The use of RWA restricts the coupling strength to the values much lower than the characteristic energies in the system, such as the optical transition or photon energy. The emerging studies of the so-called ultra-strong coupling regime [146] have to go beyond the RWA. Nevertheless, for the vast majority of experiments, including nonperturbative strong coupling dynamics and entanglement, the RWA is adequate and provides some crucial simplifications that allow one to obtain analytic solutions.

In particular, within Schrödinger's description, the equations of motion for the components of an infinitely dimensional state vector $|\Psi\rangle$ that describes a coupled fermion-boson system can be split into the blocks of low dimensions if the RWA is applied. This is true even if the dynamics of the fermion subsystem is nonperturbative, e.g. the effects of saturation are important. Note that there is no such simplification in the Heisenberg representation, except within the perturbation theory; see e.g. [158]. This is because boson operators are defined on a basis of infinite dimension and truncation of their dynamics into blocks of small dimensions is generally not possible (see also [154]). The Schrödinger's approach also leads to fewer equations for the state vector components than the approach based on the von Neumann master equation for the elements of the density matrix. This is especially true for a system with many degrees of freedom, e.g., many electron states coupled to multiple boson field modes.

Obviously, the Schrödinger equation in its standard form cannot be applied to describe open systems coupled to a dissipative reservoir. In this case the stochastic versions of the equation of evolution for the state vector have been developed, e.g. the method of quantum jumps [158, 159]. This method is optimal for numerical analysis in the Monte-Carlo type schemes. Here we formulate the stochastic equation which is more conducive to the analytic treatment. In [154] we showed that the stochastic equation of evolution for the state vector can be derived directly from the Heisenberg-Langevin formalism.

The paper is structured as follows. Section 5.2 formulates the model and the Hamiltonian for two-level electron system and a quantized EM field in a nanocavity with time-variable parameters. It treats a single-mode cavity in detail as a particular case and describes simple manipulations with

a single cavity mode coupled to a single fermionic qubit. Section 5.3 considers the dynamics of two time-modulated cavity modes coupled to a single quantum emitter and Sec. 5.4 treats the case of a variable frequency of the optical transition in a fermion qubit. Section 5.5 solves the quantum dynamics for an open time-dependent system with the coupling to dissipative reservoirs taken into account. An interesting phenomenon of modulation-induced transparency is analyzed. Numerical estimations for various nanophotonic systems reported in the literature are presented. Conclusions are in Section 5.6. Appendix I describes the quantization procedure for a plasmon cavity field with strongly subwavelength localization. Appendix J summarizes the main properties of the stochastic equation of evolution and compares with the Lindblad density-matrix formalism.

5.2 Cavity QED with time-variable parameters

5.2.1 Standard cavity QED Hamiltonian for a quantized field coupled to a two-level emitter

For reference, we start from summarizing basic textbook facts about a quantized electron system resonantly coupled to the quantum multimode EM field of a nanocavity without any time dependence, and then consider the time-dependent models in the next sections.

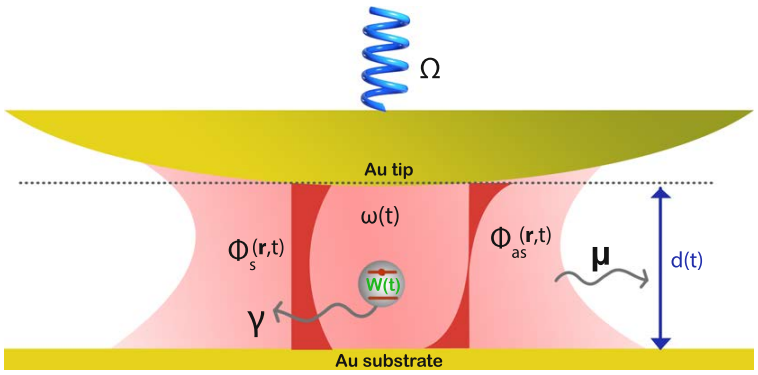

(a)

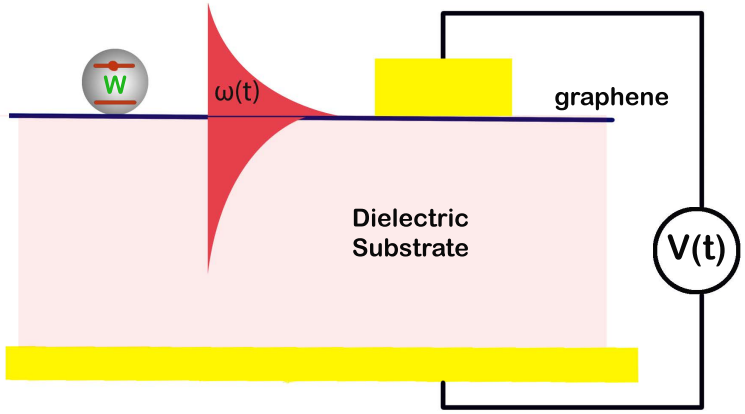

(b)

Figure 5.1: (a) A sketch of a quantum emitter (e.g. a quantum dot or a single molecule) in a nanocavity with time-dependent parameters created by a metallic nanotip of the scanning probe and a metallic substrate. The profiles of the electric potential $\Phi(\mathbf{r}, t)$ for the symmetric and anti-symmetric mode (see Appendix I) are sketched. Other parameters are the transition energy $W(t)$ for a quantum emitter, the optical field frequency $\omega(t)$, the cavity height $d(t)$, and the relaxation constants of the cavity field, μ, and a quantum emitter, γ. (b) A quantum emitter coupled to the cavity surface plasmon field supported by graphene. The mode frequency $\omega(t)$ can be varied by applying variable voltage $V(t)$ which modifies the charge density in graphene.

Consider the simplest version of the fermion subsystem: two electron states $|0\rangle$ and $|1\rangle$ with energies 0 and W, respectively. We will call it an "atom" for brevity, although it can be electron states of a molecule, a quantum dot, a defect in a semiconductor, or any other electron system. Introduce creation and annihilation operators of the excited state $|1\rangle$, $\hat{\sigma} = |0\rangle\langle 1|$, $\hat{\sigma}^\dagger = |1\rangle\langle 0|$,

which satisfy standard commutation relations for fermions:

$$\hat{\sigma}^{\dagger}\left|0\right\rangle =\left|1\right\rangle ,\hat{\sigma}\left|1\right\rangle =\left|0\right\rangle ,\hat{\sigma}\hat{\sigma}=\hat{\sigma}^{\dagger}\hat{\sigma}^{\dagger}=0;\left[\hat{\sigma},\hat{\sigma}^{\dagger}\right]_{+}=\hat{\sigma}\hat{\sigma}^{\dagger}+\hat{\sigma}^{\dagger}\hat{\sigma}=1.$$

The Hamiltonian of an atom is

$$\hat{H}_{a}=W\hat{\sigma}^{\dagger}\hat{\sigma}. \tag{5.1}$$

We will also need the dipole moment operator, $\hat{\mathbf{d}}=\mathbf{d}\left(\hat{\sigma}^{\dagger}+\hat{\sigma}\right)$, where $\mathbf{d}=\left\langle 1\right|\hat{\mathbf{d}}\left|0\right\rangle$ is a real vector. For a finite motion we can always choose the coordinate representation of stationary states in terms of real functions.

We assume that an atom is placed in a nanocavity and is resonantly coupled to the electric field of quantized cavity modes. Figure 5.1 sketches two out of many possible geometries of a time-variable nanocavity, e.g. formed by the nanotip of the scanning probe and the metallic substrate (Fig. 5.1a), similar to the recent experiments with strong coupling to single quantum emitters [140, 141, 142, 143]. Of course many other cavity geometries are possible, such as the one in Fig. 5.1b where the quantum emitter is coupled to the cavity surface plasmon field supported by graphene. Here the optical transition energy $W(t)$, the photon mode frequency $\omega(t)$, and field amplitudes described by an electric potential $\Phi\left(\mathbf{r},t\right)$ are all subject to external modulation by e.g. varying the tip distance to the substrate, the position of a quantum emitter in a cavity, or a variable voltage applied to graphene or to a QD in a semiconductor nanostructure, but we will start from the Hamiltonian without any time dependence for future comparison.

We use a standard representation for the electric field operator in a cavity:

$$\hat{\mathbf{E}}=\sum_{i}\left[\mathbf{E}_{i}\left(\mathbf{r}\right)\hat{c}_{i}+\mathbf{E}_{i}^{*}\left(\mathbf{r}\right)\hat{c}_{i}^{\dagger}\right], \tag{5.2}$$

where $\hat{c}_{i}^{\dagger},\hat{c}_{i}$ are creation and annihilation operators for photons at frequency ω_{i}; the functions $\mathbf{E}_{i}\left(\mathbf{r}\right)$ describe the spatial structure of the EM modes in a cavity. The relation between the modal frequency ω_{i} and the function $\mathbf{E}_{i}\left(\mathbf{r}\right)$ can be found by solving the boundary-value problem of the

classical electrodynamics [158]. The normalization conditions [110]

$$\int_V \frac{\partial\left[\omega_i^2 \varepsilon\left(\omega_i, \mathbf{r}\right)\right]}{\omega_i \partial \omega_i} \mathbf{E}_i^*\left(\mathbf{r}\right) \mathbf{E}_i\left(\mathbf{r}\right) d^3 r = 4\pi\hbar\omega_i \tag{5.3}$$

ensure correct bosonic commutators $\left[\hat{c}_i, \hat{c}_i^\dagger\right] = \delta_{ij}$ and the field Hamiltonian in the form

$$\hat{H}_{em} = \hbar \sum_i \omega_i \left(\hat{c}_i^\dagger \hat{c}_i + \frac{1}{2}\right). \tag{5.4}$$

Here V is a quantization volume and $\varepsilon\left(\omega, \mathbf{r}\right)$ is the dielectric function of a dispersive medium that fills the cavity.

Equation (5.3) is true for any fields satisfying Maxwell's equations as long as intracavity losses can be neglected and the flux of the Poynting vector through the total cavity surface is zero; see, e.g., Refs. [110, 160, 161, 162]. Of course the photon losses are always important when calculating the decoherence rates and fluctuations. What matters for Eq. (5.3) is that the effect of losses on the *spatial structure* of the cavity modes is insignificant. The latter is true as long as it makes sense to talk about cavity modes at all, which means in practice that the cavity Q-factor is at least around 10 or greater.

In many experiments involving strong coupling to a single quantum emitter the plasmonic cavities of nanometer size and even below 1 nm are used. The quantization procedure for a strongly subwavelength plasmon field has its peculiarities. We describe it in detail in Appendix I.

Adding the interaction Hamiltonian with a EM cavity mode in the electric dipole approximation, $-\hat{\mathbf{d}} \cdot \hat{\mathbf{E}}$, the Hamiltonian of an atom coupled to a single mode EM field is

$$\hat{H} = \hat{H}_{em} + \hat{H}_a - \mathbf{d}\left(\hat{\sigma}^\dagger + \hat{\sigma}\right) \cdot \left[\mathbf{E}\left(\mathbf{r}\right) \hat{c} + \mathbf{E}^*\left(\mathbf{r}\right) \hat{c}^\dagger\right]_{\mathbf{r}=\mathbf{r}_a}, \tag{5.5}$$

where $\mathbf{r} = \mathbf{r}_a$ denotes the position of an atom inside the cavity. This can be rewritten as

$$\hat{H} \;=\; \hat{H}_{em} + \hat{H}_a - \left(\chi \hat{\sigma}^\dagger \hat{c} + \chi^* \hat{\sigma} \hat{c}^\dagger + \chi \hat{\sigma} \hat{c} + \chi^* \hat{\sigma}^\dagger \hat{c}^\dagger\right) \tag{5.6}$$

where $\chi = (\mathbf{d} \cdot \mathbf{E})_{\mathbf{r}=\mathbf{r}_a}$.

The best conditions for entanglement are realized in the vicinity of an atom-field resonance, where one can apply the rotating wave approximation (RWA). The RWA Hamiltonian is obtained by dropping the last two terms in Eq. (5.6). Note that we can always take the functions $\mathbf{E}(\mathbf{r})$ to be real at the position of an atom. This single-mode model is of course the Jaynes-Cummings Hamiltonian [32].

5.2.2 Quantized electromagnetic field in a time-variable cavity

In a standard approach to quantization of the EM field based on Eqs. (5.2)-(5.4), a set of mode frequencies ω_i and the relation between the frequency ω_i and the spatial structure of the field mode $\mathbf{E}_i(\mathbf{r})$ are determined by solving the boundary-value problem for the classical EM field. Let's assume that the solution of this boundary-value problem depends on a certain parameter p, for example the cavity height $d(t)$ in Fig. 5.1 or the position of the emitter with respect to the field distribution. In this case $\omega_i(p)$ and $\mathbf{E}_i(\mathbf{r},p)$ are functions of p. Of course the solution depends on many parameters of the cavity, but we consider the situation when this particular parameter is adiabatically changing with time. As usual, "adiabatically" means that the change can be arbitrary (e.g. periodic or not) but it should be slow as compared to typical frequencies of all subsystems when the parameters are constant, such as the modal frequencies and the transition frequency of a quantum emitter. It is important that the rate of change of parameters can be arbitrary as compared to characteristic frequency scales which determine the interaction between subsystems, such as the Rabi frequency, as long as these scales are smaller than the modal or transition frequencies [163, 164].

For an adiabatically varying parameter Eqs. (5.2)-(5.4) depend on the instantaneous value of the parameter,

$$\hat{\mathbf{E}} = \sum_i \left[\mathbf{E}_i(\mathbf{r},p)\, \hat{c}_i + \mathbf{E}_i^*(\mathbf{r},p)\, \hat{c}_i^\dagger \right], \tag{5.7}$$

$$\hat{H} = \sum_i \hat{H}_i \quad \hat{H}_i = \hbar\omega_i(p) \left(\hat{c}_i^\dagger \hat{c}_i + \frac{1}{2} \right), \tag{5.8}$$

$$\int_{V(p)} \frac{\partial\left[\omega_i^2 \varepsilon\left(\omega_i, \mathbf{r}\right)\right]}{\omega_i \partial \omega_i} \mathbf{E}_i^*\left(\mathbf{r}, p\right) \mathbf{E}_i\left(\mathbf{r}, p\right) d^3 r = 4\pi\hbar\omega_i(p). \tag{5.9}$$

The solution of the Schrödinger equation $i\hbar\frac{\partial}{\partial t}\left|\Psi_i\right\rangle = \hat{H}_i\left|\Psi_i\right\rangle$ for a given field mode is

$$\left|\Psi_i\right\rangle = \sum_{n=0}^{\infty} C_n \left|n\right\rangle \tag{5.10}$$

where $C_n = C_n^0 e^{-i(n+\frac{1}{2})\int_0^t \omega_i(\tau)d\tau}$, $\omega_i\left(t\right) \equiv \omega_i\left(p\left(t\right)\right)$, and $\left|n\right\rangle$ are Fock states. For a bosonic field described by a standard quantized harmonic oscillator, if we choose the coordinate representation expressed via Hermite polynomials, the parameters of the polynomials will be time-dependent. One can easily see that the above solution conserves the adiabatic invariant $\frac{\langle\Psi_i|\hat{H}_i|\Psi_i\rangle}{\omega_i(t)}$, just like in a classical slowly time-varying harmonic oscillator problem [165].

5.2.3 Quantum emitter coupled to a quantized EM field with a time-variable amplitude

Let a two-level electron system (an atom) be located at the point $\mathbf{r} = \mathbf{0}$ inside the cavity. The Hamiltonian of the system including the coupling of an atom to a particular cavity mode and its adiabatic modulation can be described within the RWA,

$$\hat{H} = \hbar\omega(t)\left(\hat{c}^\dagger\hat{c} + \frac{1}{2}\right) + W\hat{\sigma}^\dagger\hat{\sigma} - \left[\mathbf{d}\cdot\mathbf{E}\left(t\right)\hat{\sigma}^\dagger\hat{c} + \mathbf{d}^*\cdot\mathbf{E}^*\left(t\right)\hat{\sigma}\hat{c}^\dagger\right], \tag{5.11}$$

where $\mathbf{E}\left(\mathbf{0}, t\right) = \mathbf{E}\left(t\right)$. The time dependence of the field amplitude follows from the parameter modulation.

The wave function of the coupled photon-electron state can be written as

$$\Psi = \sum_{n=0}^{\infty}\left(C_{n0}\left|n\right\rangle\left|0\right\rangle + C_{n1}\left|n\right\rangle\left|1\right\rangle\right), \tag{5.12}$$

where we will maintain the same order, $\left|photon\right\rangle\left|fermion\right\rangle$ of the state products everywhere. Substituting it in the Schrödinger equation and taking into account the time variation of the param-

eter, we obtain the equation for the ground energy state,

$$\dot{C}_{00} + i\omega_{00}(t) C_{00} = 0, \tag{5.13}$$

and a pair of equations for "resonant" states,

$$\dot{C}_{n0} + i\omega_{n0}(t) C_{n0} - i\Omega_R^*(t) C_{(n-1)1} = 0, \tag{5.14}$$

$$\dot{C}_{(n-1)1} + i\omega_{(n-1)1}(t) C_{(n-1)1} - i\Omega_R(t) C_{n0} = 0, \tag{5.15}$$

where

$$\omega_{n0}(t) = \omega(t)\left(n + \frac{1}{2}\right), \;\; \omega_{n1}(t) = \omega_{n0}(t) + \frac{W}{\hbar}, \;\; \Omega_R(t) = \frac{\mathbf{d}\cdot\mathbf{E}(t)}{\hbar}\sqrt{n}.$$

Equations (5.14), (5.15) can be written in a more convenient form after making a substitution

$$\begin{pmatrix} C_{n0} \\ C_{(n-1)1} \end{pmatrix} = \begin{pmatrix} G_{n0} e^{-i\int_0^t \omega_{n0}(\tau)d\tau} \\ G_{(n-1)1} e^{-i\int_0^t \omega_{(n-1)1}(\tau)d\tau} \end{pmatrix}, \tag{5.16}$$

which gives

$$\dot{G}_{n0} - i\Omega_R^*(t) e^{i\int_0^t \delta(\tau)d\tau} G_{(n-1)1} = 0, \tag{5.17}$$

$$\dot{G}_{(n-1)1} - i\Omega_R(t) e^{-i\int_0^t \delta(\tau)d\tau} G_{n0} = 0, \tag{5.18}$$

where $\delta(t) = \omega(t) - \frac{W}{\hbar}$.

When there is no modulation, i.e. δ, ω, and Ω_R are constant, Eqs. (5.17), (5.18) have a simple solution $G_{(n-1)1}, G_{n0} \propto e^{-i\nu t}$, where the eigenvalues are

$$\nu_{1,2} = \frac{\delta}{2} \pm \sqrt{\frac{\delta^2}{4} + |\Omega_R|^2}, \tag{5.19}$$

and the eigenvectors satisfy

$$K_{1,2} = \left[\frac{G_{n0}}{G_{(n-1)1}}\right]_{1,2} = \frac{\nu_{1,2}e^{i\delta t}}{\Omega_R}, \tag{5.20}$$

where $K_1 K_2^* = -1$. The eigenvalues $\nu_{1,2}$ as a function of detuning δ are shown in Fig. 5.2. It is easy to verify that in the region $\delta \ll -|\Omega_R|$ the eigenvalue ν_1 corresponds to the dominant state $|n-1\rangle|1\rangle$, whereas in the region $\delta \gg |\Omega_R|$ this eigenvalue corresponds to dominant state $|n\rangle|0\rangle$. For the eigenvalue ν_2 it is exactly the opposite.

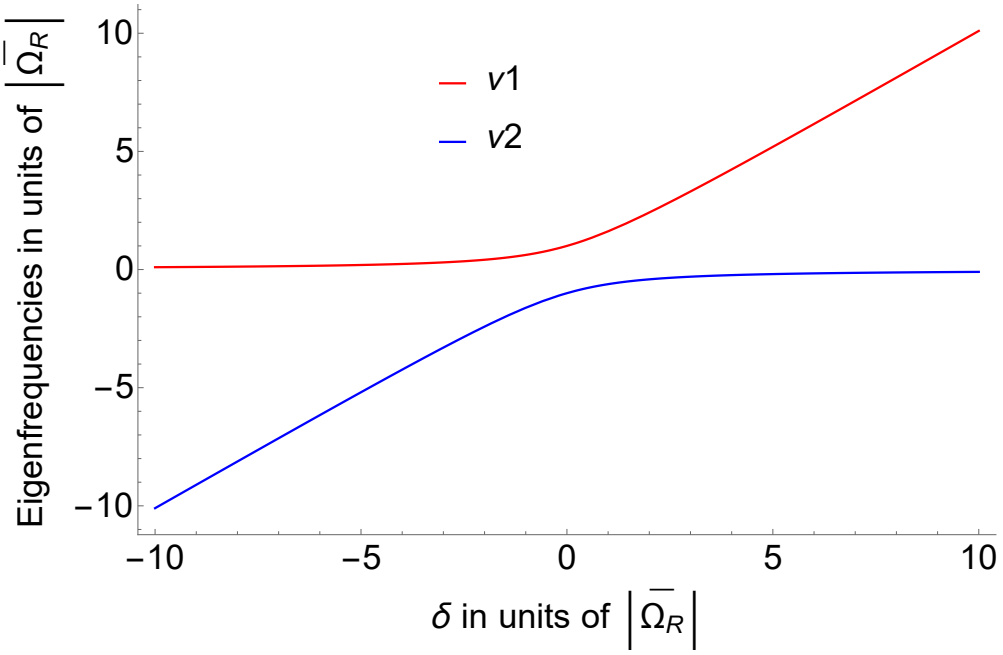

(a)

Figure 5.2: Frequency eigenvalues $\nu_{1,2}$ from Eq. (5.19) as a function of detuning δ from the resonance, $\delta = \frac{W}{\hbar} - \omega$. All frequencies are in units of the average Rabi frequency $\overline{\Omega_R}$.

When a cavity parameter is modulated, for example, a cavity height $d(t)$ in Fig. 5.1, both frequencies and field amplitudes $\mathbf{E}_i(\mathbf{r},p)$ get modulated; see Eq. (5.9). Therefore, the Rabi frequency Ω_R gets modulated. For a periodic modulation, the function $\Omega_R(t)\, e^{-i\int_0^t \delta(\tau)d\tau}$ is periodic and can

be expanded in the Fourier series,

$$\Omega_R(t)\, e^{-i\int_0^t \delta(\tau)d\tau} = \sum_{n=-\infty}^{\infty} R_n e^{-in\Omega t}, \tag{5.21}$$

where Ω is the modulation frequency. The explicit expressions for the Fourier amplitudes R_n can be obtained for any specific model of a cavity; see, e.g., Appendix I for the plasmonic cavity, which shows specific examples of the cavity mode frequencies, field amplitudes, and their modulation.

When the modulation frequency and amplitude of the eigenmode frequencies are small enough, one can neglect the modulation of the Rabi frequency in Eqs. (5.17), (5.18). This corresponds to the WKB approximation and one can see it by taking the time derivative of Eq. (5.18):

$$\frac{d^2G_{(n-1)1}}{dt^2} + \left(i\delta(t) - \frac{1}{\Omega_R(t)}\frac{d\Omega_R}{dt}\right)\frac{dG_{(n-1)1}}{dt} + |\Omega_R(t)|^2 G_{(n-1)1} = 0. \tag{5.22}$$

Now we can estimate the order of magnitude of different terms in Eq. (5.22). Assume that the cavity mode frequency is modulated as $\omega_i(t) = \bar{\omega} + \delta(t)$. Since Eq. (5.9) defines a certain dependence $\Omega_R(\omega_i)$, one can estimate $\left|\frac{\Omega_R^{-1}\dot{\Omega}_R}{\delta}\right| \sim \left|\frac{\dot{\delta}}{\Omega_R\delta}\frac{d\Omega_R}{d\omega_i}\right|_{\omega_i=\bar{\omega}}$ and $\left|\Omega_R - \overline{\Omega_R}\right| \sim \left|\frac{d\Omega_R}{d\omega_i}\delta\right|$. For estimations we take $\frac{d\Omega_R}{d\omega_i} \sim \frac{\overline{\Omega_R}}{\bar{\omega}}$, $\delta \sim \Delta\omega$, and $\dot{\delta} \sim \Omega\Delta\omega$ where $\overline{\Omega_R} = \Omega_R(\bar{\omega})$ and $\Delta\omega$ is the frequency change over the time Ω^{-1}. This gives $\left|\frac{\Omega_R^{-1}\dot{\Omega}_R}{\delta}\right| \sim \frac{\Omega}{\bar{\omega}}$ and $\left|\Omega_R - \overline{\Omega_R}\right| \sim \overline{\Omega_R}\frac{\Delta\omega}{\bar{\omega}}$. If $\Delta\omega, \Omega \ll \bar{\omega}$, Eq. (5.22) becomes

$$\frac{d^2G_{(n-1)1}}{dt^2} + i\delta(t)\frac{dG_{(n-1)1}}{dt} + \left|\overline{\Omega_R}\right|^2 G_{(n-1)1} = 0. \tag{5.23}$$

Equation (5.23) corresponds to the set of Eqs. (5.14), (5.15) with $\Omega_R = \text{const} = \overline{\Omega_R}$.

If we consider for definiteness a sinusoidal modulation of the frequency of a given mode, $\omega(t) = \bar{\omega} - \Delta\omega \cdot \sin(\Omega t)$, and take into account that $\Delta\omega, \Omega, \overline{\Omega_R} \ll \overline{\omega}$, the Fourier amplitudes in Eq. (5.21) can be expressed through the Bessel functions,

$$R_0 = \overline{\Omega_R} J_0\left(\frac{\Delta\omega}{\Omega}\right),\ R_n = (-i)^{|n|}\overline{\Omega_R} J_{|n|}\left(\frac{\Delta\omega}{\Omega}\right). \tag{5.24}$$

The decoherence processes can be added within the stochastic equation of evolution for the

state vector, which is derived in Appendix J. However, we postpone doing this until we consider a more complex case of two quantized modes interacting with a quantum emitter.

5.2.4 Simple manipulations with a qubit coupled to a single-mode field

A single emitter coupled to a single-mode field in a time-variable cavity permits simple manipulations: a slow or fast sweep through the resonance $\omega(t) = W/\hbar$, bringing an electron-photon system in and out of entanglement by changing the values of coefficients in Eq. (5.12), transduction of the excitation between an atom and the EM field, e.g., between $|0\rangle\,|1\rangle$ and $|1\rangle\,|0\rangle$ states, etc.

Note that the rate of modulation or parameter variation has to be slow only as compared to the optical frequency. It does not have to be slow as compared to the average Rabi frequency $\overline{\Omega_R}$. Therefore, in the strong coupling regime a desired switching can be completed faster than the Rabi oscillations and decoherence rates.

Let's look at some of these control operations in more detail. The sweep through resonance can be calculated exactly for each specific time dependence $\delta(t)$, but the limiting cases are well understood from the vast amount of literature on the linear coupling of the optical modes, Landau-Zener-type problems, etc [163, 164, 166, 167, 168].

For a slow sweep, $\left|\frac{d\delta}{dt}\right| \ll \overline{|\Omega_R|^2}$, the system will follow each eigenvalue branch plotted in Fig. 5.2 without jumping between them: for example, if the system starts from ν_1 at $\delta \ll -\overline{|\Omega_R|}$, it will stay on ν_1 as it moves through resonance to $\delta \gg \overline{|\Omega_R|}$. This means that the quantum state of the system will be switched from $|n-1\rangle\,|1\rangle$ to $|n\rangle\,|0\rangle$.

In the opposite limit of a fast sweep, $\left|\frac{d\delta}{dt}\right| \gg \overline{|\Omega_R|^2}$, as the system moves through resonance from $\delta \ll -\overline{|\Omega_R|}$ to $\delta \gg \overline{|\Omega_R|}$ it jumps from one eigenvalue branch to another. As a result, the quantum state stays unchanged.

In the intermediate region $\left|\frac{d\delta}{dt}\right| \sim \overline{|\Omega_R|^2}$, by varying the sweep rate or the Rabi frequency $\overline{|\Omega_R|}$ one can get any desired combination of the quantum states at the output. In particular, for linear variation of the detuning, $\delta(t) = \beta t$ where β is a constant, one can obtain an exact analytic solution

of Eq. (5.23) to predict the evolution of the system:

$$G_{(n-1)1}(t) = e^{-\frac{i\beta t^2}{4}} \left[c_1 D_{i\frac{\overline{|\Omega_R|}^2}{\beta}} \left(\sqrt{\beta} e^{-\frac{i\pi}{4}} t \right) + c_2 D_{-i\frac{\overline{|\Omega_R|}^2}{\beta}-1} \left(i\sqrt{\beta} e^{-\frac{i\pi}{4}} t \right) \right], \tag{5.25}$$

where D_ν are the parabolic cylinder functions [169] and $c_{1,2}$ are arbitrary constants determined by initial conditions. This solution can be used, for example, to calculate the efficiency of the $|n-1\rangle|1\rangle$ quantum state tunneling, i.e., the probability of the transition from the top to bottom branch in Fig. 5.2 as the detuning $\delta(t)$ varies from $-\infty$ to $+\infty$:

$$\left|C_{(n-1)1}\right|^2_{\delta\to\infty} \approx e^{-\frac{\overline{2\pi|\Omega_R|}^2}{\beta}} \left|C_{(n-1)1}\right|^2_{\delta\to-\infty}.$$

As expected, the probability is approaching 1 when $\left|\frac{d\delta}{dt}\right| = \beta \gg \overline{|\Omega_R|}^2$ and becomes exponentially small in the opposite limit.

5.3 Dynamics of two modulated cavity modes coupled to a quantum emitter

In order to perform more complex operations on the photonic qubits and get more functionality, we need to add one more quantized degree of freedom to the system. Here we consider *two* cavity modes in a time-variable cavity,

$$\hat{\mathbf{E}} = \mathbf{E}_a(\mathbf{r},t)\,\hat{a} + \mathbf{E}_a^*(\mathbf{r},t)\,\hat{a}^\dagger + \mathbf{E}_b(\mathbf{r},t)\,\hat{b} + \mathbf{E}_b^*(\mathbf{r},t)\,\hat{b}^\dagger. \tag{5.26}$$

We assume that the modulation of both frequencies has a small amplitude and average frequencies of both modes $\bar{\omega}_{a,b}$ are close to the transition frequency. In this case the RWA Hamiltonian for an atom + field system is

$$\hat{H} = \hbar\omega_a(t)\left(\hat{a}^\dagger\hat{a} + \frac{1}{2}\right) + \hbar\omega_b(t)\left(\hat{b}^\dagger\hat{b} + \frac{1}{2}\right) + W\hat{\sigma}^\dagger\hat{\sigma} - \left[\hat{\sigma}^\dagger\left(\chi_a\hat{a} + \chi_b\hat{b}\right) + \hat{\sigma}\left(\chi_a^*\hat{a}^\dagger + \chi_b^*\hat{b}^\dagger\right)\right], \tag{5.27}$$

where $\chi_{a,b}(t) = \mathbf{d}\cdot\mathbf{E}_{a,b}(t)$.

The Schrödinger equation can be solved analytically within the RWA [154]. As a simple ex-

ample, we include only the transitions between the states with lowest energies, namely

$$|0_a\rangle |0_b\rangle |0\rangle , |0_a\rangle |0_b\rangle |1\rangle , |1_a\rangle |0_b\rangle |0\rangle , |0_a\rangle |1_b\rangle |0\rangle ,$$

i.e. we seek the solution in the form

$$\Psi = C_{000} |0_a\rangle |0_b\rangle |0\rangle + C_{001} |0_a\rangle |0_b\rangle |1\rangle + C_{100} |1_a\rangle |0_b\rangle |0\rangle + C_{010} |0_a\rangle |1_b\rangle |0\rangle . \tag{5.28}$$

For arbitrary coefficients C the state (5.28) is a tripartite entangled state which can be reduced to standard GHZ states by local operations [170, 171], e.g. by rotations on the Bloch sphere of each qubit. In most cases discussed in the literature the GHZ states are made of identical subsystems, e.g., photons [172, 173]. In our case the subsystems are of different nature: a fermionic electron system and bosonic EM field modes. This makes their rotations more complicated, but on the other hand, enables other interesting applications. For example, one can determine the statistics of atomic excitations by measuring the statistics of photons, or change the entangled state of coupled photon modes by changing the atomic state with a classical control field.

Similarly to [154], the equations for the coefficients are

$$\dot{C}_{000} + i\frac{\omega_a (t) + \omega_b (t)}{2} C_{000} = 0; \tag{5.29}$$

$$\dot{C}_{001} + i \left(\frac{1}{2}\omega_a (t) + \frac{1}{2}\omega_b (t) + \frac{W}{\hbar} \right) C_{001} - i\Omega_{Ra}(t) C_{100} - i\Omega_{Rb}(t) C_{010} = 0, \tag{5.30}$$

$$\dot{C}_{100} + i \left(\frac{3}{2}\omega_a (t) + \frac{1}{2}\omega_b (t) \right) C_{100} - i\Omega^*_{Ra}(t) C_{001} = 0, \tag{5.31}$$

$$\dot{C}_{010} + i \left(\frac{1}{2}\omega_a (t) + \frac{3}{2}\omega_b (t) \right) C_{010} - i\Omega^*_{Rb}(t) C_{001} = 0, \tag{5.32}$$

where $\Omega_{Ra,b} = \frac{\chi_{a,b}}{\hbar}$. Making the substitution

$$\begin{pmatrix} C_{001} \\ C_{100} \\ C_{010} \end{pmatrix} = \begin{pmatrix} G_0 \exp\left[-i\int_0^t \left(\frac{1}{2}\omega_a(\tau) + \frac{1}{2}\omega_b(\tau) + \frac{W}{\hbar}\right)d\tau\right] \\ G_a \exp\left[-i\int_0^t \left(\frac{3}{2}\omega_a(\tau) + \frac{1}{2}\omega_b(\tau)\right)d\tau\right] \\ G_b \exp\left[-i\int_0^t \left(\frac{1}{2}\omega_a(\tau) + \frac{3}{2}\omega_b(\tau)\right)d\tau\right] \end{pmatrix}, \tag{5.33}$$

we obtain

$$\dot{G}_0 - i\Omega_{Ra}(t)G_a \exp\left[-i\int_0^t \left(\omega_a(\tau) - \frac{W}{\hbar}\right)d\tau\right] - i\Omega_{Rb}(t)G_b \exp\left[-i\int_0^t \left(\omega_b(\tau) - \frac{W}{\hbar}\right)d\tau\right] = 0, \tag{5.34}$$

$$\dot{G}_a - i\Omega_{Ra}^*(t)G_0 \exp\left[i\int_0^t \left(\omega_a(\tau) - \frac{W}{\hbar}\right)d\tau\right] = 0, \tag{5.35}$$

$$\dot{G}_b - i\Omega_{Rb}^*(t)G_0 \exp\left[i\int_0^t \left(\omega_b(\tau) - \frac{W}{\hbar}\right)d\tau\right] = 0, \tag{5.36}$$

In Fig. 5.3, we show the eigenstates of the system described by Eqs. (5.30), (5.31) and (5.32) as a function of frequency detuning defined as $\omega_a - W/\hbar$. Here we assumed that $\Omega_{Ra} = \Omega_{Rb} \equiv \Omega_R$ and kept the difference $\omega_b - \omega_a = 5\Omega_R$ constant, which can be achieved either by varying $W/\hbar$ while keeping constant $\omega_{a,b}$ or by varying ω_a and ω_b at the same rate while keeping $W/\hbar$ constant. The anticrossings are clearly seen in the plot of eigenfrequencies, when either ω_a or ω_b is resonant with the optical transition of an atom. As compared to Fig. 5.2, Fig. 5.3(b) shows more possibilities for switching between the three product states as the detuning is swept through the two resonances at the rate slower than the Rabi frequencies and the generation of both bipartite and tripartite entangled states in the vicinity of resonances if the sweeping rate is comparable to the Rabi frequencies.

Since the functions $\omega_{a,b}(t)$ and $\Omega_{a,b}$ are periodic with period $2\pi/\Omega$, we can use the expansion (5.21) in Eqs. (5.34)-(5.36).

If we keep only the resonant terms, assuming for example the following resonances, $\bar{\omega}_a = \frac{W}{\hbar}$ and $\bar{\omega}_b + m\Omega = \frac{W}{\hbar}$, where m is the number of a particular Fourier harmonic, the equations get

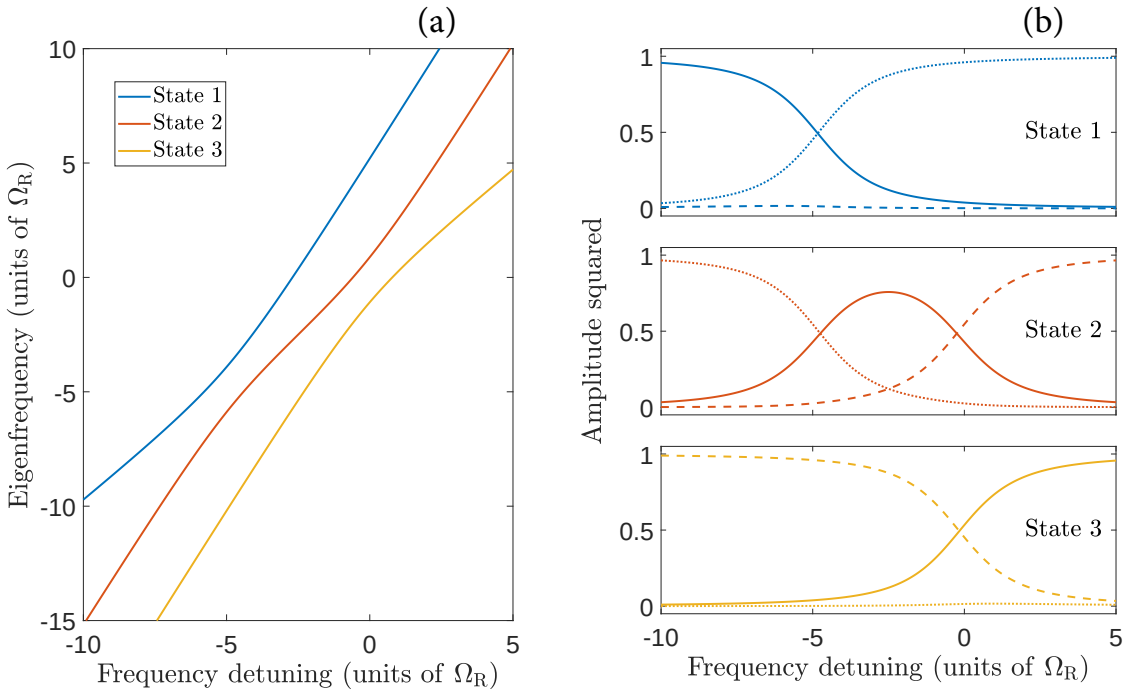

Figure 5.3: The eigenstates of the system described by Eqs. (5.30), (5.31) and (5.32) as a function of frequency detuning defined as $\omega_a - W/\hbar$, whereas the difference of modal frequencies $\omega_b - \omega_a = 5\Omega_R$ is kept constant. The eigenfrequencies are shown in (a), and the amplitudes of the eigenstates are shown in (b), in which the amplitudes of C_{001}, C_{100} and C_{010} are represented by the solid, dashed and dotted lines, respectively. The eigenfrequencies are shifted by $\left(\frac{1}{2}\omega_a + \frac{1}{2}\omega_b + \frac{W}{\hbar}\right)\Big|_{\omega_a = W/\hbar}$.

simplified,

$$\frac{d}{dt}\begin{pmatrix} G_0 \\ G_a \\ G_b \end{pmatrix} + \begin{pmatrix} 0 & -iR_{a0} & -iR_{bm} \\ -iR_{a0}^* & 0 & 0 \\ -iR_{bm}^* & 0 & 0 \end{pmatrix}\begin{pmatrix} G_0 \\ G_a \\ G_b \end{pmatrix} = 0. \tag{5.37}$$

Other (nonresonant) harmonics can be neglected only if $\Omega_{Ra,b} \ll \Omega$, see [154]. When the modulation amplitude is zero, $R_{a0} = \Omega_{Ra}$ and $R_{bm} = 0$. In this case one of the eigenvalues Γ_0 corresponds to the decoupled state $|0_a\rangle\,|1_b\rangle\,|0\rangle$. Two other eigenvalues $\Gamma_{1,2}$ describe the solution with Rabi oscillations between states $|0_a\rangle\,|0_b\rangle\,|1\rangle$ and $|1_a\rangle\,|0_b\rangle\,|0\rangle$.This is an obvious limit since frequency ω_a is in resonance with the transition frequency, whereas ω_b is out of resonance.

Assuming a sinusoidal modulation of the partial frequencies of both cavity modes as an exam-

ple,

$$\omega_{a,b}(t) = \bar{\omega}_{a,b} - \Delta\omega_{a,b} \cdot \sin(\Omega t), \tag{5.38}$$

and using the well-known expansion in series of the harmonics of the modulation frequency Ω, with coefficients expressed in terms of Bessel functions,

$$e^{-i\frac{\Delta\omega}{\Omega}\cos(\Omega t)} = J_0\left(\frac{\Delta\omega}{\Omega}\right) + 2\sum_{n=1}^{\infty}(-i)^n J_n\left(\frac{\Delta\omega}{\Omega}\right)\cos(n\Omega t), \tag{5.39}$$

we can express Fourier amplitudes in Eq. (5.37) through Bessel functions:

$$R_{a0} = \overline{\Omega_{Ra}} J_0\left(\frac{\Delta\omega_a}{\Omega}\right),\ R_{bm} = (-i)^{|m|}\overline{\Omega_{Rb}} J_{|m|}\left(\frac{\Delta\omega_b}{\Omega}\right). \tag{5.40}$$

Note that the modulation amplitudes in Eq. (5.38) *can be of the order of the modulation frequency*, $\frac{\Delta\omega_{a,b}}{\Omega} \sim 1$, despite the requirement $\Delta\omega_{a,b} \ll \bar{\omega}_{a,b}$.

As usual, to solve Eq. (5.37) one has to find the eigenvalues $\Gamma_{0,1,2}$ and eigenvectors of the matrix of coefficients. The characteristic equation for the eigenvalues is $\Gamma(\Gamma^2 + \Omega_{R\Sigma}^2) = 0$, where the cumulative Rabi frequency is

$$\Omega_{R\Sigma} = \sqrt{|R_{a0}|^2 + |R_{bm}|^2}. \tag{5.41}$$

The result is

$$\Gamma_0 = 0,\ \Gamma_{1,2} = \pm i\Omega_{R\Sigma}. \tag{5.42}$$

Figure 5.4 shows one example of the cumulative Rabi frequency $\Omega_{R\Sigma}$ as a function of $\Delta\omega = \Delta\omega_a = \Delta\omega_b$ for $m = 1$ and $\Omega_{Ra} = \Omega_{Rb}$. As expected, $\Omega_{R\Sigma}$ decays with detuning from resonances but the decay is nonmonotonic and depends on the order of harmonic resonances.

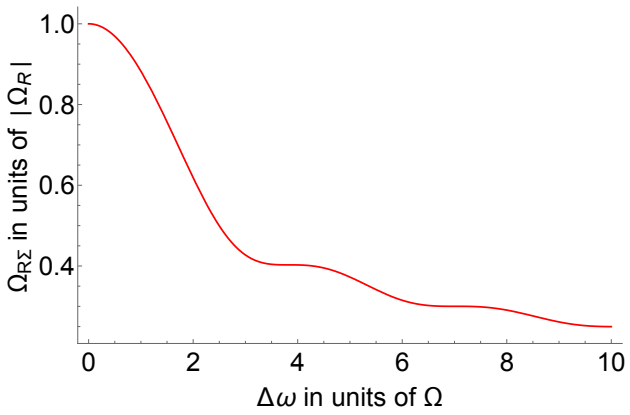

Figure 5.4: Cumulative Rabi frequency $\Omega_{R\Sigma}$ as a function of $\Delta\omega = \Delta\omega_a = \Delta\omega_b$ for $m = 1$ and $\Omega_R = \Omega_{Ra} = \Omega_{Rb}$.

The eigenvalue Γ_0 (i.e. the solution $\propto e^{-\Gamma_0 t}$) corresponds to the eigenvector $\begin{pmatrix} 0 \\ 1 \\ -\frac{R_{a0}}{R_{bm}} \end{pmatrix}$, whereas eigenvalues $\Gamma_{1,2}$ (i.e. the solution behaving as $\propto e^{-\Gamma_{1,2} t}$) correspond to the eigenvectors $\begin{pmatrix} \frac{\pm\Omega_{R\Sigma}}{R^*_{a0}} \\ 1 \\ \frac{R^*_{bm}}{R^*_{a0}}. \end{pmatrix}$. Here the eigenvectors are not normalized to 1. The resulting solution is

$$\begin{pmatrix} G_0 \\ G_a \\ G_b \end{pmatrix} = A \begin{pmatrix} 0 \\ 1 \\ -\frac{R_{a0}}{R_{bm}} \end{pmatrix} + Be^{-i\Omega_{R\Sigma} t} \begin{pmatrix} \frac{\Omega_{R\Sigma}}{R^*_{a0}} \\ 1 \\ \frac{R^*_{bm}}{R^*_{a0}}. \end{pmatrix} + Ce^{i\Omega_{R\Sigma} t} \begin{pmatrix} \frac{-\Omega_{R\Sigma}}{R^*_{a0}} \\ 1 \\ \frac{R^*_{bm}}{R^*_{a0}}. \end{pmatrix}, \tag{5.43}$$

where the constants A, B and C are determined by the initial conditions.

For an arbitrary initial state vector

$$\Psi = C_{000}(0)\,|0_a\rangle\,|0_b\rangle\,|0\rangle + C_{001}(0)\,|0_a\rangle\,|0_b\rangle\,|1\rangle + C_{100}(0)\,|1_a\rangle\,|0_b\rangle\,|0\rangle + C_{010}(0)\,|0_a\rangle\,|1_b\rangle\,|0\rangle\,, \tag{5.44}$$

satisfying the normalization condition

$$|C_{000}(0)|^2 + |C_{001}(0)|^2 + |C_{100}(0)|^2 + |C_{010}(0)|^2 = 1,$$

the constants in Eq. (5.43) are

$$\begin{aligned} A &= \frac{C_{100}(0)\frac{|R_{bm}|^2}{|R_{a0}|^2} - C_{010}(0)\frac{R_{bm}}{R_{a0}}}{1+\frac{|R_{bm}|^2}{|R_{a0}|^2}}, \\ B &= \frac{1}{2}\left(\frac{C_{100}(0) + C_{010}(0)\frac{R_{bm}}{R_{a0}}}{1+\frac{|R_{bm}|^2}{|R_{a0}|^2}} + C_{001}(0)\frac{R^*_{a0}}{\Omega_{R\Sigma}}\right), \\ C &= \frac{1}{2}\left(\frac{C_{100}(0) + C_{010}(0)\frac{R_{bm}}{R_{a0}}}{1+\frac{|R_{bm}|^2}{|R_{a0}|^2}} - C_{001}(0)\frac{R^*_{a0}}{\Omega_{R\Sigma}}\right). \end{aligned} \tag{5.45}$$

Let's consider some examples of the initial conditions to illustrate this solution.

5.3.1 An atom is excited; both modes are in the vacuum state:

The initial state vector is $\Psi(0) = |0_a\rangle\,|0_b\rangle\,|1\rangle$. In this case Eq. (5.45) gives $A = 0, B = -C = \frac{R^*_{a0}}{2\Omega_{R\Sigma}}$. The full expression for the state vector at any moment of time becomes

$$\begin{aligned} \Psi \;=\; & e^{-i\int_0^t \omega_{001}(\tau)d\tau}\cos\left(\Omega_{R\Sigma}t\right)|0_a\rangle\,|0_b\rangle\,|1\rangle - i\frac{R^*_{a0}}{\Omega_{R\Sigma}}e^{-i\int_0^t \omega_{100}(\tau)d\tau}\sin\left(\Omega_{R\Sigma}t\right)|1_a\rangle\,|0_b\rangle\,|0\rangle \\ & -i\frac{R^*_{bm}}{\Omega_{R\Sigma}}e^{-i\int_0^t \omega_{010}(\tau)d\tau}\sin\left(\Omega_{R\Sigma}t\right)|0_a\rangle\,|1_b\rangle\,|0\rangle\,, \end{aligned} \tag{5.46}$$

where

$$\omega_{001}(t) = \frac{1}{2}\omega_a(t) + \frac{1}{2}\omega_b(t) + \frac{W}{\hbar},\;\; \omega_{100}(t) = \frac{3}{2}\omega_a(t) + \frac{1}{2}\omega_b(t)\,,\quad \omega_{010}(t) = \frac{1}{2}\omega_a(t) + \frac{3}{2}\omega_b(t)\,.$$

As we see, an initial atomic excitation decays into a pair of electromagnetic modes. Their frequencies are modulated due to the modulation of the cavity geometry and are split by the cumulative Rabi frequency. In the absence of dissipation the excitation energy oscillates back and forth between an atom and the field modes at the cumulative Rabi frequency.

5.3.2 Both cavity modes are excited; the atom is in the ground state:

The initial state vector is $\Psi(0) = C_{100}(0)\left|1_a\right\rangle\left|0_b\right\rangle\left|0\right\rangle + C_{010}(0)\left|0_a\right\rangle\left|1_b\right\rangle\left|0\right\rangle$. In this case the state vector is

$$\begin{aligned}\Psi &= -2iB\frac{\Omega_{R\Sigma}}{R_{a0}^*}e^{-i\int_0^t\omega_{001}(\tau)d\tau}\sin\left(\Omega_{R\Sigma}t\right)\left|0_a\right\rangle\left|0_b\right\rangle\left|1\right\rangle + \left(A+2B\cos\left(\Omega_{R\Sigma}t\right)\right)e^{-i\int_0^t\omega_{100}(\tau)d\tau}\left|1_a\right\rangle\left|0_b\right\rangle\left|0\right\rangle \\ &+\left(2B\frac{R_{bm}^*}{R_{a0}^*}\cos\left(\Omega_{R\Sigma}t\right)-A\frac{R_{a0}}{R_{bm}}\right)e^{-i\int_0^t\omega_{010}(\tau)d\tau}\left|0_a\right\rangle\left|1_b\right\rangle\left|0\right\rangle, \end{aligned} \tag{5.47}$$

where

$$A=\frac{C_{100}(0)\frac{|R_{bm}|^2}{|R_{a0}|^2}-C_{010}(0)\frac{R_{bm}}{R_{a0}}}{1+\frac{|R_{bm}|^2}{|R_{a0}|^2}},\ B=C=\frac{1}{2}\frac{C_{100}(0)+C_{010}(0)\frac{R_{bm}}{R_{a0}}}{1+\frac{|R_{bm}|^2}{|R_{a0}|^2}}. \tag{5.48}$$

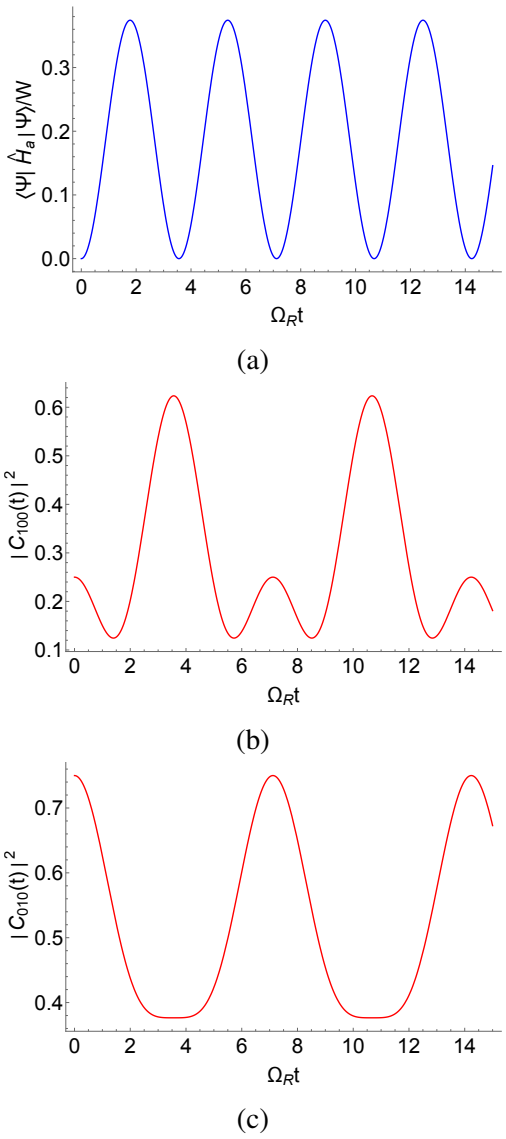

Figure 5.5: (a) The average normalized energy of an atom, (b) the number of quanta in mode a, and (c) the number of quanta in mode b as a function of normalized time. The initial conditions are $C_{000}(0) = 0$, $C_{001}(0) = 0$, $C_{100}(0) = 1/2$, and $C_{001}(0) = \sqrt{3}/2$; i.e., the two modes are initially excited with different amplitudes whereas an atom is in the ground state. Other parameters are $\Delta\omega_a = \Delta\omega_b = \Omega$, $m = 1$, and $\Omega_{Ra} = \Omega_{Rb} = \Omega_R$.

An atom, originally in its ground state, will get excited through resonant coupling to the EM field, as is obvious from Eq. (5.47). The resulting dynamics of the averaged normalized energy of an atom $\langle\Psi|\,\hat{H}_a\,|\Psi\rangle\,/W$ and the numbers of quanta in mode a, $|C_{100}(t)|^2$ and mode b, $|C_{100}(t)|^2$ is shown in Fig. H.1 for one generic set of initial conditions. Due to the presence of three coupled

degrees of freedom, the evolution is more complicated than single-sinusoidal Rabi oscillations. Moreover, there is one particular choice of initial conditions, $C_{010}(0) = -C_{100}(0)\frac{R_{a0}}{R_{bm}}$, which corresponds to $B = C = 0$ and $A = C_{100}(0)$, where the normalization condition gives $|C_{100}(0)|^2 = \left(1 + \frac{|R_{a0}|^2}{|R_{bm}|^2}\right)^{-1}$. This gives the following state vector,

$$\begin{pmatrix} C_{001} \\ C_{100} \\ C_{010} \end{pmatrix} = C_{100}(0) \begin{pmatrix} 0 \\ e^{-i\int_0^t \omega_{100}(\tau)d\tau} \\ -\frac{R_{a0}}{R_{bm}} e^{-i\int_0^t \omega_{010}(\tau)d\tau} \end{pmatrix}. \tag{5.49}$$

It corresponds to the solution in which an atom stays in the ground state and *is not excited by the electromagnetic field despite being in resonance*. It happens because of destructive interference between two frequency-modulated electromagnetic modes. In this case the three quantities shown in Fig. H.1 become constant in time, with the average atomic energy being zero at all times. This effect is discussed in more detail in Sec. 5.5 where the dissipation is taken into account.

5.4 Dynamics of two cavity modes coupled to a time-variable atom

Consider now the situation in which the cavity is not changing with time whereas the transition energy of an atom depends on the parameter p which is adiabatically modulated. For example, it could be an optical transition in a semiconductor nanostructure under an applied time-variable bias. The Hamiltonian of such an atom can be written as $\hat{H} = W(p)\,\hat{\sigma}^\dagger\hat{\sigma}$. The dynamics of an isolated atom conserves the adiabatic invariant $\frac{\langle\Psi|\hat{H}|\Psi\rangle}{\omega(t)}$, where $\omega(t) = \frac{W(p(t))}{\hbar}$.

The dipole moment of the transition is also modulated, $\langle 1|\,\hat{\mathbf{d}}\,|0\rangle = \mathbf{d}(p(t))$, because atom wave functions in the coordinate representation depend on the parameter p. We again consider small enough amplitude of modulation of the transition energy. In this case, using the arguments similar to those in Sec. 5.2.2, we can show that the dependence $\mathbf{d}(t)$ can be neglected; it is the dependence $W(t)$ which is important for the evolution of a coupled atom-field system. The RWA

Hamiltonian which describes such a system is

$$\hat{H} = \hbar\omega_a \left(\hat{a}^\dagger \hat{a} + \frac{1}{2}\right) + \hbar\omega_b \left(\hat{b}^\dagger \hat{b} + \frac{1}{2}\right) + W(t)\,\hat{\sigma}^\dagger \hat{\sigma} - \left[\hat{\sigma}^\dagger \left(\chi_a \hat{a} + \chi_b \hat{b}\right) + \hat{\sigma}\left(\chi_a^* \hat{a}^\dagger + \chi_b^* \hat{b}^\dagger\right)\right]. \tag{5.50}$$

Consider again a sinusoidal modulation of the transition energy,

$$W(t) = \bar{W} - \hbar \Delta\omega \sin(\Omega t), \tag{5.51}$$

where $\frac{\bar{W}}{\hbar} \gg \Delta\omega$.

The Schrödinger equation with this Hamiltonian allows analytic solutions. For simplicity, we again consider the basis states with lowest energies: $|0_a\rangle |0_b\rangle |0\rangle$, $|0_a\rangle |0_b\rangle |1\rangle$, $|1_a\rangle |0_b\rangle |0\rangle$, and $|0_a\rangle |1_b\rangle |0\rangle$. The corresponding wave function is

$$\Psi = C_{000} |0_a\rangle |0_b\rangle |0\rangle + C_{001} |0_a\rangle |0_b\rangle |1\rangle + C_{100} |1_a\rangle |0_b\rangle |0\rangle + C_{010} |0_a\rangle |1_b\rangle |0\rangle, \tag{5.52}$$

where the coefficients obey the equations

$$\dot{C}_{000} + i\frac{\omega_a + \omega_b}{2} C_{000} = 0; \tag{5.53}$$

$$\dot{C}_{001} + i\left(\frac{1}{2}\omega_a + \frac{1}{2}\omega_b + \frac{W(t)}{\hbar}\right) C_{001} - i\Omega_{Ra} C_{100} - i\Omega_{Rb} C_{010} = 0, \tag{5.54}$$

$$\dot{C}_{100} + i\left(\frac{3}{2}\omega_a + \frac{1}{2}\omega_b\right) C_{100} - i\Omega_{Ra}^* C_{001} = 0, \tag{5.55}$$

$$\dot{C}_{010} + i\left(\frac{1}{2}\omega_a + \frac{3}{2}\omega_b\right) C_{010} - i\Omega_{Rb}^* C_{001} = 0. \tag{5.56}$$

After the substitution

$$\begin{pmatrix} C_{001} \\ C_{100} \\ C_{010} \end{pmatrix} = \begin{pmatrix} G_0 \exp\left[-i\left(\frac{1}{2}\omega_a + \frac{1}{2}\omega_b\right) t + \int_0^t \frac{W(\tau)}{\hbar} d\tau\right] \\ G_a \exp\left[-i\left(\frac{3}{2}\omega_a + \frac{1}{2}\omega_b\right) t\right] \\ G_b \exp\left[-i\left(\frac{1}{2}\omega_a + \frac{3}{2}\omega_b\right) t\right] \end{pmatrix}, \tag{5.57}$$

we obtain

$$\dot{G}_0 - i\Omega_{Ra}G_a \exp\left[-i\left(\omega_a t - \int_0^t \frac{W(\tau)}{\hbar}d\tau\right)\right] - i\Omega_{Rb}G_b \exp\left[-i\left(\omega_b t - \int_0^t \frac{W(\tau)}{\hbar}d\tau\right)\right] = 0, \tag{5.58}$$

$$\dot{G}_a - i\Omega_{Ra}^* G_0 \exp\left[-i\left(\omega_a t - \int_0^t \frac{W(\tau)}{\hbar}d\tau\right)\right] = 0, \tag{5.59}$$

$$\dot{G}_b - i\Omega_{Rb}^* G_0 \exp\left[-i\left(\omega_b t - \int_0^t \frac{W(\tau)}{\hbar}d\tau\right)\right] = 0, \tag{5.60}$$

Similarly to the previous section, we expand the exponents in Eqs. (5.58)-(5.60) over the harmonics of the modulation frequency Ω using Eq. (5.39) and keep only the resonant terms, assuming for definiteness that $\omega_a = \frac{\bar{W}}{\hbar}$ and $\omega_b + m\Omega = \frac{\bar{W}}{\hbar}$. We again obtain Eq. (5.37), where $R_{a0} = \Omega_{Ra}J_0\left(\frac{\Delta\omega}{\Omega}\right)$, $R_{bm} = (-i)^{|m|}\Omega_{Rb}J_{|m|}\left(\frac{\Delta\omega}{\Omega}\right)$. Therefore, the modulation of the atomic transition and the cavity parameters leads to a similar dynamics.

5.5 Dynamics of open time-dependent cavity QED systems.

5.5.1 The stochastic evolution of the state vector

Consider again the dynamics of two adiabatically varying cavity modes coupled to an atom, but this time we include the processes of relaxation and decoherence in an open system, which is (weakly) coupled to a dissipative reservoir. We will use the approach based on the stochastic evolution of the state vector; see Appendix J and [154]. This is basically the Schrödinger equation modified by adding a linear relaxation operator and the noise source term with appropriate correlation properties. The latter are related to the parameters of the relaxation operator, which is a manifestation of the fluctuation-dissipation theorem [174]. In Appendix J we outlined the main properties of the stochastic equation of evolution and showed how physically reasonable constraints on the observables determine the properties of the noise sources. We also demonstrated the relationship between our approach and the Lindblad method of solving the master equation.

Within our approach the system is described by a state vector which has a fluctuating component: $|\Psi\rangle = \overline{|\Psi\rangle} + \widetilde{|\Psi\rangle}$, where the straight bar means averaging over the statistics of noise and

the wavy bar denotes the fluctuating component. This state vector is of course very different from the state vector obtained by solving a standard Schrödinger equation for a closed system. In fact, coupling to a dissipative reservoir leads to the formation of a mixed state, which can be described by a density matrix $\hat{\rho} = \overline{|\Psi\rangle} \cdot \overline{\langle\Psi|} + \overline{\widetilde{|\Psi\rangle}\widetilde{\langle\Psi|}}$. However, the density matrix equations are more cumbersome for the analytic solution as compared to the formalism used in this paper.

One can view the stochastic equation approach as a convenient formalism for calculating physical observables which allows one to obtain analytic solutions for the evolution of a coupled system in the presence of dissipation and decoherence. When the Markov approximation is applied, the results are equivalent to those obtained within the Lindblad master equation formalism. Within the Markov approximation, the relaxation operator in the stochastic equation for the state vector is obtained simply by summing up partial Lindbladians for all subsystems, whatever they are (in our case these are a fermion emitter and two EM cavity modes). Then the noise source term is determined unambiguously by conservation of the norm of the state vector and the requirement that the system should approach thermal equilibrium when the external perturbation is turned off. This immediately gives Eqs. (5.61)-(5.64) below.

Following the derivation in Appendix J, equations (5.29)-(5.32) are modified due to the terms with relaxation constants γ_{000},γ_{001},γ_{010}, and γ_{100} which are originated from the Lindladians, and the noise sources,

$$\left(\frac{\partial}{\partial t} + \gamma_{000}\right) C_{000} + i\frac{\omega_a(t) + \omega_b(t)}{2} C_{000} = -\frac{i}{\hbar}\mathfrak{R}_{000}; \tag{5.61}$$

$$\left(\frac{\partial}{\partial t} + \gamma_{001}\right) C_{001} + i\left(\frac{1}{2}\omega_a(t) + \frac{1}{2}\omega_b(t) + \frac{W}{\hbar}\right) C_{001} - i\Omega_{Ra} C_{100} - i\Omega_{Rb} C_{010} = -\frac{i}{\hbar}\mathfrak{R}_{001}, \tag{5.62}$$

$$\left(\frac{\partial}{\partial t} + \gamma_{100}\right) C_{100} + i\left(\frac{3}{2}\omega_a(t) + \frac{1}{2}\omega_b(t)\right) C_{100} - i\Omega^*_{Ra} C_{001} = -\frac{i}{\hbar}\mathfrak{R}_{100}, \tag{5.63}$$

$$\left(\frac{\partial}{\partial t} + \gamma_{010}\right) C_{010} + i\left(\frac{1}{2}\omega_a(t) + \frac{3}{2}\omega_b(t)\right) C_{010} - i\Omega^*_{Rb} C_{001} = -\frac{i}{\hbar}\mathfrak{R}_{010}. \tag{5.64}$$

We assume that noise terms in Eq. (5.61)-(5.64) become equal to zero after averaging over the

noise statistics. The averages of the quadratic combinations of noise source terms are nonzero and we assume here that they are delta-correlated in time (the Markov approximation),

$$\overline{\mathfrak{R}_{\beta}^{*}\left(t+\xi\right)\mathfrak{R}_{\alpha}\left(t\right)}=\overline{\mathfrak{R}_{\beta}^{*}\left(t\right)\mathfrak{R}_{\alpha}\left(t+\xi\right)}=\hbar^{2}\delta\left(\xi\right)D_{\alpha\beta}. \tag{5.65}$$

Here the indices α and β span a set of the lowest-energy states $|0_a\rangle\,|0_b\rangle\,|0\rangle$, $|0_a\rangle\,|0_b\rangle\,|1\rangle$, $|1_a\rangle\,|0_b\rangle\,|0\rangle$, and $|0_a\rangle\,|1_b\rangle\,|0\rangle$. Including the noise sources is crucial for consistency of the formalism: it ensures the conservation of the norm of the state vector and leads to a physically meaningful equilibrium state.

Consider the case of zero temperatures for all reservoirs, which means in practice that these temperatures in energy units are much lower than the atomic transition energy and the cavity mode frequencies. In this case the relaxation constants are greatly simplified as compared to the general expressions given in Appendix J,

$$\gamma_{000}=0,\ \gamma_{001}=\frac{\gamma}{2},\ \gamma_{100}=\frac{\mu_a}{2},\ \gamma_{010}=\frac{\mu_b}{2}, \tag{5.66}$$

where γ is the inelastic relaxation rate for an isolated atom, $\mu_{a,b}$ are relaxation rates of the EM modes determined by the cavity Q-factor; these "partial" relaxation constants are determined by couplings to their respective dissipative reservoirs. Appendix J outlines how to include elastic decoherence processes.

In this limit we can drop the noise terms in the right-hand side of all equations for the components of the state vector, except the term $\mathfrak{R}_{000}$ in the equation for C_{000}; see Appendix J. This noise term ensures conservation of the norm,

$$\overline{\left|C_{000}\right|^{2}}+\overline{\left|C_{001}\right|^{2}}+\overline{\left|C_{010}\right|^{2}}+\overline{\left|C_{100}\right|^{2}}=0,$$

if its correlator is given by

$$\overline{\mathfrak{R}_{000}\left(t+\xi\right)\mathfrak{R}_{000}^{*}\left(t\right)}=2\hbar^{2}\delta\left(\xi\right)\left(\gamma_{100}\overline{\left|C_{100}\right|^{2}}+\gamma_{001}\overline{\left|C_{001}\right|^{2}}+\gamma_{010}\overline{\left|C_{010}\right|^{2}}\right).$$

As an example, consider a high-quality cavity and neglect the cavity losses as compared to the atomic decay. In this case, and for a low temperature of an atomic reservoir, Eqs. (5.62)-(5.64) take the form

$$\left(\frac{\partial}{\partial t}+\frac{\gamma}{2}\right)C_{001}+i\left(\frac{1}{2}\omega_{a}\left(t\right)+\frac{1}{2}\omega_{b}\left(t\right)+\frac{W}{\hbar}\right)C_{001}-i\Omega_{Ra}C_{100}-i\Omega_{Rb}C_{010}=0, \tag{5.67}$$

$$\frac{\partial}{\partial t}C_{100}+i\left(\frac{3}{2}\omega_{a}\left(t\right)+\frac{1}{2}\omega_{b}\left(t\right)\right)C_{100}-i\Omega_{Ra}^{*}C_{001}=0, \tag{5.68}$$

$$\frac{\partial}{\partial t}C_{010}+i\left(\frac{1}{2}\omega_{a}\left(t\right)+\frac{3}{2}\omega_{b}\left(t\right)\right)C_{010}-i\Omega_{Rb}^{*}C_{001}=0. \tag{5.69}$$

Using the substitution of variables in Eq. (5.33) and repeating the same derivation as in Sec. 5.3, we arrive at

$$\frac{d}{dt}\begin{pmatrix}G_{0}\\G_{a}\\G_{b}\end{pmatrix}+\begin{pmatrix}\frac{\gamma}{2} & -iR_{a0} & -iR_{bm}\\-iR_{a0}^{*} & 0 & 0\\-iR_{bm}^{*} & 0 & 0\end{pmatrix}\begin{pmatrix}G_{0}\\G_{a}\\G_{b}\end{pmatrix}=0. \tag{5.70}$$

Its solution is determined by the eigenvalues and eigenvectors of the matrix in Eq. (5.70). The eigenvalues are given by

$$\Gamma\left[\left(\Gamma-\frac{\gamma}{2}\right)\Gamma+\Omega_{R\Sigma}^{2}\right]=0,$$

which yields

$$\Gamma_{0}=0,\ \Gamma_{1,2}=\frac{\gamma}{4}\pm i\sqrt{\Omega_{R\Sigma}^{2}-\frac{\gamma^{2}}{16}}. \tag{5.71}$$

The eigenvector corresponding to the eigenvalue $\Gamma_{0}=0$ is the same as in the absence of dissipation (see Sec. 5.3.2), whereas the expressions for the eigenvectors corresponding to eigenvalues $\Gamma_{1,2}$ can be obtained from "dissipationless" expressions by replacing $\pm\,\Omega_{R\Sigma}\longrightarrow\pm\sqrt{\Omega_{R\Sigma}^{2}-\frac{\gamma^{2}}{16}}-i\frac{\gamma}{4}$. As

a result, we obtain the following expression for the state vector,

$$\begin{pmatrix} C_{001} \\ C_{100} \\ C_{010} \end{pmatrix} = A \begin{pmatrix} 0 \\ e^{-i\int_0^t \omega_{100}(\tau)d\tau} \\ -\frac{R_{a0}}{R_{bm}} e^{-i\int_0^t \omega_{010}(\tau)d\tau} \end{pmatrix} + Be^{\left(-i\sqrt{\Omega_{R\Sigma}^2-\frac{\gamma^2}{16}}-\frac{\gamma}{4}\right)t} \begin{pmatrix} \frac{\sqrt{\Omega_{R\Sigma}^2-\frac{\gamma^2}{16}}-i\frac{\gamma}{4}}{R_{a0}^*} e^{-i\int_0^t \omega_{001}(\tau)d\tau} \\ e^{-i\int_0^t \omega_{100}(\tau)d\tau} \\ \frac{R_{bm}^*}{R_{a0}^*} e^{-i\int_0^t \omega_{010}(\tau)d\tau} \end{pmatrix} + Ce^{\left(i\sqrt{\Omega_{R\Sigma}^2-\frac{\gamma^2}{16}}-\frac{\gamma}{4}\right)t} \begin{pmatrix} \frac{-\sqrt{\Omega_{R\Sigma}^2-\frac{\gamma^2}{16}}-i\frac{\gamma}{4}}{R_{a0}^*} e^{-i\int_0^t \omega_{001}(\tau)d\tau} \\ e^{-i\int_0^t \omega_{100}(\tau)d\tau} \\ \frac{R_{bm}^*}{R_{a0}^*} e^{-i\int_0^t \omega_{010}(\tau)d\tau} \end{pmatrix}. \quad (5.72)$$

Where the constants A, B and C are given by initial conditions. In the limit $\Omega_{R\Sigma} \gg \gamma$ their dependence on the initial values $C_{100}(0)$, $C_{010}(0)$, and $C_{001}(0)$ is given by Eqs. (5.45) from the previous section, whereas their dependence on $C_{000}(0)$ is determined by the normalization condition.

5.5.2 Modulation-induced transparency

Note again the existence of the solution with $B = C = 0$ in which an atom initially in the ground state *is decoupled from the electromagnetic field* and stays in the ground state because of destructive interference between the EM modes. There is however an interesting difference as compared to the dissipationless case discussed in Sec. 5.3. For arbitrary initial conditions, when A, B, C are not equal to zero, part of the field energy will be resonantly transferred to the atom and dissipate through the atomic decay. However, the terms with B and C factors in Eq. (5.72) decay exponentially with time, and the solution to Eq. (5.72) at $t \gg 1/\gamma$ will acquire the same form as in the case of $B = C = 0$:

$$\Psi = A\left(e^{-i\int_0^t \omega_{100}(\tau)d\tau} |1_a\rangle |0_b\rangle |0\rangle - \frac{R_{a0}}{R_{bm}} e^{-i\int_0^t \omega_{010}(\tau)d\tau} |0_a\rangle |1_b\rangle |0\rangle\right) + C_{000} |0_a\rangle |0_b\rangle |0\rangle . \quad (5.73)$$

The value of C_{000} at $t \gg 1/\gamma$ is determined by the noise term $-\frac{i}{\hbar}\mathfrak{R}_{000}$ in the right-hand side of Eq. (5.61) and satisfies $\overline{C_{000}} = 0$, $\overline{|C_{000}|^2} = 1 - |A|^2 \left[1 + \frac{|R_{a0}|^2}{|R_{bm}|^2}\right]$ (see Appendix J).

The value of $|A|^2$ is given by

$$|A|^2 = \frac{1 - |C_{000}(0)|^2 - |C_{001}(0)|^2}{1 + |Z|^2} \left[\frac{\left|\frac{|R_{bm}|^2}{|R_{a0}|^2} - Z\frac{R_{bm}}{R_{a0}}\right|^2}{\left(1 + \frac{|R_{bm}|^2}{|R_{a0}|^2}\right)^2}\right], \tag{5.74}$$

where $Z = \dfrac{C_{010}(0)}{C_{100}(0)}$. The value of $|A|^2$ reaches a maximum when $\mathrm{Arg}[Z] = \pi - \mathrm{Arg}\left[\frac{R_{bm}}{R_{a0}}\right]$ and $|Z| = \left|\frac{R_{a0}}{R_{bm}}\right|$, which corresponds to $C_{010}(0) = -C_{100}(0)\frac{R_{a0}}{R_{bm}}$ and

$$|A|^2 = \frac{1 - |C_{000}(0)|^2 - |C_{001}(0)|^2}{1 + \frac{|R_{a0}|^2}{|R_{bm}|^2}}. \tag{5.75}$$

This equation has a simple interpretation. According to Eq. (5.73), the average steady-state number of quanta in both modes is

$$|C_{100}|^2 + |C_{010}|^2 = |A|^2 \left(1 + \frac{|R_{a0}|^2}{|R_{bm}|^2}\right). \tag{5.76}$$

Comparing Eq. (5.76) and Eq. (G.2), one can see that despite the presence of dissipation, when the value of $|A|^2$ reaches a maximum given by Eq. (G.2) the average steady-state number of field quanta given by Eq. (5.76) is equal to its initial value: $|C_{100}(0)|^2 + |C_{010}(0)|^2 = 1 - |C_{000}(0)|^2 - |C_{001}(0)|^2$.

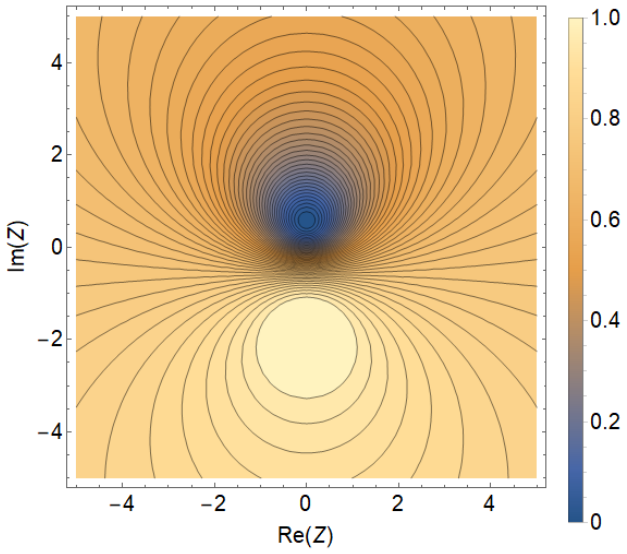

Figure 5.6: The contour plot of the normalized average number of quanta $\overline{N_q}$ on the complex Z plane for $m = 1$, $\Omega_{Ra} = \Omega_{Rb}$ and $\Delta\omega_a = \Delta\omega_b = \Omega$.

The contour plot of the average steady-state number of quanta normalized by its initial value,

$$\overline{N_q} = \frac{|A|^2 \left(1 + \frac{|R_{a0}|^2}{|R_{bm}|^2}\right)}{|C_{100}(0)|^2 + |C_{010}(0)|^2}$$

on the complex Z plane is shown in Fig. 5.6 for $m = 1$, $\Omega_{Ra} = \Omega_{Rb}$ and $\Delta\omega_a = \Delta\omega_b = \Omega$. For this particular choice of parameters, the maximum of the number of quanta is reached at $\mathrm{Arg}[Z] = -\pi/2$, i.e., it is located on the imaginary axis as shown in the figure. For $m = 2$ the maximum will be on the real axis. At its maximum, the average number of quanta is equal to its initial value, i.e. it remains constant.

For any initial conditions other than those corresponding to the maximum of $\overline{N_q}$, a part of the EM field energy will dissipate through interaction with an atom, and eventually only the part which corresponds to the combination of modes completely decoupled from an atom due to destructive interference survives. This will result in smaller values of $\overline{N_q}$. Of course, eventually the finite cavity losses will kick in and the field will dissipate to the level of quantum and thermal fluctuations.

Finally, for the initial state $\Psi(0) = |0_a\rangle |0_b\rangle |1\rangle$ (only the atom is excited) we have $A = 0$, i.e. the system goes into the ground state as expected.

To summarize, the modulated system of an atom resonantly coupled to two EM cavity modes demonstrates an interesting effect of modulation-induced transparency. In the absence of modulation, the presence of an atom experiencing an incoherent decay leads to the dissipation of the EM field even if the empty cavity is ideal, i.e. has zero losses. However, low-frequency modulation of the cavity or of the transition frequency of an atom creates the EM field distribution which is completely decoupled from an atom due to destructive interference between the cavity modes, even at resonance between the atomic transition and the cavity mode frequencies. Therefore, the atom will remain in the ground state and the field will experience no dissipation in the absence of cavity losses. For a classical field, such a destructive interference effect which switches off the field dissipation in resonant medium by introducing low-frequency modulation was considered, in particular, in Ref. [175] for acoustically modulated two-level atoms. Similar effects in the interaction of classical fields with atoms are discussed in the introduction of Ref. [176].

5.5.3 Prospects for strong coupling and quantum entanglement in various nanophotonic systems

Expressions in this section and more general expressions for the relaxation rates in Appendix J (see, e.g., Eqs. (J.28),(J.29)) allow one to calculate the effective decoherence rates from the known "partial" relaxation rates for individual subsystems: EM cavity modes and any kind of a fermionic qubit. One can compare the decoherence rates with characteristic Rabi frequencies which enter the solution for the evolution equations such as Eqs. (5.67)-(5.69) in order to determine if the strong coupling regime and quantum entanglement in the electron-photon system can be achieved. For any specific application, one should also compare the effective relaxation times with relevant operation times (gate transition time, read/write time etc.) In the discussion below, we rely on the parameters obtained from Refs. [132]-[148] which we already cited in the Introduction. Many of them are recent reviews and one can find further references there. We don't attempt to overview here the vast and rapidly growing amount of literature on the subject.

In electron-based quantum emitters the largest oscillator strengths in the visible/near-infrared range have been observed for excitons in organic molecules, followed by perovskites and more conventional inorganic semiconductor quantum dots. The typical variation of the dipole matrix element of the optical transition which enters the Rabi frequency is from tens of nm to a few Angstrom. The dipole moment grows with increasing wavelength. The relaxation times are strongly temperature and material quality-dependent, varying from tens or hundreds of ps for single quantum dots at 4 K to the μs range for defects in semiconductors and diamond at mK temperatures. At room temperature the typical decoherence rates for the optical transition are in the ~ 10 meV range.

The photon decay times are longest for dielectric micro- and nano-cavities: photonic crystal cavities, nanopillars, distributed Bragg reflector mirrors, microdisk whispering gallery mode cavities, etc. Their quality factors are typically between $10^3 - 10^7$, corresponding to photon lifetimes from sub-ns to μs range. However, the field localization in the dielectric cavities is diffraction-limited, which limits the attainable Rabi frequency values to hundreds of μeV. The effective decoherence rate in dielectric cavity QED systems is typically limited by the relaxation in the fermion quantum emitter subsystem,

In plasmonic cavities, field localization on a nm and even sub-nm scale has been achieved, but the photon losses are in the ps or even fs range and therefore, they dominate the overall decoherence rate. Still, when it comes to strong coupling at room temperature to a single quantum emitter such as a single molecule or a quantum dot, the approach utilizing plasmonic cavities has seen more success so far. In these systems the Rabi splitting of the order of 100-200 meV has been observed. In plasmonic systems it may be beneficial to consider longer-wavelength emitters with the optical transition at the mid-infrared and even terahertz wavelengths. Indeed, with increasing wavelength the plasmon losses go down, the matrix element of a dipole-allowed transition increases, whereas the plasmon localization stays largely the same.

Another factor that has to be taken into account when choosing a nanophotonic system for a specific application is the rate with which the modulation of the cavity or emitter parameters has

to be performed. For example, if the modulation at the rate comparable to the Rabi frequency or operation with π- or $\pi/2$ pulses is required, the plasmonic-based systems run into a problem: they would require $\sim 10-100$ fs pulses for modulation, which obviously can be achieved only with fs lasers. All electronic operations typically have a cutoff at tens of GHz. Finally, any function related to quantum computing requires at least 99.99% fidelity, i.e. at least 10^4 "flops" before decoherence kicks in.

5.6 Conclusions

In conclusion, we developed the analytic theory describing the dynamics and control of strongly coupled nanophotonic systems with time-variable parameters. The coupling of the fermion and photon subsystems to their dissipative reservoirs and the elastic decoherence processes are included within the stochastic equation of evolution approach, which is equivalent to the Lindblad approximation in the master equation formalism. Our analytic solution is valid in the approximation that the rate of parameter modulation and the amplitude of the frequency modulation are much smaller than the optical transition frequencies. At the same time, they can be arbitrary with respect to the generalized Rabi oscillations frequency which determines the coherent dynamics. Therefore, we can describe an arbitrary modulation of the parameters, both slower and faster than the Rabi frequency, for complete control of the quantum state. For example, one can turn on and off the entanglement between the fermionic and photonic degrees of freedom, swap between the quantum states, or decouple the fermionic qubit from the cavity field via modulation-induced transparency.

6. SUMMARY AND CONCLUSIONS

In this dissertation, we used both semiclassical and fully quantum mechanical theory to study optics of Dirac materials, including the optical properties and strong anisotropy and gyrotropy of bulk and surface polaritons in type-I magnetic Weyl semimetals, and inverse Faraday effect in graphene and Weyl semimetals. We also used the time-dependent Jaynes-Cummings model with a systematic analytic approach we developed to study the dynamics and control of strongly coupled nanophotonic systems with time-variable parameters.

We presented systematic studies of the optical properties and electromagnetic modes of Weyl semimetals in the minimal two-band model with two separated Weyl nodes. Both bulk and surface conductivity tensors are derived from a single microscopic Hamiltonian. The presence of separated Weyl nodes and associated surface states gives rise to distinct signatures in the transmission, reflection, and polarization of bulk and surface electromagnetic waves. These signatures can be used for the quantitative characterization of the electronic structure of Weyl semimetals. Particularly sensitive spectroscopic probes of bulk electronic properties include strong anisotropy in the propagation of both bulk and surface modes, birefringent dispersion and absorption spectra of ordinary and extraordinary normal modes, the frequency of bulk plasmon resonance as a function of incidence angle and doping level, and the polarization rotation and ellipticity for incident linearly polarized light. The sensitive characterization of surface electronic states can be achieved by measuring the phase change of incident plane waves' reflection coefficient, the frequency dispersion of surface plasmon-polariton modes, and strong anisotropy of surface plasmon-polaritons with respect to their propagation direction and polarization.

We showed that spectroscopy of surface polaritons could be a powerful diagnostics of topological electron states in WSMs. Strong anisotropy, gyrotropy, and the optical Hall effect for surface polaritons launched by a nanotip provide information about Weyl node position and separation, the value of the Fermi momentum, and the matrix elements of the optical transitions involving both bulk and surface electron states.

We investigated the inverse Faraday effect in materials with massless Dirac fermions, both in 2D, graphene, and 3D, such as Weyl semimetals. Both semiclassical and quantum theories were presented. The dissipation, finite size, and strong field effects were analyzed in the quasiclassical approximation. We found that the IFE magnitude can be significantly enhanced in Dirac materials compared to conventional semiconductors. This makes Dirac materials promising for the optical control of magnetization, all-optical modulation, and optical isolation in compact optoelectronic devices.

We developed the analytic theory describing the dynamics and control of strongly coupled nanophotonic systems with time-variable parameters. The coupling of the fermion and photon subsystems to their dissipative reservoirs is included within the stochastic equation of evolution approach, equivalent to the Lindblad approximation in the master equation formalism. Our analytic solution is valid in the approximation that the rate of parameter modulation and the amplitude of the frequency modulation are much smaller than the optical transition frequencies. Simultaneously, they can be arbitrary with respect to the generalized Rabi oscillations frequency, which determines the coherent dynamics. Therefore, we can describe an arbitrary modulation of the parameters, both slower and faster than the Rabi frequency, for complete control of the quantum state. For example, one can turn on and off the entanglement between the fermionic and bosonic degrees of freedom, swap between the quantum states, or decouple the fermionic qubit from the optical field via modulation-induced transparency.

REFERENCES

[1] P. A. M. Dirac, "The quantum theory of the electron," *Proc. R. Soc. Lond. Ser. A*, vol. 117, p. 610, 1928.

[2] A. H. C. Neto, F. Guinea, N. M. R. Peres, K. S. Novoselov, and A. K. Geim, "The electronic properties of graphene," *Rev. Mod. Phys.*, vol. 81, p. 109, 2009.

[3] M. I. Katsnelson, *Graphene: Carbon in Two Dimensions*. Cambridge University Press, 2012.

[4] M. Z. Hasan and C. L. Kane, "Colloquium: Topological insulators," *Rev. Mod. Phys.*, vol. 82, p. 3045, 2010.

[5] X. L. Qi and S. C. Zhang, "Topological insulators and superconductors," *Rev. Mod. Phys.*, vol. 83, p. 1057, 2011.

[6] M. Z. Hasan, S. Y. Xu, I. Belopolski, and S. M. Huang, "Discovery of weyl fermion semimetals and topological fermi arc states," *Annu. Rev. Condens. Matter Phys.*, vol. 8, p. 289, 2017.

[7] N. P. Armitage, E. J. Mele, and A. Vishwanath, "Weyl and dirac semimetals in three-dimensional solids," *Rev. Mod. Phys.*, vol. 90, no. 015001, 2018.

[8] A. K. Geim, "Nobel lecture: Random walk to graphene," *Rev. Mod. Phys.*, vol. 83, p. 851, 2011.

[9] K. S. Novoselov, "Nobel lecture: Graphene: Materials in the flatland," *Rev. Mod. Phys.*, vol. 83, p. 837, 2011.

[10] M. I. Katsnelson, "Nonlinear screening of charge impurities in graphene," *Phys. Rev. B*, vol. 74, no. 201401, 2006.

[11] K. S. Novoselov, A. K. Geim, S. V. Morozov, D. Jiang, M. I. Katsnelson, S. V. D. I. V. Grigorieva, and A. A. Firsov, "Two-dimensional gas of massless dirac fermions in graphene," *Nature*, vol. 438, p. 197, 2005.

[12] Y. Zhang, Y. Tan, H. L. Stormer, and P. Kim, "Experimental observation of the quantum hall effect and berry's phase in graphene," *Nature*, vol. 438, p. 201, 2005.

[13] K. S. Novoselov, Z. Jiang, S. V. M. Y. Zhang, H. L. Stormer, J. C. M. U. Zeitler, G. S. Boebinger, P. Kim, and A. K. Geim, "Room-temperature quantum hall effect in graphene," *Science*, vol. 315, p. 1379, 2007.

[14] K. S. Novoselov, A. K. Geim, S. V. Morozov, D. Jiang, Y. Zhang, S. V. Dubonos, I. V. Grigorieva, and A. A. Firsov, "Electric field effect in atomically thin carbon films," *Science*, vol. 306, p. 666, 2004.

[15] A. K. Geim and K. S. Novoselov, "The rise of graphene," *Nature Mater.*, vol. 6, p. 183, 2007.

[16] R. R. Nair, P. Blake, A. N. Grigorenko, K. S. Novoselov, T. J. Booth1, T. Stauber, N. M. R. Peres, and A. K. Geim, "Fine structure constant defines visual transparency of graphene," *Science*, vol. 320, p. 1308, 2008.

[17] C. H. Lui, K. F. Mak, J. Shan, and T. F. Heinz, "Ultrafast photoluminescence from graphene," *Phys. Rev. Lett.*, vol. 105, no. 127404, 2010.

[18] T. Hasan, Z. Sun, F. Wang, F. Bonaccorso, P. H. Tan, A. G. Rozhin, and A. C. Ferrari, "Nanotube-polymer composites for ultrafast photonics," *Adv. Mater.*, vol. 21, p. 3874, 2009.

[19] F. Bonaccorso, Z. Sun, T. Hasan, and A. C. Ferrari, "Graphene photonics and optoelectronics," *Nat. Photonics*, vol. 4, p. 611, 2010.

[20] S. Bae, H. Kim, Y. Lee, X. Xu, J. Park, Y. Zheng, J. Balakrishnan, a. H. K. T. Lei, Y. Song, Y. Kim, K. Kim, B. Ozyilmaz, J. Ahn, B. Hong, and S. Iijima, "Roll-to-roll production of 30-inch graphene films for transparent electrodes," *Nature Nanotech.*, vol. 5, p. 574, 2010.

[21] F. Xia, T. Mueller, Y. Lin, A. Valdes-Garcia, and P. Avouris, "Ultrafast graphene photodetector," *Nature Nanotech.*, vol. 4, p. 839, 2009.

[22] M. Mecklenburg and B. Regan, "Spin and the honeycomb lattice: Lessons from graphene," *Phys. Rev. Lett.*, vol. 106, no. 116803, 2011.

[23] L. D. Landau and E. M. Lifshits, *Quantum Mechanics: Nonrelativistic Theory, 3rd ed*. Pergamon, 1977.

[24] J. W. McClure, "Diamagnetism of graphite," *Phys. Rev.*, vol. 104, p. 666, 1956.

[25] Z. Jiang, E. A. Henriksen, L. C. Tung, Y. Wang, M. E. Schwartz, P. K. M. Y. Han, and H. L. Stormer, "Infrared spectroscopy of landau levels of graphene," *Phys. Rev. Lett.*, vol. 98, no. 197403, 2007.

[26] W. K. Tse and A. H. MacDonald, "Magneto-optical and magnetoelectric effects of topological insulators in quantizing magnetic fields," *Phys. Rev. B*, vol. 82, no. 161104(R), 2010.

[27] X. Wan, A. M. Turner, A. Vishwanath, and S. Y. Savrasov, "Topological semimetal and fermi-arc surface states in the electronic structure of pyrochlore iridates," *Phys. Rev. B*, vol. 83, no. 205101, 2011.

[28] A.Turner and A.Vishwanath, "Beyond band insulators: Topology of semi-metals and interacting phases," *arXiv:1301.0330*, 2013.

[29] H. Nielsen and M. Ninomiya, "Absence of neutrinos on a lattice: (i). proof by homotopy theory," *Nucl. Phys. B*, vol. 185, p. 20, 1981.

[30] H. Nielsen and M. Ninomiya, "A no-go theorem for regularizing chiral fermions," *Nucl. Phys. B*, vol. 105, p. 219, 1981.

[31] S. Murakami, "Phase transition between the quantum spin hall and insulator phases in 3d: emergence of a topological gapless phase," *New J. Phys.*, vol. 9, no. 356, 2007.

[32] E. T. Jaynes and F. W. Cummings, "Comparison of quantum and semiclassical radiation theories with application to the beam maser," *Proc. IEEE.*, vol. 51(1), p. 89, 1963.

[33] A. D. Greentree, J. Koch, and J. Larson, "Correlator expansion approach to stationary states of weakly coupled cavity arrays," *Journal of Physics B*, vol. 46, no. 22, 2013.

[34] G. E. Volovik, *Quantum Phase Transitions from Topology in Momentum Space, in Quantum Analogues: From Phase Transitions to Black Holes and Cosmology, Lecture Notes in Physics, Vol. 718, edited by W. Unruh and R. Schutzhold*. Springer, 2007.

[35] P. Hosur and X. Qi, "Recent developments in transport phenomena in weyl semimetals," *Compt. Rend. Phys.*, vol. 14, p. 857, 2013.

[36] B. Yan and C. Felser, "Topological materials: Weyl semimetals," *Annu. Rev. Condens. Matter Phys.*, vol. 8, p. 337, 2017.

[37] A. A. Burkov, "Weyl metals," *Rev. Condens. Matter Phys.*, vol. 9, p. 359, 2018.

[38] O. V. Kotov and Y. E. Lozovik, "Giant tunable nonreciprocity of light in weyl semimetals," *Phys. Rev. B*, vol. 98, no. 195446, 2018.

[39] A. B. Sushkov, J. B. Hofmann, G. S. Jenkins, J. Ishikawa, S. Nakatsuji, S. D. Sarma, and H. D. Drew, "Optical evidence for a weyl semimetal state in pyrochlore $\mathbf{Eu_2Ir_2O_7}$," *Phys. Rev. B*, vol. 92, no. 241108(R), 2015.

[40] S. A. Yang, H. Pan, and F. Zhang, "Chirality-dependent hall effect in weyl semimetals," *Phys. Rev. Lett.*, vol. 115, no. 156603, 2015.

[41] Q. D. Jiang, H. Jiang, H. Liu, Q. F. Sun, and X. C. Xie, "Topological imbert-fedorov shift in weyl semimetals," *Phys. Rev. Lett.*, vol. 115, no. 156602, 2015.

[42] B. Z. Spivak and A. V. Andreev, "Magnetotransport phenomena related to the chiral anomaly in weyl semimetals," *Phys. Rev. B*, vol. 93, no. 085107, 2016.

[43] J. Zhou, H. Chang, and D. Xiao, "Plasmon mode as a detection of the chiral anomaly in weyl semimetals," *Phys. Rev. B*, vol. 91, no. 035114, 2015.

[44] F. M. D. Pellegrino, M. I. Katsnelson, and M. Polini, "Helicons in weyl semimetals," *Phys. Rev. B*, vol. 92, no. 201407(R), 2015.

[45] C. J. Tabert, J. P. Carbotte, and E. J. Nicol, "Optical and transport properties in three-dimensional dirac and weyl semimetals," *Phys. Rev. B*, vol. 93, no. 085426, 2016.

[46] P. E. C. Ashby and J. P. Carbotte, "Chiral anomaly and optical absorption in weyl semimetals," *Phys. Rev. B*, vol. 89, no. 245121, 2014.

[47] J. Ma and D. A. Pesin, "Chiral magnetic effect and natural optical activity in metals with or without weyl points," *Phys. Rev. B*, vol. 92, no. 235205, 2015.

[48] E. V. Gorbar, V. A. Miransky, I. A. Shovkovy, and P. O. Sukachov, "Fermi-surface transformation across the pseudogap critical point of the cuprate superconductor $\mathbf{La}_{1.6-x}\mathbf{Nd}_{0.4}\mathbf{Sr}_x\mathbf{CuO}_4$," *Phys. Rev. B*, vol. 95, no. 115002, 2017.

[49] P. E. C. Ashby and J. P. Carbotte, "Magneto-optical conductivity of weyl semimetals," *Phys. Rev. B*, vol. 87, no. 245131, 2013.

[50] Z. Long, Y. Wang, M. Erukhimova, M. Tokman, and A. Belyanin, "Magnetopolaritons in weyl semimetals in a strong magnetic field," *Phys. Rev. Lett.*, vol. 120, no. 037403, 2018.

[51] R. Y. Chen, Z. G. Chen, X.-Y. Song, J. A. Schneeloch, G. D. Gu, F. Wang, and N. L. Wang, "Magnetoinfrared spectroscopy of landau levels and zeeman splitting of three-dimensional massless dirac fermions in $\mathbf{ZrTe}_5$," *Phys. Rev. Lett.*, vol. 115, no. 176404, 2015.

[52] C. J. Tabert and J. P. Carbotte, "Optical conductivity of weyl semimetals and signatures of the gapped semimetal phase transition," *Phys. Rev. B*, vol. 93, no. 085442, 2016.

[53] A. A. Zyuzin and A. A. Burkov, "Topological response in weyl semimetals and the chiral anomaly," *Phys. Rev. B*, vol. 86, no. 115133, 2012.

[54] M. Kargarian, M. Randeria, and N. Trivedi, "Theory of kerr and faraday rotations and linear dichroism in topological weyl semimetals," *Sci. Rep.*, vol. 5, no. 12683, 2015.

[55] J. Hofmann and S. D. Sarma, "Plasmon signature in dirac-weyl liquids," *Phys. Rev. B*, vol. 91, no. 241108, 2015.

[56] M. S. Ukhtary, A. R. T. Nugraha, and R. Saito, "Negative refraction in weyl semimetals," *J. Phys. Soc. Jpn.*, vol. 86, no. 104703, 2017.

[57] A. A. Burkov and L. Balents, "Weyl semimetal in a topological insulator multilayer," *Phys. Rev. Lett.*, vol. 107, no. 127205, 2011.

[58] R. Okugawa and S. Murakami, "Dispersion of fermi arcs in weyl semimetals and their evolutions to dirac cones," *Phys. Rev. B*, vol. 89, no. 235315, 2014.

[59] G. M. Andolina, F. M. D. Pellegrino, F. H. L. Koppens, and M. Polini, "Quantum nonlocal theory of topological fermi arc plasmons in weyl semimetals," *Phys. Rev. B*, vol. 97, no. 125431, 2018.

[60] G. Xu, H. Weng, Z. Wang, X. Dai, and Z. Fang, "Chern semimetal and the quantized anomalous hall effect in $\mathbf{HgCr_2Se_4}$," *Phys. Rev. Lett.*, vol. 107, no. 186806, 2011.

[61] E. Liu, Y. Sun, N. Kumar, L. Muechler, A. Sun, L. Jiao, S.-Y. Yang, and D. L. el at., "Giant anomalous hall effect in a ferromagnetic kagome-lattice semimetal," *Nat. Phys.*, vol. 14, no. 1125, 2018.

[62] S.-Y. Xu, I. Belopolski, N. Alidoust, M. Neupane, G. Bian, and C. Z. el at., "Discovery of a weyl fermion semimetal and topological fermi arcs," *Science*, vol. 349, no. 613, 2015.

[63] T. Arikawa, Q. Zhang, L. Ren, A. A. Belyanin, and J. Kono, "Review of anisotropic terahertz material response," *Journ. IR, THz, and MM Waves*, vol. 34, p. 724, 2013.

[64] J. C. W. Song and M. S. Rudner, "Fermi arc plasmons in weyl semimetals," *Phys. Rev. B*, vol. 96, no. 205443, 2017.

[65] W. L. Barnes, A. Dereux, and T. W. Ebbesen, "Surface plasmon subwavelength optics," *Nature*, vol. 424, p. 824, 2003.

[66] J. Homola, S. S. Yee, and G. Gauglitz, "Surface plasmon resonance sensors: review," *Sensors and Actuators B: Chemical*, vol. 54, no. 3, 1999.

[67] Agranovich and D. L. Mills, *Surface Polaritons - Electromagnetic Waves at Surfaces and Interfaces*. North-Holland Publishing Company, 1982.

[68] S. I. Kimura, H. Yokoyama, H. Watanabe, J. Sichelschmidt, V. Suss, M. Schmidt, and C. Felser, "Optical signature of weyl electronic structures in tantalum pnictides **TaPn** (**Pn**=p,as)," *Phys. Rev. B*, vol. 96, no. 075119, 2017.

[69] K. Halterman, M. Alidoust, and A. Zyuzin, "Epsilon-near-zero response and tunable perfect absorption in weyl semimetals," *Phys. Rev. B*, vol. 98, no. 085109, 2018.

[70] H. Rostami and M. Polini, "Nonlinear anomalous photocurrents in weyl semimetals," *Phys. Rev. B*, vol. 97, no. 195151, 2018.

[71] Q. Chen, A. R. Kutayiah, I. Oladyshkin, M.Tokman, and A. Belyanin, "Optical properties and electromagnetic modes of weyl semimetals," *Phys. Rev. B*, vol. 99, no. 075137, 2019.

[72] C. A. C. Garcia, J. Coulter, and P. Narang, "Optoelectronic response of the type-i weyl semimetals taas and nbas from first principles," *Phys. Rev. Research*, vol. 2, no. 013073, 2020.

[73] J. Ma, Q. Gu, Y. Liu, J. Lai, P. Yu, X. Zhuo, Z. Liu, J.-H. Chen, J. Feng, and D. Sun, "Nonlinear photoresponse of type-ii weyl semimetals," *Nat. Mater.*, vol. 18, p. 476, 2019.

[74] J. Moore, "Optical properties of weyl semimetals," *Nat. Sci. Rev.*, vol. 6, p. 206, 2019.

[75] V. Kravtsov, R. Ulbricht, J. M. Atkin, and M. B. Raschke, "Plasmonic nanofocused four-wave mixing for femtosecond near-field imaging," *Nat. Nanotechnol.*, vol. 11, p. 459, 2016.

[76] T. Jiang, V. Kravtsov, M. Tokman, A. Belyanin, and M. B. Raschke, "Ultrafast coherent nonlinear nanooptics and nanoimaging of graphene," *Nat. Nanotechnol.*, vol. 14, p. 838, 2019.

[77] Z. Fei, A. S. Rodin, G. O. Andreev, W. Bao, A. S. McLeod, M. Wagner, L. M. Zhang, Z. Zhao, a. G. D. M. Thiemens, M. M. Fogler, A. H. C. Neto, C. N. Lau, F. Keilmann,

and D. N. Basov, "Gate-tuning of graphene plasmons revealed by infrared nano-imaging," *Nature*, vol. 487, p. 82, 2012.

[78] M. I. Stockman, "Nanofocusing of optical energy in tapered plasmonic waveguides," *Phys. Rev. Lett.*, vol. 93, no. 137404, 2004.

[79] R. Piessens, *in The Transforms and Applications Handbook, 2nd ed., edited by A. D. Poularikas*. CRC, Boca Raton, 2000.

[80] M. Abramowitz and I. A. Stegun, *Handbook of Mathematical Functions: With Formulas, Graphs, and Mathematical Tables, AppliedMathematics Series No. 55*. (National Bureau of Standards, 1972.

[81] A. R. Kutayiah, M. Tokman, Y. Wang, and A. Belyanin, "Difference frequency generation of surface plasmon-polaritons in landau quantized graphene," *Phys. Rev. B*, vol. 98, no. 115410, 2018.

[82] L. D. Landau and E. M. Lifshitz, *Electrodynamics of Continuous Media*. Pergamon, 1984.

[83] L. P. Pitaevskii, "Electric forces in a transparent dispersive medium," *Sov. Phys. JETP*, vol. 12, p. 1008, 1961.

[84] J. P. van der Ziel, P. S. Pershan, and L. D. Malstrom, "Optically-induced magnetization resulting from the inverse faraday effect," *Phys. Rev. Lett.*, vol. 15, p. 190, 1965.

[85] P. S. Pershan, "Nonlinear optical properties of solids: Energy considerations," *Phys. Rev.*, vol. 130, p. 919, 1963.

[86] P. S. Pershan, J. P. van der Ziel, and L. D. Malstrom, "Theoretical discussion of the inverse faraday effect, raman scattering, and related phenomena," *Phys. Rev.*, vol. 143, p. 574, 1966.

[87] V. I. Karpman and A. G. Shagalov, "The ponderomotive force of a high-frequency electromagnetic field in a cold magnetized plasma," *J. Plasma Phys.*, vol. 27, p. 215, 1982.

[88] M. D. Tokman, "Ponderomotive force of a time-varying rf field in a plasma," *Sov. J. Plasma Phys.*, vol. 10, p. 331, 1984.

[89] Y. Horovitz, S. Eliezer, A. Ludmirsky, Z. Henis, E. Moshe, R. Shpitalnik, and B. Arad, "Measurements of inverse faraday effect and absorption of circularly polarized laser light in plasmas," *Phys. Rev. Lett.*, vol. 78, p. 1707, 1997.

[90] Z. Najmudin, M. Tatarakis, A. Pukhov, E. L. Clark, R. J. Clarke, A. E. Dangor, J. Faure, V. Malka, D. Neely, M. I. K. Santala, and K. Krushelnick, "Measurements of the inverse faraday effect from relativistic laser interactions with an underdense plasma," *Phys. Rev. Lett.*, vol. 87, no. 215004, 2001.

[91] N. Nasery, V. Y. Bychenkov, and W. Rozmus, "Self-channelling of relativistic laser pulses in large-scale underdense plasmas," *Phys. Plasmas*, vol. 17, no. 033107, 2010.

[92] R. Hertel, "Theory of the inverse faraday effect in metals," *J. Magn. Magn. Mater.*, vol. 303, p. L1, 2006.

[93] R. Hertel and M. Fahnle, "Macroscopic drift current in the inverse faraday effect," *Phys. Rev. B*, vol. 91, no. 020411(R), 2015.

[94] I. D. Tokman, "The inverse faraday effect in a harmonic "atom" and the generalized kohn's theorem," *Phys. Lett. A*, vol. 252, p. 83, 1999.

[95] C. D. Stanciu, F. Hansteen, A. V. Kimel, A. Tsukamoto, A. Itoh, A. Kirilyuk, and T. Rasing, "Ultrafast interaction of the angular momentum of photons with spins in the metallic amorphous alloy gdfeco," *Phys. Rev. Lett.*, vol. 98, no. 207401, 2007.

[96] K. Vahaplar, A. M. Kalashnikova, A. V. Kimel, S. Gerlach, D. Hinzke, U. Nowak, R. Chantrell, A. Tsukamoto, A. Itoh, A. Kirilyuk, and T. Rasing, "All-optical magnetization reversal by circularly polarized laser pulses: Experiment and multiscale modeling," *Phys. Rev. B*, vol. 85, no. 104402, 2012.

[97] F. Hansteen, A. Kimel, A. Kirilyuk, and T. Rasing, "Nonthermal ultrafast optical control of the magnetization in garnet films," *Phys. Rev. B*, vol. 73, no. 014421, 2006.

[98] A. H. M. Reid, A. V. Kimel, A. Kirilyuk, J. F. Gregg, and T. Rasing, "Optical excitation of a forbidden magnetic resonance mode in a doped lutetium-iron-garnet film via the inverse faraday effect," *Phys. Rev. Lett.*, vol. 105, no. 107402, 2010.

[99] T. Makino, F. Liu, T. Yamasaki, Y. Kozuka, A. T. K. Ueno, T. Fukumura, Y. Kong, and M. Kavasaki, "Ultrafast optical control of magnetization in euo thin films," *Phys. Rev. B*, vol. 86, no. 064403, 2012.

[100] Z. Jin, H. Ma, D. Li, G. Ma, M. Wang, and C. Zhao, "Femtosecond inverse faraday effect in magnetic ionic liquid [bmim]$\mathbf{FeCl}_4$," *J. Appl. Phys.*, vol. 109, no. 073109, 2011.

[101] T. Satoh, S.-J. Cho, R. Iida, T. Shimura, K. Kuroda, H. Ueda, Y. Ueda, B. A. Ivanov, F. Nori, and M. Fiebig, "Spin oscillations in antiferromagnetic nio triggered by circularly polarized light," *Phys. Rev. Lett.*, vol. 105, no. 077402, 2010.

[102] A. H. M. Reid, A. V. Kimel, A. Kirilyuk, J. F. Gregg, and T. Rasing, "Investigation of the femtosecond inverse faraday effect using paramagnetic $\mathbf{Dy}_3\mathbf{Al}_5\mathbf{O}_{12}$," *Phys. Rev. B*, vol. 81, no. 104404, 2010.

[103] A. Kirilyuk, A. V. Kimel, and T. Rasing, "Ultrafast optical manipulation of magnetic order," *Rev. Mod. Phys.*, vol. 82, p. 2731, 2010.

[104] R. Iida, T. Satoh, T. Shimura, K. Kuroda, B. A. Ivanov, Y. Tokunaga, and Y. Tokura, "Spectral dependence of photoinduced spin precession in $\mathbf{DyFeO}_3$," *Phys. Rev. B*, vol. 84, no. 064402, 2011.

[105] M. M. Glazov and S. D. Ganichev, "High frequency electric field induced nonlinear effects in graphene," *Phys. Rep.*, vol. 535, p. 101, 2014.

[106] T. Otsuji, S. A. B. Tombet, A. Satou, M. S. H. Fukidome, E. Sano, V. Popov, M. Ryzhii, and V. Ryzhii, "Graphene-based devices in terahertz science and technology," *J. Phys. D: Appl. Phys.*, vol. 45, no. 303001, 2012.

[107] M. M. Glazov, "Second harmonic generation in graphene," *JETP Lett.*, vol. 93, p. 366, 2011.

[108] S. A. Mikhailov, "Nonperturbative quasiclassical theory of the nonlinear electrodynamic response of graphene," *Phys. Rev. B*, vol. 95, no. 085432, 2017.

[109] M. T. X. Yao and A. Belyanin, "Efficient nonlinear generation of thz plasmons in graphene and topological insulators," *Phys. Rev. Lett.*, vol. 112, no. 055501, 2014.

[110] M. Tokman, Y. Wang, I. Oladyshkin, A. R. Kutayiah, and A. Belyanin, "Laser-driven parametric instability and generation of entangled photon-plasmon states in graphene," *Phys. Rev. B*, vol. 93, no. 235422, 2016.

[111] Y. Wang, M. Tokman, and A. Belyanin, "Second-order nonlinear optical response of graphene," *Phys. Rev. B*, vol. 94, no. 195442, 2016.

[112] J. Cheng, L. N. Vermeulen, and J. E. Sipe, "Second order optical nonlinearity of graphene due to electric quadrupole and magnetic dipole effects," *Sci. Rep.*, vol. 7, no. 43843, 2017.

[113] I. V. Oladyshkin, S. B. Bodrov, Y. A. Sergeev, A. I. Korytin, M. D. Tokman, and A. N. Stepanov, "Optical emission of graphene and electron-hole pair production induced by a strong terahertz field," *Phys. Rev. B*, vol. 96, no. 155401, 2017.

[114] J. J. Dean and H. M. van Driel, "Graphene and few-layer graphite probed by second-harmonic generation: Theory and experiment," *Phys. Rev. B*, vol. 82, no. 125411, 2010.

[115] D. A. Smirnova, I. V. Shadrivov, A. E. Miroshnichenko, A. I. Smirnov, and Y. S. Kivshar, "Second-harmonic generation by a graphene nanoparticle," *Phys. Rev. B*, vol. 90, no. 035412, 2014.

[116] S. A. Mikhailov, "Quantum theory of the third-order nonlinear electrodynamic effects of graphene," *Phys. Rev. B*, vol. 93, no. 085403, 2016.

[117] J. L. Cheng, N. Vermeulen, and J. E. Sipe, "Third order optical nonlinearity of graphene," *New J. Phys.*, vol. 16, no. 053014, 2014.

[118] M. Tokman, S. B. Bodrov, Y. A. Sergeev, A. I. Korytin, I. Oladyshkin, Y. Wang, A. Belyanin, and A. N. Stepanov, "Second harmonic generation in graphene dressed by a strong terahertz field," *Phys. Rev. B*, vol. 99, no. 155411, 2019.

[119] M. Tokman, X. Yao, and A. Belyanin, "Generation of entangled photons in graphene in a strong magnetic field," *Phys. Rev. Lett.*, vol. 110, no. 077404, 2013.

[120] S. A. Mikhailov, "Nonlinear cyclotron resonance of a massless quasiparticle in graphene," *Phys. Rev. B*, vol. 79, no. 241309(R), 2009.

[121] M. A. E. M. D. Tokman and A. Belyanin, "Nonlinear cyclotron acceleration of massless dirac charge carriers in graphene and topological insulators," *JETP Lett.*, vol. 100, p. 390, 2014.

[122] X. Yao, M. Tokman, and A. Belyanin, "Strong magneto-optical effects due to surface states in three-dimensional topological insulators," *Opt. Express*, vol. 23, p. 795, 2015.

[123] A. R. Kutayiah, M. Tokman, Y. Wang, and A. Belyanin, "Difference frequency generation of surface plasmon-polaritons in landau quantized graphene," *Phys. Rev. B*, vol. 98, no. 115410, 2018.

[124] J. Karch, C. Drexler, P. Olbrich, M. Fehrenbacher, M. Hirmer, M. M. Glazov, S. A. Tarasenko, E. L. Ivchenko, B. Birkner, J. Eroms, D. Weiss, R. Yakimova, S. Lara-Avila, S. Kubatkin, M. Ostler, T. Seyller, and S. D. Ganichev, "Terahertz radiation driven chiral edge currents in graphene," *Phys. Rev. Lett.*, vol. 107, no. 276601, 2011.

[125] M. Battiato, G. Barbalinardo, and P. M. Oppeneer, "Quantum theory of the inverse faraday effect," *Phys. Rev. B*, vol. 89, no. 014413, 2014.

[126] V. L. Ginzburg, *Theoretical Physics and Astrophysics*. Pergamon, 1979.

[127] Y. Zheng and T. Ando, "Hall conductivity of a two-dimensional graphite system," *Phys. Rev. B*, vol. 65, no. 245420, 2002.

[128] G. D. Mahan, *Many-Particle Physics, Physics of Solids and Liquids, 3rd ed.* Springer, 2000.

[129] A. Ferreira, J. Viana-Gomes, Y. V. Bludov, V. Pereira, N. M. R. Peres, and A. H. C. Neto, "Faraday effect in graphene enclosed in an optical cavity and the equation of motion method for the study of magneto-optical transport in solids," *Phys. Rev. B*, vol. 84, no. 235410, 2011.

[130] L. Levitov and G. Falkovich, "Electron viscosity, current vortices and negative nonlocal resistance in graphene," *Nat. Phys.*, vol. 12, p. 672, 2016.

[131] Y. V. Bludov, M. I. Vasilevskiy, and N. R. Peres, "Magnetic field assisted transmission of thz waves through a graphene layer combined with a periodically perforated metallic film," *Phys. Rev. B*, vol. 97, no. 045433, 2018.

[132] S. Haroche and J. M. Raymond, *Exploring the Quantum: Atoms, Cavities, and Photons*. Oxford University Press, 2006.

[133] P. Lodahl, S. Mahmoodian, and S. Stobbe, "Interfacing single photons and single quantum dots with photonic nanostructures," *Rev. Mod. Phys.*, vol. 87, p. 347, 2015.

[134] C. L. Degen, F. Reinhard, and P. Cappellaro, "Quantum sensing," *Rev. Mod. Phys.*, vol. 89, no. 035002, 2017.

[135] A. Sipahigil1, R. E. Evans, D. D. Sukachev, M. J. Burek, J. Borregaard, M. K. Bhaskar, C. T. Nguyen, J. L. Pacheco, H. A. Atikian, C. Meuwly, a. E. B. R. M. Camacho, and F. Jelezko, H. Park, M. Loncar, and M. D. Lukin, "An integrated diamond nanophotonics platform for quantum-optical networks," *Science*, vol. 354, p. 847, 2016.

[136] T. Yoshie, A. Scherer, J. Hendrickson, G. Khitrova, H. M. Gibbs, G. Rupper, C. Ell, O. B. Shchekin, and D. G. Deppe, "Vacuum rabi splitting with a single quantum dot in a photonic crystal nanocavity," *Nature*, vol. 432, p. 200, 2004.

[137] J. P. Reithmaier, G. Sek, A. Loffler, C. Hofmann, S. Kuhn, S. Reitzenstein, L. V. Keldysh, V. D. Kulakovskii, T. L. Reinecke, and A. Forchel, "Strong coupling in a single quantum dot semiconductor microcavity system," *Nature*, vol. 432, p. 197, 2004.

[138] R. Chikkaraddy, B. de Nijs, F. Benz, S. J. Barrow, O. A. Scherman, E. Rosta, A. Demetriadou, P. Fox, O. Hess, and J. J. Baumberg, "Single-molecule strong coupling at room temperature in plasmonic nanocavities," *Nature*, vol. 535, p. 127, 2016.

[139] F. Benz, M. K. Schmidt, A. Dreismann, R. Chikkaraddy, Y. Zhang, A. Demetriadou, C. Carnegie, H. Ohadi, B. de Nijs, R. Esteban, J. Aizpurua, and J. J. Baumberg, "Single molecule optomechanics in picocavities," *Science*, vol. 354, p. 726, 2016.

[140] K.-D. Park, E. A. Muller, V. Kravtsov, P. M. Sass, J. Dreyer, J. M. Atkin, and M. B. Raschke, "Variable-temperature tipenhanced raman spectroscopy of single-molecule fluctuations and dynamics," *Nano Lett.*, vol. 16, p. 479, 2016.

[141] H. Leng, B. Szychowski, M. C. Daniel, and M. Pelton, "Strong coupling and induced transparency at room temperature with single quantum dots and gap plasmons," *Nat Commun.*, vol. 9, no. 4012, 2018.

[142] H. Gross, J. M. Hamm, T. Tufarelli, O. Hess, and B. Hecht, "Near-field strong coupling of single quantum dots," *Sci. Adv.*, vol. 4, no. 3 eaar4906, 2018.

[143] K.-D. Park, M. A. May, H. Leng, J. Wang, J. A. Kropp, T. Gougousi, M. Pelton, and M. B. Raschke, "Tip-enhanced strong coupling spectroscopy, imaging, and control of a single quantum emitter," *Sci. Adv.*, vol. 5, no. 7 eaar5931, 2019.

[144] P. Torma and W. L. Barnes, "Strong coupling between surface plasmon polaritons and emitters: A review," *Rep. Prog. Phys.*, vol. 78, no. 013901, 2015.

[145] S. N. G. O. Bitton and G. Haran, "Quantum dot plasmonics: From weak to strong coupling," *Nanophotonics*, vol. 8, p. 559, 2019.

[146] P. Forn-Diaz, L. Lamata, E. Rico, J. Kono, and E. Solano, "Ultrastrong coupling regimes of light-matter interaction," *Rev. Mod. Phys.*, vol. 91, no. 025005, 2019.

[147] M. A. May, D. Fialkow, T. Wu, K.-D. Park, H. Leng, J. A. Kropp, T. Gougousi, P.Lalanne, M. Pelton, and M. B. Raschke, "Nano-cavity qed with tunable nano-tip interaction," *Adv. Quantum Technol.*, vol. 3, no. 1900087, 2020.

[148] M. Aspelmeyer, T. J. Kippenberg, and F. Marquardt, "Cavity optomechanics," *Rev. Mod. Phys.*, vol. 86, p. 1391, 2014.

[149] P. Meystre, "A short walk through quantum optomechanics," *Ann. Phys.*, vol. 525, p. 215, 2013.

[150] J. M. Pirkkalainen, S. U. Cho, F. Massel, J. Tuorila, T. T. Heikkila, P. J. Hakonen, and M. A. Sillanpaa, "Cavity optomechanics mediated by a quantum two-level system," *Nat. Commun.*, vol. 6, no. 6981, 2015.

[151] Y. Chu, P. Kharel, W. H. Renninger, L. D. Burkhart, L. Frunzio, P. T. Rakich, and R. J. Schoelkopf, "Quantum acoustics with superconducting qubits," *Science*, vol. 358, p. 199, 2017.

[152] S. Hong, R. Riedinger, I. Marinkovic, A. Wallucks, S. G. Hofer, R. A. Norte, M. Aspelmeyer, and S. Groblacher, "Hanbury brown and twiss interferometry of single phonons from an optomechanical resonator," *Science*, vol. 358, p. 203, 2017.

[153] P. Arrangoiz-Arriola, E. A. Wollack, Z. Wang, M. Pechal, W. Jiang, T. P. McKenna, J. D. Witmer, R. V. Laer, and A. H. Safavi-Naeini, "Resolving the energy levels of a nanomechanical oscillator," *Nature*, vol. 571, p. 537, 2019.

[154] M. Tokman, M. Erukhimova, Y. Wang, Q. Chen, and A. Belyanin, "Generation and dynamics of entangled fermionphoton-phonon states in nanocavities," *Nanophotonics*, vol. 10, p. 491, 2021.

[155] N. A. Sinitsyn, E. A. Yuzbashian, V. Y. Chernyak, A. Patra, and C. Sun, "Integrable time-dependent quantum hamiltonians," *Phys. Rev. Lett.*, vol. 120, no. 190402, 2018.

[156] V. Y. Chernyak, N. A. Sinitsyn, and C. Sun, "A large class of solvable multistate landau-zener models and quantum integrability," *J. Phys. A: Math. Theor.*, vol. 51, no. 245201, 2018.

[157] F. Li, V. Y. Chernyak, and N. A. Sinitsyn, "Quantum annealing and thermalization: Insights from integrability," *Phys. Rev. Lett.*, vol. 121, no. 190601, 2018.

[158] M. O. Scully and M. S. Zubairy, *Quantum Optics*. Cambridge University Press, 1997.

[159] M. B. Plenio and P. L. Knight, "The quantum-jump approach to dissipative dynamics in quantum optics," *Rev. Mod. Phys.*, vol. 70, p. 101, 1998.

[160] M. Tokman, X. Yao, and A. Belyanin, "Generation of entangled photons in graphene in a strong magnetic field," *Phys. Rev. Lett.*, vol. 110, no. 077404, 2013.

[161] M. D. Tokman, M. A. Erukhimova, and V. V. Vdovin, "The features of a quantum description of radiation in an optically dense medium," *Ann. Phys.*, vol. 360, p. 571, 2015.

[162] M. Tokman, Z. Long, S. A. Mutairi, Y. Wang, M. Belkin, and A. Belyanin, "Enhancement of the spontaneous emission in subwavelength quasi-two-dimensional waveguides and resonators," *Phys. Rev. A*, vol. 97, no. 043801, 2018.

[163] M. Kruskal, "Asymptotic theory of hamiltonian and other systems with all solutions nearly periodic," *J. Math. Phys.*, vol. 3, p. 806, 1962.

[164] M. D. Tokman and M. A. Erukhimova, "Modification of the adiabatic invariants method in the studies of resonant dissipative systems," *Phys. Rev. E*, vol. 84, no. 056610, 2011.

[165] L. D. Landau and E. M. Lifshitz, *Mechanics*. Elsevier, 1976.

[166] V. V. Zheleznyakov, V. V. Kocharovskii, and V. V. Kocharovskii, "Linear coupling of electromagnetic waves in inhomogeneous weakly-ionized media," *Sov. Phys. Usp.*, vol. 26, p. 877, 1983.

[167] J. Hallin and P. Liljenberg, "Fermionic and bosonic pair creation in an external electric field at finite temperature using the functional schrodinger representation," *Phys. Rev. D*, vol. 52, p. 1150, 1995.

[168] N. Yokomizo, "Radiation from electrons in graphene in strong electric field," *Ann. Phys.*, vol. 351, p. 166, 2014.

[169] H. Bateman, *Higher Transcendental Functions, Vol. 2.* (McGraw-Hill, 1953.

[170] W. Dur, G. Vidal, and J. I. Cirac, "Three qubits can be entangled in two inequivalent ways," *Phys. Rev. A*, vol. 62, no. 062314, 2000.

[171] M. M. Cunha, A. Fonseca, and E. O. Silva, "Tripartite entanglement: Foundations and applications," *Universe*, vol. 5, no. 209, 2019.

[172] L. K. Shalm, D. R. Hamel, C. S. Z. Yan, K. J. Resch, and T. Jennewein, "Three-photon energy-time entanglement," *Nat. Phys.*, vol. 9, p. 19, 2012.

[173] A. Agusti, C. W. S. Chang, F. Quijandria, G. Johansson, C. M. Wilson, and C. Sabin, "Tripartite genuine non-gaussian entanglement in three-mode spontaneous parametric down-conversion," *Phys. Rev. Lett.*, vol. 125, no. 020502, 2020.

[174] L. D. Landau and E. M. Lifshitz, *Statistical Physics, Part 1*. (Pergamon, 1965.

[175] Y. V. Radeonychev, M. D. Tokman, A. G. Litvak, and O. Kocharovskaya, "Acoustically induced transparency in optically dense resonance medium," *Phys. Rev. Lett.*, vol. 96, no. 093602, 2006.

[176] Y. V. Radeonychev, I. R. Khairulin, F. G. Vagizov, M. Scully, and O. Kocharovskaya, "Observation of acoustically induced transparency for γ-ray photons," *Phys. Rev. Lett.*, vol. 124, no. 163602, 2020.

[177] E. H. Hwang and S. D. Sarma, "Dielectric function, screening, and plasmons in two-dimensional graphene," *Phys. Rev. B*, vol. 75, no. 205418, 2007.

[178] C. Gardiner and P. Zoller, *Quantum Noise*. Springer-Verlag, 2004.

[179] V. M. Fain and Y. I. Khanin, *Quantum Electronics: Basic Theory*. MIT Press, 1969.

[180] K. Blum, *Density Matrix Theory and Applications*. Springer, 2012.

APPENDIX A

EVALUATION OF THE MATRIX ELEMENTS OF THE CURRENT DENSITY OPERATOR

We denote everywhere the bulk states by Latin letters, and the surface states by Greek letters, i.e. $|n\rangle = |B\rangle, |\mu\rangle = |S\rangle$. In this section we evaluate the matrix elements of the current density operator that enter Eq. (2.28) for the components of bulk and surface conductivity tensors.

$$
\begin{aligned}
&(j_x)_{nm} = \langle n|\, \hat{j}_x\, |m\rangle \\
&= \frac{ev_F}{\hbar b}\int d^3r \left(\Psi^B_{\boldsymbol{k_n},s_n}(\boldsymbol{r})\right)^\dagger (-i\hbar\partial_x)\, \hat{\sigma}_x \Psi^B_{\boldsymbol{k_m},s_m}(\boldsymbol{r}) \\
&= \frac{ev_F}{2b} k_{nx}\delta_{\boldsymbol{k}_n,\boldsymbol{k}_m} \\
&\times \left[s_m\sqrt{(1+s_m\cos\theta_{\boldsymbol{k_n}})\,(1-s_n\cos\theta_{\boldsymbol{k_n}})}e^{i\phi_{\boldsymbol{k}_n}} + s_n\sqrt{(1+s_n\cos\theta_{\boldsymbol{k_n}})\,(1-s_m\cos\theta_{\boldsymbol{k_n}})}e^{-i\phi_{\boldsymbol{k}_n}}\right]
\end{aligned}
$$

$$
(j_x)_{\mu\nu} = \langle\mu|\, \hat{j}_x\, |\nu\rangle = \frac{ev_F}{\hbar b}\int d^3r \left(\Psi^S_{\boldsymbol{k}_\mu}(\boldsymbol{r})\right)^\dagger (-i\hbar\partial_x)\, \hat{\sigma}_x \Psi^S_{\boldsymbol{k}_\nu}(\boldsymbol{r}) = 0,
$$

$$
\begin{aligned}
(j_x)_{\mu m} &= \langle\mu|\, \hat{j}_x\, |m\rangle = \frac{ev_F}{\hbar b}\int d^3r \left(\Psi^S_{\boldsymbol{k}_\mu}(\boldsymbol{r})\right)^\dagger (-i\hbar\partial_x)\, \hat{\sigma}_x \Psi^B_{\boldsymbol{k_m},s_m}(\boldsymbol{r}) \\
&= \frac{2ev_F s_m k_{mx} k_{mz}}{ib(\kappa_m^2 + k_{mz}^2)}\sqrt{\frac{\kappa_m\,(1+s_m\cos\theta_{\boldsymbol{k}_m})}{L_z}}\delta_{k_{mx},k_{\mu x}}\delta_{k_{my},k_{\mu y}}
\end{aligned}
\tag{A.1}
$$

$$
\begin{aligned}
(j_y)_{nm} &= \frac{ev_F}{\hbar b}\int d^3r \left(\Psi^B_{\boldsymbol{k_n},s_n}(\boldsymbol{r})\right)^\dagger (-i\hbar\partial_y)\, \hat{\sigma}_x \Psi^B_{\boldsymbol{k_m},s_m}(\boldsymbol{r}) - ev_F\int d^3r \left(\Psi^B_{\boldsymbol{k_n},s_n}(\boldsymbol{r})\right)^\dagger \hat{\sigma}_z \Psi^B_{\boldsymbol{k_m},s_m}(\boldsymbol{r}) \\
&= \frac{ev_F}{2b} k_{ny}\delta_{\boldsymbol{k}_n,\boldsymbol{k}_m} \\
&\times \left[s_m\sqrt{(1+s_m\cos\theta_{\boldsymbol{k}_n})\,(1-s_n\cos\theta_{\boldsymbol{k}_n})}e^{i\phi_{\boldsymbol{k}_n}} + s_n\sqrt{(1+s_n\cos\theta_{\boldsymbol{k}_n})\,(1-s_m\cos\theta_{\boldsymbol{k}_n})}e^{-i\phi_{\boldsymbol{k}_n}}\right]
\end{aligned}
$$

$$+\frac{ev_F}{2}\delta_{\boldsymbol{k}_n,\boldsymbol{k}_m}\left[s_n s_m\sqrt{\left(1+s_n\cos\theta_{\boldsymbol{k}_\mathrm{n}}\right)\left(1+s_m\cos\theta_{\boldsymbol{k}_n}\right)}-\sqrt{\left(1-s_n\cos\theta_{\boldsymbol{k}_n}\right)\left(1-s_m\cos\theta_{\boldsymbol{k}_\mathrm{n}}\right)}\right] \tag{A.2}$$

$$\begin{aligned}(j_y)_{\mu\nu}&=\frac{ev_F}{\hbar b}\int d^3r\left(\Psi^S_{\boldsymbol{k}_\mu}(\boldsymbol{r})\right)^\dagger\left(-i\hbar\partial_y\right)\hat{\sigma}_x\Psi^S_{\boldsymbol{k}_\nu}(\boldsymbol{r})-ev_F\int d^3r\left(\Psi^S_{\boldsymbol{k}_\mu}(\boldsymbol{r})\right)^\dagger\hat{\sigma}_z\Psi^S_{\boldsymbol{k}_\nu}(\boldsymbol{r})\\&=-ev_F\delta_{k_{\mu x},k_{\nu x}}\delta_{k_{\mu y},k_{\nu y}}\end{aligned} \tag{A.3}$$

$$\begin{aligned}(j_y)_{\mu m}&=\frac{ev_F}{\hbar b}\int d^3r\left(\Psi^S_{\boldsymbol{k}_\mu}(\boldsymbol{r})\right)^\dagger\left(-i\hbar\partial_y\right)\hat{\sigma}_x\Psi^B_{\boldsymbol{k_m},s_m}(\boldsymbol{r})-ev_F\int d^3r\left(\Psi^S_{\boldsymbol{k}_\mu}(\boldsymbol{r})\right)^\dagger\hat{\sigma}_z\Psi^B_{\boldsymbol{k_m},s_m}(\boldsymbol{r})\\&=\frac{2ev_Fs_mk_{my}k_{mz}}{ib(\kappa_m^2+k_{mz}^2)}\sqrt{\frac{\kappa_m\left(1+s_m\cos\theta_{\boldsymbol{k}_m}\right)}{L_z}}\delta_{k_{mx},k_{\mu x}}\delta_{k_{my},k_{\mu y}};\end{aligned} \tag{A.4}$$

$$\begin{aligned}(j_z)_{nm}&=ev_F\int d^3r\left(\Psi^B_{\boldsymbol{k_n},s_n}(\boldsymbol{r})\right)^\dagger\hat{\sigma}_y\Psi^B_{\boldsymbol{k_m},s_m}(\boldsymbol{r})=i\frac{ev_F}{2}\delta_{\boldsymbol{k}_n,\boldsymbol{k}_m}\\&\times\left[s_n\sqrt{\left(1+s_n\cos\theta_{\boldsymbol{k}_\mathrm{n}}\right)\left(1-s_m\cos\theta_{\boldsymbol{k}_\mathrm{n}}\right)}e^{-i\phi_{\boldsymbol{k}_n}}-s_m\sqrt{\left(1+s_m\cos\theta_{\boldsymbol{k}_\mathrm{n}}\right)\left(1-s_n\cos\theta_{\boldsymbol{k}_\mathrm{n}}\right)}e^{i\phi_{\boldsymbol{k}_\mathrm{n}}}\right]\end{aligned} \tag{A.5}$$

$$(j_z)_{\mu\nu}=ev_F\int d^3r\left(\Psi^S_{\boldsymbol{k}_\mu}(\boldsymbol{r})\right)^\dagger\hat{\sigma}_y\Psi^S_{\boldsymbol{k}_\nu}(\boldsymbol{r})=0,$$

$$\begin{aligned}(j_z)_{\mu m}&=ev_F\int d^3r\left(\Psi^S_{\boldsymbol{k}_\mu}(\boldsymbol{r})\right)^\dagger\hat{\sigma}_y\Psi^B_{\boldsymbol{k_m},s_m}(\boldsymbol{r})\\&=-\frac{2ev_Fs_mk_{mz}}{\kappa_m^2+k_{mz}^2}\sqrt{\frac{\kappa_m\left(1+s_m\cos\theta_{\boldsymbol{k}_m}\right)}{L_z}}\delta_{k_{mx},k_{\mu x}}\delta_{k_{my},k_{\mu y}},\end{aligned} \tag{A.6}$$

where we have used $\kappa=\frac{b^2-\left(k_x^2+k_y^2\right)}{2b}$.

APPENDIX B

CALCULATION OF THE BULK OPTICAL CONDUCTIVITY TENSOR

The 3D integrals over electron momenta cannot be evaluated analytically in most cases, even in the zero temperature limit. Whenever the integrals remain in the final expression, they were evaluated numerically for the plots in the main text.

B.1 Contribution of intraband transitions ($s = +1 \to s = +1$)

In this case the matrix elements $\boldsymbol{j}_{nm}^{(\boldsymbol{q})}$ of the current density operator reduce to

$$(j_x)_{nn} = ev_F s_n \frac{k_{nx}}{b} \left|\sin\theta_{\boldsymbol{k}_n}\right| \cos\phi_{\boldsymbol{k}_n}, \tag{B.1}$$

$$(j_y)_{nn} = ev_F s_n \left(\frac{k_{ny}}{b} \left|\sin\theta_{\boldsymbol{k}_n}\right| \cos\phi_{\boldsymbol{k}_n} + \cos\theta_{\boldsymbol{k}_n} \right), \tag{B.2}$$

$$(j_z)_{nn} = ev_F s_n \left|\sin\theta_{\boldsymbol{k}_n}\right| \sin\phi_{\boldsymbol{k}_n}. \tag{B.3}$$

Therefore, we obtain

$$\begin{aligned}
\sigma_{xx}^{intra}(\omega) &= g\frac{i\hbar}{V} \sum_{mn} \left(\frac{f_n - f_m}{E_m - E_n} \right) \frac{\left|\langle n| \hat{j}_x |m\rangle\right|^2}{\hbar(\omega + i\gamma) + (E_n - E_m)} \\
&= \frac{ige^2 v_F^2}{b^2(\omega + i\gamma)} \frac{1}{V} \sum_n \left(-\frac{\partial f_n}{\partial E_n} \right) k_{nx}^2 \sin^2\theta_{\boldsymbol{k}_n} \cos^2\phi_{\boldsymbol{k}_n} \\
&= \frac{ige^2 v_F^2}{b^2(\omega + i\gamma)} \int_\infty \frac{d^3k}{(2\pi)^3} \delta(E_B - E_F) k_x^2 \sin^2\theta_{\boldsymbol{k}} \cos^2\phi_{\boldsymbol{k}} \\
&= \frac{ige^2 v_F}{4\pi^3 b^2 k_F \hbar(\omega + i\gamma)} \int_{-\infty}^{\infty} dk_x \int_{-\infty}^{\infty} dk_y \frac{k_x^2 K_x^2 \Theta\left(k_F - \sqrt{K_x^2 + k_y^2}\right)}{\sqrt{k_F^2 - \left(K_x^2 + k_y^2\right)}}
\end{aligned} \tag{B.4}$$

Similarly,

$$\sigma_{yy}^{intra}(\omega)=\frac{ige^2v_F}{4\pi^3b^2k_F\hbar(\omega+i\gamma)}\int_{-\infty}^{\infty}dk_x\int_{-\infty}^{\infty}dk_y\frac{k_y^2\left(K_x+b\right)^2\Theta\left(k_F-\sqrt{K_x^2+k_y^2}\right)}{\sqrt{k_F^2-\left(K_x^2+k_y^2\right)}} \tag{B.5}$$

$$\sigma_{zz}^{intra}(\omega)=\frac{ige^2v_F}{4\pi^3k_F\hbar(\omega+i\gamma)}\int_{-\infty}^{\infty}dk_x\int_{-\infty}^{\infty}dk_y\Theta\left(k_F-\sqrt{K_x^2+k_y^2}\right)\sqrt{k_F^2-\left(K_x^2+k_y^2\right)} \tag{B.6}$$

Here $\Theta(k)$ is the step function and we have used $\cos\theta_{\boldsymbol{k}}=\frac{k_y}{\sqrt{K_x^2+k_y^2+k_z^2}}$, $e^{i\phi_{\boldsymbol{k}}}=\frac{K_x+ik_z}{\sqrt{K_x^2+k_z^2}}$, $K_x\equiv\frac{\left(k_x^2+k_y^2\right)-b^2}{2b}$, and $k_F\equiv\frac{E_F}{\hbar v_F}$.

$$\sigma_{xy}^{intra}(\omega)=\sigma_{xz}^{intra}(\omega)=\sigma_{yz}^{intra}(\omega)=0. \tag{B.7}$$

B.2 Contribution of interband transitions ($s\to -s$, $|B\rangle\leftrightarrow|S\rangle$)

In this case, i.e. $s_m=-s_n=\pm1$, $n\neq m$, the matrix elements $\boldsymbol{j}_{nm}^{(\boldsymbol{q})}$ of the current density operator reduce to

$$(j_x)_{nm}=ev_Fs_n\delta_{\boldsymbol{k}_n,\boldsymbol{k}_m}\frac{k_{nx}}{b}\left(s_n\cos\theta_{\boldsymbol{k}_n}\cos\phi_{\boldsymbol{k}_n}-i\sin\phi_{\boldsymbol{k}_n}\right), \tag{B.8}$$

$$(j_y)_{nm}=ev_Fs_n\delta_{\boldsymbol{k}_n,\boldsymbol{k}_m}\left[\frac{k_{ny}}{b}\left(s_n\cos\theta_{\boldsymbol{k}_n}\cos\phi_{\boldsymbol{k}_n}-i\sin\phi_{\boldsymbol{k}_n}\right)-s_n\left|\sin\theta_{\boldsymbol{k}_n}\right|\right], \tag{B.9}$$

$$(j_z)_{nm}=ev_Fs_n\delta_{\boldsymbol{k}_n,\boldsymbol{k}_m}\left(i\cos\phi_{\boldsymbol{k}_n}+s_n\cos\theta_{\boldsymbol{k}_n}\sin\phi_{\boldsymbol{k}_n}\right), \tag{B.10}$$

where $n\neq m$. Therefore, we obtain

$$\sigma_{xx}^{inter}(\omega)=g\frac{i\hbar}{V}\sum_{s=\pm1}\sum_{mn}\left(\frac{f_{n(-s)}-f_{m(s)}}{E_{m(s)}-E_{n(-s)}}\right)\frac{\left|\langle -sn|\,\hat{j}_x\,|ms\rangle\right|^2}{\hbar(\omega+i\gamma)+(E_{n(-s)}-E_{m(s)})}$$
$$=i\hbar g\sum_{s=\pm1}\int_{\infty}\frac{d^3k}{(2\pi)^3}\left(\frac{f_{\boldsymbol{k}(-s)}-f_{\boldsymbol{k}(s)}}{E_{\boldsymbol{k}(s)}-E_{\boldsymbol{k}(-s)}}\right)\frac{e^2v_F^2k_x^2\left(\cos^2\theta_{\boldsymbol{k}}\cos^2\phi_{\boldsymbol{k}}+\sin^2\phi_{\boldsymbol{k}}\right)}{b^2\left[\hbar(\omega+i\gamma)+(E_{\boldsymbol{k}(-s)}-E_{\boldsymbol{k}(s)})\right]}$$
$$=\frac{ige^2(\omega+i\gamma)}{8\pi^3b^2\hbar v_F}\int_{-\infty}^{\infty}dk_x\int_{-\infty}^{\infty}dk_y\times\Big[\Theta\left(k_F-\sqrt{K_x^2+k_y^2}\right)$$
$$\times2k_x^2\left(\frac{K_x^2\sqrt{k_F^2-K_x^2-k_y^2}}{k_F\left(\frac{\omega+i\gamma}{v_F}\right)^2\left(K_x^2+k_y^2\right)}+\frac{\left[\left(\frac{\omega+i\gamma}{v_F}\right)^2-4K_x^2\right]\arctan\left[\frac{\left(\frac{\omega+i\gamma}{v_F}\right)\sqrt{k_F^2-K_x^2-k_y^2}}{k_F\sqrt{4\left(K_x^2+k_y^2\right)-\left(\frac{\omega+i\gamma}{v_F}\right)^2}}\right]}{\left(\frac{\omega+i\gamma}{v_F}\right)^3\sqrt{4\left(K_x^2+k_y^2\right)-\left(\frac{\omega+i\gamma}{v_F}\right)^2}}\right)$$
$$-\Theta\left(K-\sqrt{K_x^2+k_y^2}\right)$$
$$\times2k_x^2\left(\frac{K_x^2\sqrt{K^2-K_x^2-k_y^2}}{K\left(\frac{\omega+i\gamma}{v_F}\right)^2\left(K_x^2+k_y^2\right)}+\frac{\left[\left(\frac{\omega+i\gamma}{v_F}\right)^2-4K_x^2\right]\arctan\left[\frac{\left(\frac{\omega+i\gamma}{v_F}\right)\sqrt{K^2-K_x^2-k_y^2}}{K\sqrt{4\left(K_x^2+k_y^2\right)-\left(\frac{\omega+i\gamma}{v_F}\right)^2}}\right]}{\left(\frac{\omega+i\gamma}{v_F}\right)^3\sqrt{4\left(K_x^2+k_y^2\right)-\left(\frac{\omega+i\gamma}{v_F}\right)^2}}\right)\Big] \tag{B.11}$$

where we have used $K_x\equiv\frac{\left(k_x^2+k_y^2\right)-b^2}{2b}=-\kappa$, $\cos\theta_{\boldsymbol{k}}(-k_x)=\cos\theta_{\boldsymbol{k}}(k_x)$,$\sin\theta_{\boldsymbol{k}}(-k_x)=\sin\theta_{\boldsymbol{k}}(k_x)$ $\cos\phi_{\boldsymbol{k}}(-k_x)=\cos\phi_{\boldsymbol{k}}(k_x)$, and $\sin\phi_{\boldsymbol{k}}(-k_x)=\sin\phi_{\boldsymbol{k}}(k_x)$.

Similarly,

$$\sigma_{yy}^{inter}(\omega)=\frac{ige^2(\omega+i\gamma)}{4\pi^3b^2\hbar v_F}\int_{-\infty}^{\infty}dk_x\int_{-\infty}^{\infty}dk_y\times\Big[\Theta\left(k_F-\sqrt{K_x^2+k_y^2}\right)\times$$
$$\left(\frac{(b+K_x)^2k_y^2\sqrt{k_F^2-K_x^2-k_y^2}}{k_F\left(\frac{\omega+i\gamma}{v_F}\right)^2\left(K_x^2+k_y^2\right)}+\frac{\left[\left(\frac{\omega+i\gamma}{v_F}\right)^2\left(b^2+k_y^2\right)-4(b+K_x)^2k_y^2\right]\arctan\left[\frac{\left(\frac{\omega+i\gamma}{v_F}\right)\sqrt{k_F^2-K_x^2-k_y^2}}{k_F\sqrt{4\left(K_x^2+k_y^2\right)-\left(\frac{\omega+i\gamma}{v_F}\right)^2}}\right]}{\left(\frac{\omega+i\gamma}{v_F}\right)^3\sqrt{4\left(K_x^2+k_y^2\right)-\left(\frac{\omega+i\gamma}{v_F}\right)^2}}\right)$$
$$-\Theta\left(K-\sqrt{K_x^2+k_y^2}\right)\times$$

$$\left(\frac{(b+K_x)^2 k_y^2 \sqrt{K^2-K_x^2-k_y^2}}{K\left(\frac{\omega+i\gamma}{v_F}\right)^2\left(K_x^2+k_y^2\right)} + \frac{\left[\left(\frac{\omega+i\gamma}{v_F}\right)^2\left(b^2+k_y^2\right)-4\left(b+K_x\right)^2 k_y^2\right]\arctan\left[\frac{\left(\frac{\omega+i\gamma}{v_F}\right)\sqrt{K^2-K_x^2-k_y^2}}{K\sqrt{4\left(K_x^2+k_y^2\right)-\left(\frac{\omega+i\gamma}{v_F}\right)^2}}\right]}{\left(\frac{\omega+i\gamma}{v_F}\right)^3\sqrt{4\left(K_x^2+k_y^2\right)-\left(\frac{\omega+i\gamma}{v_F}\right)^2}} \right)\Bigg] \tag{B.12}$$

$$\sigma_{zz}^{inter}(\omega) = \frac{ige^2(\omega+i\gamma)}{8\pi^3\hbar v_F}\int_{-\infty}^{\infty}dk_x\int_{-\infty}^{\infty}dk_y\left(K_x^2+k_y^2\right)\Bigg[\Theta\left(K-\sqrt{K_x^2+k_y^2}\right)$$
$$\times\left(\frac{2\sqrt{K^2-K_x^2-k_y^2}}{K\left(\frac{\omega+i\gamma}{v_F}\right)^2\left(K_x^2+k_y^2\right)} - \frac{8\left[\left(\frac{\omega+i\gamma}{v_F}\right)^2-4K_x^2\right]\arctan\left[\frac{\left(\frac{\omega+i\gamma}{v_F}\right)\sqrt{K^2-K_x^2-k_y^2}}{K\sqrt{4\left(K_x^2+k_y^2\right)-\left(\frac{\omega+i\gamma}{v_F}\right)^2}}\right]}{\left(\frac{\omega+i\gamma}{v_F}\right)^3\sqrt{4\left(K_x^2+k_y^2\right)-\left(\frac{\omega+i\gamma}{v_F}\right)^2}}\right)$$
$$-\Theta\left(k_F-\sqrt{K_x^2+k_y^2}\right)$$
$$\times\left(\frac{2\sqrt{k_F^2-K_x^2-k_y^2}}{k_F\left(\frac{\omega+i\gamma}{v_F}\right)^2\left(K_x^2+k_y^2\right)} - \frac{8\left[\left(\frac{\omega+i\gamma}{v_F}\right)^2-4K_x^2\right]\arctan\left[\frac{\left(\frac{\omega+i\gamma}{v_F}\right)\sqrt{k_F^2-K_x^2-k_y^2}}{k_F\sqrt{4\left(K_x^2+k_y^2\right)-\left(\frac{\omega+i\gamma}{v_F}\right)^2}}\right]}{\left(\frac{\omega+i\gamma}{v_F}\right)^3\sqrt{4\left(K_x^2+k_y^2\right)-\left(\frac{\omega+i\gamma}{v_F}\right)^2}}\right)\Bigg]. \tag{B.13}$$

The only nonzero off-diagonal element is $\sigma_{zy}^{inter}(\omega) = -\sigma_{yz}^{inter}(\omega)$, as expected:

$$\sigma_{yz}^{inter}(\omega) = \frac{-ge^2}{4\pi^3 b\hbar}\int_{-\infty}^{\infty}dk_x\int_{-\infty}^{\infty}dk_y\left(k_y^2-bK_x\right)$$
$$\times\left(\Theta\left(k_F-\sqrt{K_x^2+k_y^2}\right)\frac{2\arctan\left[\frac{\left(\frac{\omega+i\gamma}{v_F}\right)\sqrt{k_F^2-K_x^2-k_y^2}}{k_F\sqrt{4\left(K_x^2+k_y^2\right)-\left(\frac{\omega+i\gamma}{v_F}\right)^2}}\right]}{\left(\frac{\omega+i\gamma}{v_F}\right)\sqrt{4\left(K_x^2+k_y^2\right)-\left(\frac{\omega+i\gamma}{v_F}\right)^2}}\right.$$

$$-\Theta\left(K-\sqrt{K_x^2+k_y^2}\right)\frac{2\arctan\left[\frac{\left(\frac{\omega+i\gamma}{v_F}\right)\sqrt{K^2-K_x^2-k_y^2}}{K\sqrt{4\left(K_x^2+k_y^2\right)-\left(\frac{\omega+i\gamma}{v_F}\right)^2}}\right]}{\left(\frac{\omega+i\gamma}{v_F}\right)\sqrt{4\left(K_x^2+k_y^2\right)-\left(\frac{\omega+i\gamma}{v_F}\right)^2}}\Bigg) \tag{B.14}$$

Here we have introduced a cutoff at $k = K$ in the integration over electron momenta in order to regularize the divergent integral $\int \frac{d^3k}{(2\pi)^3}$ which comes from $\frac{1}{V}\sum_n \to \int \frac{d^3k}{(2\pi)^3}$. The divergence is an artifact of the effective Hamiltonian Eq. (2.1) which has a "bottomless" valence band with electrons occupying all states to $k \to \infty$. The regularization makes the valence band bounded from below. We chose the cutoff at the momentum corresponding to the energy of 2 eV, i.e. much higher than the range of interest to us near the Weyl nodes. In the numerical examples in the paper the value of half-separation between Weyl nodes $\hbar v_F b$ is chosen to be 100 meV. We have verified that an exact value of the cutoff has a negligible effect on the low-energy optical response below 350 meV, as long as K is large enough.

APPENDIX C

CALCULATION OF THE SURFACE ELECTRICAL CONDUCTIVITY

C.1 Surface-to-surface states intraband transitions

$$\sigma_{yy}^{intra}(\omega) = g\frac{i\hbar}{S}\sum_{\mu\nu}\left(\frac{f_\mu - f_\nu}{E_\nu - E_\mu}\right)\frac{\left|\langle\mu|\,\hat{j}_y\,|\nu\rangle\right|^2}{\hbar(\omega+i\gamma)+(E_\mu - E_\nu)}$$
$$= \frac{ig\hbar e^2 v_F^2}{S}\sum_{\mu}\left(-\frac{\partial f_\mu}{\partial E_\mu}\right)\frac{1}{\hbar(\omega+i\gamma)} = \Theta(b-k_F)\,\frac{ige^2 v_F\sqrt{b^2-k_F^2}}{2\pi^2\hbar(\omega+i\gamma)}. \tag{C.1}$$

All other tensor components are equal to zero.

C.2 Surface-to-bulk states transitions

$$\sigma_{xx}^{inter}(\omega) = g\frac{i\hbar}{S}\sum_{s=\pm1}\sum_{m\mu}\left(\frac{f_\mu - f_{m(s)}}{E_{m(s)} - E_\mu}\right)\frac{\left|\langle\mu|\,\hat{j}_x\,|ms\rangle\right|^2}{\hbar(\omega+i\gamma)+(E_\mu - E_{m(s)})}$$
$$= \frac{i4ge^2v_F^2\hbar}{b^2}\sum_{s=\pm1}\int_\infty\frac{d^3k}{(2\pi)^3}\Theta\left[b^2-\left(k_x^2+k_y^2\right)\right]\Theta(k_z)$$
$$\times\left(\frac{f_{\boldsymbol{k}}^S - f_{\boldsymbol{k}(s)}}{E_{\boldsymbol{k}(s)} - E_{\boldsymbol{k}}^S}\right)\frac{k_x^2k_z^2\kappa(1+s\cos\theta_{\boldsymbol{k}})}{(\kappa^2+k_z^2)^2\left[\hbar(\omega+i\gamma)+(E_{\boldsymbol{k}}^S - E_{\boldsymbol{k}(s)})\right]}$$
$$= \frac{ige^2}{h}\int_0^\infty dk_z\int_{-\infty}^\infty dk_x\int_{-\infty}^\infty dk_y\Theta\left[b^2-\left(k_x^2+k_y^2\right)\right]\frac{k_z^2k_x^2K_x}{\pi^2(K_x^2+k_z^2)^2b^2}$$
$$\times\left[\frac{\Theta\left(k_F-\sqrt{K_x^2+k_y^2+k_z^2}\right)-\Theta(k_F+k_y)}{\sqrt{K_x^2+k_y^2+k_z^2}\left[\left(\frac{\omega+i\gamma}{v_F}-k_y\right)-\sqrt{K_x^2+k_y^2+k_z^2}\right]}\right.$$
$$\left.-\frac{\Theta(-k_F-k_y)}{\sqrt{K_x^2+k_y^2+k_z^2}\left[\left(\frac{\omega+i\gamma}{v_F}-k_y\right)+\sqrt{K_x^2+k_y^2+k_z^2}\right]}\right] \tag{C.2}$$

Similarly,

$$\sigma_{yy}^{inter}(\omega)=\frac{ige^2}{h}\int_0^\infty dk_z\int_{-\infty}^\infty dk_x\int_{-\infty}^\infty dk_y\Theta\left[b^2-\left(k_x^2+k_y^2\right)\right]\frac{k_z^2k_y^2K_x}{\pi^2(K_x^2+k_z^2)^2b^2}$$
$$\times\left[\frac{\Theta\left(k_F-\sqrt{K_x^2+k_y^2+k_z^2}\right)-\Theta\left(k_F+k_y\right)}{\sqrt{K_x^2+k_y^2+k_z^2}\left[\left(\frac{\omega+i\gamma}{v_F}-k_y\right)-\sqrt{K_x^2+k_y^2+k_z^2}\right]}\right.$$
$$\left.-\frac{\Theta\left(-k_F-k_y\right)}{\sqrt{K_x^2+k_y^2+k_z^2}\left[\left(\frac{\omega+i\gamma}{v_F}-k_y\right)+\sqrt{K_x^2+k_y^2+k_z^2}\right]}\right] \tag{C.3}$$

$$\sigma_{zz}^{inter}(\omega)=\frac{ige^2}{h}\int_0^\infty dk_z\int_{-\infty}^\infty dk_x\int_{-\infty}^\infty dk_y\Theta\left[b^2-\left(k_x^2+k_y^2\right)\right]\frac{k_z^2K_x}{\pi^2(K_x^2+k_z^2)^2}$$
$$\times\left[\frac{\Theta\left(k_F-\sqrt{K_x^2+k_y^2+k_z^2}\right)-\Theta\left(k_F+k_y\right)}{\sqrt{K_x^2+k_y^2+k_z^2}\left[\left(\frac{\omega+i\gamma}{v_F}-k_y\right)-\sqrt{K_x^2+k_y^2+k_z^2}\right]}\right.$$
$$\left.-\frac{\Theta\left(-k_F-k_y\right)}{\sqrt{K_x^2+k_y^2+k_z^2}\left[\left(\frac{\omega+i\gamma}{v_F}-k_y\right)+\sqrt{K_x^2+k_y^2+k_z^2}\right]}\right]. \tag{C.4}$$

The only nonzero off-diagonal element is

$$\sigma_{yz}^{inter}(\omega)=\frac{-ge^2}{h}\int_0^\infty dk_z\int_{-\infty}^\infty dk_x\int_{-\infty}^\infty dk_y\Theta\left[b^2-\left(k_x^2+k_y^2\right)\right]\frac{k_z^2k_yK_x}{\pi^2(K_x^2+k_z^2)^2b}$$
$$\times\left[\frac{\Theta\left(k_F-\sqrt{K_x^2+k_y^2+k_z^2}\right)-\Theta\left(k_F+k_y\right)}{\sqrt{K_x^2+k_y^2+k_z^2}\left[\left(\frac{\omega+i\gamma}{v_F}-k_y\right)-\sqrt{K_x^2+k_y^2+k_z^2}\right]}\right.$$
$$\left.-\frac{\Theta\left(-k_F-k_y\right)}{\sqrt{K_x^2+k_y^2+k_z^2}\left[\left(\frac{\omega+i\gamma}{v_F}-k_y\right)+\sqrt{K_x^2+k_y^2+k_z^2}\right]}\right]. \tag{C.5}$$

In Eqs. (C.2)-(C.5) the integral over k_z can be carried out analytically in terms of elementary functions, leading however to very lengthy expressions which we do not present here. The remaining integration was carried out numerically. All integrals are finite, i.e. no cutoff is necessary.

APPENDIX D

DRUDE-LIKE LOW-FREQUENCY LIMIT

In the limit when the frequency and the Fermi energy are much smaller than $\hbar v_F b$, only the electron momenta close to the corresponding Weyl point $k_x = \pm b$ matter. Therefore, we introduce $\delta k_x = k_x - b$ for electron states near one Weyl point and replace the degeneracy factor by $2 \times g$ to account for the contribution from the second Weyl point. In this case, $K_x \sim \frac{(k_x - b)(k_x + b)}{2b} \approx \delta k_x$, $k_x = b + \delta k_x$, and all diagonal intraband components have the same Drude form:

$$\sigma_{xx}^{intra}(\omega) = \sigma_{yy}^{intra}(\omega) = \sigma_{zz}^{intra}(\omega) = \frac{g e^2 v_F k_F^2}{3\pi^2 \hbar(-i\omega + \gamma)}. \tag{D.1}$$

All off-diagonal conductivity elements are zero in this limit.

APPENDIX E

SMALL B EXPANSION

In the limit $b \ll 1$, we can expand the conductivity in powers of b to the leading order: $b \ll 1$, $\frac{1}{b} \gg 1$, $K_x = \frac{\left(k_x^2+k_y^2\right)-b^2}{2b} \sim \frac{\left(k_x^2+k_y^2\right)}{2b} \sim \frac{\left(k_x^2+k_y^2+k_z^2\right)}{2b} \gg k_{x,y,z}, \frac{\omega}{v_F}$ for $k_{x,y,z} \neq 0$. Then we obtain

$$\sigma_{yz}^{B}(\omega) \approx \frac{-ge^2}{3\sqrt{2}\pi^2\hbar}\frac{b^{3/2}}{k_F^{1/2}} \tag{E.1}$$

$$\sigma_{xx}^{B}(\omega) \approx \frac{ge^2k_F^2v_F}{3\pi^2\hbar(-i\omega+\gamma)} + \frac{2\sqrt{2}ge^2(-i\omega+\gamma)}{45\pi^2\hbar v_F}\frac{b^{3/2}}{k_F^{3/2}} \tag{E.2}$$

$$\sigma_{yy}^{B}(\omega) \approx \frac{ge^2k_F^2v_F}{3\pi^2\hbar(-i\omega+\gamma)} + \frac{7\sqrt{2}ge^2(-i\omega+\gamma)}{360\pi^2\hbar v_F}\frac{b^{3/2}}{k_F^{3/2}} \tag{E.3}$$

$$\sigma_{zz}^{B}(\omega) \approx \frac{ge^2k_F^2v_F}{3\pi^2\hbar(-i\omega+\gamma)} + \frac{ge^2(-i\omega+\gamma)}{6\sqrt{2}\pi^2\hbar v_F}\frac{b^{3/2}}{k_F^{3/2}} \tag{E.4}$$

$$\sigma_{xx}^{S}(\omega) = \sigma_{yy}^{S}(\omega) = \sigma_{zz}^{S}(\omega) \approx \frac{ge^2v_F}{2\sqrt{2k_F}\pi^3\hbar(-i\omega+\gamma)}b^{\frac{3}{2}}. \tag{E.5}$$

All off-diagonal surface terms are zero.

APPENDIX F

REFLECTION IN THE VICINITY OF PLASMON RESONANCE

For oblique incidence $\theta \neq 0$ and small losses the calculations of the reflection in the vicinity of plasmon resonance have a technical subtlety, related to the presence of the term $n_X \cos\theta \left(\cos\theta_X - \sin\theta_X K_X\right)$ in Eq. (2.62). Indeed, at the plasmon frequency $n_X \to \infty$ as losses $\gamma \to 0$; however, for a plasmon we also have $K_X \to \frac{1}{\tan\theta_X}$, i.e. $\left(\cos\theta_X - \sin\theta_X K_X\right) \to 0$. One needs to treat the resulting uncertainty of the product with caution.

We substitute the relationship $\sin\theta_X = \frac{n_{up}\sin\theta}{n_X}$ into the expression for the refractive index of an extraordinary wave:

$$n_X^2 = \frac{\varepsilon_{yy}\varepsilon_{zz} - g^2}{\cos^2\theta_X \varepsilon_{zz} + \sin^2\theta_X \varepsilon_{yy}} = \frac{\varepsilon_{yy}\varepsilon_{zz} - g^2}{\varepsilon_{zz} - \sin^2\theta \left(\frac{n_{up}}{n_X}\right)^2 \left(\varepsilon_{zz} - \varepsilon_{yy}\right)},$$

which gives

$$n_X^2 = \varepsilon_{yy} - \frac{g^2}{\varepsilon_{zz}} + \sin^2\theta n_{up}^2 \left(1 - \frac{\varepsilon_{yy}}{\varepsilon_{zz}}\right) \tag{F.1}$$

In the case $\varepsilon_{yy} = \varepsilon_{zz} = \varepsilon_\perp$, Eq. (F.1) for an arbitrary angle θ leads to the familiar expression $n_X^2 = \varepsilon_\perp - \frac{g^2}{\varepsilon_\perp}$. Next we use Eq. (2.40):

$$K_X = \frac{ig - n_X^2 \sin\theta_X \cos\theta_X}{\varepsilon_{zz} - n_X^2 \sin^2\theta_X} = \frac{ig - n_{up}\sin\theta n_X \sqrt{1 - \left(\frac{\sin\theta n_{up}}{n_X}\right)^2}}{\varepsilon_{zz} - \sin^2\theta n_{up}^2}.$$

Consider the expression $n_X \cos\theta \left(\cos\theta_X - \sin\theta_X K_X\right)$:

$$n_X \cos\theta \left(\cos\theta_X - \sin\theta_X K_X\right)$$
$$= n_X \cos\theta \left(\cos\theta_X - \frac{ig\sin\theta_X - \sin\theta_X n_{up}\sin\theta n_X \sqrt{1 - \left(\frac{\sin\theta n_{up}}{n_X}\right)^2}}{\varepsilon_{zz} - \sin^2\theta n_{up}^2} \right)$$

$$= n_X \cos\theta \left(\sqrt{1 - \left(\frac{\sin\theta n_{up}}{n_X} \right)^2} - \frac{ig\frac{\sin\theta n_{up}}{n_X} - \sin^2\theta n_{up}^2 \sqrt{1 - \left(\frac{\sin\theta n_{up}}{n_X} \right)^2}}{\varepsilon_{zz} - \sin^2\theta n_{up}^2} \right).$$

The condition $\frac{n_X}{n_{up}} \gg 1$, which is satisfied at the plasmon frequency, allows one to simplify the above expressions for any angle of incidence θ

$$K_X = \frac{ig - n_X^2 \sin\theta_X \cos\theta_X}{\varepsilon_{zz} - n_X^2 \sin^2\theta_X} \approx \frac{ig - n_X n_{up} \sin\theta}{\varepsilon_{zz} - \sin^2\theta n_{up}^2} \tag{F.2}$$

$$n_X cos\theta \left(\cos\theta_X - \sin\theta_X K_X \right) \approx n_X \cos\theta \left(1 - \frac{ig\frac{\sin\theta n_{up}}{n_X} - \sin^2\theta n_{up}^2}{\varepsilon_{zz} - \sin^2\theta n_{up}^2} \right) \tag{F.3}$$

Since for $\frac{n_X}{n_{up}} \gg 1$ we always have $\sin\theta_X \ll 1$, the plasmon frequency always corresponds to $|\varepsilon_{zz}| \ll 1$ (at normal incidence, $\varepsilon_{zz} = 0$ exactly). Taking into account Eq. (F.1), we obtain $1 \gg |\varepsilon_{zz}| \sim n_X^{-2}$.

Now let us consider the range of incidence angles close to normal incidence, when $\sin^2\theta \ll 1$. Two cases need to be treated separately: $|\varepsilon_{zz}| \ll \sin^2\theta n_{up}^2 \ll 1$ and $\sin^2\theta n_{up}^2 \ll |\varepsilon_{zz}| \ll 1$.

(i) $|\varepsilon_{zz}| \ll sin^2\theta n_{up}^2 \ll 1$

In this case

$$n_X^2 \approx \varepsilon_{yy} - \frac{g^2}{\varepsilon_{zz}}, \quad K_X \approx \frac{n_X}{n_{up} sin\theta} \tag{F.4}$$

$$n_X \cos\theta \left(1 - \frac{ig\frac{\sin\theta n_{up}}{n_X} - \sin^2\theta n_{up}^2}{\varepsilon_{zz} - \sin^2\theta n_{up}^2} \right) \approx \frac{ig}{sin\theta n_{up}} \tag{F.5}$$

where $g = \frac{4\pi\sigma_{yz}^B}{\omega}$,

$$R \approx \frac{n_{up}^2 \sin\theta - i\frac{4\pi\sigma_{yz}^B}{\omega} + \frac{4\pi}{c}\sigma_{yz}^S n_X}{n_{up}^2 \sin\theta + i\frac{4\pi\sigma_{yz}^B}{\omega} + \frac{4\pi}{c}\sigma_{yz}^S n_X}. \tag{F.6}$$

For real $\sigma_{yz}^{(B,S)}$ we always have $|R| = 1$; however, the phase of the reflected field depends on the contribution of surface states. Since in the vicinity of plasmon resonance $n_X \sim \frac{1}{\sqrt{|\varepsilon_{zz}|}} \gg 1$, at these frequencies the contribution of surface states may become important. This is especially clear

in the limit of small enough angles, when $n_{up}^2 sin\theta \ll |\frac{4\pi\sigma_{yz}^B}{\omega}|$. In this case

$$R \approx \frac{-i\frac{4\pi\sigma_{yz}^B}{\omega} + \frac{4\pi}{c}\sigma_{yz}^S n_X}{+i\frac{4\pi\sigma_{yz}^B}{\omega} + \frac{4\pi}{c}\sigma_{yz}^S n_X}. \tag{F.7}$$

When the bulk contribution dominates we have $R = -1$, whereas if the surface contribution dominates we obtain $R = +1$, i.e. the phase of the reflected field flips.

The relative contribution of surface states is determined by the ratio $\frac{|\sigma_{yz}^S n_X|}{\frac{c}{\omega}|\sigma_{yz}^B|}$. Taking into account that $|n_X| \approx \frac{|g|}{\sqrt{|\varepsilon_{zz}|}}$ and $|g| = \frac{4\pi|\sigma_{yz}^B|}{\omega}$, the above ratio can be reduced to $\frac{\frac{4\pi|\sigma_{yz}^S|}{c}}{\sqrt{|\varepsilon_{zz}|}}$.

(ii) $\sin^2\theta n_{up}^2 \ll |\varepsilon_{zz}| \ll 1$

This case is similar to the one at $\theta = 0$. Indeed, for this range of parameters we obtain

$$n_X^2 \approx \varepsilon_{yy} - \frac{g^2}{\varepsilon_{zz}}, \quad K_X \approx \frac{ig}{\varepsilon_{zz}} \tag{F.8}$$

$$n_X cos\theta \left(1 - \frac{ig\frac{sin\theta n_{up}}{n_X} - sin^2\theta n_{up}^2}{\varepsilon_{zz}}\right) \approx n_X. \tag{F.9}$$

$$R \approx \frac{-n_X + \frac{4\pi}{c}\sigma_{yz}^S \frac{ig}{\varepsilon_{zz}}}{n_X + \frac{4\pi}{c}\sigma_{yz}^S \frac{ig}{\varepsilon_{zz}}} \tag{F.10}$$

Eqs. (F.8), (F.9) are the same as for the normal incidence. Eq. (F.10) can be obtained from the normal incidence formula Eq. (2.63) if $|\sigma_{yy}^S| \ll |\sigma_{yz}^S \frac{g}{\varepsilon_{zz}}|$ and $n_X \gg n_{up}$; the latter inequalities are valid near the plasmon resonance, where $n_X \sim \frac{1}{\sqrt{|\varepsilon_{zz}|}} \to \infty$.

For real values of $\sigma_{yz}^{(S)}$ we always have $|R| = 1$, but the phase of the reflected field depends on the contribution of surface states. Again, when the bulk contribution dominates we have $R = -1$, whereas if the surface contribution dominates we obtain $R = +1$.

The relative contribution of surface states is determined by the ratio $\frac{\frac{4\pi}{c}|\sigma_{yz}^S \frac{g}{\varepsilon_{zz}}|}{|n_X|}$. Again taking into account $|n_X| \approx \frac{|g|}{\sqrt{|\varepsilon_{zz}|}}$ and $|g| = \frac{4\pi|\sigma_{yz}^B|}{\omega}$ we obtain that the above ratio is reduced to exactly

the same expression as before: $\frac{4\pi|\sigma^S_{yz}|/c}{\sqrt{|\varepsilon_{zz}|}}$.

To summarize, the effect of surface states on the reflected wave is determined by the ratio

$$\frac{|\sigma^S_{yz}|}{c\sqrt{|\varepsilon_{zz}|}/4\pi}$$

and therefore becomes significant or dominant at the plasmon resonance frequency, when $\varepsilon_{zz} = \varepsilon^{(0)}_{zz} + i\frac{4\pi}{\omega}\sigma^B_{zz} \to 0$.

APPENDIX G

FINITE SAMPLE EFFECTS AND THE DEPOLARIZATION FIELD

Consider a sample shaped as a thin disk of radius R in the (x, y) plane and introduce polar coordinates r and φ on the disk. Consider a circularly polarized optical field incident on a disk, with electric field vector components

$$E_x = E_0 \cos(\omega t), \quad E_y = -E_0 \sin(\omega t), \tag{G.1}$$

where $\omega > 0$ corresponds to the clockwise rotation of the vector $\mathbf{E}$ and $\omega < 0$ to the counterclockwise rotation. The rotating field excites a rotating current in the disk:

$$j_x = j_0 \cos(\omega t + \phi), \quad j_y = -j_0 \sin(\omega t + \phi), \tag{G.2}$$

where the phase shift ϕ is determined by dissipative processes in the sample. The current given by Eqs. (G.2) corresponds to the rotating electric polarization:

$$P_x = P_0 \sin(\omega t + \phi), \quad P_y = P_0 \cos(\omega t + \phi), \tag{G.3}$$

where $P_0 = \frac{j_0}{\omega}$, i.e. $\dot{P}_x = j_x$, $\dot{P}_y = j_y$.

The current excitation by a time-dependent external field in a finite sample leads to an uncompensated time-dependent charge at a certain distance l from the disk edge. The magnitude of the charge depends on the specific mechanism of interaction of carriers with a boundary. Strictly speaking, both the current and the electric polarization are described by Eqs. (G.2),(G.3) only at a certain distance $\rho \geq l$ from the disk edge. Since we don't want to get into the details of the carrier-boundary interaction, we will assume that the width of the boundary layer is much smaller than the disk radius: $l \ll R$.

Let's denote an uncompensated charge per unit length along the disk edge as $\delta\rho\,(t,\varphi)$. It can be expressed as $\delta\rho = P_r$, where P_r is the normal component of the polarization vector: $P_r = P_x\cos\varphi + P_y\sin\varphi$. The edge charge leads to generation of the depolarization field $\mathbf{E}_p$ [82]. For a uniform external field given by Eqs. (G.1), we can use the solution of a corresponding electrostatic problem in [82]. If we approximate a thin disk with an ellipsoid of rotation with semiminor axis $a \ll R$, we get

$$\mathbf{E}_p = -\frac{\pi^2}{2R}\mathbf{P},$$

where $\mathbf{P}$ is a 2D density of the dipole moment. Taking into account the effect of the depolarization field and Eqs. (G.1)-(G.3), we obtain

$$\sigma\left[E_0 - i\frac{\pi^2}{2R\omega}j_0e^{-i\phi}\right] = j_0e^{-i\phi},\;\; j_0e^{-i\phi} = E_0\frac{\sigma}{1+i\sigma\frac{\pi^2}{2R\omega}},$$

where σ is a 2D conductivity of the layer including relaxation processes. Using Eq. (4.31) for the magnetic moment, we arrive at the expression which generalizes Eq. (4.35):

$$m_z = m_z^{(0)}\frac{\omega^4}{\left(\omega^2-\omega_p^2\right)^2+\omega^2\tau^{-2}}, \tag{G.4}$$

where $m_z^{(0)}$ is the magnitude of the magnetic moment generated by a circularly polarized field without including dissipation and depolarization effects, $\omega_p = \sqrt{\frac{\pi g e^2 p_F v_F}{8\hbar^2 R}}$, where $\frac{\partial W}{\partial p} = v_F$. The resonant frequency ω_p in Eq. (G.4) coincides up to a numerical factor with the frequency of 2D plasmons in graphene at wavelength $2R$; see e.g. [177]. In the limit $R \to \infty$ Eq. (G.4) gives the result for an infinite medium.

APPENDIX H

IFE IN GRAPHENE BEYOND SMALL PERTURBATION

Here we consider an incident radiation of an arbitrarily strong intensity and go beyond the linear approximation. Let's again assume a circularly polarized field given by Eqs. (G.1). The kinetic equation Eq. (4.6) with $\mathbf{H}=\mathbf{0}$ and relaxation operator $\hat{Q}(f)=\frac{f_F-f}{\tau}$ takes the form

$$\frac{\partial f(\mathbf{p},t)}{\partial t}-eE_0\cos(\omega t)\frac{\partial f(\mathbf{p},t)}{\partial p_x}+eE_0\sin(\omega t)\frac{\partial f(\mathbf{p},t)}{\partial p_y}=\frac{f_F(p)-f(\mathbf{p},t)}{\tau}. \tag{H.1}$$

Its solution in quadratures can be found by the method of characteristics. At times $t\gg\tau$ for any initial conditions the solution approaches

$$f=e^{-\frac{t}{\tau}}\frac{1}{\tau}\int_0^t dt' e^{\frac{t'}{\tau}} f_F\left[p_x+\frac{eE_0}{\omega}(\sin\omega t-\sin\omega t'),p_y+\frac{eE_0}{\omega}(\cos\omega t-\cos\omega t')\right] \tag{H.2}$$

After cumbersome but fairly straightforward derivation, the surface current density $\mathbf{j}=-egv_F\int\frac{\mathbf{p}}{p}fd^2p$ can be found:

$$j_x=-en_FV_x(t),\quad j_y=-en_FV_y(t). \tag{H.3}$$

Here the functions $V_{x,y}(t)$ are given by

$$V_x(t)=\frac{v_F}{1-e^{-\frac{2\pi}{|\omega|\tau}}}\int_0^{\frac{2\pi}{|\omega|\tau}}e^{-z}\Phi\left(\frac{eE_0}{\omega p_F},\omega\tau z\right)\{[1-\cos(\omega\tau z)]\sin(\omega t)+\sin(\omega\tau z)\cos(\omega t)\}dz \tag{H.4}$$

$$V_y(t)=\frac{v_F}{1-e^{-\frac{2\pi}{|\omega|\tau}}}\int_0^{\frac{2\pi}{|\omega|\tau}}e^{-z}\Phi\left(\frac{eE_0}{\omega p_F},\omega\tau z\right)\{[1-\cos(\omega\tau z)]\cos(\omega t)+\sin(\omega\tau z)\sin(\omega t)\}dz \tag{H.5}$$

where

$$\Phi\left(\frac{eE_0}{\omega p_F},\omega\tau z\right)=\left(\frac{2eE_0}{\pi\omega p_F}\right)\int_0^{\pi}\frac{\sin^2\alpha}{\sqrt{1+4\left(\frac{eE_0}{\omega p_F}\right)^2\sin^2\left(\frac{\omega\tau z}{2}\right)+4\left|\frac{eE_0}{\omega p_F}\sin\left(\frac{\omega\tau z}{2}\right)\right|\cos\alpha}}d\alpha. \tag{H.6}$$

It follows from (H.3-H.6) that the surface current density vector can be presented in the form of Eqs. (G.2), in which

$$j_0 = ev_F n_F F\left(\frac{eE_0}{\omega p_F}, \omega\tau\right), \tag{H.7}$$

$$F\left(\frac{eE_0}{\omega p_F}, \omega\tau\right) = \left(1 - e^{-\frac{2\pi}{|\omega|\tau}}\right)^{-1} \times \left(\left\{\int_0^{\frac{2\pi}{|\omega|\tau}} e^{-z}\Phi\left(\frac{eE_0}{\omega p_F}, \omega\tau z\right)\left[1 - \cos\left(\omega\tau z\right)\right] dz\right\}^2 + \left\{\int_0^{\frac{2\pi}{|\omega|\tau}} e^{-z}\Phi\left(\frac{eE_0}{\omega p_F}, \omega\tau z\right)\sin\left(\omega\tau z\right) dz\right\}^2\right)^{1/2}. \tag{H.8}$$

The value of the phase shift ϕ does not matter in this case.

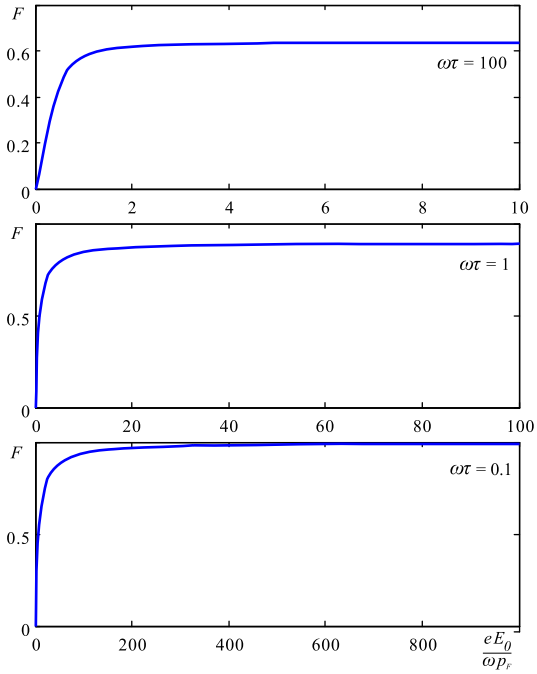

Figure H.1: $F\left(\frac{eE_0}{\omega p_F}, \omega\tau\right)$ as a function of the parameter $\frac{eE_0}{\omega p_F}$ at different $\omega\tau$.

Figure H.1 shows the dependence $F\left(\frac{eE_0}{\omega p_F}, \omega\tau\right)$ on the parameter $\frac{eE_0}{\omega p_F}$ at different $\omega\tau$. There is an obvious saturation effect at $\frac{eE_0}{\omega p_F} \gg 1$.

The current defined by Eqs. (G.2),(H.8) corresponds to the surface polarization given by Eq. (G.3). Using the expression Eq. (4.31) for the magnetization, we arrive at

$$m_z = \frac{e n_F v_F^2}{2c\omega} F^2 \left(\frac{eE_0}{\omega p_F}, \omega\tau \right). \tag{H.9}$$

For weak fields, when $\frac{eE_0}{\omega p_F} \ll 1$, we have the limit

$$\Phi \left(\frac{eE_0}{\omega p_F}, \omega\tau z \right) \cong \frac{eE_0}{\omega p_F}, \qquad F \left(\frac{eE_0}{\omega p_F}, \omega\tau \right) \cong \frac{eE_0}{p_F \sqrt{\tau^{-2} + \omega^2}}$$

In this case Eq. (H.9) is reduced to Eq. (4.35) for $\tilde{E}_y = -i\, \tilde{E}_x$, $\tilde{E}_x = E_0$.

The expression in Eq. (H.9) allows one to estimate the magnitude of the IFE for strong fields, when $\frac{eE_0}{\omega p_F} \geq 1$.

APPENDIX I

QUANTIZATION OF A CAVITY SURFACE PLASMON FIELD

Consider a planar cavity oriented parallel to (x, y) plane and sandwiched between two layers of material with isotropic dielectric constant $\varepsilon(\omega)$ which could be dielectric or metal. The transverse size of a cavity along z is from $z = -d$ to $z = +d$. The dielectric constant inside the cavity is $\varepsilon_g(\omega)$, also assumed isotropic.

I.1 Spatial structure of the field and frequency dispersion

Whether or not the field is quantized, its distribution in space and frequencies of modes are determined from solving the boundary value problem of classical electrodynamics. Here we consider the field localized to a subwavelength region, to scales $l_{SP} \ll \frac{c}{\varepsilon_g(\omega)\omega}, \frac{c}{|\varepsilon(\omega)|\omega}$, which allows us to use electrostatic approximation. We seek the solution for the electric potential as $\varphi = \Phi(z) e^{i\mathbf{k}\cdot\mathbf{r} - i\omega t}$, where the 2D vectors $\mathbf{r}, \mathbf{k}$ are in the x, y plane. The Poisson's equation for the potential in every region has a form

$$\frac{\partial^2 \Phi}{\partial z^2} = k^2 \Phi \tag{I.1}$$

In the region $z < -d$ the solution is $\Phi = \Phi_- e^{kz}$, whereas in $z > d$ the solution is $\Phi = \Phi_+ e^{-kz}$.

Since the cavity is symmetric with respect to $z = 0$, the spatial distribution inside the cavity can be either symmetric, $\Phi = \Phi_s \cosh(kz)$, or antisymmetric, $\Phi = \Phi_{as} \sinh(kz)$.

The boundary conditions include the continuity of the potential and the z-component of the electric induction.

(i) Symmetric solution: $\Phi_- = \Phi_+$. Substituting $z = -d$ the boundary conditions give

$$\tanh(kd) = -\frac{\varepsilon}{\varepsilon_g}. \tag{I.2}$$

i.e. we always need $\varepsilon(\omega) < 0$ for positive ε_g. In the limit $kd \gg 1$, Eq. (I.2) corresponds to the

dispersion equation for a surface plasmon at the boundary between the two infinite media

$$1 = -\frac{\varepsilon}{\varepsilon_g}, \tag{I.3}$$

whereas in the opposite limit $kd \longrightarrow 0$ and assuming that ε_g is positive and not too small, we obtain a standard dispersion equation for a plasmon in the bulk medium: $\varepsilon(\omega) = 0$.

Therefore, when kd changes from 0 to ∞ the symmetric surface plasmon exists within a frequency bandwidth determined by the variation of $\frac{\varepsilon}{\varepsilon_g}$ from -0 to -1.

(ii) Antisymmetric solution: $\Phi_- = -\Phi_+$. The boundary conditions give

$$\coth(kd) = -\frac{\varepsilon}{\varepsilon_g}. \tag{I.4}$$

i.e. again $\varepsilon(\omega) < 0$ for positive ε_g .

In the limit of a wide cavity, when $kd \gg 1$ the solution should again corresponds to the surface plasmon at the boundary between the two infinite media, i.e. we arrive at Eq. (I.3).

In the opposite limit $kd \longrightarrow 0$ and assuming that ε_g is positive and not too small, we obtain that $\varepsilon(\omega) \longrightarrow -\infty$. Therefore, when kd changes from 0 to ∞ the antisymmetric surface plasmon exists within a frequency bandwidth determined by the variation of $\frac{\varepsilon(\omega)}{\varepsilon_g(\omega)}$ from $-\infty$ to -1.

Note that in any case the electrostatic solution requires that $k \gg \frac{\varepsilon_g \omega}{c}, \frac{|\varepsilon|\omega}{c}$.

I.2 Field quantization

Following [110], we consider a cylinder with an axis of symmetry along z (i.e. orthogonal to the boundaries) and area S in the x, y plane. We assume that the field goes to 0 when $z \longrightarrow \pm\infty$ and satisfies periodic boundary conditions at the side surface of the cylinder:

$$\hat{\mathbf{E}} = \sum_{\mathbf{k},p} \mathbf{E}_{\mathbf{k},p}(z)\, e^{i\mathbf{k}\cdot\mathbf{r} - i\omega_{\mathbf{k},p} t} \hat{c}_{\mathbf{k},p} + H.c., \tag{I.5}$$

where $p = s, as$.

The spatial distribution of the field $\mathbf{E}_{\mathbf{k},p}(z)\, e^{i\mathbf{k}\cdot\mathbf{r}}$ and its frequency $\omega_{\mathbf{k},p}$ are given by the so-

lution of the classical boundary value problem in the previous section. The Hamiltonian $\hat{H} = \hbar \sum_{\mathbf{k},p} \omega_{\mathbf{k},p} \left(\hat{c}^{\dagger}_{\mathbf{k},p} \hat{c}_{\mathbf{k},p} + \frac{1}{2} \right)$ can be obtained from the normalization condition [110]:

$$S \int_{-\infty}^{\infty} \left(\frac{\partial \left[\omega \varepsilon \left(\omega, z \right) \right]}{\partial \omega} \mathbf{E}^{*}_{\mathbf{k},p} \left(z \right) \mathbf{E}_{\mathbf{k},p} \left(z \right) + \mathbf{B}^{*}_{\mathbf{k},p} \left(z \right) \mathbf{B}_{\mathbf{k},p} \left(z \right) \right) dz = 4\pi \hbar \omega_{\mathbf{k},p} \tag{I.6}$$

where $S \int_{-\infty}^{\infty} \left(\cdots \right) dz = \int_{V} \left(\cdots \right) dV$. For periodic or "cavity" boundary conditions we always have [110]:

$$\int_{V} \mathbf{B}^{*}_{\mathbf{k},p} \mathbf{B}_{\mathbf{k},p} dV = \int_{V} \varepsilon \mathbf{E}^{*}_{\mathbf{k},p} \mathbf{E}_{\mathbf{k},p} dV, \tag{I.7}$$

Which allows us to rewrite Eq. (I.6) as

$$S \int_{-\infty}^{\infty} \frac{\partial \left[\omega^2 \varepsilon \left(\omega, z \right) \right]}{\omega \partial \omega} \mathbf{E}^{*}_{\mathbf{k},p} \left(z \right) \mathbf{E}_{\mathbf{k},p} \left(z \right) dz = 4\pi \hbar \omega_{\mathbf{k},p}. \tag{I.8}$$

For the fields $\mathbf{E}_{\mathbf{k},p} \left(z \right)$ obtained in the electrostatic approximation, we always obtain $\int_{V} \varepsilon \mathbf{E}^{*}_{\mathbf{k},p} \mathbf{E}_{\mathbf{k},p} dV = 0$, since in this approximation $\mathbf{B}_{\mathbf{k},p} = 0$. In this case we can use the normalization in the electrostatic limit:

$$S \int_{-\infty}^{\infty} \frac{\partial \left[\omega \varepsilon \left(\omega, z \right) \right]}{\partial \omega} \mathbf{E}^{*}_{\mathbf{k},p} \left(z \right) \mathbf{E}_{\mathbf{k},p} \left(z \right) dz = 4\pi \hbar \omega_{\mathbf{k},p}. \tag{I.9}$$

As a result, we obtain:

(i) Symmetric mode ($p = s$). The normalization condition:

$$S \left| \Phi_{s} \right|^2 k \left[\frac{\partial \left(\omega \varepsilon_{g} \right)}{\partial \omega} \sinh \left(2kd \right) + 2 \cosh^2 \left(kd \right) \frac{\partial \left(\omega \varepsilon \right)}{\partial \omega} \right] = 4\pi \hbar \omega_{\mathbf{k},s} \tag{I.10}$$

(ii)Antisymmetric mode ($p = as$). The normalization condition:

$$S \left| \Phi_{as} \right|^2 k \left[\frac{\partial \left(\omega \varepsilon_{g} \right)}{\partial \omega} \sinh \left(2kd \right) + 2 \sinh^2 \left(kd \right) \frac{\partial \left(\omega \varepsilon \right)}{\partial \omega} \right] = 4\pi \hbar \omega_{\mathbf{k},as} \tag{I.11}$$

Taking for simplicity $\varepsilon_{g} = 1$ (air) and $\varepsilon \left(\omega \right) = 1 - \frac{\omega_{pl}^2}{\omega^2}$ (Drude dispersion) gives

(i) Symmetric mode ($p = s$):

$$S\left|\Phi_s\right|^2 k\left[2\sinh\left(2kd\right)+4\cosh^2\left(kd\right)\right]=4\pi\hbar\omega_{\mathbf{k},s} \tag{I.12}$$

(ii)Antisymmetric mode ($p=as$):

$$S\left|\Phi_{as}\right|^2 k\left[2\sinh\left(2kd\right)+4\sinh^2\left(kd\right)\right]=4\pi\hbar\omega_{\mathbf{k},as} \tag{I.13}$$

In order to calculate the coupling strength, it is important to know the magnitude of the normalization field $\mathbf{E}_{\mathbf{k},p}$ at the cavity boundary. Introducing the notation $\mathbf{E}_{\mathbf{k},p}\left(-d\right)=\tilde{\mathbf{E}}_{\mathbf{k},p}$ and taking into account Eqs. (I.1),(I.1),(I.12) and (I.13), we obtain

$$\tilde{\mathbf{E}}_{\mathbf{k},s}=\left[\mathbf{z}_0 k\sinh\left(kd\right)-i\mathbf{k}\cosh\left(kd\right)\right]\sqrt{\frac{4\pi\hbar\omega_{\mathbf{k},s}}{Sk\left[2\sinh\left(2kd\right)+4\cosh^2\left(kd\right)\right]}}, \tag{I.14}$$

where

$$\omega_{\mathbf{k},s}=\frac{\omega_{pl}}{\sqrt{1+\tanh\left(kd\right)}}; \tag{I.15}$$

$$\tilde{\mathbf{E}}_{\mathbf{k},as}=\left[-\mathbf{z}_0 k\cosh\left(kd\right)-i\mathbf{k}\sinh\left(kd\right)\right]\sqrt{\frac{4\pi\hbar\omega_{\mathbf{k},as}}{Sk\left[2\sinh\left(2kd\right)+4\cosh^2\left(kd\right)\right]}}, \tag{I.16}$$

where

$$\omega_{\mathbf{k},as}=\frac{\omega_{pl}}{\sqrt{1+\coth\left(kd\right)}}. \tag{I.17}$$

Figure I.1 shows an example of normalized frequencies and field amplitudes of the symmetric and antisymmetric cavity modes given by Eqs. (I.14)-(I.17) as a function of normalized time Ωt when the cavity height d is modulated as $d(t)=d_0(1+0.1\sin(\Omega t))$. In this example $kd_0=1$. Even though the dependence of frequencies and field amplitudes on kd is strongly nonlinear, their modulation amplitudes remain small.

I.3 Field quantization when the cavity thickness is changing adiabatically

Let the cavity half-thickness d change with time adiabatically, $d\left(t\right)$, for given k and S. In this case the adiabatic invariant $\frac{W_{\mathbf{k},p}}{\omega_{\mathbf{k},p}}$ is conserved, where $W_{\mathbf{k},p}$ is an average (observable) energy of the

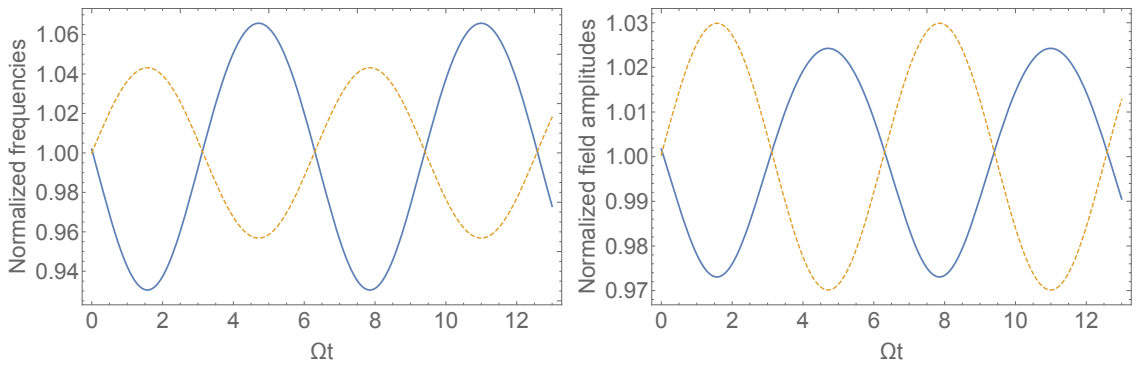

(a) (b)

Figure I.1: (a) Normalized frequencies and (b) normalized field amplitudes of the symmetric (solid line) and antisymmetric (dashed line) cavity modes given by Eqs. (I.14)-(I.17) as a function of normalized time Ωt when the cavity height d is modulated as $d(t) = d_0(1 + 0.1\sin(\Omega t))$, where $kd_0 = 1$. Frequencies and field amplitudes are normalized by their time-averaged values.

mode. This is equivalent to conservation of the number of photons in a cavity with slowly changing parameters. As is well known, the photon number is conserved for a standard Hamiltonian of an ensemble of harmonic oscillators:

$$\hat{H} = \hbar \sum_{\mathbf{k},p} \omega_{\mathbf{k},p} \left(\hat{c}^{\dagger}_{\mathbf{k},p} \hat{c}_{\mathbf{k},p} + \frac{1}{2} \right), \tag{I.18}$$

whereas the normalization field is still described by Eqs. (I.10),(I.11). At the same time, all results will contain the variables $\omega_{\mathbf{k},p}(t)$ and $\tilde{\mathbf{E}}_{\mathbf{k},p}(t)$ which depend on time through their dependence on the parameter $d(t)$.

APPENDIX J

THE STOCHASTIC EQUATION OF EVOLUTION FOR THE STATE VECTOR

The description of open quantum systems within the stochastic equation of evolution for the state vector is usually formulated for a Monte-Carlo type numerical scheme, e.g. the method of quantum jumps [158, 159]. We developed an approach suitable for analytic derivations. Our stochastic equation of evolution is basically the Schrödinger equation modified by adding a linear relaxation operator and the noise source term with appropriate correlation properties. The latter are related to the parameters of the relaxation operator in such a way that the expressions for the statistically averaged quantities satisfy certain physically meaningful conditions.

The protocol of introducing the relaxation operator with a corresponding noise source term to the quantum dynamics is well known in the Heisenberg picture, where it is called the Heisenberg-Langevin method [158, 178, 160]. Here we use a conceptually similar approach for the Schrödinger equation. The general form of the stochastic equation of evolution was derived from the Heisenberg-Langevin equations in [154]. Here we outline how certain physically reasonable constraints on the observables determine the correlation properties of the noise sources.

J.1 General properties of the stochastic equation of evolution for the state vector

An open system interacting with a reservoir is generally in a mixed state and should be described by the density matrix. We are describing the state of the system with a state vector which has a fluctuating component. For example, in a certain basis $|\alpha\rangle$ the state vector will be $C_\alpha(t) = \overline{C_\alpha} + \widetilde{C_\alpha}$, where the fluctuating component is denoted with a wavy bar. The elements of the density matrix of the corresponding mixed state are $\rho_{\alpha\beta} = \overline{C_\alpha C_\beta^*} = \overline{C_\alpha} \cdot \overline{C_\beta^*} + \overline{\widetilde{C_\alpha} \cdot \widetilde{C_\beta}^*}$.

The stochastic equation of evolution for the state vector and its Hermitian conjugate have the general form [154]

$$\frac{d}{dt}|\Psi\rangle = -\frac{i}{\hbar}\hat{H}_{eff}|\Psi\rangle - \frac{i}{\hbar}|\mathfrak{R}(t)\rangle \tag{J.1}$$

$$\frac{d}{dt}\langle\Psi| = \frac{i}{\hbar}\langle\Psi|\hat{H}_{eff}^{\dagger} + \frac{i}{\hbar}\langle\Re(t)|, \tag{J.2}$$

where the non-Hermitian component of the effective Hamiltonian $\hat{H}_{eff}$ corresponds to the relaxation operator and the term $|\Re(t)\rangle$ denotes the noise term. We will also need Eqs. (J.1) and (J.2) in a particular basis $|\alpha\rangle$:

$$\frac{d}{dt}C_{\alpha} = -\frac{i}{\hbar}\sum_{\nu}\left(\hat{H}_{eff}\right)_{\alpha\nu}C_{\nu} - \frac{i}{\hbar}\Re_{\alpha}, \tag{J.3}$$

$$\frac{d}{dt}C_{\alpha}^{*} = \frac{i}{\hbar}\sum_{\nu}C_{\nu}^{*}\left(\hat{H}_{eff}^{\dagger}\right)_{\nu\alpha} + \frac{i}{\hbar}\Re_{\alpha}^{*}, \tag{J.4}$$

where $\Re_{\alpha} = \langle\alpha|\Re\rangle$, $\left(\hat{H}_{eff}\right)_{\alpha\beta} = \langle\alpha|\hat{H}_{eff}|\beta\rangle$.

In general, statistical properties of noise that ensure certain physically meaningful requirements impose certain constraints on the noise source $|\Re\rangle$ which enters the right-hand side of the stochastic equation for the state vector. In particular, it is natural to require that the statistically averaged quantity $\overline{|\Re\rangle} = 0$. We will also require that the noise source $|\Re\rangle$ has the correlation properties that preserve the norm of the state vector averaged over the reservoir statistics:

$$\overline{\langle\Psi(t)|\Psi(t)\rangle} = 1. \tag{J.5}$$

J.2 Noise correlator

The solution to Eqs. (J.1) and (J.2) can be formally written as

$$|\Psi\rangle = e^{-\frac{i}{\hbar}\hat{H}_{eff}t}|\Psi_0\rangle - \frac{i}{\hbar}\int_0^t e^{\frac{i}{\hbar}\hat{H}_{eff}(\tau-t)}|\Re(\tau)\rangle\, d\tau, \tag{J.6}$$

$$\langle\Psi| = \langle\Psi_0|e^{\frac{i}{\hbar}\hat{H}_{eff}^{\dagger}t} + \frac{i}{\hbar}\int_0^t \langle\Re(\tau)|e^{-\frac{i}{\hbar}\hat{H}_{eff}^{\dagger}(\tau-t)}d\tau, \tag{J.7}$$

In the basis $|\alpha\rangle$, Eqs. (J.6),(J.7) can be transformed into

$$C_{\alpha} = \langle\alpha|e^{-\frac{i}{\hbar}\hat{H}_{eff}t}|\Psi_0\rangle - \frac{i}{\hbar}\int_0^t \langle\alpha|e^{\frac{i}{\hbar}\hat{H}_{eff}(\tau-t)}|\Re(\tau)\rangle\, d\tau, \tag{J.8}$$

$$C_\alpha^* = \langle \Psi_0 | \, e^{\frac{i}{\hbar}\hat{H}_{eff}^\dagger t} \, |\alpha\rangle + \frac{i}{\hbar}\int_0^t \langle \mathfrak{R}(\tau)| \, e^{-\frac{i}{\hbar}\hat{H}_{eff}^\dagger(\tau - t)} \, |\alpha\rangle \, d\tau. \tag{J.9}$$

In order to calculate the observables, we need to know the expressions for the averaged dyadic combinations of the amplitudes. We can find them using Eqs. (J.3) and (J.4):

$$\begin{aligned} \frac{d}{dt}\overline{C_\alpha C_\beta^*} &= -\frac{i}{\hbar}\sum_\nu \left(H_{\alpha\nu}^{(h)} \overline{C_\nu C_\beta^*} - \overline{C_\alpha C_\nu^*} H_{\nu\beta}^{(h)} \right) - \frac{i}{\hbar}\sum_\nu \left(H_{\alpha\nu}^{(ah)} \overline{C_\nu C_\beta^*} + \overline{C_\alpha C_\nu^*} H_{\nu\beta}^{(ah)} \right) \\ &\quad + \left(-\frac{i}{\hbar}\overline{C_\beta^* \mathfrak{R}_\alpha} + \frac{i}{\hbar}\overline{\mathfrak{R}_\beta^* C_\alpha} \right), \end{aligned} \tag{J.10}$$

where we separated the Hermitian and anti-Hermitian components of the effective Hamiltonian: $\langle \alpha | \, \hat{H}_{eff} \, | \beta \rangle = H_{\alpha\beta}^{(h)} + H_{\alpha\beta}^{(ah)}$. Substituting Eqs. (J.8) and (J.9) into the last term in Eq. (J.10), we obtain

$$\begin{aligned} -\frac{i}{\hbar}\overline{C_\beta^* \mathfrak{R}_\alpha} + \frac{i}{\hbar}\overline{C_\alpha \mathfrak{R}_\beta^*} &= \frac{1}{\hbar^2}\int_{-t}^0 \overline{\langle \mathfrak{R}(t+\xi)| \, e^{-\frac{i}{\hbar}\hat{H}_{eff}^\dagger \xi} \, |\beta\rangle \, \langle \alpha \, | \mathfrak{R}(t)\rangle} d\xi \\ &\quad + \frac{1}{\hbar^2}\int_{-t}^0 \overline{\langle \mathfrak{R}(t) \, |\beta\rangle \, \langle \alpha| \, e^{\frac{i}{\hbar}\hat{H}_{eff}\xi} \, |\mathfrak{R}(t+\xi)\rangle} d\xi. \end{aligned}$$

To proceed further with analytical results, we need to evaluate these integrals. The simplest situation is when the noise source terms are delta-correlated in time (Markovian). In this case only the point $\xi = 0$ contributes to the integrals. As a result, Eq. (J.10)) is transformed to

$$\frac{d}{dt}\overline{C_\alpha C_\beta^*} = -\frac{i}{\hbar}\sum_\nu \left(H_{\alpha\nu}^{(h)} \overline{C_\nu C_\beta^*} - \overline{C_\alpha C_\nu^*} H_{\nu\beta}^{(h)} \right) - \frac{i}{\hbar}\sum_\nu \left(H_{\alpha\nu}^{(ah)} \overline{C_\nu C_\beta^*} + \overline{C_\alpha C_\nu^*} H_{\nu\beta}^{(ah)} \right) + D_{\alpha\beta}, \tag{J.11}$$

where the correlator $D_{\alpha\beta}$ is defined by

$$\overline{\mathfrak{R}_\beta^*(t+\xi)\,\mathfrak{R}_\alpha(t)} = \overline{\mathfrak{R}_\beta^*(t)\,\mathfrak{R}_\alpha(t+\xi)} = \hbar^2 \delta(\xi) \, D_{\alpha\beta}. \tag{J.12}$$

The time derivative of the norm of the state vector is given by

$$\frac{d}{dt}\sum_{\alpha}\overline{|C_\alpha|^2} = -\sum_{\alpha}\left[\frac{i}{\hbar}\sum_{\nu}\left(H^{(ah)}_{\alpha\nu}\overline{C_\nu C^*_\alpha} + \overline{C_\alpha C^*_\nu}H^{(ah)}_{\nu\alpha}\right) - D_{\alpha\alpha}\right]. \tag{J.13}$$

Clearly, the components $D_{\alpha\alpha}$ of the noise correlator need to compensate the decrease in the norm due to the anti-Hermitian component of the effective Hamiltonian. Therefore the expressions for $H^{(ah)}_{\alpha\beta}$and $D_{\alpha\alpha}$ have to be mutually consistent. This is the manifestation of the fluctuation-dissipation theorem [174].

As an example, consider a simple diagonal anti-Hermitian operator $H^{(ah)}_{\alpha\nu}$:

$$H^{(ah)}_{\alpha\nu} = -i\hbar\gamma_\alpha\delta_{\alpha\nu} \tag{J.14}$$

and introduce the following models:

(i) Populations relax much slower than coherences (expected for condensed matter systems). In this case we can choose $D_{\alpha\neq\beta} = 0$, $D_{\alpha\alpha} = 2\gamma_\alpha\overline{|C_\alpha|^2}$; within this model the population at each state will be preserved.

(ii) The state $\alpha = \alpha_{down}$ has a minimal energy, while the reservoir temperature $T = 0$. In this case it is expected that all populations approach zero in equilibrium whereas the occupation number of the ground state approaches 1, similar to the Weisskopf-Wigner model. The adequate choice of correlators is $D_{\alpha\neq\beta} = 0$, $D_{\alpha\alpha} \propto \delta_{\alpha\alpha_{down}}$, $\gamma_{\alpha_{down}} = 0$. The expression for the remaining nonzero correlator,

$$D_{\alpha_{down}\alpha_{down}} = \sum_{\alpha\neq\alpha_{down}} 2\gamma_\alpha\overline{|C_\alpha|^2}, \tag{J.15}$$

ensures the conservation of the norm:

$$\frac{d}{dt}\sum_{\alpha\neq\alpha_{down}}\overline{|C_\alpha|^2} = -\sum_{\alpha\neq\alpha_{down}} 2\gamma_\alpha\overline{|C_\alpha|^2} = -\frac{d}{dt}\overline{|C_{\alpha_{down}}|^2}.$$

This is an example of the correlator's dependence on the state vector that we discussed before.

(iii) A two-level system with states $|0\rangle$ and $|1\rangle$ and relaxation rates of populations $\frac{1}{T_1}$ and

coherence $\frac{1}{T_2} = \frac{1}{2T_1} + \gamma_{el}$, where γ_{el} is an elastic relaxation constant. If the equilibrium corresponds to a zero population of the excited state, we have to choose

$$\gamma_0 = 0,\ \gamma_1 = \frac{1}{T_2},\ D_{10} = D_{01} = 0,\ D_{00} = \frac{1}{T_1}\overline{|C_1|^2},\ D_{11} = 2\gamma_{el}\overline{|C_1|^2}.$$

It is easy to see that with this choice of relaxation constants and noise correlators Eqs. (J.11) for $\overline{C_\alpha C_\beta^*}$ where $\alpha, \beta = 1, 2$ coincide with well-known equations for the density matrix $\rho_{\alpha\beta}$ of a two-level system [158, 179].

J.3 Comparison with the Lindblad method

One can choose the anti-Hermitian Hamiltonian $H_{\alpha\beta}^{(ah)}$ and correlators $D_{\alpha\beta}$ in the stochastic equation of motion in such a way that Eq. (J.11) for the dyadics $\overline{C_n C_m^*}$ correspond exactly to the equations for the density matrix elements in the Lindblad approach. Indeed, the Lindblad form of the master equation has the form [158, 159]

$$\frac{d}{dt}\hat{\rho} = -\frac{i}{\hbar}\left[\hat{H}, \hat{\rho}\right] + \hat{L}\left(\hat{\rho}\right) \tag{J.16}$$

where $\hat{L}\left(\hat{\rho}\right)$ is the Lindbladian:

$$\hat{L}\left(\hat{\rho}\right) = -\frac{1}{2}\sum_k \gamma_k \left(\hat{l}_k^\dagger \hat{l}_k \hat{\rho} + \hat{\rho}\hat{l}_k^\dagger \hat{l}_k - 2\hat{l}_k \hat{\rho} \hat{l}_k^\dagger\right), \tag{J.17}$$

Operators $\hat{l}_k$ in Eq. (J.17) and their number are determined by the model which describes the coupling of the dynamical system to the reservoir. The form of the relaxation operator given by Eq. (J.17) preserves automatically the conservation of the trace of the density matrix, whereas the specific choice of relaxation constants ensures that the system approaches a proper steady state given by thermal equilibrium or supported by an incoherent pumping.

Eq. (J.16) is convenient to represent in a slightly different form:

$$\frac{d}{dt}\hat{\rho} = -\frac{i}{\hbar}\left(\hat{H}_{eff}\hat{\rho} - \hat{\rho}\hat{H}_{eff}^\dagger\right) + \delta\hat{L}\left(\hat{\rho}\right) \tag{J.18}$$

where

$$\hat{H}_{eff} = \hat{H} - i\hbar \sum_k \gamma_k \hat{l}_k^\dagger \hat{l}_k, \quad \delta\hat{L}\left(\hat{\rho}\right) = \sum_k \gamma_k \hat{l}_k \hat{\rho} \hat{l}_k^\dagger. \tag{J.19}$$

Writing the anti-Hermitian component of the Hamiltonian in Eqs. (J.3),(J.4) as

$$H_{\alpha\beta}^{(ah)} = -i\hbar \left\langle \alpha \right| \sum_k \gamma_k \hat{l}_k^\dagger \hat{l}_k \left| \beta \right\rangle, \tag{J.20}$$

and defining the corresponding correlator of the noise source as

$$\overline{\mathfrak{R}_\beta^* \left(t+\xi\right) \mathfrak{R}_\alpha \left(t\right)} = \hbar^2 \delta\left(\xi\right) D_{\alpha\beta}, \quad D_{\alpha\beta} = \left\langle \alpha \right| \delta\hat{L}\left(\hat{\rho}\right) \left| \beta \right\rangle_{\rho_{nm} = \overline{C_n C_m^*}}, \tag{J.21}$$

we obtain the solution in which averaged over noise statistics dyadics $\overline{C_n C_m^*}$ correspond exactly to the elements of the density matrix within the Lindblad method.

Instead of deriving the stochastic equation of evolution of the state vector from the Heisenberg-Langevin equations we could postulate it from the very beginning. After that, we could justify the choice of the effective Hamiltonian and noise correlators by ensuring that they lead to the same observables as the solution of the density matrix equations with the relaxation operator in Lindblad form [159, 180]. However, the demonstration of direct connection between the stochastic equation of evolution of the state vector and the Heisenberg-Langevin equation provides an important physical insight.

J.4 Relaxation rates for coupled subystems interacting with a reservoir

Whenever we have several coupled subsystems (such as electrons, photon modes, phonons etc.), each coupled to its reservoir, the determination of relaxation rates of the whole system becomes nontrivial. The problem can be solved if we assume that these "partial" reservoirs are statistically independent.In this case it is possible to add up partial Lindbladians and obtain the total effective Hamiltonian.

Consider again the Hamiltonian (5.27) for a two-level electron system resonantly coupled to

two quantized EM cavity modes,

$$\hat{H} = \hbar\omega_a(t)\left(\hat{a}^\dagger\hat{a} + \frac{1}{2}\right) + \hbar\omega_b(t)\left(\hat{b}^\dagger\hat{b} + \frac{1}{2}\right) + W\hat{\sigma}^\dagger\hat{\sigma} + \hat{V}, \tag{J.22}$$

where

$$\hat{V} = -\hat{\sigma}^\dagger\left(\chi_a\hat{a} + \chi_b\hat{b}\right) - \hat{\sigma}\left(\chi_a^*\hat{a}^\dagger + \chi_b^*\hat{b}^\dagger\right)$$

and $\chi_{a,b}(t) = \mathbf{d}\cdot\mathbf{E}_{a,b}$.

Summing up the known (see e.g. [158, 159]) partial Lindbladians of two bosonic (infinite amount of energy levels) and one fermionic (two-level) subsystems, we obtain

$$\begin{aligned} L(\hat{\rho}) \;=\; & -\frac{\gamma}{2}N_1^{T_a}\left(\hat{\sigma}\hat{\sigma}^\dagger\hat{\rho} + \hat{\rho}\hat{\sigma}\hat{\sigma}^\dagger - 2\hat{\sigma}^\dagger\hat{\rho}\hat{\sigma}\right) - \frac{\gamma}{2}N_0^{T_a}\left(\hat{\sigma}^\dagger\hat{\sigma}\hat{\rho} + \hat{\rho}\hat{\sigma}^\dagger\hat{\sigma} - 2\hat{\sigma}\hat{\rho}\hat{\sigma}^\dagger\right) \\ & -\frac{\mu_a}{2}\overline{n}_a^{T_{em}}\left(\hat{a}\hat{a}^\dagger\hat{\rho} + \hat{\rho}\hat{a}^\dagger\hat{a} - 2\hat{a}^\dagger\hat{\rho}\hat{a}\right) - \frac{\mu_a}{2}\left(\overline{n}_a^{T_{em}} + 1\right)\left(\hat{a}^\dagger\hat{a}\hat{\rho} + \hat{\rho}\hat{a}\hat{a}^\dagger - 2\hat{a}\hat{\rho}\hat{a}^\dagger\right) \\ & -\frac{\mu_b}{2}\overline{n}_b^{T_{em}}\left(\hat{b}\hat{b}^\dagger\hat{\rho} + \hat{\rho}\hat{b}^\dagger\hat{b} - 2\hat{b}^\dagger\hat{\rho}\hat{b}\right) - \frac{\mu_b}{2}\left(\overline{n}_b^{T_{em}} + 1\right)\left(\hat{b}^\dagger\hat{b}\hat{\rho} + \hat{\rho}\hat{b}\hat{b}^\dagger - 2\hat{b}\hat{\rho}\hat{b}^\dagger\right), \end{aligned} \tag{J.23}$$

where γ is an inelastic relaxation constant for an isolated atom, $\mu_{a,b}$ are relaxation constants of the EM modes determined by the cavity Q-factor;

$$N_0^{T_a} = \frac{1}{1 + e^{-\frac{W}{T_a}}},\; N_1^{T_a} = \frac{e^{-\frac{W}{T_a}}}{1 + e^{-\frac{W}{T_a}}},\; \overline{n}_{a,b}^{T_{em}} = \frac{1}{e^{\frac{\hbar\omega_{a,b}}{T_{em}}} - 1},$$

where $T_{a,em}$ are the temperatures of the atomic and EM dissipative reservoirs, respectively. It is assumed that these reservoirs are statistically independent.

For the Lindblad master equation in the form Eq. (J.18) we get

$$\hat{H}_{eff} = \hat{H} - i\hat{\Lambda}, \tag{J.24}$$

where

$$\hat{\Lambda} = \frac{\hbar}{2}\left\{\gamma\left(N_1^{T_a}\hat{\sigma}\hat{\sigma}^\dagger + N_0^{T_a}\hat{\sigma}^\dagger\hat{\sigma}\right) + \mu_a\left[\overline{n}_a^{T_{em}}\hat{a}\hat{a}^\dagger + \left(\overline{n}_a^{T_{em}}+1\right)\hat{a}^\dagger\hat{a}\right] + \mu_b\left[\overline{n}_b^{T_{em}}\hat{b}\hat{b}^\dagger + \left(\overline{n}_b^{T_{em}}+1\right)\hat{b}^\dagger\hat{b}\right]\right\}. \tag{J.25}$$

Using the effective Hamiltonian given by Eqs. (J.24),(J.25), we arrive at the stochastic equation for the state vector in the following form:

$$\left(\frac{\partial}{\partial t} + \gamma_{n_a n_b 1}\right) C_{n_a n_b 1} + i\left(\left(n_a + \frac{1}{2}\right)\omega_a(t) + \left(n_b + \frac{1}{2}\right)\omega_b(t) + \frac{W}{\hbar}\right) C_{n_a n_b 1}$$
$$- \frac{i}{\hbar}\langle n_a|\langle n_b|\langle 1|\hat{V}|\Psi\rangle = -\frac{i}{\hbar}\mathfrak{R}_{n_a n_b 1}, \tag{J.26}$$

$$\left(\frac{\partial}{\partial t} + \gamma_{n_a n_b 0}\right) C_{n_a n_b 0} + i\left(\left(n_a + \frac{1}{2}\right)\omega_a(t) + \left(n_b + \frac{1}{2}\right)\omega_b(t)\right) C_{n_a n_b 0}$$
$$- \frac{i}{\hbar}\langle n_a|\langle n_b|\langle 0|\hat{V}|\Psi\rangle = -\frac{i}{\hbar}\mathfrak{R}_{n_a n_b 0}, \tag{J.27}$$

where

$$\gamma_{n_a n_b 0} = \frac{\gamma}{2}N_1^{T_a} + \frac{\mu_a}{2}\left[\overline{n}_a^{T_{em}}(n_a+1) + \left(\overline{n}_a^{T_{em}}+1\right)n_a\right] + \frac{\mu_b}{2}\left[\overline{n}_b^{T_{em}}(n_b+1) + \left(\overline{n}_b^{T_{em}}+1\right)n_b\right], \tag{J.28}$$

$$\gamma_{n_a n_b 1} = \frac{\gamma}{2}N_0^{T_a} + \frac{\mu_a}{2}\left[\overline{n}_a^{T_{em}}(n_a+1) + \left(\overline{n}_a^{T_{em}}+1\right)n_a\right] + \frac{\mu_b}{2}\left[\overline{n}_b^{T_{em}}(n_b+1) + \left(\overline{n}_b^{T_{em}}+1\right)n_b\right], \tag{J.29}$$

Eqs. (J.28),(J.29) determine the rules of combining the "partial" relaxation rates for several coupled subsystems.

The above expressions include only inelastic relaxation rates. The general procedure of adding elastic relaxation (pure dephasing) is described in [154]. For the simple RWA models considered in this paper this procedure is reduced to adding γ_{el} to γ_{001} and changing the noise correlator according to $D_{001;001} \Rightarrow D_{001;001} + 2\gamma_{el}\overline{|C_{001}|^2}$.